Universitat Autònoma de Barcelona

Probing beyond the Standard Model physics using effective field theory

Thibaud Vantalon

PROBING BEYOND THE STANDARD MODEL PHYSICS USING EFFECTIVE FIELD THEORY

A dissertation aimed at the achievement of Ph.D. in physics

Author
THIBAUD VANTALON

Supervisor
Prof. Christophe Grojean

Tutor
Dr. Oriol Pujolás Boix

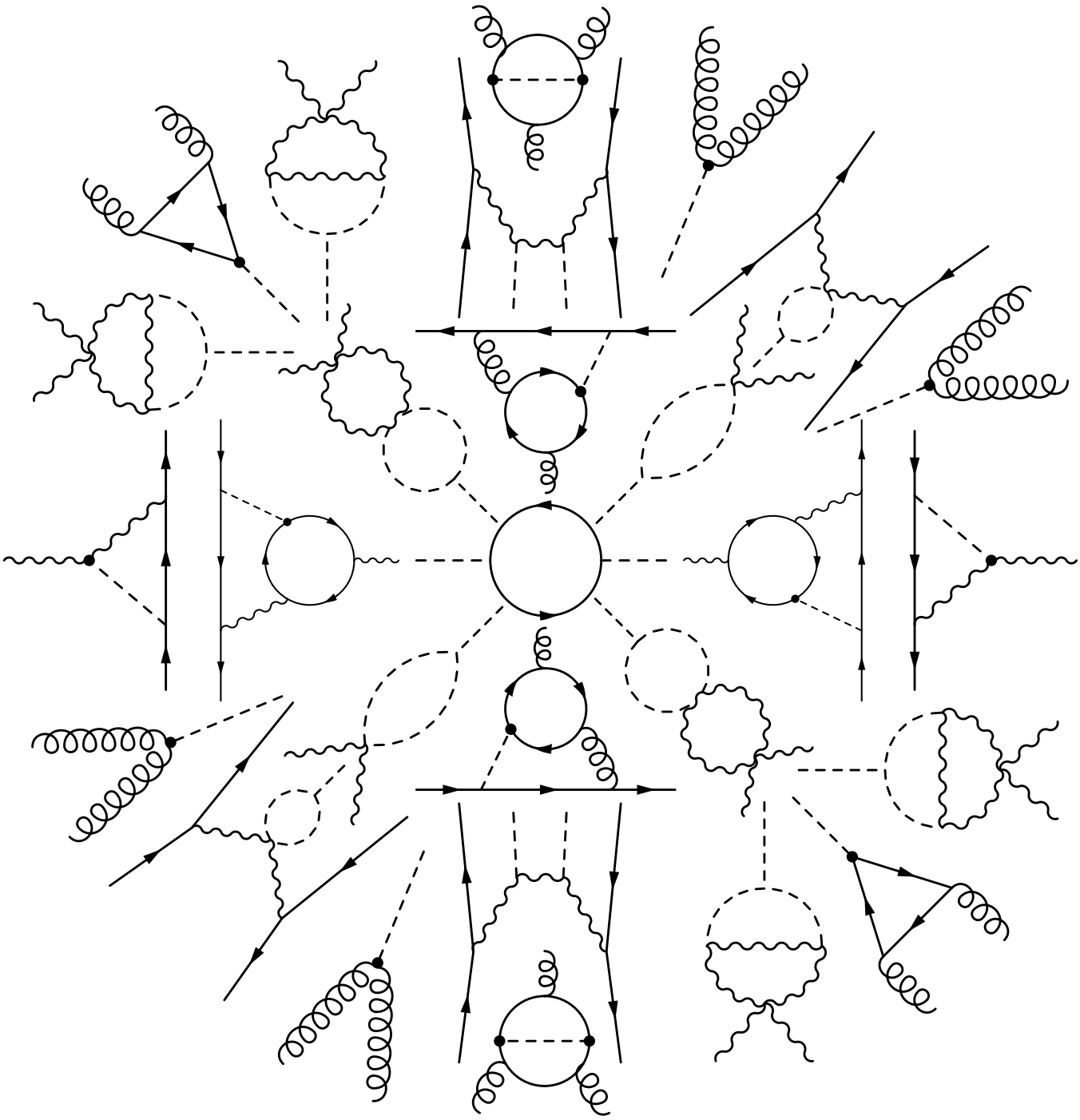

Institut de Física d'Altes Energies
Grup de Física Teòrica
Departament de Física – Facultat de Ciències
Universitat Autònoma de Barcelona

2018

Probing beyond the Standard Model physics using effective field theory

A dissertation aimed at the achievement of Ph.D. in physics

Author:
Thibaud Vantalon

Supervisor:
Prof. Christophe Grojean

Tutor:
Dr. Oriol Pujolás Boix

Institut de Física d'Altes Energies
Grup de Física Teòrica
Departament de Física – Facultat de Ciències
Universitat Autònoma de Barcelona

February 26, 2018

To the tuning which brought me here.

Research is a wasteful process

— Gian Francesco Giudice

ABSTRACT

Now the LHC has provided 120 fb^{-1} of data, the evidence for an energy gap between the Standard Model (SM) and new physics has grown strong. This makes effective field theory (EFT) a versatile method to constrain new physics with minimal model dependence. In this thesis, based on work done during my PhD candidature [1–4], we make use of EFT techniques in a variety of studies. We start by exploring the prospect of extracting the Higgs trilinear self-coupling at current hadron and future lepton colliders, using both higher order corrections to the single-Higgs process and di-Higgs production. Our analysis minimizes model dependence thanks to the use of EFT. We argue that in order to constrain the different possible deviations to the Standard Model, a global fit with the inclusion of as many observables as possible is needed. We found that the inclusion of the trilinear correction in single-Higgs processes has a marginal effect at the LHC and will give a bound on the trilinear of order one. The situation is different at lepton colliders, where the high precision and different running energies can give bound of order 50%. We then extend our EFT by adding a scalar singlet to study the CP properties of the particle which could have been behind the infamous 750 GeV di-photon excess. We define the CP sensitive asymmetries, in both the vector and gluon fusion channels, and study their power to differentiate between the CP odd or even hypotheses. Finally, we move somewhat away from EFT, and use a simplified model to compare the constraints on composite Higgs models coming from low energy neutron and electron electric dipole moment (EDM) measurements and LHC searches. Effective field theory is not completely absent, since we compute the two loop corrections of the light quarks and leptons EDM to match our simplified model to the higher dimensional operators of a low energy effective Lagrangian, and obtain bounds for our model. We then recast LHC searches and compare the present and future bounds. We found that the current bounds are competitive with the one coming from the LHC direct search and are of order a few TeV. The future upgrade of the experiment measuring the electron dipole moment should bring the bounds to the 5-10 TeV range.

LIST OF WORKS

Papers realized during the PhD and presented in this thesis:

1. Probing light top partners with CP violation
   Giuliano Panico, Marc Riembau , Thibaud Vantalon
   Submitted to JHEP for publication, arXiv:1712.06337 [hep-ph]

2. A global view on the Higgs self-coupling at lepton colliders
   Stefano Di Vita, Gauthier Durieux, Christophe Grojean, Jiayin Gu, Zhen Liu, Giuliano Panico, Marc Riembau, Thibaud Vantalon
   JHEP to be published, arXiv:1711.03978 [hep-ph]

3. A global view on the Higgs self-coupling
   Stefano Di Vita, Christophe Grojean, Giuliano Panico, Marc Riembau, Thibaud Vantalon.
   JHEP09(2017)069, arXiv:1704.01953 [hep-ph]

4. Deciphering the CP nature of the 750 GeV resonance
   Mikael Chala, Christophe Grojean, Marc Riembau, Thibaud Vantalon
   Phys. lett. B. 2016.06.050, arXiv:1604.02029 [hep-ph]

Paper realized before the PhD:

5. Composite Charge 8/3 Resonances at the LHC
   Oleksii Matsedonskyi, Francesco Riva, Thibaud Vantalon
   JHEP1404(2014)059, arXiv:1401.3740 [hep-ph]

ACKNOWLEDGEMENT

I am monstrously grateful to all the people without whom I would not be here today. In a somehow chronological order,

Je veux commencer par remercier toute ma famille et particulièrement, ma mère Martine, mon père, Jacky et ma grande petite sœur Sarah qui ont toujours été là pour moi. Un énorme merci à tous mes amis d'enfance en commençant par Louis à qui je dois la plupart de mon savoir informatique. Mes amis Corentin, Jérôme, Cyril, Antony, Arnaud sur qui je pourrai toujours compter. L'ordre chronologique nous amène finalement où les choses sérieuses ont commencé. Je voudrai remercier les "3 Mousquetaires", Sam, Emmanuel et Victor sans qui tout aurai été "vachement" moins drôle !

Which bring us to Riccardo Rattazzi and Francesco Riva, who introduced me to quantum field theory and helped me to get my PhD student position. Which at last bring me to Christophe Grojean who accepted me as his student and taught me and helped me during those four years. A big thank to José Ramón Espinosa Sedano for the physics discussion. Without him, Clara and the two Marc my Catalan and Spanish level would never have allowed me to survived the Spanish administration.

I am also very grateful to my IFAE and DESY colleagues and friends, (Marc)$^{i\,1}$, Clara, Mateo, Mat^{2}eo (no higher order presently known), Sergi, Joan, Lindber, Xabier, Bernat, Daniel, Oriol, Sebastian, Oleksii, Marco, Felix, Filippo, Iason, Jiayin, Nayara, Yann, Thomas, Valerie, Yannick, Riccardo, Benedict, Ibrahim. A special mention is worth for my collaborators Giuliano, Marc, Stefano, Jiayin, Zhen, Gauthier, Mikael, Emanuele and Christophe.

A special thanks to the bouldering crew especially Rob Klabbers for the extra challenge! And my flatmate for the Catan game and the fun time: Moli, Alex, Javier, Anna, Christoph, Frederike, Jakab.

A huge thanks to Jérome for the title page and Iason, Gauthier, Benedict and Nayara for their valuable comments and try to minimize the number of spelling mistakes.

I am also grateful to the creators of the classicthesis LaTeX template which I used to write this document.

1 With i the generation index running from 1 to 2

CONTENTS

PREFACE

July 4, 2012, early morning, after an overnight wait for some, people are impatiently in line, not for the new trendy gadget or to watch the premier of the new blockbuster movie, this queue is not in front of a shop, or a cinema but in front of an auditorium at conseil européen pour la recherche nucléaire (CERN). There are indeed three stars in this day and an announcement which is synonym, for the two present, of a Nobel prize. Indeed, after approximatively $10\,\text{fb}^{-1}$, distributed between 7 TeV and 8 TeV, of acquired data, both large hadron collider (LHC) [5] experiments ATLAS [6] and CMS [7] see a bump at 125 GeV in the four-lepton and di-photon invariant mass distributions. The significance of this bump finally reached the 5σ level, favoring the signal hypothesis over the background only one. This mean the discovery of a new particle. The data are compatible with the Glashow-Weinberg-Salam theory of weak interaction [8–10]. This model uses the Brout-Englert-Higgs mechanism [11–13] (named after the three stars of the day) to explain how the gauge bosons and fermions acquire a mass. It also means that all the particles of the standard model (SM) have finally been discovered.

This is a big revolution; we finally have a model explaining the interactions between elementary particles which is mathematically consistent up to the Planck scale. Six years later, the interactions of this new particle are being measured more and more precisely and have been so far consistent with the SM.

This is of course not the end of the story. Despite the fact this model can be extrapolated up to the scale at which gravity is expected to enter the game, a scale orders of magnitude above what present human made experiments can probe, it is incomplete. It still fails to explain the motion of stars far from the center of their host galaxy and comes with several unanswered questions. We do not understand why the mass of the Higgs boson is so small, since the mass of an elementary scalar particle should receive huge quantum corrections. This calls for an explanation. While two appealing explanations, composite Higgs (CH) and super symmetry (SUSY) call for new physics at the weak scale, there are also experimentally less appealing solutions (due to their lack of observable consequences) like the multiverse and its anthropic principle or the new recent dynamical solution using the relaxion mechanism.

We now stand six years after the discovery and no new physics is to be found. Meanwhile, few excesses here and there, but the bounds of beyond the standard model (BSM) models start to reach 1 TeV. The community starts to wonder where the new physics is hiding. In this thesis, we will look at the prospects of using effective field theory (EFT) to probe BSM physics. Indeed, EFT is a powerful tool to achieve this goal, since it allows us to parametrize deviations from the SM coming from high scale physics with a minimal dependency on the underlying model. The higher the energy scale of new physics, the more precise this method becomes. That is why it is adapted to study the LHC data. Of course some care is needed, and the possibility for low energy new physics such as stealth SUSY or dark matter (DM) with light mediators cannot be ignored. Specific searches using other approaches are needed to handle such cases. Throughout this work, we are going to go through several uses of EFT.

This thesis starts in Part i by reviewing the basics. Chapter 1 is dedicated to a quick review of the SM and the Higgs mechanism and the questions the SM leaves open. We follow by presenting in section 2.2 a natural way to expend the SM assuming new physics is heavy. In this chapter, we use the available freedom to define the Higgs basis. As its name indicates, this basis is useful to study Higgs physics.

In the Part ii of the thesis, we study the trilinear Higgs self-coupling. Despite all the evidence pointing toward a SM like Higgs boson, several of its couplings have not yet been directly measured. Unfortunately, this is a challenging task, since the relevant processes suffer from small cross sections. We review the current constraints on the Higgs sector and on how to parametrize new physics in chapter 3. We combine the usual method, double-Higgs production, and a novel approach using higher order effects in single-Higgs production, to look at the prospect of measuring the Higgs trilinear at high luminosity LHC (HL-LHC) in chapter 4, and at future lepton collider in chapter 5. These analyses are done minimizing model dependence thanks to the use of EFT. These two parts contain respectively the papers in references [2, 3] with small modifications.

In Part iii, we look at the possibility of studying and constraining new physics. In chapter 7, we look at a different EFT. Based on the (in)famous excess of Christmas 2015, we study the possibility of measuring the charge conjugation and parity (CP) property of a new scalar particle decaying into photons. This time, we minimally extend the SM by adding one field and assume the particles coupling to this new boson are heavy enough to be integrated out. This allow us to write the allowed interactions between the SM and this new field using higher dimensional operators. We study several channels where asymmetries sensitive to the CP property of the boson can be built and study the constraints the HL-LHC would give. This part contains the work in reference [4]. In chapter 8, we want to study a more specific class of models, and focus on the CH scenario. In order to do so, we change our approach and use a simplified Lagrangian capturing the relevant effects. We study and compare the constraints coming from low energy physics, more specifically electric dipole moment measurements, on the mass of possible new top partners coming from the composite sector, with the ones from LHC. While we are not directly using EFT, it is interesting to note that the bounds on the dipole moments are given in terms of higher dimensional operators and that we match our simplified model to these operators to obtain the bounds.

DISCLAIMER

This thesis has been submitted in March 2018 and presents work realized between 2014 and end of 2017, which means that part of the work may be outdated. This is the case of the presented experimental results. Indeed, as these lines are being written, both ATLAS and CMS have recorded around $50\,\text{fb}^{-1}$ of additional data, for which the public results are not available yet. This situation is going to change after the Moriond conference at the end of March, where the latest results may be made available.

Considering the work, most of it could eventually led updated using the latest experimental results, however, the main message should not change, with the exception of the work based on the (in)famous 750 GeV excess. The concerning the latter are already outdated, however, the technique used could be transposed to any new excess seen in the relevant channels.

It should also be noted that parts of this thesis come directly from the work published or submitted for publication in references [1–4], with some modifications to keep the coherence of ensemble.

Part I

THE FRAMEWORK

1 THE STANDARD MODEL

1.1 FIELDS AND SYMMETRIES

The SM is the minimal model which can explain almost all the collider physics experiments and more generally most of the high energy data. One notable failure being the observation of neutrino oscillations. Of course, we can also take into account deviation in the muon magnetic dipole moment or in b physics. While the neutrino oscillation can be explained by a minimal addition to the SM. None of the other deviation have reached the 5σ statistical significance needed to be considered a discovery. In order to reach this impressive description of nature, physicists had to unify quantum mechanics and special relativity into quantum field theory (QFT), in which nature is described by interacting quantized fields, the quanta being particles. By construction, it does not include gravity which is too weak to be probed by high energy physics experiment. In this chapter, we propose a brief review of the main features of the SM based on references [14–17].

The SM is described by the most general Lagrangian following two rules and a given field content. The first rule demands the Lagrangian to be re-normalizable, which in practice limits the operators' mass dimension to be equal to or smaller than four. The second rule is the symmetry under which the Lagrangian is invariant. It should be invariant under both the global Poincaré symmetry and the gauge group:

$$SU(3) \times SU(2)_L \times U(1)_Y. \tag{1.1}$$

Finally we need to specify the field content and its transformation properties under the different symmetries. The list of representations are given in Table 1.1. The fermionic degrees of freedoms come in three generations:

$$e_R^i = (e_R, \mu_R, \tau_R)^T,\ u_R^i = (u_R, c_R, t_R)^T,\ d_R^i = (d_R, s_R, b_R)^T \tag{1.2}$$

and the three generation of left-handed doublets

$$Q_L^i = \begin{pmatrix} u_L^i \\ d_L^i \end{pmatrix}, \qquad L_L^i = \begin{pmatrix} e_L^i \\ \nu_L^i \end{pmatrix}, \tag{1.3}$$

where the left handed component of the doublets are the same as their right handed counterpart

$$e_L^i = (e_L, \mu_L, \tau_L)^T,\ u_L^i = (u_L, c_L, t_L)^T,\ d_L^i = (d_L, s_L, b_L)^T \tag{1.4}$$

with the addition of the left-handed neutrinos $\nu_{eL}^i = (\nu_{eL}, \nu_{\mu L}, \nu_{\tau L})^T$.

An interesting game to play is to compare the most general Lagrangian of dimension less than or equal to 4 that we can write versus a "phenomenological" Lagrangian describing experimental data. The Lagrangian with the fields in gauge eigenstates can schematically be written as,

$$\mathscr{L}_{SM} = \mathscr{L}^{kin}_{Gauge} + \mathscr{L}^{topo}_{Gauge} + \mathscr{L}^{kin}_{fermion} + \mathscr{L}_{Higgs} + \mathscr{L}_{Yukawa}\,, \tag{1.5}$$

Field	$SL(3,\mathbb{C})$	$SU(3)$	$SU(2)$	$U(1)$
Q_L^i	$(\frac{1}{2},0)$	**3**	**2**	$\frac{1}{6}$
u_R^i	$(0,\frac{1}{2})$	**3**	**1**	$\frac{2}{3}$
d_R^i	$(0,\frac{1}{2})$	**3**	**1**	$-\frac{1}{3}$
L_L^i	$(\frac{1}{2},0)$	**1**	**2**	$-\frac{1}{2}$
e_R^i	$(0,\frac{1}{2})$	**1**	**1**	-1
W	$(\frac{1}{2},\frac{1}{2})$	**1**	**adj**	0
B	$(\frac{1}{2},\frac{1}{2})$	**1**	**1**	0
G	$(\frac{1}{2},\frac{1}{2})$	**adj**	**1**	0
H	$(0,0)$	**1**	**2**	$\frac{1}{2}$

Table 1.1: Standard Model field quantum number. The adjoint representation is indicated by "**adj**".

and is given by:

$$\mathscr{L}_{SM} = -\frac{1}{4}G^{\mu\nu}G_{\mu\nu} - \frac{1}{4}W^{\mu\nu}W_{\mu\nu} - \frac{1}{4}B^{\mu\nu}B_{\mu\nu} \tag{1.6}$$

$$- \frac{\theta_s}{16\pi^2}G^{\mu\nu}\tilde{G}_{\mu\nu} - \frac{\theta_w}{16\pi^2}W^{\mu\nu}\tilde{W}_{\mu\nu} - \frac{\theta_b}{16\pi^2}B^{\mu\nu}\tilde{B}_{\mu\nu} \tag{1.7}$$

$$+ i\bar{Q}_L^i \not{D} Q_L^i + i\bar{u}_R^i \not{D} u_R^i + i\bar{d}_R^i \not{D} d_R^i + i\bar{L}_R^i \not{D} L_R^i + i\bar{e}_R^i \not{D} e_R^i \tag{1.8}$$

$$+ |D_\mu H|^2 + \mu^2 HH^\dagger - \lambda(HH^\dagger)^2 \tag{1.9}$$

$$- \left(Y_u^{ij}\bar{Q}_L^i \tilde{H} u_R^j + Y_d^{ij}\bar{Q}_L^i H d_R^j + Y_e^{ij}\bar{L}_L^i H e_R^j + \text{h. c.}\right), \tag{1.10}$$

where the G, W, B are the $SU(3)$, $SU(2)_L$ and $U(1)_Y$ field strengths, given for a generic gauge field F by $F^a_{\mu\nu} \equiv \partial_\mu F^a_\nu - \partial_\nu F^a_\mu - i g_f f^{abc} F^b_\mu F^c_\nu$. here g_f is the corresponding gauge coupling and f the antisymmetric structure constants of the gauge group. For example, for the Abelian group $U(1)$ f vanishes, for $SU(2)$ f is the Levi-Civita tensor ϵ. $\tilde{F}$ is the dual defined as $\tilde{F}^{\mu\nu} = \frac{1}{2}\epsilon^{\mu\nu\alpha\beta}F_{\alpha\beta}$ and D is the covariant derivative given by

$$D_\mu \equiv \partial_\mu - i g_s \lambda_a G^a_\mu - i g T^a W^a_\mu - i g' Y B_\mu\,, \tag{1.11}$$

with λ the $SU(3)$ generators, T the $SU(2)$ ones and Y the hypercharge.

We can compare this Lagrangian with a phenomenological one, which can be written as

$$\mathscr{L}_{PH} = \mathscr{L}^{kin}_{Gauge} + \mathscr{L}^{kin}_{fermion} + \mathscr{L}_{Higgs} + \mathscr{L}_{mass} + \mathscr{L}_{Yukawa}\,, \tag{1.12}$$

containing new fields which, with the exception of the Higgs field h, are related to the ones of the Lagrangian in Equation 1.6 by a change of variables. It reads:

$$\mathscr{L}_{PH} = -\frac{1}{4}G^{\mu\nu}G_{\mu\nu} - \frac{1}{2}W^{+\mu\nu}W^-_{\mu\nu} - \frac{1}{4}Z^{\mu\nu}Z_{\mu\nu} - \frac{1}{4}A^{\mu\nu}A_{\mu\nu} \tag{1.13}$$

$$+ i\bar{Q}_L'^i \not{D}' Q_L'^i + i\bar{u}_R'^i \not{D} u_R'^i + i\bar{d}_R'^i \not{D} d_R'^i + i\bar{L}_L'^i \not{D} L_L'^i + i\bar{e}_R'^i \not{D} e_R'^i \tag{1.14}$$

$$+ {m_W}^2 W^{\mu-} W^+_\mu + \frac{{m_Z}^2}{2} Z^\mu Z_\mu \tag{1.15}$$

Field	$0^+(3,1)$	$SU(3)$	$SU(2)$	$U(1)$
ν_R	$(0,\frac{1}{2})$	1	1	0

Table 1.2: Quantum numbers of the extra neutrino

$$+\frac{1}{2}|D_\mu h|^2 - \frac{{m_h}^2}{2}h^2 - \frac{{m_h}^2}{2v}h^3 - \frac{{m_h}^2}{8v^2}h^4 \tag{1.16}$$
$$-\left(m_u^i \bar{u}_L'^i u_R'^i + m_d^i \bar{d}_L'^i d_R'^i + m_e^i \bar{e}_L'^i e_R'^i + \text{h. c.}\right) \tag{1.17}$$
$$-\frac{h}{v}\left(m_u^i \bar{u}_L'^i u_R'^i + m_d^i \bar{d}_L'^i d_R'^i + m_e^i \bar{e}_L'^i e_R'^i + \text{h. c.}\right), \tag{1.18}$$

In the following section, we review how the two Lagrangians are linked. It can also be noted that $\mathscr{L}_{\text{PH}}$ is not completely phenomenological, in the sense that some couplings have not yet been measured and that we are missing the neutrino masses. We also stay vague about the exact definition of the fields[1], since we only want to focus on some keys differences between the two Lagrangians.

At the first sight the two Lagrangians are not compatible. Indeed, the gauge boson and fermion mass terms break the gauge symmetry and seem incompatible with Table 1.1. The Higgs doublet field H as been replaced with a new real field called h. We also added a prime in the covariant derivative of the left-handed fermions. Finally, we removed the topological terms.

Before solving the apparent contradictions between the two Lagrangians, another remark can be done; there is no mass term for the neutrinos. Observation of neutrino oscillation is a direct proof that neutrinos have masses. However, with the given field content and with terms of dimension lower than five it is impossible to have neutrino mass terms.

This problem has several solutions. We quickly cite two of them here. The most minimalistic could be the introduction of a right-handed singlet neutrino field as show in Table 1.2. With this extra field writing a mass term of dimension lower than five is now allowed by the symmetries. Another interesting solution would be to allow terms of higher dimension in the Lagrangian. Indeed, the dimension-5 Weinberg operator,

$$\frac{1}{2}\frac{c_{\alpha\beta}}{\Lambda}\bar{L}^c_{L\alpha}\tilde{H}^*\tilde{H}^\dagger L_{L\beta} + \text{h. c.}, \tag{1.19}$$

with $\tilde{H} \equiv i\sigma_2 H^*$, generates a Majorana mass term for the neutrinos after electroweak symmetry breaking (EWSB). A Majorana mass term only involve left or right handed fermions with the main consequence that the fermion should be its own ant-particle.

1.2 THE BROUT-ENGLERT-HIGGS MECHANISM

1.2.1 *Gauge boson masses*

One of the issues with the Lagrangian (1.13) is that mass term for fermions and gauge bosons are forbidden as they break the $SU(2)$ gauge symmetry. As a side remark, it is interesting to note that without the Higgs mechanism which we discuss below, the W

1 For example the gauge field strenghts are hiding the gauge boson interactions.

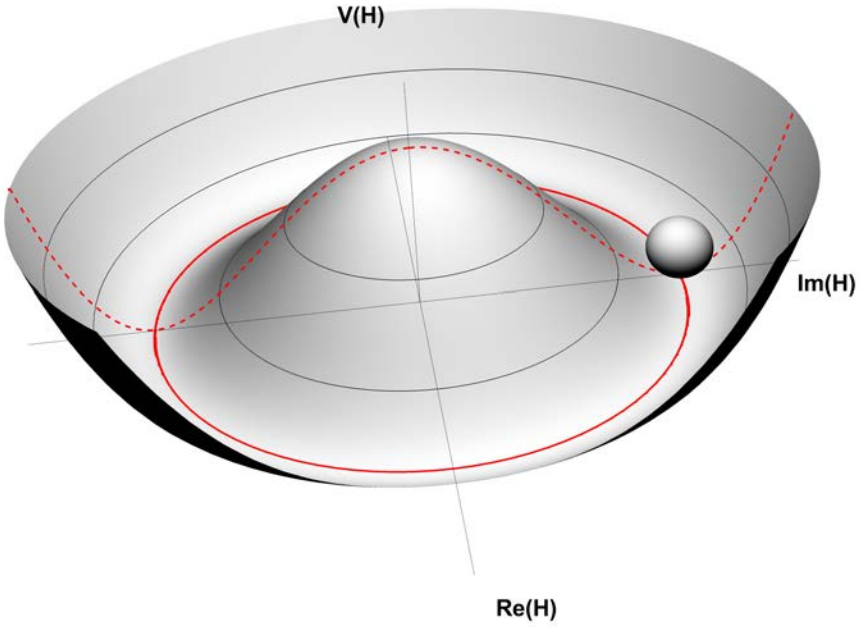

Figure 1.1: Higgs potential with a ball representing one of the possible minima.

gauge bosons would not be massless. Due to a quantum chromo-dynamics (QCD) effect in the form of pion exchange, they would get a mass of order 29 MeV [18]. The electroweak (EW) symmetry being broken at low energy by the quark condensate. Despite being an interesting effect, it is far from enough to reproduce the experimental masses.

The gauge boson masses instead come, not from the quark condensate, but from another mechanism. Extracting the potential and kinetic term of Equation 1.6:

$$\mathscr{L}_{\text{Higgs}} = |D_\mu H|^2 + \mu^2 H H^\dagger - \lambda (H H^\dagger)^2 \,, \tag{1.20}$$

we can see a peculiarity: the mass squared term is negative! This allows the potential for the Higgs doublet to posses a degenerate set of minima for field values

$$|H| = \frac{v}{\sqrt{2}}, \quad \text{where} \quad v \equiv \left(\frac{\mu^2}{\lambda}\right)^{\frac{1}{2}} \tag{1.21}$$

as represented with a continuous red line in Figure 1.1. Here v is called the vacuum expectation value (vev). A chosen minimum is not invariant under the same symmetry as the Langrangian since we can rotate it and obtain another valid minimum. This mechanism is also known as spontaneous symmetry breaking. Without entering in the details of the Goldstone theorem, the perturbation of the potential in the angular direction correspond to the massless Goldstone bosons (the broken symmetry generators), while the radial perturbation (in dotted) corresponds to the massive degree of freedom (*i. e.* the physical Higgs boson). Choosing a vacuum spontaneously breaks the SM symmetries

$$SU(3) \times SU(2)_L \times U(1)_Y \to SU(3) \times U(1)_{\text{em}} \,, \tag{1.22}$$

with a total of 3 broken generators. Without fixing the gauge, we would see three massless degrees of freedom in the theory. Going into the unitary gauge, however, we can make

these degrees of freedom disappear from the Lagrangian in exchange for an explicit mass term for the gauge bosons. This is the so called Brout-Englert-Higgs mechanism [11–13].

Explicitly, we do a gauge transformation and rewrite the doublet field as

$$H = \frac{1}{\sqrt{2}} \begin{pmatrix} 0 \\ v + h(x) \end{pmatrix} . \tag{1.23}$$

With theses new variables, the Higgs potential becomes

$$V = \frac{1}{2} m_h^2 h^2 + \frac{m_h^2}{2v} h^3 + \frac{m_h^2}{8v^2} h^4 \tag{1.24}$$

and the Higgs field obtains a tree level mass

$$m_h = v\sqrt{2\lambda} . \tag{1.25}$$

Rewriting the Higgs kinetic term in term of theses new degrees of freedom and expanding the covariant derivative of the Higgs doublet, one finds;

$$(DH)^2 = \frac{1}{2}(\partial_\mu h)^2 + \frac{1}{2}\frac{(v+h)^2}{4}\left[g^2(W_\mu^1)^2 + g^2(W_\mu^2)^2 + (-g(W_\mu^3) + g'B)^2\right] . \tag{1.26}$$

We see that the gauge bosons became massive, and in addition W^3 and B mix. The mass eigenstates are given by

$$\begin{aligned} W_\mu^\pm = \frac{1}{\sqrt{2}}\left(W_\mu^1 \pm i W_\mu^2\right) , \qquad Z_\mu^0 = \frac{1}{\sqrt{g^2+g'^2}}\left(g W_\mu^3 - g' B_\mu\right) , \\ A_\mu = \frac{1}{\sqrt{g^2+g'^2}}\left(g' W_\mu^3 + g B_\mu\right) \end{aligned} \tag{1.27}$$

and have leading order masses given respectively by $m_W = \frac{gv}{2}$, $m_Z = \frac{v}{2}\sqrt{g^2+g'^2}$, and $m_A = 0$. Although the photon stays massless at all orders in perturbation theory, the other gauge bosons receive correction to their masses. We define the Weinberg rotation angles

$$\cos\theta_w = c_{\theta_w} = \frac{g}{\sqrt{g^2+g'^2}} , \qquad \sin\theta_w = s_{\theta_w} = \frac{g'}{\sqrt{g^2+g'^2}} . \tag{1.28}$$

The expression of the covariant derivatives Equation 1.11 in the new variables, becomes

$$\begin{aligned} D_\mu = \partial_\mu - i g_s \lambda_a G_\mu^a - i\frac{g}{\sqrt{2}}\left(W_\mu^+ T^+ + \text{h.c.}\right) - i\frac{1}{\sqrt{g^2+g'^2}} Z_\mu \left(g^2 T^3 - g'^2 Y\right) \\ - i\frac{g g'}{\sqrt{g^2+g'^2}} A_\mu \left(T^3 + Y\right) , \end{aligned} \tag{1.29}$$

where $T^\pm = \left(T^1 \pm i T^2\right)$. The term with the photon can be used to read off the electric charge in therms of the gauge coupling:

$$e = \frac{g g'}{\sqrt{g^2+g'^2}} . \tag{1.30}$$

Finally, we define the famous ρ parameter,

$$\rho = \frac{m_w^2}{m_z^2 \cos\theta} , \tag{1.31}$$

which is equal to 1 at leading order; a consequence of the approximate custodial symmetry of the Higgs sector.

This mechanism, where the three massless Goldstone bosons are "eaten up"[2] by the vectors is due to Brout, Englert and Higgs. Englert and Higgs won the Nobel prize in 2013 for their research. Unfortunately, Brout passed away in 2011 and therefore missed both the Higgs boson discovery and the Nobel prize.

1.2.2 *Fermion masses and implications*

The mechanism we presented in the previous section, allows us to do more than give a mass to the gauge bosons. Since the fermion mass terms also break the gauge symmetry, it can be expected that the spontaneous breaking of the symmetry can also be used to solve this issue. The term:

$$\mathscr{L} \supset Y_u^{ij} \bar{Q}_L^i \tilde{H} u_R^j + Y_d^{ij} \bar{Q}_L^i H d_R^j + Y_e^{ij} \bar{L}_L^i H e_R^j + \text{h. c.}\,, \tag{1.32}$$

becomes, after the Higgs takes a vev,

$$\mathscr{L} \supset v \left(\frac{Y_u^{ij}}{\sqrt{2}} \bar{u}_L^i u_R^j + \frac{Y_d^{ij}}{\sqrt{2}} \bar{d}_L^i d_R^j + \frac{Y_e^{ij}}{\sqrt{2}} \bar{e}_L^i e_R^j + \text{h. c.} \right) + (v \to h) \tag{1.33}$$

and gives mass terms to almost all the fermion. As said before, some extension to the SM is needed to take into account neutrino masses. However, the Yukawa matrices Y_u, Y_d and Y_e are not diagonal, we need to change variables to obtain the propagating degrees of freedom. This is achieved using a bi-unitary transformation:

$$U_L Y U_R = \text{diag}(y_1, y_2, y_3)\,, \tag{1.34}$$

where we have a pair of U matrices for each Yukawa matrix. The matrices U_L and U_R are the matrices diagonalizing $YY^\dagger$ and $Y^\dagger Y$ respectively. In this basis, each fermion gets a mass term given by

$$m^i = \frac{v}{\sqrt{2}} y^i. \tag{1.35}$$

These rotations are not without consequence for the left-handed fermions kinetic terms since they do not commute with the covariant derivative. The right-handed fermions are not affected since they do not couple to the weak force and the $SU(3)$ symmetry is flavor blind, meaning the change of basis commutes with the derivative. The situation is different for the left-handed quarks because the W links the upper and lower part of the quark doublets:

$$\begin{aligned} i\bar{Q}_L^i \not{D} Q_L^i \supset & \frac{g}{\sqrt{2}} \begin{pmatrix} \bar{u}_L'^i & \bar{d}_L'^i \end{pmatrix} \begin{pmatrix} 0 & \not{W}^+ \\ \not{W}^- & 0 \end{pmatrix} \begin{pmatrix} u_L'^i \\ d_L'^i \end{pmatrix} \\ = & \frac{g}{\sqrt{2}} \left(\bar{u}_L'^i \not{W}^+ d_L'^i + \text{h. c.} \right) \\ = & \frac{g}{\sqrt{2}} \left(\bar{u}_L^k U_u^{\dagger ki} \not{W}^+ U_d^{ij} d_L^j + \text{h. c.} \right) \end{aligned}$$

2 This term comes from the fact that the massless degrees of freedom disappear in the unitary gauge and a mass term for the Gauge bosons appears.

$$= \frac{g}{\sqrt{2}} \left(u_L^k V_{CKM}^{\dagger ki} W^+ d_L^i + \text{h. c.} \right) .$$

Here, we have defined the Cabibbo–Kobayashi–Maskawa (CKM) matrix [19, 20] $V_{CKM} = U_u^\dagger U_d$. Being the product of two unitary matrices, it is also a unitary matrix . The usual counting tells us that an N by N unitary matrices has N^2 parameters, in this case 3 angles and 6 phases. However, not all those parameters are physical. $2N - 1$ of them can be removed by redefining the left and right quarks field. The minus one comes from the global phase which is not physical and cannot be used to remove a parameter. This leave us with the 3 angles and one phase.

There is some freedom in the parametrization of the CKM matrix, one of the usual parametrization uses three Euler angles and one phase.

$$V_{CKM} = \begin{pmatrix} c_{12}c_{13} & s_{12}c_{13} & s_{13}e^{-i\delta_{13}} \\ -s_{12}c_{23} - c_{12}s_{23}s_{12}e^{i\delta_{13}} & c_{12}c_{23} - s_{12}s_{23}s_{13}e^{i\delta_{13}} & c_{23}c_{13} \\ s_{12}s_{23} - c_{12}c_{23}c_{13}e^{i\delta_{13}} & -c_{12}s_{23} - s_{12}c_{23}s_{13}e^{i\delta_{13}} & c_{23}c_{13} \end{pmatrix}, \quad (1.36)$$

where $c_{ij} = \cos\theta_{ij}$ and $s_{ij} = \sin\theta_{ij}$. The angle θ_{12} is called the Cabbibo angle.

The phase has a great phenomenological importance, since it violates the CP symmetry. The Lagrangian transform as follows under CP

$$\frac{g}{\sqrt{2}} \left(\bar{u}_L^i V_{CKM}^{ij} W^+ d_L^j + \bar{d}_L^i V_{CKM}^{ij*} W^- u_L^j \right) \xrightarrow{CP} \frac{g}{\sqrt{2}} \left(\bar{d}_L^i V_{CKM}^{ij} W^- u_L^j + \bar{u}_L^i V_{CKM}^{ij*} W^+ d_L^j \right) , \quad (1.37)$$

and therefore CP conservation would require that the CKM matrix is real, *i. e.* the complex phase δ_{13} should vanish. Experimentally, however this phase is not vanishing and the SM has explicit CP violation [21]. It is interesting to note that the CKM matrix needs at least three families to contain a complex phase and therefore, the SM has the minimal of needed number of families to violate CP. As we are going to discuss in the following section, another CP violating term is allowed in the Lagrangian, however it is constrained to be very small.

A BSM CP violation can also come from the neutrino sector. Giving a mass to the three neutrinos introduces an analog of the CKM matrix called the Pontecorvo–Maki–Nakagawa–Sakata (PMNS) matrix [22, 23]. The PMNS matrix can have two extra phases if the neutrinos get a Majorana mass term instead of a Dirac one.

1.3 THE $\bar{\theta}$ PARAMETERS

We are interested in the topological term of the Lagrangian:

$$\mathcal{L}_{SM} \supset \frac{\theta_s}{16\pi^2} G^{\mu\nu} \tilde{G}_{\mu\nu} + \frac{\theta_w}{16\pi^2} W^{\mu\nu} \tilde{W}_{\mu\nu} + \frac{\theta_b}{16\pi^2} B^{\mu\nu} \tilde{B}_{\mu\nu} , \quad (1.38)$$

$$\mathcal{L}_{PH} \supset \emptyset , \quad (1.39)$$

The θ parameters are not directly physical. The only physical combination is given by

$$\bar{\theta} = \theta_s - \theta_F \qquad \text{with} \qquad \theta_F = \arg\det Y_d Y_u , \quad (1.40)$$

with Y the Yukawa matrix. The phase from θ_s can be moved to the Yukawa matrix using a chiral rotation. This transformation leaves the quantity $\bar{\theta}$ unchanged. Therefore, it is possible to make θ_F vanish, and move all the effect into:

$$\frac{\bar{\theta}}{16\pi^2} G^{\mu\nu}\tilde{G}_{\mu\nu}\,. \tag{1.41}$$

It may seem surprising that a chiral rotation of the quarks modifies a term with no quark field. This is due to the chiral anomaly, *i.e.* the chiral symmetry is broken by quantum effects. In the path integral formalism, this means the action is invariant under the symmetry while the measure is not:

$$\int D\bar{\psi}D\psi \to \int D\bar{\psi}D\psi e^{i\int \theta \frac{g^2}{16\pi^2} F\tilde{F}}\,. \tag{1.42}$$

Here, F and g are the gauge groups under which the rotated quarks are charged. The angle is given by $\theta = \arg\det R^\dagger L$ for a chiral rotation with R and L acting on the right- and left-handed quarks respectively.

At first sight, $\bar{\theta}$ should not have a physical effect since it can be rewritten as a total derivative of the Chern-Simons current K,

$$K_\mu = \epsilon_{\mu\nu\alpha\beta}\left(A^a_\nu F^a_{\alpha\beta} - \frac{g}{3} f^{abc} A^a_\nu A^b_\alpha A^c_\beta\right) \to F_{\mu\nu}\tilde{F}^{\mu\nu} = 2\partial_\mu K^\mu\,, \tag{1.43}$$

and could be removed from the Lagrangian by integration by parts, up to a boundary term which usually vanishes. Nevertheless, some non-pertubative field configurations called instantons, give physical meaning to this term.

If, at least one quark mass was vanishing, the $\bar{\theta}$ term would not be physical since after a rotation

$$\arg\det Y_d Y_u = \arg\det M_d M_u = 0\,. \tag{1.44}$$

In contrast, θ_w and θ_b are not physical, since we can take advantage of the fact that the right-handed quarks and neutrino[3] are not charged under $SU(2)$ and $U(1)$ respectively to rotate the phase away. We can first move the phase from $F\tilde{F}$ to the Yukawa coupling and then rotate the right-handed fields to completely remove it.

The $\bar{\theta}$ term is called the strong CP phase since the $G\tilde{G}$ term breaks this symmetry. However, as (1.39) insinuate, the $\bar{\theta}$ term is currently not experimentally present in the SM. While the absence of term linked to the $SU(2)$ and $U(1)$ dual field strength as a mathematical explanation, the situation for $\bar{\theta}$ is only based on experimental evidence, which puts an upper bound of around $\bar{\theta} < 10^{-10}$ [24]. The smallness of $\bar{\theta}$ is puzzling, since we know the EW sector violates CP and there is therefore no reason for this term to be so small.

1.4 THE STANDARD MODEL IN NUMBERS

On top of the symmetry and field representation, we need to fix 19 parameters to completely define the SM. One of the possible choices is to fix the fermion masses, 6 for the quarks and 3 for the leptons, and the Higgs mass. In order to complete the scheme, we

3 If the neutrinos are massless, the determinant would vanish.

Fermions	m_u	m_d	m_c	m_s	m_t	m_b	m_e	m_μ	m_τ
[GeV]	0.002	0.005	1	0.1	173	4	0.0005	0.1	2

Boson	m_g	m_γ	m_W	m_Z	m_h
[GeV]	0	0	80	91	125

Table 1.3: Masses of the Standard Model

g'	g	g_s	θ_{12}	θ_{23}	θ_{13}	δ	v	$\bar{\theta}$
0.36	0.65	1.2	13°	2.4°	0.2°	57°	246 [GeV]	$\leqslant 10^{-10}$

Table 1.4: Gauge couplings, CKM mixing angles, vacuum expectation value and bound on the $\bar{\theta}$ parameter [25].

can add the Fermi constant (G_f), the Z mass m_Z, the strong and electric coupling constants α_s and α, the $\bar{\theta}$ parameter, the phase and the 3 angles of the CKM matrix. A few comments can be made on the precision of the measurements: the light quarks masses are known with a precision of order 10%, and the knowledge of the heavy ones reach the percent level, this is due to the difficulty in measuring light quark masses due to confinement. The situation for the leptons is inverted. This is due, in this case, to the lifetime and different decay channels. It can be noted that the Higgs mass is already known, six years after its discovery, to the sub-percent level. The chosen input parameters have an interesting consequence. The W mass is the only mass which is not an input of the theory but a prediction. In order to reproduce the experimental measurement of 80.385(15) GeV, loop effects need to be taken into account.

In order to make a link with the parameter seen in the previous section, we shown in Table 1.3 and Table 1.4 their numerical values. It should be noted that the tables have 22 parameters and therefore some of them are not independent. While the input parameters have the advantage to make a more direct link with experimental observables, the parameters presented in the tables are closer to the Lagrangian. A few comments can be made, the first one is about the fermion mass hierarchy; the masses grow with generation.[4] We also see that the complex phase of the CKM matrix is not vanishing and therefore a source of CP violation. Computing the entries of the CKM matrix, we schematically get an interesting structure

$$|V_{CKM}| \approx \begin{pmatrix} 0.97 & 0.23 & 0.0036 \\ 0.23 & 0.97 & 0.041 \\ 0.0087 & 0.040 & 1 \end{pmatrix} \sim \begin{pmatrix} 1 & \lambda & \lambda^3 \\ \lambda & 1 & \lambda^2 \\ \lambda^3 & \lambda^2 & 1 \end{pmatrix}, \tag{1.45}$$

with $\lambda \approx 0.2$. The matrix is therefore almost diagonal and the transition between generations are numerically strongly suppressed.

Adding Dirac neutrino masses, we need 3 extra mass parameters, 3 mixing angles and a complex phase, pushing the number of input parameters to 26. For Majorana neutrino, two extra phases are added for a total of 28 parameters.

4 The neutrino sector is still not experimentally constrained enough to confirm or invalidate this statement.

1.5 NEW PHYSICS OPPORTUNITIES

The Higgs discovery was a milestone for the SM, indeed, the last missing particle was discovered. More importantly, it also unitarised the theory. Without the Higgs, mathematical consistency is lost around the TeV scale. After the Higgs discovery the SM can be consistently extrapolated to the Planck scale without loss of unitarity or a Landau pole.

Nevertheless, this does not mean that the SM explains everything. Mathematical inconsistency has the advantage to give an upper bound for the scale at which new physics should be observed. This was the case before the construction of the LHC, where thanks to loss of unitarity in gauge boson scattering, new physics discovery was guaranteed. Today, this is no longer the case. Nevertheless, this section reviews some major gaps left in the SM, which demand new physics to be explained. We divide this list in two categories, the first part is theoretically motivated and the second data driven.

GRAVITY The SM is incomplete by construction, indeed, it explains only three of the four fundamental forces we observe in nature. Unfortunately[5] for physicists, gravity is naively expected to become important at the quantum level only around the Planck scale, 2.435×10^{18} GeV or 14 order of magnitude above the scale current colliders can probe; a scale which seems inaccessible. One loophole in this argument is linked to the possible presence of large extra dimensions which can allow for this scale to be pushed to as low as the TeV scale.

HIERACHY PROBLEM The hierarchy problem is linked to the smallness of the Higgs boson mass. It can be summarized as follows: scalar masses are not stable under quantum corrections, this mean that we expect the physics from higher scales, *e. g.* the Planck scale to correct the Higgs mass and push it to a huge value. However, the Higgs boson mass is the same order as the weak scale. This either:

1. Calls for an enormous amount of fine-tuning between contributions to the Higgs mass from low energy physics and from the ultraviolet (UV) scale, so that they cancel each other with high accuracy.
2. There exists a mechanism protecting the Higgs mass. Usual scenarios solving this issue involve new physics at the TeV scale.

COSMOLOGICAL CONSTANT Adding gravity to the SM, one operator not protected by a symmetry and of dimension lower than the Higgs mass operator appears, implying an even bigger fine-tunning problem than the one related to the Higgs.

GUT Running the gauge couplings to higher scale leads to a surprising observation; the three gauge couplings almost meet around 10^{16} GeV. What makes this fact even more intriguing is that the super-symmetric version of the SM improves the accuracy at which the couplings match. We can take advantage of this fact to write models which unify the three gauge couplings and embed the three SM group in a bigger one in a model commonly called grand unification theory (GUT) [26, 27].

STRONG CP PROBLEM The QCD sector allows the topological terms:

$$\theta \frac{1}{16\pi^2} G^{\mu\nu} \tilde{G}_{\mu\nu} \tag{1.46}$$

5 but fortunate for life as we know it

which violates the CP symmetry. However, the measure of the neutron electric dipole moment (EDM) constrains the θ parameter to be unexpectedly small $\theta < 10^{-10}$. Once more, dynamical explanations have been proposed. One of the favorite being the proposal by Peccei and Quinn involving an extra symmetry and a new very light particle called the axion [28, 29].

FLAVOR AND FAMILIES The flavor sector of the SM is peculiar for two reasons. One theory driven and the other data driven. The SM fermion masses are all arbitrary, they are just given by the Yukawas which are all free parameters. Combined with the lack of explanation of why they appear in three families with growing masses, together with the peculiar structure of the CKM matrix, this calls for a UV explanation.

CHARGE QUANTIZATION Only the gauge bosons are forced to appear in the adjoint representations. The other fields have no particular reason to be in low dimensional representation. More intriguingly, the $U(1)_Y$ charge are not constrained, however, they all appear as rational numbers, making the final electric charges multiples of $\frac{e}{3}$. This could be explained if the hypercharge was a remnant of an non-Abelian spontaneously broken symmetry.

We also have several data driven opportunities for new physics:

NEUTRINO MASS The SM does not account for neutrino masses, as already mentioned, and several possibilities exist to fix this issue. One of them is to add the dimension five Weinberg operators to the Lagrangian in Equation 1.19. The Λ term is expected to be the scale of new physics, and $c_{\alpha\beta}$ is a parameter of order one. Setting the Higgs field to its vev and asking the neutrino mass to be of order eV, pushes Λ close to the grand unification theory (GUT) scale.

DARK MATTER The dark matter problem started with inconsistency in galaxy rotation curves and was followed by lensing evidence and the observation of the famous bullet cluster. All these phenomenona can be explained by the existence of at least one new stable particle which escapes detection and accounts for around 85% of the matter content of the universe. While a plethora of solutions exist, going from primordial black holes to an extremely light boson, a famous solution is a weakly interacting particle, called a WIMP with a mass of order the weak scale.

CMB The cosmic microwave background (CMB) is a snapshot of the last photons scattering before the protons captured electrons and the universe became transparent. However, those photons are correlated on scales which are, if we rewind the history of the universe using SM physics, not causally connected. One solution to this problem is to add new physics causing the universe to have a period of exponential expansion called inflation, allowing a larger correlation range.

MATTER ANTI-MATTER ASYMETRY Why are we surrounded by matter and not anti-matter? In order to explain that, the three Sakharov conditions [30]

1. Baryon number violation
2. Charge conjugation (C) and CP violation
3. Out of equilibrium interaction

must be satisfied. While the SM satisfies the three conditions, it cannot account for the observed asymmetry.

DIRECT MEASUREMENTS OF COUPLINGS Despite the fact that most of the SM parameters are precisely measured, with a few exceptions such as the $\bar{\theta}$ parameter, for which we currently only have an upper bound, or the light quark masses for which we have only 10% precision, we still need a direct determination of several couplings. This is the case for the light quark Yukawas couplings and as we are going to see later, the two Higgs self-coupling parameters. In these sectors, large deviations are still possible. We also need to check for the smallest of higher dimensional operators, since even if they are formally absent from the SM, they are expected to be present due to higher energy physics.

OTHER NOTABLE DISCREPENCIES Despite this strong agreement with the data, some notable excesses exist. We quickly cite two of them:

1. Experiments testing flavor physics observed several excesses which each separately only have an average significance. Nevertheless, they get close the 5σ level taken together [31].
2. A long-standing discrepancy exists between the theoretical prediction and the experimental measurement of the muon magnetic moment (g-2). The latest experiment, at Brookhaven, has measured it between 2.2 and 2.7σ away from the theory prediction [32]. The nature of this excess should determined in the following years, thanks to the upgraded experiment, planned to finish around 2020.

The SM leaves several open questions. The final answers are going to come from experimental measurements. That is why in the following part of this thesis, we are going to analyse LHC data using EFT, to constrain or study the possible new physics. The main point of the list above we are going to tackle are the direct measurement of couplings in Part ii, an excess in chapter 7 and the hierarchy problem in chapter 8. It can be noted, that by constraining couplings, we can obtain indirect insight on other points of the list. For example, a deviation in the Higgs trilinear coupling could be a sign of a first order electroweak phase transition, which could then give us information on baryogenesis and the matter anti-matter asymmetry. The study of the hierarchy problem is also addressed indirectly, since we are bounding the parameter space of models designed to solve this issue.

2 EFFECTIVE FIELD THEORY

2.1 THE SM AS AN EFT

Do we need to understand microscopic physics to reliably describe macroscopic effects? Luckily for physicists, the answer to this question is in most cases "no". Indeed, we do not need to know quantum field theory to understand why the eggs you cook become hard. This is true for a broad range of theory. This means we can describe nature without necessarily knowing the smallest scale physics. In QFT this is reflected in the classification of operators in relevant, irrelevant and marginal categories. More specifically, the irrelevant operators encode our absence of knowledge of the microscopic theory. Indeed, these operators become less important when the energy scale decreases. This is where their name comes from, while the relevant operators become more important at low energy. The marginal operators are not energy dependent. In QFT, the "naive" counting without taking the anomalous dimension into account, tells us that operators of dimension smaller than four are relevant, while dimension-4 are marginal and higher dimensional operators are irrelevant.

This fact, combined with the plethora of measurements in agreement with the SM, and the searches for new physics pushing the bound on new state's masses higher and higher, is a strong case for the existence of a gap in the energy spectrum. Justifying a posteriori the truncation of the operators above dimension-4. Nevertheless, this theory has to be seen as effective, in the sense that it has as range of validity, which is currently unknown. This situation can be compared to the one the SM was in before the discovery of the Higgs boson and top quark. Indeed, not taking the Higgs into account, we could see the Higgsless model as an effective field theory with a clear upper bound for the cutoff. This EFT loses its mathematical consistency around the TeV scale, because of the gauge boson scattering amplitude growing with energy, ultimately causing the theory to lose unitarity. As we discuss in the next section, the existence of an energy gap can be used to naturally go beyond the effective theory truncated at dimension-4 and parametrize deviations from the SM with minimal model dependence. In the following section, we review how the SM can be expanded, with the main assumption being that EWSB is linearly realized, or in other words that the Higgs is part of a doublet and that the structure of the theory is such that operators of dimension higher than 6 can be neglected. This allows us to define a complete basis parameterizing new physics effects. Later in Part ii, we select the relevant operators in this basis, and constrain new physics in the Higgs sector. We then minimally extend this approach by adding a new degree of freedom to the theory in order to study an LHC excess.

2.2 THE STANDARD MODEL EFT

Truncating the Lagrangian to operators with dimension-4 or below is attractive for predictability since the theory becomes renormalizable, but does not do justice to our understanding of quantum field theory. As we discussed in the previous section, the successful

predictions of the SM could be due to the existence of a mass gap, allowing the truncation to be accurate. It is tempting, however, to continue the expansion by allowing higher dimensional operators and writing our Lagrangian in the following form:

$$\mathscr{L} = \mathscr{L}_{SM} + \sum_i \frac{c_i^{(5)}}{\Lambda} \mathcal{O}_i^{(5)} + \sum_i \frac{c_i^{(6)}}{\Lambda^2} \mathcal{O}_i^{(6)} + ..., \tag{2.1}$$

where the c_i are the so-called Wilson coefficients, $\mathcal{O}^{(i)}$ is an operator of dimension i, and Λ is the scale at which new physics becomes important. In the following discussion, we assume that the structure of new physics is such that Λ^{-1} can be used as an expansion parameter, allowing us to truncate the series at a given Λ order. The first higher order term allowed has dimension five. It is an interesting term, since our rule to truncate the Lagrangian has an interesting side effect. The SM has what we call accidental symmetries; which are global symmetries present once all gauge invariant operators up to a given dimension are written down. The Lagrangian (1.6) has several extra $U(1)$ symmetries linked to baryon and lepton number conservation. In practice both symmetry are anomalous and only B-L is realized at the quantum level, but the anomaly has no effect in low energy physics, since the B+L violating process takes place through sphalerons, which are highly suppressed at low temperature. Only one kind of operator can be added at dimension five, the so called Weinberg operator:

$$\frac{1}{2} \frac{c_{\alpha\beta}}{\Lambda} \bar{L}_{L\alpha}^{c} \tilde{H}^* \tilde{H}^\dagger L_{L\beta} + \text{h. c.}\,, \tag{2.2}$$

which explicitly breaks the lepton number conservation. Indeed all higher dimensional odd operators, violate B-L. The strong experimental constraint on these operators make them safe to ignore for the rest of this work.

The number of operators with dimension smaller than 6 is rather limited. This situation drastically changes when we include dimension-6 operators. Allowing all the flavor structure, the Lagrangian then needs 2499 real coefficients [33] to be described. This forces us to give-up on some model independence, since having enough observables to bound all the coefficients is impracticable. The situation would be made worse with the inclusion of dimension-8 operators. A strong constraint is to assume a given flavor structure, since ignoring flavor can lower the total number of new operators at dimension-6 to 59 [34].

Expanding the Lagrangian to include dimension-6 terms is not as simple as writing all allowed terms, since not all operators are independent. Using the equations of motion, integrating by parts, using Fierz transformations or field redefinitions, gives the freedom to define different bases for the Lagrangian. By basis we mean a complete non-redundant set of operators. The basis choice is arbitrary; different bases may be more advantageous to choose, depending on the situation, since they allow us to single out the physics of interest. Two famous basis choice are the SILH [35] and the Warsaw basis [34]. Both are written in term of the Gauge states making explicit the $SU(3) \times SU(2)_L \times U(1)_Y$ symmetries. In this thesis, the Higgs basis is used. This basis is written in the broken phase in terms of the mass eigenstates and in the unitary gauge. The mass eigenstates have the advantage to be closer to the phenomenology. In this section we follow the presentation of the Higgs basis given in reference [36, 37]. This somewhat "early" gauge choice is not a problem for leading order observables. This statement also holds true as we discuss later for the higher order observables we compute in Part ii.

As its name indicates, the Higgs basis has been developed to make the study of the Higgs sector phenomenology easier. In order to do so, we use the extra freedom available to make our Lagrangian satisfy the following conditions [37]:

1. Only diagonal and canonical mass and kinetic terms.
2. Non-derivative photon and gluon interactions are SM like.
3. The leading order relation between input observables G_f, α, m_Z and m_h and electroweak parameters v, g', g and λ are not modified.
4. No Higgs self-interaction term containing two derivatives Also, the Higgs to gauge boson couplings have no derivative acting on the Higgs.
5. Corrections to $V_\mu \bar{f}\gamma_\mu f$ are equal to their Higgs counterpart $\left(2\frac{h}{v}+\frac{h^2}{v^2}\right)V_\mu \bar{f}\gamma_\mu f$.

Condition 1 is an obvious choice since it allows the use of standard perturbative techniques to compute observables. Conditions 2 and 3 are here to keep the link between the usual input parameters, the gauge couplings, and v the same at tree level. The remaining conditions are somewhat more arbitrary and fix the remaining basis freedom.

Although, the SILH and Warsaw basis can be written in compact form, there is a cost on being in the broken phase; it makes the Lagrangian lengthy and introduce several dependent parameters. In order to obtain the relations between the parameters, one usually starts from another basis in the unbroken phase and transforms it, applying the conditions. This allows one to find the dependence between the different Wilson coefficients. We start here by naming the arbitrarily chosen independent coefficients. We can naturally classify them; from the (currently) less relevant for Higgs physics, to the most relevant. We start by mentioning the 25 independent matrices with 4 flavor indexes used to describe the four fermion operators that we are not writing here since they are less relevant for LHC physics. Followed by the gauge self-couplings which do not enter Higgs physics at leading order (LO):

$$\lambda_z,\ \tilde{\lambda}_z,\ c_{3G},\ \tilde{c}_{3G}\,. \tag{2.3}$$

We now enter the categories which directly impact Higgs physics. The difference between the two classes is that, although both enter Higgs physics at LO, the first has already been constrained by precision and low energy observables. The first category parameterizes the shift in the W mass and the different couplings of EW gauge bosons and fermions:

$$\begin{aligned}&\delta m,\ [\delta g_L^{Ze}]_{i,j},\ [\delta g_R^{Ze}]_{i,j},\ [\delta g_L^{Wl}]_{i,j},\ [\delta g_L^{Zu}]_{i,j},\ [\delta g_R^{Zu}]_{i,j},\ [\delta g_L^{Zd}]_{i,j},\ [\delta g_R^{Zd}]_{i,j},\ [\delta g_L^{Wq}]_{i,j}\\ &[d_{Gu}]_{i,j},\ [d_{Gd}]_{i,j},\ [d_{Ae}]_{i,j},\ [d_{Au}]_{i,j},\ [d_{Ad}]_{i,j},\ [d_{Ze}]_{i,j},\ [d_{Zu}]_{i,j},\ [d_{Zd}]_{i,j}\,.\end{aligned} \tag{2.4}$$

Finally, we have the couplings modifying Higgs interactions to bosons in the first line, and bosons in the second:

$$\begin{aligned}&\delta c_z,\ c_{gg},\ c_{z\gamma},\ c_{zz},\ c_{z\Box},\ \tilde{c}_{gg},\ \tilde{c}_{z\gamma},\ \tilde{c}_{zz},\ \tilde{c}_{z\Box},\delta\lambda_3,\\ &[\delta y_u]_{ij},\ [\delta y_d]_{ij},\ [\delta y_e]_{ij},\ [\phi_u]_{ij},\ [\phi_d]_{ij},\ [\phi_e]_{ij}.\end{aligned} \tag{2.5}$$

Once the two combinations of Wilson coefficients impacting di-boson physics and which are not precisely measured at the large electron-positron collider (LEP) are removed , the number of parameters can be understood by an easy counting. Neglecting the CP odd coefficients (the ones with a $\sim$), if the Higgs is replaced by its vev, the second line

corresponds to redefinition of the masses and the first line corresponds to redefinitions of the 3 gauge couplings and both the Z and Higgs masses. This mean that these operators could not have been observed in the vacuum (*i.e.* processes without Higgs) and explains the lack of a current constraint. We reproduce in this section the terms relevant for collider physics following the classification of reference [36]. The Lagrangian is written in the form:

$$\mathscr{L}_{\text{eft}} = \mathscr{L}_{\text{sm}} + \mathscr{L}_{\text{dim-6}}, \tag{2.6}$$

where $\mathscr{L}_{\text{dim-6}}$ are the terms coming from the dimension-6 corrections. We can further separate $\mathscr{L}_{\text{dim-6}}$ into different sectors:

$$\begin{aligned}\mathscr{L}_{\text{dim-6}} = \mathscr{L}_{\text{mass}} + \mathscr{L}_{\text{vertex}} + \mathscr{L}_{\text{dipole}} + \mathscr{L}_{\text{tgc}} + \mathscr{L}_{hff} + \mathscr{L}_{hvv} + \mathscr{L}_{hdvff} \\ + \mathscr{L}_{h,\text{self}} + \mathscr{L}_{h^2} + \mathscr{L}_{\text{other}}\,.\end{aligned} \tag{2.7}$$

The first correction appears in the mass term of the W and is parametrized by

$$\mathscr{L}_{\text{mass}} = \frac{g^2 v^2}{4}\left(2\delta m + \delta m^2\right) W^+_\mu W^-_\mu\,. \tag{2.8}$$

As required by the condition 1 and 3, the Z mass is not corrected. The next term is the corrections to the EW gauge boson to fermion coupling:

$$\begin{aligned}\mathscr{L}_{\text{vertex}} = \frac{g}{\sqrt{2}} W^+_\mu \left(\delta g_L^{Wl}\bar{\nu}_L\gamma_\mu e_L + \delta g_L^{Wq}\bar{u}_L\gamma_\mu d_L + \delta g_R^{Wq}\bar{u}_R\gamma_\mu d_R\right) + \text{h. c.} \\ + \sqrt{g^2+g'^2} Z_\mu \left[\sum_{f\in u,d,e,\nu} \delta g_L^{Zf}\bar{f}_L\gamma_\mu f_L + \sum_{f\in u,d,e} \delta g_R^{Zf}\bar{f}_R\gamma_\mu f_R\right],\end{aligned} \tag{2.9}$$

where the δg_L are Hermitian matrices in generation space and the δg_R are generic complex matrices. The dependent parameters are given by

$$\delta g_L^{Z\nu} = \delta g_L^{Ze} + \delta g_L^{Wl}, \quad \delta g_L^{Zq} = \delta g_L^{Zu} V_{CKM} - V_{CKM}\delta g_L^{Zd}. \tag{2.10}$$

While the previous terms correct operators appearing at tree level in the SM Lagrangian, the dipoles introduce correction to loop induced operators:

$$\begin{aligned}\mathscr{L}_{\text{dipole}} = -\frac{1}{4v}\Bigg[& g_s \sum_{f\in u,d} \frac{\sqrt{m_{f_i} m_{f_j}}}{v}\bar{f}_{L,i}\sigma_{\mu\nu} T^a [d_{Gf}]_{ij} f_{R,j} G^a_{\mu\nu} \\ & + e \sum_{f\in u,d,e} \frac{\sqrt{m_{f_i} m_{f_j}}}{v}\bar{f}_{L,i}\sigma_{\mu\nu} [d_{Af}]_{ij} f_{R,j} A_{\mu\nu} \\ & + \sqrt{g^2+g'^2} \sum_{f\in u,d,e} \frac{\sqrt{m_{f_i} m_{f_j}}}{v}\bar{f}_{L,i}\sigma_{\mu\nu} [d_{Zf}]_{ij} f_{R,j} Z_{\mu\nu} \\ & + \sqrt{2} g \frac{\sqrt{m_{u_i} m_{u_j}}}{v}\bar{d}_{L,i}\sigma_{\mu\nu} [d_{Wu}]_{ij} u_{R,j} W^-_{\mu\nu} \\ & + \sqrt{2} g \frac{\sqrt{m_{d_i} m_{d_j}}}{v}\bar{u}_{L,i}\sigma_{\mu\nu} [d_{Wu}]_{ij} d_{R,j} W^+_{\mu\nu} \\ & + \sqrt{2} g \frac{\sqrt{m_{e_i} m_{e_j}}}{v}\bar{\nu}_{L,i}\sigma_{\mu\nu} [d_{We}]_{ij} e_{R,j} W^+_{\mu\nu}\Bigg] + \text{h. c.}\end{aligned} \tag{2.11}$$

All the Wilson coefficients are 3×3 complex matrices and $\sigma_{\mu\nu} = i[\gamma_\mu, \gamma_\nu]/2$. The dependent coefficients are given by:

$$d_{Wf} = n_f(d_{Zf} + \frac{g^2}{g^2+g'^2} d_{Af}) \quad \text{with } n_u = 1\,, \quad n_{d,e} = -1\,. \tag{2.12}$$

The next term are the triple gauge couplings, which as we see later are complementary to Higgs physics:

$$\begin{aligned}
\mathscr{L}_{tgc} = {} & ie\left[\delta\kappa_\gamma A_{\mu\nu} W^+_\mu W^-_\nu + \tilde{\kappa}_\gamma \tilde{A}_{\mu\nu} W^+_\mu W^-_\nu\right] \\
& + ig\frac{g}{\sqrt{g^2+g'^2}}\left[\delta g_{1,Z}\left(W^+_{\mu\nu}W^-_\mu - W^-_{\mu\nu}W^+_\mu\right) Z_\nu \right. \\
& \qquad \left. + \delta\kappa_Z Z_{\mu\nu} W^+_\mu W^-_\nu + \tilde{\kappa}_Z \tilde{Z}_{\mu\nu} W^+_\mu W^-_\nu\right] \\
& + i\frac{e}{m_W^2}\left[\lambda_\gamma W^+_{\mu\nu} W^-_{\nu\rho} A_{\rho\mu} + \tilde{\lambda}_\gamma W^+_{\mu\nu} W^-_{\nu\rho} \tilde{A}_{\rho\mu}\right] \\
& + i\frac{g}{m_W^2}\frac{g}{\sqrt{g^2+g'^2}}\left[\lambda_Z W^+_{\mu\nu} W^-_{\nu\rho} Z_{\rho\mu} + \tilde{\lambda}_Z W^+_{\mu\nu} W^-_{\nu\rho} \tilde{Z}_{\rho\mu}\right] \\
& + \frac{c_{3g}}{v^2} g_s^3 f^{abc} G^a_{\mu\nu} G^b_{\nu\rho} G^c_{\rho\nu} + \frac{c_{3g}}{v^2} g_s^3 f^{abc} \tilde{G}^a_{\mu\nu} G^b_{\nu\rho} G^c_{\rho\nu}.
\end{aligned} \tag{2.13}$$

The operators with tilded Wilson coeffcients violate CP. The dependent coefficients are given by:

$$\begin{aligned}
\delta g_{1,z} = {} & \frac{g'^2}{2(g^2-g'^2)}\left[c_{\gamma\gamma} e^2 + c_{z\gamma}(g^2-g'^2) - \right. \\
& \qquad \left. c_{zz}\left(g^2+g'^2\right) - c_{z\Box}\frac{g^2}{g'^2}\left(g^2+g'^2\right)\right]\,, \\
\delta\kappa_\gamma = {} & -\frac{g^2}{2(g^2+g'^2)}\left[c_{\gamma\gamma} e^2 + c_{z\gamma}(g^2-g'^2) - c_{zz}(g^2+g'^2)\right]\,, \\
\delta\kappa_z = {} & \delta g_{1,z} - \frac{g'^2}{g^2}\delta\kappa_\gamma\,, \\
\tilde{\kappa}_z = {} & \frac{g'^2}{g^2}\tilde{\kappa}_\gamma\,, \\
\lambda_\gamma = {} & \lambda_z\,, \\
\tilde{\lambda}_\gamma = {} & \tilde{\lambda}_z\,.
\end{aligned} \tag{2.14}$$

We finally reach the modification to the Higgs couplings, starting with the modification to Higgs Yukawa, encoded with two 3×3 real matrices $[\delta y_f]_{i,j}$ and $\phi_{i,j}$:

$$\mathscr{L}_{hff} = -\frac{h}{v}\sum_{f\in u,d,e}\sum_{ij}\sqrt{m_{f_i} m_{f_j}}\left([\delta y_f]_{ij} e^{i[\phi_f]_{ij}}\right)\bar{f}_{R,i} f_{L,j} + \text{h. c.} \tag{2.15}$$

Followed by the correction to the Higgs to gauge boson coupling:

$$\begin{aligned}
\mathscr{L}_{hvv} = \frac{h}{v}\Bigg[& \delta c_w \frac{g^2 v^2}{2} W^+_\mu W^{-\mu} + \delta c_z \frac{(g^2+g'^2)v^2}{4} Z_\mu Z^\mu \\
& + c_{ww}\frac{g^2}{2} W^+_{\mu\nu} W^{-\mu\nu} + c_{zz}\frac{g^2+g'^2}{4} Z_{\mu\nu} Z^{\mu\nu} \\
& + c_{z\gamma}\frac{e\sqrt{g^2+g'^2}}{2} Z_{\mu\nu} A^{\mu\nu} + c_{\gamma\gamma}\frac{e^2}{4} A_{\mu\nu} A^{\mu\nu} + c_{gg}\frac{g_s^2}{4} G^a_{\mu\nu} G^a_{\mu\nu}
\end{aligned}$$

$$
\begin{aligned}
&+\tilde{c}_{zz}\frac{g^2+g'^2}{4}Z_{\mu\nu}\tilde{Z}^{\mu\nu}+\tilde{c}_{ww}\frac{g^2}{2}W^+_{\mu\nu}\tilde{W}^{-\mu\nu}\\
&+\tilde{c}_{z\gamma}\frac{e\sqrt{g^2+g'^2}}{2}Z_{\mu\nu}\tilde{A}^{\mu\nu}+\tilde{c}_{\gamma\gamma}\frac{e^2}{4}A_{\mu\nu}\tilde{A}^{\mu\nu}+\tilde{c}_{gg}\frac{g_s^2}{4}G^a_{\mu\nu}\tilde{G}^a_{\mu\nu}\\
&+c_{w\Box}g^2\left(W^-_\mu\partial_\nu W^{+\mu\nu}+\text{h.c.}\right)+c_{z\Box}g^2Z_\mu\partial_\nu Z^{\mu\nu}\\
&+c_{\gamma\Box}gg'Z_\mu\partial_\nu A^{\mu\nu}\Bigg].
\end{aligned}
\tag{2.16}
$$

As we already remarked before, not all the operators presented are independent due to gauge invariance. Furthermore, it is interesting to note that the Wilson coefficients without "δ" generate Lorentz structures which do not appear at tree level in the SM. Those two features are naturally captured by EFTs but not in the usual κ scheme. The latter parametrizes new physics by only rescaling the SM couplings not taking into account the new possible Lorentz structure, and constraints due to symmetry. For $\mathscr{L}_{hvv}$, the relations of the dependent parameters are

$$
\begin{aligned}
\delta c_w &= \delta c_z + 4\delta m\,,\\
c_{ww} &= c_{zz}+2\frac{g'^2}{(g^2+g'^2)}c_{z\gamma}+\frac{g'^4}{(g^2+g'^2)^2}c_{\gamma\gamma}\,,\\
c_{w\Box} &= \frac{1}{g^2-g'^2}\left[g^2c_{z\Box}+g'^2c_{zz}-e^2\frac{g'^2}{(g^2+g'^2)}c_{\gamma\gamma}-(g^2-g'^2)\frac{g'^2}{(g^2+g'^2)}c_{z\gamma}\right],\\
c_{\gamma\Box} &= \frac{1}{g^2-g'^2}\left[2g^2c_{z\Box}+\left(g^2+g'^2\right)c_{zz}-e^2c_{\gamma\gamma}-(g^2-g'^2)c_{z\gamma}\right].
\end{aligned}
$$

The interaction between Higgs, W or Z and fermion are given by:

$$
\begin{aligned}
\mathscr{L}_{hvff} = \sqrt{2}g\frac{h}{v}W^+_\mu\left(\bar{u}_L\gamma_\mu\delta g^{hWq}_L d_L+\bar{u}_R\gamma_\mu\delta g^{hWq}_R d_R+\bar{\nu}_L\gamma_\mu\delta g^{hWl}_R e_L\right)+\text{h.c.}\\
+2\frac{h}{v}\sqrt{g^2+g'^2}Z_\mu\left[\sum_{f\in u,d,e,\nu}\bar{f}_L\gamma_\mu\delta g^{hZf}_L f_L+\sum_{f\in u,d,e}\bar{f}_R\gamma_\mu\delta g^{hZf}_R f_R\right],
\end{aligned}
\tag{2.17}
$$

with the dependent coefficients given by:

$$
\delta g^{hZf}=\delta g^{Zf},\qquad \delta g^{hWf}=\delta g^{Wf}\,,
\tag{2.18}
$$

as required by condition 5. While the dipoles are:

$$
\begin{aligned}
\mathscr{L}_{hdvff} = -\frac{h}{4v^2}\Bigg[&g_s\sum_{f\in u,d}\frac{\sqrt{m_{f_i}m_{f_j}}}{v}\bar{f}_{L,i}\sigma_{\mu\nu}T^a[d_{hGf}]_{ij}f_{R,j}G^a_{\mu\nu}\\
&+e\sum_{u,d,e}\frac{\sqrt{m_{f_i}m_{f_j}}}{v}\bar{f}_{L,i}\sigma_{\mu\nu}[d_{hAf}]_{ij}f_{R,j}A_{\mu\nu}\\
&+\sqrt{g^2+g'^2}\sum_{u,d,e}\frac{\sqrt{m_{f_i}m_{f_j}}}{v}\bar{f}_{L,i}\sigma_{\mu\nu}[d_{hZf}]_{ij}f_{R,j}Z_{\mu\nu}\\
&+\sqrt{2}g\frac{\sqrt{m_{u_i}m_{u_j}}}{v}\bar{d}_{L,i}\sigma_{\mu\nu}[d_{hWu}]_{ij}u_{R,j}W^-_{\mu\nu}\\
&+\sqrt{2}g\frac{\sqrt{m_{d_i}m_{d_j}}}{v}\bar{u}_{L,i}\sigma_{\mu\nu}[d_{hWd}]_{ij}d_{R,j}W^+_{\mu\nu}
\end{aligned}
$$

$$+\sqrt{2}g\frac{\sqrt{m_{e_i}m_{e_j}}}{v}\bar{\nu}_{L,i}\sigma_{\mu\nu}[d_{hWe}]_{ij}e_{R,j}W^{+}_{\mu\nu}\Bigg] + \text{h. c.} \tag{2.19}$$

where the Wilson coefficients are given by complex matrices in generation space. The dependent parameters are given by:

$$d_{hVf} = d_{Vf}\,, \quad \tilde{d}_{hVf} = \tilde{d}_{Vf}\,, \quad V \in \{G, W, Z, A\}\,. \tag{2.20}$$

We then have the Higgs self-coupling correction that we study in detail in the next section:

$$\mathscr{L}_{h,\text{self}} = -\delta\lambda_3 v h^3. \tag{2.21}$$

The vertices containing two Higgses are:

$$\begin{aligned}
\mathscr{L}_{h^2} = h^2 &\left(2\delta c_z^{(2)}\frac{g^2+g'^2}{4}Z_\mu Z_\mu + 2\delta c_w^{(2)}\frac{g^2}{2}W_\mu W_\mu\right)\\
&- \frac{h^2}{2v^2}\sum_f \sqrt{m_{f_i}m_{f_j}}\left[\bar{f}_{i,R}[y_f^{(2)}]_{ij}f_{j,L} + \text{h. c.}\right]\\
&+ \frac{h^2}{8v^2}\Big[c_{gg}^{(2)}g_s^2 G^a_{\mu\nu}G^a_{\mu\nu} + c_{ww}^{(2)}g^2 W^+_{\mu\nu}W^-_{\mu\nu} + c_{zz}^{(2)}\left(g^2+g'^2\right)Z_{\mu\nu}Z_{\mu\nu}\\
&\qquad + 2c_{z\gamma}^{(2)}gg' Z_{\mu\nu}A_{\mu\nu} + c_{\gamma\gamma}^{(2)}eA_{\mu\nu}A_{\mu\nu}\Big]\\
&+ \frac{h^2}{8v^2}\Big[\tilde{c}_{gg}^{(2)}g_s^2 G^a_{\mu\nu}\tilde{G}^a_{\mu\nu} + \tilde{c}_{ww}^{(2)}g^2 W^+_{\mu\nu}\tilde{W}^-_{\mu\nu} + \tilde{c}_{zz}^{(2)}\left(g^2+g'^2\right)Z_{\mu\nu}\tilde{Z}_{\mu\nu}\\
&\qquad + 2\tilde{c}_{z\gamma}^{(2)}gg' Z_{\mu\nu}\tilde{A}_{\mu\nu} + \tilde{c}_{\gamma\gamma}^{(2)}eA_{\mu\nu}\tilde{A}_{\mu\nu}\Big]\\
&- \frac{h^2}{2v^2}\Big[c_{w\Box}^{(2)}g^2\left(W^+_\mu\partial_\mu W^-_{\nu\mu} + W^-_\mu\partial_\mu W^+_{\nu\mu}\right)\\
&\qquad + c_{z\Box}^{(2)}g^2 Z_\mu\partial_\nu Z_{\mu\nu} + c_{\gamma\Box}^{(2)}gg' Z_\mu\partial_\nu A_{\mu\nu}\Big]\,.
\end{aligned} \tag{2.22}$$

This list has no independent operator. It should not be a surprise, we can choose to have all the couplings including two Higgses dependent. Since we assume the Higgs to be part of a doublet, we can set one Higgs to its vev and obtain another allowed operator. This is not the case for single-Higgs operators because after the replacement, the new operator can be absorbed in the definition of Yukawa or Gauge coupling. The relations are given by

$$\begin{aligned}
&\delta c_z^{(2)} = \delta c_z, \quad \delta c_w^{(2)} = \delta c_z + 3\delta m,\\
&[y_f^{(2)}] = 3[\delta y_f]_{ij}e^{i\phi_{ij}} - \delta c_z\delta_{ij},\\
&c_{vv}^{(2)} = c_{vv}, \quad \tilde{c}_{vv}^{(2)} = \tilde{c}_{vv} \quad v \in \{g, w, z, \gamma\},\\
&c_{v\Box}^{(2)} = c_{v\Box}, \quad v \in \{w, z, \gamma\}\,.
\end{aligned} \tag{2.23}$$

Even with this long list of operators we did not review all the possibilities since $\mathscr{L}_{\text{other}}$ contains operator less relevant for LHC searches and is not repoduced here. It contains four fermion couplings, Higgs to more than 2 gauge bosons couplings, quartic self-interactions

for the Higgs and the Gauge bosons, dipole like interactions between Gauge bosons and fermions and interactions with more than 4 fields.

In Part ii, we select the relevant operators of this list and study the ability for current and next generation colliders to extract the Higgs trilinear self-coupling. In chapter 7, we change approach. Due to the observation of a signal hinting towards new physics, we add a new field to the SM. None of the previous operators is relevant for our study and therefore we neglect them. We, however, extends the SM adding dimension-5 operators containing a new field. Finally, in chapter 8, we start from a simplified model and in order to use the current experimental bounds, we integrate out the field to match our simplified Lagrangian to the relevant higher dimension operator and set bounds. We also go beyond EFT, when we directly use the simplified model to use direct search bounds.

Part II

CONSTRAINING THE STANDARD MODEL EFT

3

WHICH HIGGS?

This part of the thesis reproduce the papers [2, 3] with minor modifications, a reworked introduction to link the two, and the addition of a global conclusion.

3.1 CURRENT CONSTRAINTS

We started exploring the Higgs sector only six years ago. The plethora of results and the fact that the Higgs mass is already constrained at the percent level show how much experimentalists and theorists focused their efforts to explore this new sector. Despite the number of results available, one question remains unanswered: how close to the SM Higgs boson is the particle whose discovery was announced on 4 July 2012? We already know with high confidence that we are observing a CP even, scalar particle [38, 39]. The ultimate answer is probably going to come from the measurement of the coupling of this new boson to the other SM particles. The theory of EWSB is very predictive for the different Higgs boson couplings. Up to loop effects, all of them are proportional to the masses of the particles the Higgs couples to. We already measured the coupling to the heavy particle of the SM. Nevertheless, this statement is model dependent since the LHC is not directly measuring the couplings and some theory assumptions are needed to extract the couplings from the experimental data.

Data with the least model dependence are show in Figure 3.1, since they directly count the number of events seen in the detector corresponding to a production and subsequent decay of the Higgs boson and normalize it to the SM value. The resulting quantity is called signal strength:

$$\mu = \frac{\sigma_{exp}}{\sigma_{SM}} \,. \tag{3.1}$$

Most measurements are compatible with the SM at the 1σ level, despite some channels having low precision, most measurement are expected to reach the ten to twenty percent precision at the end of the HL-LHC (as we discuss later, see Table 4.1).

This is, however, not the end of the story. The situation is drastically different for the couplings to the light particles and the Higgs self-coupling. While obtaining high statistics at the HL-LHC will allow us to probe the coupling to the muon and the effective Higgs-Z-γ, vertex thanks to the corresponding rare decay, the couplings of the Higgs to the electron, or light quarks are out of reach.

In this part of the thesis, we focus on the Higgs trilinear self-coupling. Measuring the Higgs self-coupling is an important consistency check, since the SM Higgs potential:

$$\mathcal{L} \supset -\frac{m_h^2}{2}h^2 - \lambda_3^{SM} v h^3 - \lambda_4^{SM} h^4, \tag{3.2}$$

$$\lambda_3^{SM} = \frac{m_h^2}{2v^2}, \qquad \lambda_4^{SM} = \frac{m_h^2}{8v^2}, \tag{3.3}$$

only depends on two already well measured parameters. The vev is directly related to the Fermi constant and the mass is obtained by fitting the position of the bump over the

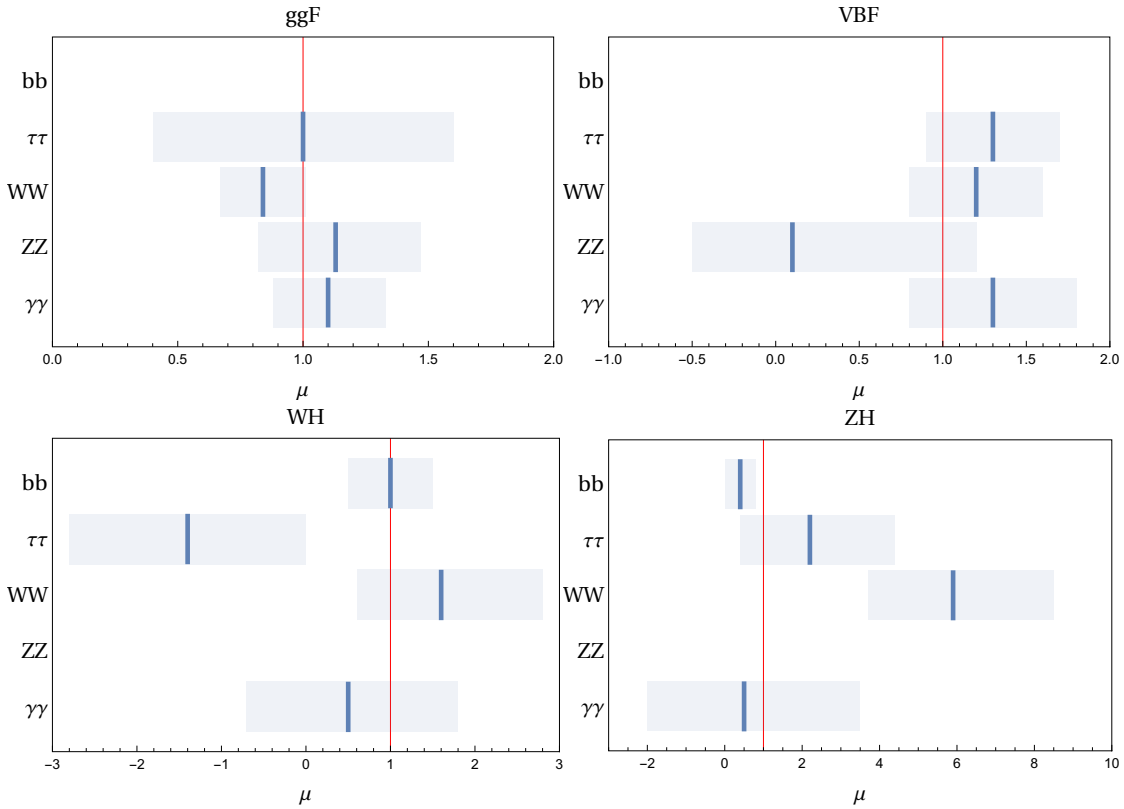

Figure 3.1: Combined ATLAS and CMS run 1 Higgs results from reference [40]

smooth falling background in the different decay channels. Beside the different scenarios predicting a large anomalous trilinear (some examples can be found in reference [25]), a direct measurement of the quartic and trilinear self-coupling is an important check that we are indeed looking at a boson coming from the SM theory of EWSB. Deviation from the predicted value could also signal that baryogenesis proceeded through a first order phase transition. Measuring the quartic self-coupling would also be important. Unfortunately, a lot of patience is needed, since even a 100 TeV machine would struggle to achieve this task.

The current best bound on the trilinear comes from double-Higgs production, where the self-coupling enters at LO. Due to the small cross section of di-Higgs production, combined with the small branching ratio of the channel minimizing the background, the bounds are only forbidding values which are several times the SM, as can be seen in Table 3.1. The pair-production cross section is roughly a thousand times smaller than single-Higgs (49 pb compared to 33 fb). This is partially due to the negative interference between the diagrams in Figure 3.2 which lowers the cross section by around 50%. On top of that, we need the two Higgses to decay into an observationally favorable combination of channels, therefore paying the cost of two branching ratios. Currently, the $hh \to b\bar{b}\gamma\gamma$ channel is expected to give the best bound thanks to its balanced trade-off between precision and statistics.

Given that large deviations are still allowed, an approach originally proposed by reference [41] for lepton colliders was revived by several collaborations in references [42–44]. The idea is to look at higher order corrections containing the trilinear vertex. It is not surprising this idea originated for precision machines since we are looking at loop suppressed

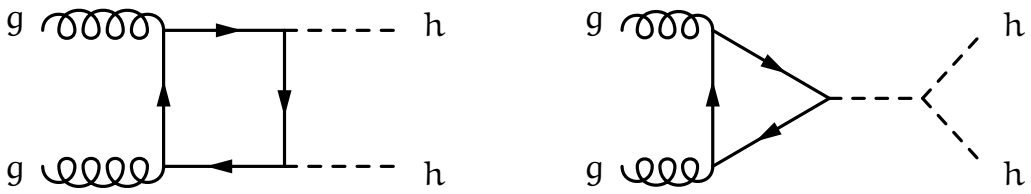

Figure 3.2: Two of the diagrams contributing to double Higgs production and interfering destructively

$\left(\frac{\sigma_{hh}}{\sigma_{SM}}\right)_{max}$	ATLAS		CMS	
	obs.	exp.	obs.	exp.
$b\bar{b}\gamma\gamma$	177	162[iii]	19	16[i]
$b\bar{b}\tau\tau$		-	30	25[i]
$b\bar{b}b\bar{b}$	29	38[ii]	342	308[iii]
$b\bar{b}WW^*$		-	79	89[i]
$\gamma\gamma WW^*$	750	386[ii]		-

Table 3.1: Summary of expected and observed 95% CL limits on double Higgs production cross section at $\sqrt{s} = 13\,TeV$ for i) $35.9\,fb^{-1}$, i) $13.3\,fb^{-1}$ and iii) 2.3-3.2 fb^{-1}, taken from reference [48].

effects. Nevertheless, the very weak bound on the trilinear allows for sizable corrections and is therefore suitable for LHC studies. This is an interesting change of paradigm for the LHC, since we want to use an hadronic machines usually seen as a discovery machine with a challenging environment, for precision physics.[1] Assuming that the only coupling deviating from its SM value is the trilinear, references [42–44] obtained complementary and even competitive bounds with the one coming from double-Higgs production. Those analyses were extended by looking at precision EW observables in reference [46, 47] with once more competitive bounds. These conclusions push us to address several questions in the following section. The most obvious one to ask is to which kind of new physics scenarios these bounds apply. Also, more importantly, is to wonder as to the fate of the existing single-Higgs measurement fit which did not take these corrections into account. Since at first sight, it seems some non-negligible effects were not accounted for. This bring us to a generic issue that any fit suffers from; which are the hidden assumptions they rely on and to which UV models do they apply?

In order to study these questions, we relax the assumption that only the trilinear can be anomalous. We parameterize our new physics in a less model dependent way by using EFT and test the robustness of the existing fit. Allowing more generic new physics is a natural thing to do since, even for UV models with a parametric enhancement of the trilinear, other competing effects can be present. Loop suppressed modification of the Higgs coupling to bosons or fermions, would enter at LO in single-Higgs production and therefore be comparable in size with the next to leading order (NLO) trilinear correction. Armed with our more generic EFT, we can do a global fit and study these questions. In section 3.2, we start by presenting the relevant higher dimensional operators and the

1 This is not the only case where a task thought to be reserved for lepton colliders seems to be in the reach of a hadronic machine, for example see reference [45]

basis used. We then list the other possible deviations also contributing to single-Higgs observables and justify why we neglect them. We subsequently study the validity of our framework, and present a case where the trilinear is parametrically bigger than the other operators.

In chapter 4, we perform a global fit using only inclusive single-Higgs taking into account the trilinear. We show that, due to an unconstrained direction, no information on the coupling can be extracted. We suggest a solution to this problem, and study how usual determination of single-Higgs coupling are affected, we find that adding double-Higgs solves the flat direction problem. We then consider using differential observables to improve the trilinear determination. After studying the robustness of our assumptions, we summarize the situation for HL-LHC.

Once this is done, we naturally extend the discussion to the next generation of colliders. Indeed, if no surprising large anomalous trilinear is measured, the HL-LHC is only going to give us higher and lower bounds of order one on the trilinear. We expect the next generation of machines to be lepton colliders, which will initially have center of mass (COM) bellow the threshold of double-Higgs production. This is a perfect opportunity to update the idea of reference [41] with the new data available and to look at the power and possible complementarity of the combination of hadronic and leptonic machine. We extend this analysis by studying the prospect brought by higher COM leptonic machine allowing for direct measurement of double-Higgs production. After summarizing the situation at lepton collider, we discuss the prospect of measuring the trilinear using all the planned colliders. In Appendix A, we give details on the computation of EFT corrections to the signal strenghts for hadron colliders and in Appendix B we propose some technical formulae and additional results for secondary benchmark scenarios for lepton colliders. Extra results are given in an ancillary file which is available along the arxiv submission of reference [2].

3.2 PARAMETERIZING NEW PHYSICS IN THE HIGGS SECTOR

3.2.1 *Higgs primary couplings*

In a large class of scenarios, if a sizable gap is present between the SM states and the mass scale of the BSM dynamics, the new-physics effects can be conveniently encapsulated into an EFT framework, as already discussed in chapter 2. The EFT operators can be organized according to their canonical dimension, thus expanding the effective Lagrangian into a series

$$\mathcal{L} = \mathcal{L}_{SM} + \sum_i \frac{c_i^{(6)}}{\Lambda^2}\mathcal{O}_i^{(6)} + \sum_i \frac{c_i^{(8)}}{\Lambda^4}\mathcal{O}_i^{(8)} + \cdots , \tag{3.4}$$

where $\mathcal{L}_{SM}$ is the SM Lagrangian, $\mathcal{O}_i^{(D)}$ denote operators of dimension D and Λ is the SM cut-off, i.e. the scale at which the new dynamics is present.[2]

The leading new-physics effects are usually associated with EFT operators with the lowest dimensionality, namely the dimension-6 ones. In the following we restrict our attention

2 In the above expansion we neglected operators with odd energy dimension since they violate lepton number conservation (for $D = 5$) and $B - L$ invariance (for all odd D). These effects are constrained to be extremely small and do not play any role in our analysis.

to these operators and neglect higher-order effects. To further simplify our analysis we also assume that the new physics is CP-preserving and flavor universal. With these restrictions we are left with 10 independent operators that affect Higgs physics at leading order and have not been tested below the % accuracy in existing precision measurements [49].[3]

Before discussing our operator basis, it is important to mention that a much larger set of dimension-6 operators could in principle be relevant for Higgs physics. A first class of these operators include deformations of the SM Lagrangian involving the light SM fermions. They correct at tree level the Higgs processes but also affect observables not involving the Higgs. Therefore most of them have already been tested with good precision in EW measurements. A second set of dimension-6 operators involve the top quark and are typically much less constrained. However they affect Higgs physics only at loop level, thus their effects are usually not very large. We postpone a more detailed discussion to subsection 3.2.2.

A convenient choice for dimension-6 operators is provided by the "Higgs basis" [36, 37] in which the Higgs is assumed to be part of an $SU(2)_L$ doublet and operators connected to the LHC Higgs searches are separated from the others that can be tested in observables not involving the Higgs.[4] The 10 effective operators we will focus on can be split into three classes: the first one contains deformations of the Higgs couplings to the SM gauge bosons, parametrized by

$$\delta c_z\,,\ c_{zz}\,,\ c_{z\Box}\,,\ \hat{c}_{z\gamma}\,,\ \hat{c}_{\gamma\gamma}\,,\ \hat{c}_{gg}\,, \tag{3.5}$$

the second class is related to deformations of the fermion Yukawa's

$$\delta y_t\,,\ \delta y_b\,,\ \delta y_\tau\,, \tag{3.6}$$

and finally the last effect is a distortion of the Higgs trilinear self-coupling

$$\kappa_\lambda\,. \tag{3.7}$$

The corresponding corrections to the Higgs interactions in the unitary gauge are given by

$$\begin{aligned}
\mathscr{L} \supset \frac{h}{v}\Bigg[&\delta c_w \frac{g^2v^2}{2}W^+_\mu W^{-\mu} + \delta c_z \frac{(g^2+g'^2)v^2}{4}Z_\mu Z^\mu + c_{ww}\frac{g^2}{2}W^+_{\mu\nu}W^{-\mu\nu} \\
&+ c_{w\Box}g^2\left(W^-_\mu \partial_\nu W^{+\mu\nu} + \text{h.c.}\right) + \hat{c}_{\gamma\gamma}\frac{e^2}{4\pi^2}A_{\mu\nu}A^{\mu\nu} + c_{zz}\frac{g^2+g'^2}{4}Z_{\mu\nu}Z^{\mu\nu} \\
&+ \hat{c}_{z\gamma}\frac{e\sqrt{g^2+g'^2}}{2\pi^2}Z_{\mu\nu}A^{\mu\nu} + c_{z\Box}g^2 Z_\mu \partial_\nu Z^{\mu\nu} + c_{\gamma\Box}gg' Z_\mu \partial_\nu A^{\mu\nu}\Bigg] \\
&+ \frac{g_s^2}{48\pi^2}\left(\hat{c}_{gg}\frac{h}{v} + \hat{c}^{(2)}_{gg}\frac{h^2}{2v^2}\right)G_{\mu\nu}G^{\mu\nu} \\
&- \sum_f \left[m_f\left(\delta y_f \frac{h}{v} + \delta y_f^{(2)}\frac{h^2}{2v^2}\right)\bar{f}_R f_L + \text{h.c.}\right] - (\kappa_\lambda - 1)\lambda_3^{SM} v h^3\,,
\end{aligned} \tag{3.8}$$

3 The assumption of flavor universality is not crucial for our analysis. It is only introduced to restrict the EFT analysis to the operators that can only be tested in Higgs physics. The same can be done in several other flavor scenarios, as for instance minimal flavor violation and anarchic partial compositeness.

4 For the relation between the independent couplings in the Higgs basis and the Wilson coefficients of other operator bases, see reference [37] or section 2.2.

where the parameters δc_w, c_{ww}, $c_{w\Box}$, $c_{\gamma\Box}$, $\hat{c}_{gg}^{(2)}$ and $\delta y_f^{(2)}$ are dependent quantities, defined as

$$\begin{aligned}
\delta c_w &= \delta c_z\,, \\
c_{ww} &= c_{zz} + 2\frac{g'^2}{\pi^2(g^2+g'^2)}\hat{c}_{z\gamma} + \frac{g'^4}{\pi^2(g^2+g'^2)^2}\hat{c}_{\gamma\gamma}\,, \\
c_{w\Box} &= \frac{1}{g^2-g'^2}\left[g^2 c_{z\Box} + g'^2 c_{zz} - e^2\frac{g'^2}{\pi^2(g^2+g'^2)}\hat{c}_{\gamma\gamma}\right. \\
&\qquad \left. - (g^2-g'^2)\frac{g'^2}{\pi^2(g^2+g'^2)}\hat{c}_{z\gamma}\right]\,, \\
c_{\gamma\Box} &= \frac{1}{g^2-g'^2}\left[2g^2 c_{z\Box} + \left(g^2+g'^2\right)c_{zz} - \frac{e^2}{\pi^2}\hat{c}_{\gamma\gamma} - \frac{g^2-g'^2}{\pi^2}\hat{c}_{z\gamma}\right]\,, \\
\hat{c}_{gg}^{(2)} &= \hat{c}_{gg}\,, \\
\delta y_f^{(2)} &= 3\delta y_f - \delta c_z\,.
\end{aligned} \tag{3.9}$$

In the above expressions we denoted by g, g', g_s the $SU(2)_L$, $U(1)_Y$ and $SU(3)_c$ gauge couplings respectively. The electric charge e is defined by the expression $e = \frac{gg'}{\sqrt{g^2+g'^2}}$.

Notice that in the Higgs basis the distortion of the trilinear Higgs coupling is encoded in the parameter $\delta\lambda_3$ and denotes an additive shift in the coupling, $\mathscr{L}_{\rm self} \supset -(\lambda_3^{\rm SM} + \delta\lambda_3)v h^3$. In our notation κ_λ denotes instead a rescaling of the Higgs trilinear coupling, as specified in Equation 3.8. We use this modified notation in order to make contact with previous literature discussing the measurement of the Higgs self-coupling.

In Equation 3.8 and (3.9) we also used a non-standard normalization for the $\hat{c}_{gg}$, $\hat{c}_{\gamma\gamma}$ and $\hat{c}_{z\gamma}$ parameters. The contact Higgs coupling to gluons has been normalized to the LO top loop prediction in the SM computed in the infinite m_t limit, whereas we included an additional factor $1/\pi^2$ in the couplings $\hat{c}_{\gamma\gamma}$ and $\hat{c}_{z\gamma}$. The relation with the standard normalization of reference [36] is given by

$$c_{gg} = \frac{1}{12\pi^2}\hat{c}_{gg} \simeq 0.00844\hat{c}_{gg}\,, \quad c_{\gamma\gamma} = \frac{1}{\pi^2}\hat{c}_{\gamma\gamma} \simeq 0.101\hat{c}_{\gamma\gamma}\,, \tag{3.10}$$

$$c_{z\gamma} = \frac{1}{\pi^2}\hat{c}_{z\gamma} \simeq 0.101\hat{c}_{z\gamma}\,. \tag{3.11}$$

With these normalizations values of order one for $\hat{c}_{gg}$, $\hat{c}_{\gamma\gamma}$ and $\hat{c}_{z\gamma}$ correspond to BSM contributions of the same order of the SM gluon fusion amplitude and of the $H \to \gamma\gamma$ and $H \to Z\gamma$ partial widths.

Since our analysis takes into account NLO corrections to the single-Higgs production and decay rates, it is important to discuss the issue of renormalizability in our EFT setup. In general, when we deform the SM Lagrangian with higher-dimensional operators, a careful renormalization procedure is needed when computing effects beyond the LO. However, as discussed in reference [43], if we are only interested in NLO effects induced by a modified Higgs trilinear self-coupling, no UV divergent contributions are generated. This is a consequence of the fact that the Higgs trilinear coupling does not enter at LO in single-Higgs observables but only starts to contribute at NLO. As far as the modified trilinear is concerned, our setup essentially coincides with that of reference [43], so we can carry over to our framework their results. We report them in section A.2 for completeness.

Possible subtleties could instead arise considering the NLO contributions due to deformations of the single-Higgs couplings, since these interactions already enter in the LO contributions. The deviations in single-Higgs couplings, however, are already constrained to be relatively small, and will be tested in the future with a precision of the order of 10% or below. Their contributions at NLO can thus be safely neglected. For this reason we will include their effects only at LO, in which case no subtleties about renormalization arise.

3.2.2 *Additional operators contributing to Higgs observables*

As we already mentioned, a larger set of dimension-6 operators can in principle affect Higgs observables. We will list them in the following and discuss how they can be constrained through measurements not involving the Higgs.

VERTEX CORRECTIONS. A first class of operators include the vertex corrections mediated by interactions of the form

$$\mathcal{O}_{vert} = (iH^\dagger \overleftrightarrow{D}_\mu H)(\bar{f}\gamma^\mu f)\,, \qquad \mathcal{O}^{(3)}_{vert} = (iH^\dagger \sigma^a \overleftrightarrow{D}_\mu H)(\bar{f}\gamma^\mu \sigma^a f)\,. \tag{3.12}$$

They give rise at the same time to deformations of the couplings of the Z and W bosons with the fermions and to $hVff$ contact interactions. Both these effects can modify Higgs physics at tree level. The gauge couplings deformations, for instance, affect the production cross section in vector boson fusion. The $hVff$ vertices, instead, modify the cross section of ZH and WH production and the decay rates in the $h \to VV^* \to 4f$ channels.

Under the assumption of flavor universality, all the vertex-correction operators can be constrained at the $10^{-2} - 10^{-3}$ level [50–52]. Even in the HL-LHC phase, Higgs observables will have at least *few* % errors. Vertex corrections in flavor universal theories are thus too small to be probed in Higgs physics and can be safely neglected.

If the assumption of flavor universality is relaxed, larger corrections to specific vertex operators are allowed [51].[5] The gauge couplings involving leptons are still very well constrained and below detection in Higgs physics. Sizable corrections can instead modify the quark couplings. In particular the couplings involving the first generation quarks can deviate at the level of *few* % and Higgs measurements at the HL-LHC could be sensitive to them. The gauge couplings involving second generation quarks or the bottom are still very well constrained. Finally the couplings involving the top quark are very poorly bounded. In particular the coupling $Z\bar{t}_R t_R$ at present is practically unconstrained, while in the future it could be tested with some accuracy in $t\bar{t}Z$ production.

DIPOLE OPERATORS. A second class of operators that can correct Higgs observables are dipole-like contact interactions of the generic form

$$\mathcal{O}_{dip} = \bar{f} H \sigma_{\mu\nu} T^a f F^{a\,\mu\nu}\,. \tag{3.13}$$

These operators induce at the same time dipole interactions of the gauge bosons with the fermions and vertices of the form $h\,\partial Vff$. The $h\,\partial Vff$ operators can modify

5 In this discussion we do not consider new-physics contributions to the W boson couplings with the right-handed fermions. Contributions induced by these couplings do not interfere with the SM amplitudes and are thus typically too small to play any significant role.

Higgs decays into four fermions. However in this case the dipole contributions do not interfere with the SM amplitudes since they have a different helicity structure. Moreover the experimental bounds on dipole moments put strong constraints on the coefficients of the dipole operators, in particular for the light generation fermions. For these reasons dipole operators can typically be neglected in Higgs physics [49]. A possible exception is the chromomagnetic operator involving the top quark, which can modify the $t\bar{t}H$ production channel. Although in many BSM scenarios this operator is expected to be safely small, the current direct bounds from the $t\bar{t}$ process are relatively weak [53], so that the top dipole operator could still play a role in Higgs physics [54].

FOUR-FERMION OPERATORS. A third set of operators that can affect Higgs physics is given by four-fermion interactions. Operators involving light generation fermions and the top quark can correct at tree-level the $t\bar{t}H$ production channel. These effects are suppressed in several BSM scenarios since they would be correlated to 4-fermion interactions involving only light quarks, which are tightly constrained by dijet searches. However the direct bounds on operators involving top quarks, which can be tested in $t\bar{t}$ production, are not strong enough yet to forbid non-negligible effects in Higgs physics.[6]

On the other hand, 4-fermion operators involving only third generation fermions do not modify Higgs observables at tree-level, but can induce loop corrections. Obviously the loop factor gives a strong suppression for these effects. Nevertheless four-fermion operators involving the top quark are poorly constrained at present, so that large coefficients are allowed, which could compensate the loop suppression. For instance four-top operators can correct the gluon-fusion cross section, while operators with top and bottom quarks can modify the Higgs branching ratio into a bottom pair.

Taking into account the possible chirality structures, 12 four-fermion operators involving only third generation quarks can be written. A few constraints on some combination of them are available at present. The strongest one comes from the measurement of the $Z\bar{b}_L b_L$ vertex, which receives loop corrections from four-fermion operators involving the left-handed quark chirality [55]. Additional constraints can be obtained from bounds on the $\bar{t}t$ and $\bar{t}t\bar{t}t$ cross sections. For instance the current LHC measurements put a bounds of order $1/(600\,\mathrm{GeV})^2$ on the coefficient of the $(\bar{t}_R\gamma^\mu t_R)(\bar{t}_R\gamma_\mu t_R)$ operator [56]. A suppression of this size is enough to ensure that the loop corrections to Higgs physics are smaller than the achievable precision.

Of course a fully model-independent analysis of the four-fermion operators should be done by considering all operators simultaneously and not just one at a time (as done in the experimental analysis of reference [56]). Such study is beyond the scope of this work, so we will neglect the effects of four-fermion operators in our analysis.

A final comment is in order. In the above discussion we assumed that the BSM effects are parametrized by dimension-6 operators in which the electroweak symmetry is linearly realized. This assumption allows to relate the $hVff$ and $h\,\partial Vff$ operators to the vertex and dipole operators, so that these operators can be tested in processes not involving the Higgs. If the electroweak symmetry is not linearly realized (or equivalently if the expansion in

6 We thank E. Vryonidou for pointing this out to us.

Higgs powers is not valid) the interactions involving the Higgs become independent and can not be constrained any more in non-Higgs physics. In such case a more complicated analysis, taking into account all the operators, must be performed. We will give more details about the non-linear Lagrangian in the following subsection.

3.2.3 *Large Higgs self-interactions in a consistent EFT expansion*

An important issue to take into account when using the effective framework is the range of validity of the EFT approximation. This is a delicate issue, crucially depending on the choice of power counting encoding the assumptions about the UV dynamics. Here we only include a concise discussion with a few examples and refer the reader to the literature [57] for possible subtleties.

As we will see in the following, the LHC measurements, especially in the high-luminosity phase, can probe inclusive single-Higgs observables with a precision of the order or slightly below 10%. In the absence of new physics, possible BSM effects will thus be constrained to be significantly smaller than the SM contributions. This translates into tight bounds on the coefficients of the operators that correct the Higgs interactions with the gauge bosons (Equation 3.5) and with the fermions (Equation 3.6). The leading effects due to these operators arise from the interference with the SM amplitude, while quadratic terms are subleading. Corrections arising from dimension-8 operators lead to effects that are generically of the same order of the square of the dimension-6 ones and are subleading as well.[7] This justifies our approximation of keeping only the leading EFT operators.

The discussion about the trilinear Higgs self-coupling is instead more subtle. As we will see in the following, the constraints on κ_λ we can obtain from the LHC data are quite loose. The Higgs trilinear coupling can only be tested at order one, even at the end of the HL-LHC program. Such large deviations in κ_λ, accompanied by small deviations in the Higgs couplings to gauge fields and fermions, can only be obtained in very special BSM scenarios. Indeed in generic new-physics models the deviations in all Higgs couplings are expected to be roughly of the same order. For instance in models that follow the strongly interacting light Higgs (SILH) power counting [58–60] we expect

$$\delta c_z \sim v^2/f^2\,, \qquad \delta\kappa_\lambda \equiv \kappa_\lambda - 1 \sim v^2/f^2\,, \tag{3.14}$$

where the f parameter is related to the typical coupling g_* and mass scale m_* of the new dynamics by $f \sim m_*/g_*$. In this class of models the deviations in the Higgs self-interactions are typically small, much below the LHC sensitivity. A fit of the single-Higgs couplings, neglecting the trilinear Higgs modifications is thus fully justified in these scenarios. At the same time the constraints achievable on κ_λ at the LHC will hardly have any impact in probing the parameter space of SILH theories. The situation could however change at future high-energy machines, as for instance a 100 TeV hadron collider, which could test κ_λ with a precision below 10%, implying non-trivial constraints on models following the SILH power counting [58, 61].

Enhanced deviations only in Higgs self-couplings are possible in other classes of models. Interesting possibilities are provided for instance (i) by scenarios in which the Higgs is a generic bound state of a strongly coupled dynamics (i.e. not a Goldstone boson) (see

7 There exist particular classes of theories in which the size of effects coming from the dimension-8 operators is enhanced with respect to the square of the dimension-6 ones. We will not consider these scenarios in our analysis. For a discussion of these effects see for instance references [57, 58].

discussion in reference [58]), (ii) by bosonic technicolor scenarios and (iii) by Higgs-portal models. In all these cases large deviations in the Higgs self-couplings can be present and accompanied by small corrections in single Higgs interactions. As an explicit example, we will analyze the Higgs portal scenarios later on.

It is important to stress that, in the presence of large corrections to Higgs self-interactions, the EFT expansion in Higgs field insertions may break down. In this case the expansion in derivatives can still be valid, since it is controlled by the expansion parameter E/Λ, but we can not neglect operators with arbitrary powers of the Higgs field. The effective parametrization can still be used in such situation provided that we interpret the effective operators as a "resummation" of the effects coming from operators with arbitrary Higgs insertions. This is equivalent to a "non-linear" effective parametrization in which the Higgs is not assumed to be part of an $SU(2)_L$ doublet, but is instead treated as a full singlet (see reference [36] for a brief account on non-linear EFT and for a list of further references). The only caveat with this parametrization is the fact that interactions with multiple Higgs fields are not connected any more to the single-Higgs couplings. In this case a different global fit should be performed, in which $c_{gg}^{(2)}$ and $\delta y_f^{(2)}$ are treated as independent parameters. Notice also that the $hVff$ and $h\,\partial Vff$ operators should a priori be included in the analysis, as we discussed in subsection 3.2.2 and EW precision data and Higgs data cannot be analyzed separately any longer.

To clarify the issues discussed above, we now analyze an explicit class of models, the Higgs portal scenarios. As a concrete example, we assume that a new scalar singlet φ, neutral under the SM gauge group, is described by the Lagrangian[8]

$$\mathcal{L} \supset \theta g_* m_* H^\dagger H \varphi - \frac{m_*^4}{g_*^2} V(g_* \varphi / m_*) \,, \tag{3.15}$$

where the dimensionless parameter θ measures the mixing between the Higgs sector and the neutral sector, and V is a generic potential. In the EFT description obtained after integrating out φ the derivative expansion is valid if $E/m_* \ll 1$, while the expansion in Higgs-field insertions is valid when

$$\varepsilon \equiv \frac{\theta g_*^2 v^2}{m_*^2} \ll 1 \,. \tag{3.16}$$

Note that θ and ε are truly dimensionless quantities in mass and coupling dimensions. The corrections to the Higgs couplings with gauge fields come indirectly from operators of the type $\partial_\mu(H^\dagger H)\partial^\mu(H^\dagger H)$ and can be estimated as

$$\delta c_z \sim \theta^2 g_*^2 \frac{v^2}{m_*^2} \,. \tag{3.17}$$

The corrections to the Higgs trilinear coupling are instead given by

$$\delta\kappa_\lambda \sim \theta^3 g_*^4 \frac{1}{\lambda_3^{SM}} \frac{v^2}{m_*^2} \,. \tag{3.18}$$

8 The power counting we derive in the following applies also to more general Higgs portal models. In particular it is valid for scenarios characterized by a single coupling g_* and a single mass scale m_* in which the Higgs is coupled to the new dynamics through interactions of the type $\theta H^\dagger H \mathcal{O}$, where $\mathcal{O}$ is a generic new-physics operator. Note that a different power counting can arise for portal scenarios in which the new-physics sector is charged under the SM (see reference [62] for a classification of possible scenarios).

First of all, we can notice that $\delta\kappa_\lambda \sim \theta g_*^2/\lambda_3^{SM}\delta c_z$, thus a large hierarchy between the corrections to linear Higgs couplings and the deviation in the self-interactions requires sizable values of the Higgs portal coupling θ (and/or large values of the new-sector coupling g_*).

When the corrections to the Higgs potential become large, some amount of tuning is typically needed to fix the correct properties of the Higgs potential. Notice that Higgs-portal scenarios do not typically provide a solution to the hierarchy problem. Thus they will in general suffer from some amount of tuning in the Higgs mass term, exactly as generic extensions of the SM. On top of this some additional tuning in the Higgs quartic coupling can also be present. In the following we will refer only to this additional tuning, which we denote by Δ. We can estimate Δ by noticing that the quartic coupling needs to be fixed with a precision of the order of λ_3^{SM}. By comparing the new-physics corrections to the quartic coupling with the SM value we get

$$\Delta \sim \frac{\theta^2 g_*^2}{\lambda_3^{SM}}\,. \tag{3.19}$$

We can easily relate $\delta\kappa_\lambda$ given in (Equation 3.18) to the amount of tuning Δ as

$$\delta\kappa_\lambda \sim \varepsilon\Delta. \tag{3.20}$$

This relation has an interesting consequence. If we require the expansion in Higgs insertions to be valid ($\varepsilon \lesssim 1$) and the model not to suffer additional tuning ($\Delta \lesssim 1$), we get that the corrections to the Higgs trilinear coupling can be at most of order one ($\delta\kappa_\lambda \lesssim 1$). Larger corrections can however be obtained if at least one of the two conditions $\varepsilon \lesssim 1$ and $\Delta \lesssim 1$ is violated.

As we already mentioned, if the expansion in Higgs insertions is not valid ($\varepsilon > 1$), large deviations in the Higgs couplings are possible. In particular single- and multiple-Higgs couplings are not related any more and a non-linear effective parametrization must be used. In this scenario, however, large corrections to the linear Higgs couplings to the SM fields are expected, so that significant tuning is required to pass the precision constraints from single-Higgs processes.

A second scenario, in which $\varepsilon \lesssim 1$ while some tuning is present in the Higgs potential ($\Delta > 1$), can instead naturally lead to small deviations in the linear Higgs couplings. For instance by taking $\theta \simeq 1$, $g_* \simeq 3$ and $m_* \simeq 2.5\,TeV$ we get

$$\varepsilon \simeq 0.1\,, \quad 1/\Delta \simeq 1.5\%\,, \quad \delta c_z \simeq 0.1\,, \quad \delta\kappa_\lambda \simeq 6\,. \tag{3.21}$$

Since we are going to consider sizable deviations in the trilinear Higgs coupling, it is important to understand whether such corrections are compatible with a high-enough cut-off of the effective description. If large corrections are present in the Higgs self-interactions, scattering processes involving longitudinally polarized vector bosons and Higgses, in particular $V_L V_L \to V_L V_L h^n$, loose perturbative unitarity at relatively low energy scales. The upper bound for the cut-off of the EFT description can be estimated as [63, 64]

$$\Lambda \lesssim \frac{4\pi v}{\sqrt{|\kappa_\lambda - 1|}}\sqrt{\frac{32\pi}{15}}\frac{v}{m_h}\,. \tag{3.22}$$

This bound is not very stringent: for $|\kappa_\lambda| \lesssim 10$ one gets $\Lambda \lesssim 5\,TeV$. For values of κ_λ within the expected HL-LHC bounds, perturbativity loss is thus well above the energy range directly testable at the LHC.

As a last point, we comment on the issue of the stability of the Higgs vacuum. As pointed out in reference [43], if the only deformation of the Higgs potential is due to the $(H^\dagger H)^3$ operator, the usual vacuum is not a global minimum for $\kappa_\lambda \gtrsim 3$. In this case the vacuum becomes metastable, although it could still have a long enough lifetime. Additional deformations from higher-dimensional operators can remove the metastability bound, even for large values of κ_λ. A lower bound $\kappa_\lambda > 1$ can also be extracted if we naively require the Higgs potential to be bounded from below for arbitrary values of the Higgs vev $\langle h \rangle$, i.e. if we require the coefficient of the $(H^\dagger H)^3$ operator to be positive. This constraint, however, is typically too restrictive. Our estimate of the effective potential, in fact, is only valid for relatively small values of the Higgs vev, which satisfy $\varepsilon = \theta g_*^2 \langle h \rangle^2 / m_*^2 \lesssim 1$. For large values of $\langle h \rangle$ the expansion in the Higgs field breaks down and the estimate of the potential obtained by including only dimension-6 operators is not reliable any more and the whole tower of higher-dimensional operators should be considered. In this case large negative corrections to the Higgs trilinear coupling could be compatible with a stable vacuum. Examples of such scenarios are the composite Higgs models in which the Higgs field is identified with a Goldstone boson. In these models the Higgs potential is periodic and a negative coefficient for the effective $(H^\dagger H)^3$ operator does not generate a runaway behavior of the potential.

4

TESTING THE HIGGS TRILINEAR AT A HADRON COLLIDER

4.1 FIT FROM INCLUSIVE SINGLE-HIGGS MEASUREMENTS

As we mentioned in the previous chapter, single-Higgs production measurements can be sensitive to large variations of the Higgs trilinear self-coupling. These effects arise at loop level and can be used to extract some constraints on the κ_λ parameter. Under the assumption that only the trilinear Higgs coupling is modified, κ_λ can be constrained to the range $\kappa_\lambda \in [-0.7, 4.2]$ at the 1σ level and $\kappa_\lambda \in [-2.0, 6.8]$ at 2σ [43] at the end of the high luminosity phase of the LHC. This result was obtained by assuming that the experimental uncertainties are given by the "Scenario 2" estimates of CMS [65, 66], in which the theory uncertainties are halved with respect to the 8 TeV LHC run and the other systematic uncertainties are scaled as the statistical errors. The actual precision achievable in the HL-LHC phase could be worse than this estimate, leading to a slightly smaller sensitivity on κ_λ. Nevertheless the result shows that single-Higgs production could be competitive with other measurements, for instance double-Higgs production, in the determination of the Higgs self coupling.

A similar analysis, focusing only on the gluon fusion cross section and on the $H \to \gamma\gamma$ branching ratio, was presented in reference [42]. With this procedure a bound $\kappa_\lambda \in [-7.0, 6.1]$ at the 2σ level was derived, whose overall size is in rough agreement with the result of reference [43].

In subsection 3.2.3 we saw that large corrections to the Higgs self-couplings are seldom generated alone and are typically accompanied by deviations in the other Higgs interactions. In scenarios that predict $\mathcal{O}(1)$ corrections to κ_λ, single-Higgs couplings, such as Yukawa interactions or couplings with the gauge bosons, usually receive corrections of the order of $5 - 10\%$. Since these corrections modify single-Higgs processes at tree level, their effects are comparable with the ones induced at loop level by a modification of the Higgs self-coupling. In these scenarios, a reliable determination of κ_λ thus requires a global fit, in which also the single-Higgs coupling distortions are properly included.

In this section we will perform such a fit, taking into account deformations of the SM encoded by the 10 effective operators introduced in section 3.2 (see Equation 3.8). As we will see, when all the effective operators are turned on simultaneously, some cancellations are possible, resulting in an unconstrained combination of the effective operators. This flat direction can not be resolved by taking into account only inclusive single-Higgs production measurements. Additional observables are thus needed to disentangle deviations in the Higgs self-coupling from distortions of single-Higgs interactions. We will discuss various possibilities along this line in section 4.2 and 4.3.

Before performing the actual fit, it is also important to mention that large deviations in κ_λ could in principle also have an impact on the determination of single-Higgs couplings. We will discuss this point in subsection 4.1.3.

4.1.1 *Single-Higgs rates and single-Higgs couplings*

As a preliminary step in our analysis, we focus on single-Higgs couplings neglecting the effects of κ_λ and we perform a global fit exploiting single-Higgs processes.

Measurements of the production and decay rates of the Higgs boson are usually reported in terms of signal strengths, i.e. the ratio of the measured rates with respect to the SM predictions. The total signal strength, μ_i^f, for a given production mode i and decay channel $h \to f$, is thus given by

$$\mu_i^f = \mu_i \times \mu^f = \frac{\sigma_i}{(\sigma_i)_{SM}} \times \frac{BR[f]}{(BR[f])_{SM}} \,. \tag{4.1}$$

Obviously the production and decay signal strengths can not be separately measured and only their products are directly accessible.

Single-Higgs production can be extracted with good accuracy at the LHC in five main modes: gluon gluon fusion (ggF), vector boson fusion (VBF), associated production with a W or a Z (WH, ZH), and associated production with a top quark pair ($t\bar{t}H$). Moreover the main Higgs decay channels are into ZZ, WW, $\gamma\gamma$, $\tau^+\tau^-$ and $b\bar{b}$.[1] A large subset of all the combinations of these production and decay modes can be extracted at the HL-LHC with a precision better than $10-20\%$. It is thus possible to linearly expand the signal strengths as

$$\mu_i^f \simeq 1 + \delta\mu_i + \delta\mu^f \,, \tag{4.2}$$

since quadratic terms are negligible.

As can be seen from Equation 4.2, a rescaling of the production rates $\mu_i \to \mu_i + \delta$ can be exactly compensated by a rescaling of the branching ratios $\mu^f \to \mu^f - \delta$. For this reason, out of the 10 quantities describing the production and decay of an on-shell particle (5 productions and 5 decays), only 9 independent constraints can be derived experimentally, which are enough to determine the set of single-Higgs couplings ($\delta c_z, c_{zz}, c_{z\Box}, \hat{c}_{z\gamma}, \hat{c}_{\gamma\gamma}, \hat{c}_{gg}, \delta y_t, \delta y_b, \delta y_\tau$).

In our numerical analysis we estimate the theory and experimental systematic uncertainties by following the ATLAS projections presented in reference [67]. The full list of uncertainties is given in Table 4.1. Notice that, with respect to the ATLAS analysis we introduced a few updates. We reduced the theory uncertainty in the gluon fusion production cross section to take into account the recent improvement in the theory predictions [36, 68]. In addition, we updated the entries corresponding to the VBF production mode with ZZ final state using the more recent estimates presented in reference [69]. To estimate the separate uncertainties in the WH and the ZH production modes with ZZ final state, which are considered together in reference [67], we divided the experimental uncertainty for VH by the square root of the corresponding event fractions.[2]

Our projections are also in fair agreement with the "Scenario 1" in the CMS extrapolations [65], in which the systematic uncertainties are assumed to be the same as in the 8 TeV LHC run. Notice that our choice is more conservative than the one made in reference [43], and should be interpreted as a "pessimistic" scenario. We will comment in subsection 4.3.2 on how the numerical results change as a function of the systematic uncertainties.

1 For simplicity we neglect the $\mu^+\mu^-$ and $c\bar{c}$ decay modes and assume that no invisible decay channels are present.

2 In this way, we get that the ratio of uncertainties between the WH and ZH channels with ZZ final state is in good agreement with a previous estimate by ATLAS [70].

Process		Combination	Theory	Experimental
$H \to \gamma\gamma$	ggF	0.07	0.05	0.05
	VBF	0.22	0.16	0.15
	$t\bar{t}H$	0.17	0.12	0.12
	WH	0.19	0.08	0.17
	ZH	0.28	0.07	0.27
$H \to ZZ$	ggF	0.06	0.05	0.04
	VBF	0.17	0.10	0.14
	$t\bar{t}H$	0.20	0.12	0.16
	WH	0.16	0.06	0.15
	ZH	0.21	0.08	0.20
$H \to WW$	ggF	0.07	0.05	0.05
	VBF	0.15	0.12	0.09
$H \to Z\gamma$	incl.	0.30	0.13	0.27
$H \to b\bar{b}$	WH	0.37	0.09	0.36
	ZH	0.14	0.05	0.13
$H \to \tau^+\tau^-$	VBF	0.19	0.12	0.15

Table 4.1: Estimated relative uncertainties on the determination of single-Higgs production channels at the HL-LHC (14 TeV center of mass energy, $3\,ab^{-1}$ integrated luminosity and pile-up 140 events/bunch-crossing). The theory, experimental (systematic plus statistic) and combined uncertainties are listed in the "Theory", "Experimental" and "Combination" columns respectively. All the estimates are derived from refs. [67, 69] and [36, 68].

To extract the fit we assume that the central values of the measured signal strengths are equal to the SM predictions, i.e. $\mu_i^f = 1$, and we perform a simple statistical analysis by constructing the χ^2 function

$$\chi^2 = \sum_{i,f} \frac{(\mu_i^f - 1)^2}{(\sigma_i^f)^2}\,, \tag{4.3}$$

where σ_i^f are the errors associated to each channel.

If we consider only small deviations in the single-Higgs couplings, we can linearly expand the signal strengths in terms of the 9 fit parameters (the numerical expressions are given in section A.2). In this way the χ^2 function becomes quadratic in the parameters and we end up in a Gaussian limit. The 1σ intervals and the full correlation matrix (with large

correlations enlightened in boldface) for the parameters are given by (by construction the best fit coincides with the SM point, where all the coefficients vanish)

$$\begin{pmatrix} \hat{c}_{gg} \\ \delta c_z \\ c_{zz} \\ c_{z\Box} \\ \hat{c}_{z\gamma} \\ \hat{c}_{\gamma\gamma} \\ \delta y_t \\ \delta y_b \\ \delta y_\tau \end{pmatrix} = \pm \begin{bmatrix} 0.07\ (0.02) \\ 0.07\ (0.01) \\ 0.64\ (0.02) \\ 0.24\ (0.01) \\ 4.94\ (0.65) \\ 0.08\ (0.02) \\ 0.09\ (0.02) \\ 0.14\ (0.03) \\ 0.17\ (0.09) \end{bmatrix} \begin{bmatrix} 1 & -0.01 & -0.02 & 0.03 & 0.08 & 0.01 & \mathbf{-0.71} & 0.03 & 0.01 \\ & 1 & -0.45 & 0.36 & -0.61 & -0.33 & 0.18 & \mathbf{0.89} & 0.53 \\ & & 1 & \mathbf{-0.99} & 0.69 & 0.11 & 0.38 & -0.47 & \mathbf{-0.74} \\ & & & 1 & -0.58 & -0.23 & -0.42 & 0.42 & \mathbf{0.71} \\ & & & & 1 & -0.58 & 0.09 & -0.46 & -0.63 \\ & & & & & 1 & 0.14 & 0.04 & 0.04 \\ & & & & & & 1 & 0.25 & -0.08 \\ & & & & & & & 1 & 0.57 \\ & & & & & & & & 1 \end{bmatrix} . \tag{4.4}$$

The numbers listed in parentheses correspond to the 1σ uncertainties obtained by considering only one parameter at a time, i.e. by setting to zero the coefficients of all the other effective operators.

The comparison between the global fit and the fit to individual operators shows that some bounds can significantly vary with the two procedures. The most striking case, as noticed already in reference [49], involves the c_{zz} and $c_{z\Box}$ coefficients, whose fit shows a high degree of correlation. As a consequence, the constraints obtained in the global fit are more than one order of magnitude weaker than the individual fit ones. This high degeneracy can be lifted by including in the fit constraints coming from EW observables. Indeed, as we will discuss later on, a combination of the c_{zz} and $c_{z\Box}$ operators also modifies the triple gauge couplings, generating an interesting interplay between Higgs physics and vector boson pair production.

Another element of particular interest in the correlation matrix is the $\hat{c}_{gg} - \delta y_t$ entry. The cleanest observable constraining these couplings is the gluon fusion cross section, which however can only test a combination of the two parameters. In order to disentangle them one needs to consider the $t\bar{t}H$ production mode. This process, however, has a limited precision at the LHC, explaining the large correlation between $\hat{c}_{gg}$ and δy_t and the weaker bounds in the global fit. Other ways to gain information about the top Yukawa coupling are to rely on an exclusive analysis of gluon fusion with an extra hard jet [71] or to consider the effects of off-shell Higgs production [72, 73]

High correlations are also present between the bottom Yukawa parameter δy_b and all the other parameters except $\hat{c}_{gg}$ and δy_t. The origin of the correlations can be traced back to the fact that the main impact of a modified bottom Yukawa is a rescaling of the Higgs branching ratios. Since the $b\bar{b}$ decay channel can only be tested with limited accuracy, the main constraints on δy_b come exploiting the gluon fusion channel with the Higgs decaying into $\gamma\gamma$, ZZ, *WW* and $\tau\tau$. A variation of the bottom Yukawa leaves the gluon fusion cross section nearly unchanged, thus to recover the SM predictions one needs to compensate the variations in the branching ratios induced by δy_b with contributions from the δc_z, c_{zz}, $c_{z\Box}$, $\hat{c}_{z\gamma}$, $\hat{c}_{\gamma\gamma}$ and δy_τ. This feature gives rise to the large correlations between δy_b and these parameters.

The presence of sizable correlations among various parameters significantly limits the robustness of the results shown in Equation 4.4. In particular the Gaussian approximation we used to derive the bounds is not fully justified. We checked that, by using the full

expressions for the signal rates the 1σ limits are significantly modified. The largest effects are found in the c_{zz} and $c_{z\Box}$ bounds, which change at order one. Such large sensitivity to the quadratic (and higher-order) terms in the fit also signals that corrections coming from higher-dimensional effective operators could also affect the fit in a non-negligible way. To solve this problem we need to lift the approximate flat directions related to the large entries in the correlation matrix. One way to achieve this goal is to include in the fit additional observables that can provide independent constraints on the Higgs couplings. We will list in the following a few possibilities.

DI-BOSON DATA. A first set of observables that has an interplay with Higgs physics is given by the EW boson triple gauge couplings (TGCs). In the Higgs basis the deviations of two TGCs are correlated to the single-Higgs couplings modifications. Measurements of the WWZ and $WW\gamma$ interactions can be converted into constraints on two linear combinations of the $\hat{c}_{\gamma\gamma}$, $\hat{c}_{z\gamma}$, c_{zz} and $c_{z\Box}$ parameters (see the explicit expressions in Equations (2.14) and (2.13)), which can be used to remove the correlation between c_{zz} and $c_{z\Box}$. At present the WWZ and $WW\gamma$ couplings are tested with an accuracy of order $\sim 5\%$ [74, 75]. For our numerical analyses we will assume a precision of order 1% at the end of the HL-LHC phase.

RARE HIGGS DECAYS. Another set of observables related to the Higgs couplings is obtained by considering additional, more rare Higgs decays. The inclusion of the $h \to Z\gamma$ decay, which is expected to be measured with $\sim 30\%$ accuracy at the HL-LHC [76], can be used to constrain the $\hat{c}_{z\gamma}$ parameter. The $h \to \mu^+\mu^-$ decay, on the other hand, has a limited impact on the fit, since it depends on an additional parameter, the deviation in the muon Yukawa δy_μ. In the flavor universal case, however, the muon and tau Yukawa receive equal new-physics contributions, $\delta y_\mu = \delta y_\tau$, and the determination of δy_μ can be used to improve the fit on δy_τ. The improvement is anyhow limited, since the precision achievable in the measurement of the $h \to \mu^+\mu^-$ decay is comparable with the one achievable directly on the τ Yukawa. Apart from the impact on δy_τ, the influence of the $h \to \mu^+\mu^-$ channel on the fit of the remaining single-Higgs couplings is negligible.

The above constraints, in particular the ones coming from TGCs and $h \to Z\gamma$, significantly help in improving the fit on single-Higgs couplings and lowering the correlations. The 1σ fit intervals on the EFT parameters and the correlation matrix are modified as

$$\begin{pmatrix} \hat{c}_{gg} \\ \delta c_z \\ c_{zz} \\ c_{z\Box} \\ \hat{c}_{z\gamma} \\ \hat{c}_{\gamma\gamma} \\ \delta y_t \\ \delta y_b \\ \delta y_\tau \end{pmatrix} = \pm \begin{pmatrix} 0.07\ (0.02) \\ 0.05\ (0.01) \\ 0.05\ (0.02) \\ 0.02\ (0.01) \\ 0.09\ (0.09) \\ 0.03\ (0.02) \\ 0.08\ (0.02) \\ 0.12\ (0.03) \\ 0.11\ (0.09) \end{pmatrix} \begin{bmatrix} 1 & 0.04 & -0.01 & -0.01 & 0.04 & 0.31 & \mathbf{-0.76} & 0.05 & 0.02 \\ & 1 & -0.07 & -0.26 & 0.01 & 0.01 & 0.36 & \mathbf{0.88} & 0.27 \\ & & 1 & \mathbf{-0.87} & 0.13 & 0.20 & 0.03 & -0.07 & -0.06 \\ & & & 1 & -0.09 & -0.09 & -0.09 & -0.17 & 0.08 \\ & & & & 1 & 0.05 & -0.02 & -0.02 & -0.03 \\ & & & & & 1 & -0.32 & -0.19 & -0.12 \\ & & & & & & 1 & 0.50 & 0.28 \\ & & & & & & & 1 & 0.36 \\ & & & & & & & & 1 \end{bmatrix} . \quad (4.5)$$

These results have been obtained by linearizing the signal strengths. We however checked that, by using the full expressions for the μ_i^f, the results in Equation 4.5

remain basically unchanged. The additional constraints coming from the TGCs and $h \to Z\gamma$ measurements thus effectively resolve the approximate flat directions making our linearized EFT fit fully consistent and robust.

HIGGS WIDTH. Finally one could also consider the constraint on the Higgs total width, which could be extracted by comparing off-shell and on-shell Higgs measurements [77–81].[3] ATLAS estimated that a precision of 40% could be reached at the end of the HL-LHC [84]. If we include this piece of information in the fit, we find that also this constraint has a negligible impact on the flat directions. To assess whether an improvement on such projections could have an effect on the global fit, we repeated our analysis varying the estimated precision on the width. As expected, the most sensitive coefficients are δy_b and δc_z. In order to affect their 1σ fit intervals, one needs a precision on the width of at least 20%. In particular, we find that if we assume a precision of 40%, 20%, and 10%, the 1σ bound on δy_b of Equation 4.5 shrinks to 0.11, 0.09, and 0.06, while the one on δc_z is reduced respectively to 0.05, 0.04 and 0.03.

To conclude the discussion about single-Higgs couplings, it is useful to report on what happens if we relax the assumption of small deviations in the Higgs interactions. In this case the linear expansion in the signal strengths is no longer appropriate and the full expressions must be retained. Additional minima are then present in the fit. Trivial ones are obtained by reversing the sign of the tau ($\delta y_\tau \simeq -2$) or bottom ($\delta y_b \simeq -2$) Yukawas, which leave the production cross sections and decay branching ratios unchanged.[4] Other minima are obtained by choosing $\hat{c}_{gg}$ in such a way that its contribution to the gluon fusion amplitude is minus twice the SM one ($\hat{c}_{gg} \simeq -2$) or by choosing $\hat{c}_{\gamma\gamma}$ so that it reverses the amplitude for Higgs decay into a photon pair ($\hat{c}_{\gamma\gamma} \simeq 1.6$). Less trivial minima are instead obtained by reversing the top Yukawa coupling ($\delta y_t \simeq -2$), with either $\hat{c}_{gg} \simeq 0$ or $\hat{c}_{gg} \simeq 2$. In this case the interference between the W and top contributions to the branching ratio $h \to \gamma\gamma$ changes sign and must be compensated by a contribution from $\hat{c}_{\gamma\gamma}$ ($\hat{c}_{\gamma\gamma} \simeq 2.1$ or $\hat{c}_{\gamma\gamma} \simeq 0.46$). An additional possibility is to reverse the sign of the associated production channels amplitude ($\delta c_z \simeq -2$), in which case the change in the $h \to \gamma\gamma$ amplitude can be compensated by $\hat{c}_{\gamma\gamma} \simeq -0.45$ or $\hat{c}_{\gamma\gamma} \simeq -2.1$. Finally by reversing both the sign of both the top Yukawa and of the associated production channels amplitude, one finds two additional minima with $\hat{c}_{\gamma\gamma} \simeq -1.6$ or $\hat{c}_{\gamma\gamma} \simeq 0.01$.

Some of these additional minima can be probed by considering other observables. The sign of the top Yukawa can be extracted from the measurement of h + top production, as shown in references [85–87]. Large contributions to $\hat{c}_{gg}$ can instead be probed in double-Higgs production, which can be used to exclude the $\hat{c}_{gg} \simeq -2$ minimum [58]. The sign of the bottom Yukawa can instead be tested by considering the transverse momentum distributions in Higgs production with an extra jet [88] (see also reference [89]).[5] We are instead not aware of any process which could be sensitive to the sign of the tau Yukawa.

In our analysis we also assumed that the sign of the hWW and hZZ couplings are the same (fixing them to be positive for definiteness). Such assumption is well motivated

3 See also refs. [72, 82, 83] for possible issues related to the EFT interpretation of these measurements.

4 In the case of a "wrong-sign" botton Yukawa with an unchanged top Yukawa a small contribution from $\hat{c}_{gg}$ is needed to compensate for the small change in the gluon fusion cross section.

5 An additional Higgs associated production channel, namely $H\gamma$, could be used to test large deviations in $\hat{c}_{\gamma\gamma}$ [90].

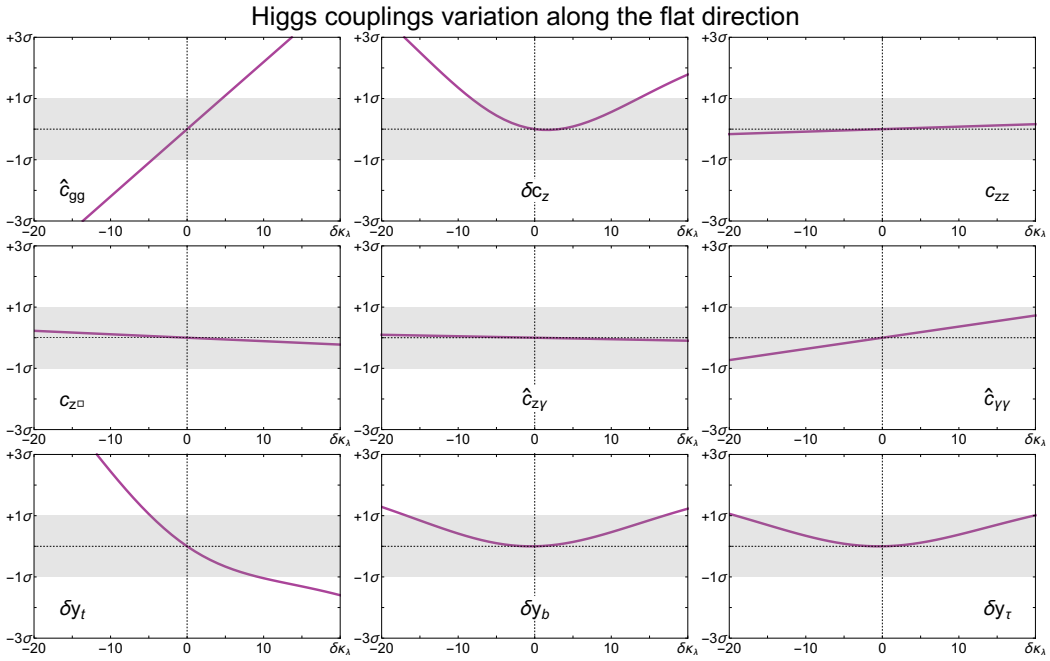

Figure 4.1: Variation of the Higgs basis parameters along the flat direction as a function of the Higgs trilinear coupling κ_λ. The gray bands correspond to the 1σ error bands at the HL-LHC (see Equation 4.4).

theoretically, since a sign difference would imply large contributions to custodial breaking operators. From the experimental point of view, however, testing the sign of the hWW and hZZ couplings explicitly is very difficult at the LHC. It could be possible at future lepton colliders, which could be sensitive to the relative sign of the two couplings in ZH and ZHH production [91].

4.1.2 *Global fit including Higgs self-coupling*

We can now discuss how the above picture changes when we introduce in the fit the additional parameter κ_λ controlling the Higgs self-coupling deformations. As we saw in the previous subsection, the measurement of 5 production and 5 Higgs decay channels allows us to extract 9 independent constraints on the coefficients of the EFT Lagrangian. By introducing κ_λ in our fit, we reach a total of 10 independent parameters, thus we expect one linear combination to remain unconstrained in the fit. This is indeed what happens. The global fit has an exact flat direction along which the χ^2 vanishes.

In Figure 4.1 we plot the values of the single-Higgs coupling parameters as a function of κ_λ along the flat direction. It is interesting to notice that a strong correlation is found between the Higgs trilinear coupling κ_λ, the Higgs contact interaction with gluons $\hat{c}_{gg}$ and the top Yukawa δy_t. When we limit the κ_λ variation to the region $\kappa_\lambda \in [-1, 10]$, as indicated by the constraints coming from double-Higgs production, $\hat{c}_{gg}$ and δy_t vary by an amount comparable with the 1σ error at the HL-LHC (obtained in a fit without κ_λ). On the other hand, along the flat direction, the remaining parameters vary by a much lower

amount ($\hat{c}_{\gamma\gamma}$, δc_z, δy_b and δy_τ) or, in some cases, remain almost unchanged (c_{zz}, $c_{z\Box}$, $\hat{c}_{z\gamma}$).[6]

It must be stressed that the exact flat direction could in principle be lifted if we include in the signal strengths computation also terms quadratic in the EFT parameters. The additional terms, however, become relevant only for very large values of κ_λ, so that for all practical purposes we can treat the flat direction as exact. Notice moreover that, when the quadratic terms become important, one must a priori also worry about possible corrections from higher-dimensional operators, which could become comparable to the square of dimension-6 operators.

As we discussed in the previous section, additional observables can provide independent bounds on the Higgs couplings. In particular some of the strongest constraints come from the measurements of TGCs and of the $h \to Z\gamma$ branching ratio. In the fit of the single-Higgs couplings these constraints were enough to get rid of the large correlation between c_{zz} and $c_{z\Box}$ and to improve the bound on $\hat{c}_{z\gamma}$. The impact on the global fit including the Higgs trilinear coupling is instead limited. The reason is the fact that the combination of parameters tested in TGCs (see Equations (2.14) and (2.13)) and in $h \to Z\gamma$ are "aligned" with the flat direction, i.e. they involve couplings whose values along the flat direction change very slowly (see Figure 4.1). Although the flat direction is no more exact, even assuming that the TGCs and $c_{z\gamma}$ can be tested with arbitrary precision, very large deviations in the Higgs self-coupling would still be allowed.

An additional way to probe the flat direction is to compare single-Higgs production rates at different collider energies. This possibility stems from the fact that the kinematic distributions in Higgs production channels with associated objects (VBF, ZH, WH and $t\bar{t}H$) change in a non-trivial way as a function of the collider energy [43, 44]. As a consequence the impact of the modification of the Higgs couplings on the production rates shows some dependence on the energy as well. As one can see from the numerical results reported in section A.2, the dependence of the VBF, ZH and WH rates on the c_{zz}, $c_{z\Box}$, $\hat{c}_{z\gamma}$ and $\hat{c}_{\gamma\gamma}$ parameters changes as a function of the collider energy (Equations (A.4), (A.5) and (A.6)). The corrections due to κ_λ also show a dependence on the energy. In particular the strongest effects are present in the $t\bar{t}H$ production rate, as can be seen from Equation A.16 and the list of coefficients in Table A.2.

The difference in the new physics effects at the different LHC energies are quite small, so that they do not really allow for an improvement in the fit, taking also into account the fact that accurate enough predictions will be obtained only for one center of mass energy. Future colliders (as for instance a 33 TeV hadron machine) could lead to more pronounced changes in the parameter dependence.[7] However the improvement achievable with a combined fit is only marginal. A more efficient way of exploiting higher-energy machines is to look for double-Higgs production which could probe κ_λ with enough accuracy to make its contributions to single-Higgs processes negligible (assuming that no significant deviation with respect to the SM is found) [61].

To conclude the discussion on the extraction of the Higgs self-coupling, we show in Figure 4.2 the χ^2 obtained from the global fit on single-Higgs observables. The fit also

6 An interesting feature is the fact that along the flat direction not only $\delta\mu_i^f = 0$, but also the individual production and decay signal strengths are approximately equal to the SM ones, namely $|\delta\mu_i| < 0.005$, $|\delta\mu^f| < 0.005$ for $|\kappa_\lambda| < 20$.

7 We thank D. Pagani for providing us with the results for the κ_λ contribution to the inclusive observables at 33 and 100 TeV.

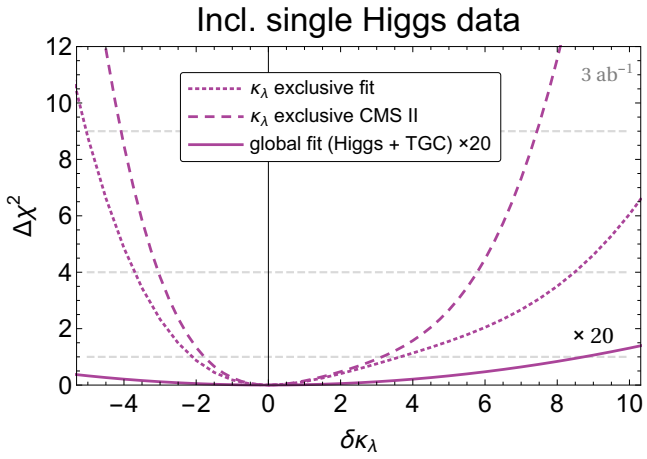

Figure 4.2: χ^2 as a function of the Higgs trilinear coupling κ_λ obtained by performing a global fit including the constraints coming from TGCs measurements and the bound on the $h \to Z\gamma$ decay rate. The results are obtained by assuming an integrated luminosity of $3\,\text{ab}^{-1}$ at $14\,\text{TeV}$. The dotted curve corresponds to the result obtained by setting to zero all the other the Higgs-coupling parameters, while the solid curve is obtained by profiling and is multiplied by a factor 20 to improve its visibility. To compare with previous literature (reference [43]), we also display the exclusive fit performed assuming the uncertainty projections from the more optimistic "Scenario 2" of CMS [65] (dashed curve).

includes the constraints from TGCs and the bound on the $h \to Z\gamma$ decay rate.[8] The results have been derived by assuming a $14\,\text{TeV}$ LHC energy with an integrated luminosity of $3\,\text{ab}^{-1}$. The dashed curve shows the χ^2 obtained by setting all the single-Higgs couplings deviations to zero. One can see that the Higgs self-coupling can be restricted to the interval $\kappa_\lambda \in [-1.1, 4.7]$ at the 1σ level. To compare with the existing literature, we also show the exclusive fit obtained in the optimistic "Scenario 2" of CMS (dashed curve), which is in very good agreement with the results of reference [43].

On the other hand by profiling over the single-Higgs couplings we find that the Higgs trilinear coupling remains basically unconstrained (see solid curve in Figure 4.2).[9] As expected, even with the inclusion of the TGCs constraints and of the bounds on the $h \to Z\gamma$ decay rate, an almost flat direction is still present in the fit.

4.1.3 *Impact of the trilinear coupling on single-Higgs couplings*

The presence of a flat direction can also have an impact on the fit of the single-Higgs couplings. If we perform a global fit and we allow κ_λ to take arbitrary values we also lose predictivity on the single-Higgs EFT parameters. The effect is more pronounced on the couplings that show larger variations along the flat direction, namely $\hat{c}_{gg}$ and δy_t. A milder impact is found for the δc_z, δy_b, δy_τ and $\hat{c}_{\gamma\gamma}$, whereas c_{zz}, $c_{z\Box}$ and $\hat{c}_{z\gamma}$ are almost unaffected, unless extremely large values of κ_λ are allowed.

8 A full computation of the corrections to the $h \to Z\gamma$ branching ratio due to the Higgs trilinear interaction is not available at present. For this reason we only took into account the effect of the Higgs wavefunction renormalization, which scales as κ_λ^2 (see section A.2), and we neglected the additional corrections linear in κ_λ which are not known.

9 Since in our linear approximation the χ^2 as a function of the single-Higgs couplings is quadratic the resulting distribution is Gaussian. In this case a profiling procedure gives the same result as a marginalization.

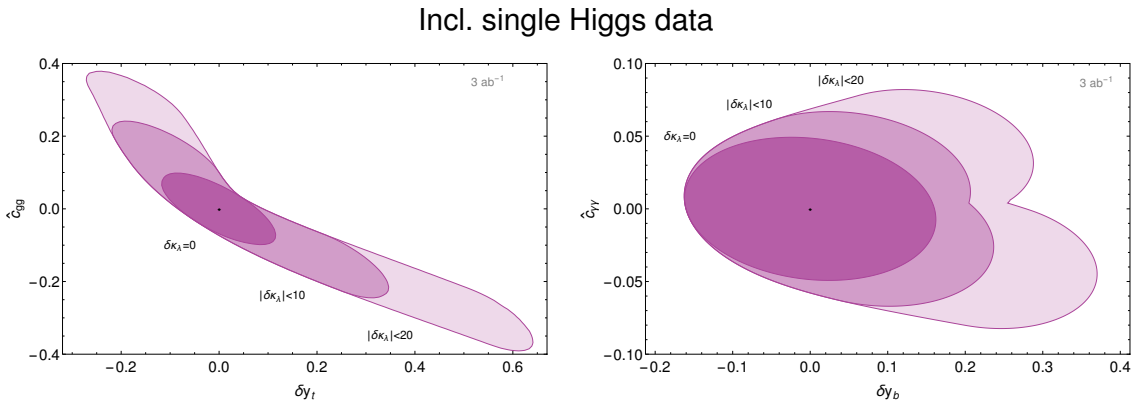

Figure 4.3: Constraints in the planes $(\delta y_t, \hat{c}_{gg})$ (left panel) and $(\delta y_b, \hat{c}_{\gamma\gamma})$ (right panel) obtained from a global fit on the single-Higgs processes. The darker regions are obtained by fixing the Higgs trilinear to the SM value $\kappa_\lambda = 1$, while the lighter ones are obtained through profiling by restricting $\delta\kappa_\lambda$ in the ranges $|\delta\kappa_\lambda| \leqslant 10$ and $|\delta\kappa_\lambda| \leqslant 20$ respectively. The regions correspond to 68% confidence level (defined in the Gaussian limit corresponding to $\Delta\chi^2 = 2.3$).

In Figure 4.3 we compare the fit in the $(\delta y_t, \hat{c}_{gg})$ and $(\delta y_b, \hat{c}_{\gamma\gamma})$ planes obtained by setting the Higgs trilinear to the SM value ($\delta\kappa_\lambda = 0$), with the results obtained by allowing $\delta\kappa_\lambda$ to vary in the ranges $|\delta\kappa_\lambda| \leqslant 10$ and $|\delta\kappa_\lambda| \leqslant 20$.

In the $(\delta y_t, \hat{c}_{gg})$ case (left panel of Figure 4.3), there is a strong (anti-)correlation between the two parameters as we explained in subsection 4.1.1. When the Higgs self-coupling is included in the fit the strong correlation is still present. The constraint along the correlated direction becomes significantly weaker, even if we restrict $\delta\kappa_\lambda$ to the range $|\delta\kappa_\lambda| \leqslant 10$. The constraint in the orthogonal direction is instead only marginally affected.

In the case of the $(\delta y_b, \hat{c}_{\gamma\gamma})$ observables, we find that the 1σ uncertainty on the determination of the two parameters is roughly doubled if the Higgs trilinear coupling is allowed to take values up to $|\delta\kappa_\lambda| \sim 20$.

This above discussion makes clear that a global fit on the single-Higgs observables can not be properly done without including some assumption on the allowed values of the trilinear self-coupling of the Higgs (see subsection 3.2.3). If κ_λ can sizably deviate from the SM value ($\delta\kappa_\lambda \gtrsim 5$) including it into the fit is mandatory in order to obtain accurate predictions for the single-Higgs couplings. On the other hand, if we have some theoretical bias that constrains the Higgs self-coupling modifications to be small ($\delta\kappa_\lambda \lesssim$ few), a restricted fit in which only the corrections to single-Higgs couplings are included is reliable.

We will see in the following that the situation can drastically change if we include in the fit additional measurements that can lift the flat direction. In particular we will focus on the measurement of double-Higgs production in the next section and of differential single-Higgs distributions in section 4.3.

4.2 DOUBLE-HIGGS PRODUCTION

A natural way to extract information about the Higgs self-coupling is to consider Higgs pair production channels. Among this class of processes, the production mode with the largest cross section [92], which we can hope to test with better accuracy at the LHC, is

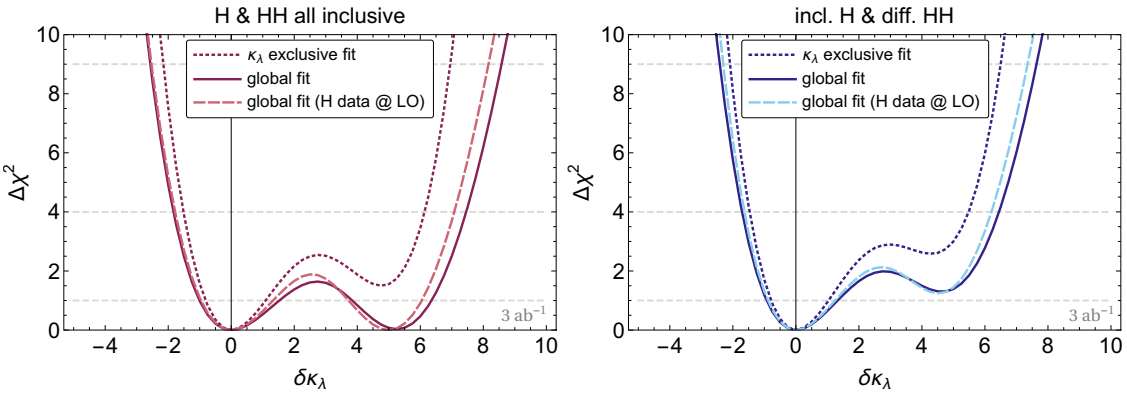

Figure 4.4: LEFT: The solid curve shows the global χ^2 as a function of the corrections to the Higgs trilinear self-coupling obtained from a fit exploiting inclusive single-Higgs and inclusive double-Higgs observables. The dashed line shows the fit obtained by neglecting the dependence on $\delta\kappa_\lambda$ in single-Higgs observables. The dotted line is obtained by exclusive fit in which all the EFT parameters, except for $\delta\kappa_\lambda$, are set to zero. RIGHT: The same but using differential observables for double-Higgs.

gluon fusion.[10] Several analyses are available in the literature, focusing on the various Higgs decay modes. The channel believed to be measurable with the highest precision is $hh \to b\bar{b}\gamma\gamma$ [58, 96, 101–107]. In spite of the small branching ratio (BR $\simeq 0.264\%$), its clean final state allows for high reconstruction efficiency and low levels of backgrounds. In the following we will thus focus on this channel for our analysis.

Additional final states have also been considered in the literature, in particular $hh \to b\bar{b}b\bar{b}$ [108–111], $hh \to b\bar{b}WW^*$ [96, 109, 112] and $hh \to b\bar{b}\tau^+\tau^-$ [96, 108, 109, 113, 114]. All these channels are plagued by much larger backgrounds. In order to extract the signal, one must rely on configurations with boosted final states and more involved reconstruction techniques, which limit the achievable precision.

The dependence of the double-Higgs production cross section on the EFT parameters has been studied in reference [58, 114–116]. It has been shown that a differential analysis taking into account the Higgs pair invariant mass distribution can help in extracting better bounds on the relevant EFT parameters.

On top of the dependence on κ_λ, double-Higgs production is sensitive at leading order to 4 additional EFT parameters, namely δy_t, $\delta y_t^{(2)}$, $\hat{c}_{gg}$ and $\hat{c}_{gg}^{(2)}$. The explicit expression of the cross section is given in section A.2, Equation A.19. As we discussed in section 3.2, in the linear EFT description only δy_t and $\hat{c}_{gg}$ are independent parameters, while the other two correspond to the combinations given in Equation 3.9. By a suitable cut-and-count analysis strategy, the total SM Higgs pair production cross section is expected to be measured with a precision $\sim 50\%$ at the HL-LHC [58]. These estimates are in good agreement with the recent projections by ATLAS [107].

10 It has been pointed out in reference [93] that the WHH and ZHH production modes could provide a good sensitivity to positive deviations in the Higgs self-coupling (see also references [94–96]). As we will see in the following, the gluon fusion channel is instead more sensitive to negative deviations. The associated double-Higgs production channels could therefore provide useful complementary information for the determination of κ_λ. For simplicity we only focus on the gluon fusion channels in the present analysis. We leave the study of the VHH channels, as well as of the double-Higgs production mode in VBF (see references [95, 97–100]), for future work.

As a first point, we focus on the determination of the trilinear Higgs self-coupling. In the left panel of Figure 4.4 we show the χ^2 as a function of κ_λ. The solid curve corresponds to the result of a global fit including single-Higgs and inclusive double-Higgs observables. All the single-Higgs EFT parameters have been eliminated by profiling. The dashed curve shows how the fit is modified if we neglect the dependence on κ_λ in single-Higgs processes. Finally, the dotted curve is obtained by performing an exclusive fit, in which all the deviations in single-Higgs couplings are set to zero.

As expected, the measurement of double-Higgs production removes the flat direction that was present in the fit coming only from single-Higgs observables. The global fit constrains the Higgs trilinear self-coupling to the intervals $\kappa_\lambda \in [0.0, 2.5] \cup [4.9, 7.4]$ at 68% confidence level and $\kappa_\lambda \in [-0.8, 8.5]$ at 95%. As we can see by comparing the solid and dashed lines in Figure 4.4, the fit of κ_λ is almost completely determined by Higgs pair production. This result is expected and is coherent with the fact that a flat direction involving κ_λ is present in the single-Higgs fit. On the other hand if we perform an exclusive fit in which we set to zero all the deviations in single-Higgs couplings, the determination of the Higgs trilinear self-coupling is significantly modified. In particular the exclusive fit disfavors large deviations in κ_λ, so that values $\delta\kappa_\lambda \sim 5$, which were allowed by the global fit, are now excluded at the 1σ level. The 95% fit region is also slightly reduced becoming $\kappa_\lambda \in [-0.5, 7.1]$.

It is also interesting to discuss what happens if we include in the fit a differential analysis of double-Higgs production. As shown in reference [58], each new physics effect deforms the Higgs-pair invariant mass distribution in a different way. Deviations in the Higgs self-coupling mostly affect the threshold distribution, while they have a limited impact in the high invariant-mass tail. On the contrary δy_t and $\hat{c}_{gg}$ modify more strongly the peak and tail of the distribution. A differential analysis can exploit this different behavior to extract better constraints on the various EFT coefficients. The fits including the differential information on Higgs pair production are shown in the right panel of Figure 4.4. Sizable positive corrections to κ_λ are now disfavored even in a global fit. The 1σ interval is now reduced to $\kappa_\lambda \in [0.1, 2.3]$, while the 2σ interval is $\kappa_\lambda \in [-0.7, 7.5]$.

Another aspect worth discussing is the impact of double-Higgs production measurement on the determination of the single-Higgs couplings. We find that the global fit determines the latter couplings with a precision comparable with the one obtained by neglecting the deviations in κ_λ (see subsection 4.1.1, Equation 4.4). This result may look surprising at a first sight. Double-Higgs measurements at the LHC can only probe the order of magnitude of the Higgs trilinear self-coupling, so that large deviations from the SM value, $\kappa_\lambda \sim 6$, will be allowed at the 68% confidence level. Such big deviations could in turn compensate non-negligible corrections to the single-Higgs measurements (by moving along the flat direction of the single-Higgs observables fit). The reason why this does not happen is related to the fact that double-Higgs production is sensitive not only to κ_λ, but also to δy_t and $\hat{c}_{gg}$. Actually, the sensitivity on the latter two parameters is relatively strong, so that the bounds on δy_t and $\hat{c}_{gg}$ coming from double-Higgs alone are not much weaker than the ones coming from single-Higgs processes [58]. These results hold with the assumption that EW symmetry is linearly realized. We will see in subsection 4.3.2 how they are modified in the context of a non-linear EFT.

4.3 DIFFERENTIAL OBSERVABLES

Up to now we focused on inclusive single-Higgs observables, which allowed us to get robust predictions backed up by the estimates made by the ATLAS and CMS experimental collaborations. It is however clear that inclusive observables do not maximize the information attainable from the data. Important additional information can be extracted by exploiting differential single-Higgs distributions. This can be crucial in our analysis since flat directions are present in the inclusive fit. Inclusive double-Higgs data is enough to lift this flat direction. Still it leaves a second minimum degenerate with the SM. Differential information can help removing this degeneracy in addition to improving the precise determination of the Higgs trilinear coupling around the SM.

The exploitation of differential distributions can help to break the degeneracy thanks to the fact that the various effective operators affect the kinematic distributions in different ways. Consider for instance associated production of a Higgs with a vector boson. EFT operators that modify the single-Higgs couplings give effects that grow with the centre of mass energy, hence they mostly affect the high-energy tail of the invariant mass or transverse momentum distributions. On the contrary, the effect of a modified Higgs trilinear self-coupling is larger near threshold. This different behavior is the key feature than can allow us to efficiently disentangle the two effects [43, 44].

The change in the differential single-Higgs distributions, in particular in the WH, ZH, $t\bar{t}H$ and VBF channels, as a function of the distortion of the Higgs self-coupling has been studied in reference [43, 44].[11] In this section we will use these results as a building block to perform a first assessment of the impact of the differential single-Higgs measurements on the extraction of the Higgs self-interactions and on the global fit of the Higgs couplings.

4.3.1 *Impact of single-Higgs differential measurements*

In the following we focus our attention on the differential distributions in associated Higgs production channels, ZH, WH and $t\bar{t}H$. We instead neglect the VBF channel, which was found to have a negligible impact on the determination of the trilinear Higgs coupling in references [43, 44].

For our analysis we consider the differential distributions in the total invariant mass of the processes. As we discussed in section 3.2, considering high energetic bins in differential distributions might lead to issues with the validity of the EFT interpretation. For this reason we only include in our analysis bins with an invariant mass up to three times the threshold energy for the various channels, which corresponds to $\sim 600\,\mathrm{GeV}$ for associated production with a gauge boson and to $\sim 1.4\,\mathrm{TeV}$ for $t\bar{t}H$. The numerical LO predictions of the ZH and WH cross sections in each bin as a function of the single-Higgs EFT parameters are given in section A.2, while the signal strength for $t\bar{t}H$ is instead modified at LO in an energy-independent way. Concerning the loop-induced effect of κ_λ on the invariant mass distributions of the ZH, WH, and $t\bar{t}H$ cross-sections, only the $13\,\mathrm{TeV}$ results are known [43]. Therefore we use this center of mass energy for our numerical study. We however expect that our results provide a fair assessment of the precision achievable at

11 Recently, reference [117] also computed the impact of the Higgs coupling deviations in the Higgs basis on angular distributions in the four-lepton decay channels of the Higgs boson. We have not included these effects in our analysis.

the 14 TeV HL-LHC, since the differences with respect to the 13 TeV case should not be very large.

For our numerical analysis we estimate the statistical and systematic uncertainties from the HL-LHC ATLAS projections [67]. A comprehensive analysis of the uncertainties at the differential level is beyond the scope of our study. We therefore adopt some simplified assumptions to provide a first assessment of the benefit of including differential distributions in our global fit of single-Higgs observables. In order to evaluate the dependence of our results on the experimental accuracy we consider two different procedures to estimate the uncertainties. In the first, more optimistic procedure, the systematic uncertainty is assumed to be the same in all the invariant mass bins, whereas the statistical uncertainty is rescaled according to the expected number of events in each bin. In the second, more pessimistic estimate, we extract the uncertainty for each bin by rescaling the total experimental error according to the expected number of events in each bin. In this way we are effectively inflating the systematic errors assuming that they degrade as the statistical ones in bins with fewer events. The uncertainties for the two scenarios are reported in Tables A.6 and A.7.

Notice that the invariant mass of some processes is not directly accessible experimentally, since the event kinematics can not be fully reconstructed. We nevertheless use it for our analysis for simplicity. As a cross check, we verified that performing the analysis with transverse momentum binning does not significantly modify the results of the fit. Since our estimates of the experimental uncertainties and our analysis strategy are quite crude, we do not expect our numerical results to be fully accurate. They must instead be interpreted as rough estimates which can however give an idea of the discriminating power that we could expect by the exploitation of differential single-Higgs distributions.

As a first step we consider the impact on the determination of single-Higgs couplings. Including the differential information in the fit helps in reducing the correlation between c_{zz} and $c_{z\Box}$. The overall change in the fit is however small and the 1σ intervals are nearly unchanged with respect to the ones we obtained in the inclusive analysis (see Equation 4.5).

More interesting results are instead obtained when we focus on the extraction of the Higgs trilinear self-coupling. We find that differential distributions are able to lift the flat direction we found in the inclusive single-Higgs observables fit. The solid green lines in Figure 4.5 show the χ^2 obtained in a global fit on single-Higgs observables including the differential information from associated production modes. The two lines correspond to the "optimistic" and "pessimistic" assumptions on the experimental uncertainties. Through this procedure one could constrain the Higgs trilinear coupling to the interval $|\delta\kappa_\lambda| \lesssim 5$ at the 1σ level. An exclusive fit, in which all the single-Higgs couplings deviations are set to zero, gives a range $\kappa_\lambda \in [-0.8, 3.5]$ at 1σ and $\kappa_\lambda \in [-2, 7]$ at 2σ (dotted green lines), which is significantly smaller than the one obtained through a global fit, as can be seen by comparing with the solid lines in Figure 4.5.

The results in Figure 4.5 show that in a global fit the impact of differential single-Higgs measurements on the extraction of κ_λ is weaker than the one of differential double-Higgs production. This can be clearly seen by comparing the solid green lines with the solid dark blue curve which represent the χ^2 coming from double-Higgs measurements (this curve coincides with the results shown on the right panel of Figure 4.4). Nevertheless, combining the single-Higgs differential information with the double-Higgs fit helps in

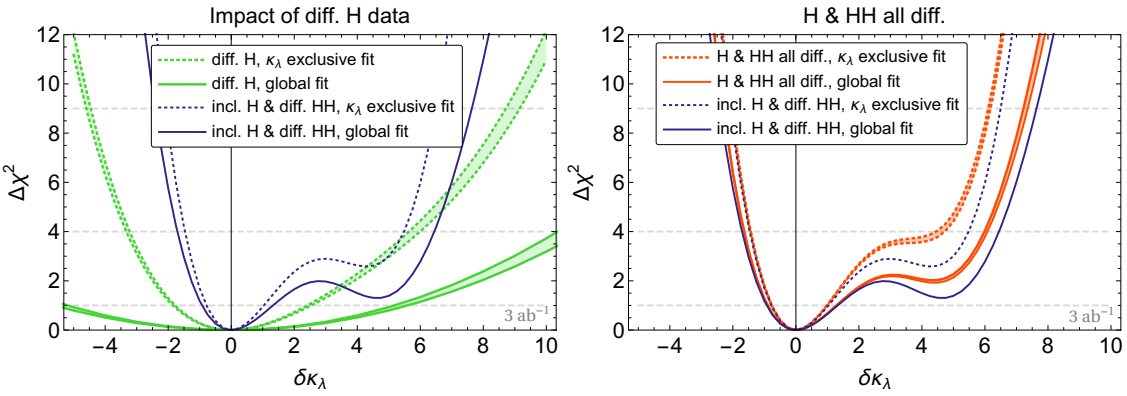

Figure 4.5: LEFT: χ^2 as a function of the Higgs trilinear self-coupling. The green bands are obtained from the differential analysis on single-Higgs observables and are delimited by the fits corresponding to the optimistic and pessimistic estimates of the experimental uncertainties. The dotted green curves correspond to a fit performed exclusively on $\delta\kappa_\lambda$ setting to zero all the other parameters, while the solid green lines are obtained by a global fit profiling over the single-Higgs coupling parameters. RIGHT: The red lines show the fits obtained by a combination of single-Higgs and double-Higgs differential observables. In both panels the dark blue curves are obtained by considering only double-Higgs differential observables and coincide with the results shown in Figure 4.4.

testing large positive deviations in κ_λ, increasing the χ^2 value for values $\delta\kappa_\lambda \sim 5$. This improvement can be seen on the right panel of Figure 4.5 (solid curves).

Differential single-Higgs measurements have a significantly more relevant role in exclusive fits in which the single-Higgs parameters are set to zero. One can see in the left panel of Figure 4.5 that the sensitivity of the single-Higgs differential fit (dotted blue line) is comparable with the one of double-Higgs measurements, especially for positive deviations in κ_λ. Combining single-Higgs and double-Higgs information provides a good improvement in the fit, in particular at the 2σ level, as can be seen in the right panel of Figure 4.5 (dotted lines).

4.3.2 *Robustness of the fits*

As a final point we want to discuss how much the determination of the Higgs trilinear self-interaction and of the single-Higgs couplings depends on the experimental accuracy and on the theoretical assumptions underlying the EFT parametrization.

In the left panel of Figure 4.6 we show how the fit on κ_λ changes if we rescale the errors on single-Higgs measurements by a factor in the range $[1/2, 2]$. One can see that the χ^2 function around the SM point $\delta\kappa_\lambda = 0$ is not strongly affected, so that the 1σ region is only mildly modified. Large positive deviations from the SM can instead be probed with significantly different accuracy. In particular the 2σ region is enlarged to $\kappa_\lambda \in [-0.8, 7.7]$ if we double the uncertainties, whereas it shrinks to $\kappa_\lambda \in [-0.5, 5.3]$ if we reduce the errors by a factor $1/2$.

A second point worth investigating is how the fit changes if we modify the assumptions on the EFT parametrization. As an illustrative example we analyze a scenario in which the EFT Lagrangian has a non-linear form, i.e. the expansion in Higgs powers breaks down. As we already discussed in subsection 3.2.3, in this case operators containing Higgs fields can not be tested any more in precision measurements not involving the Higgs. A

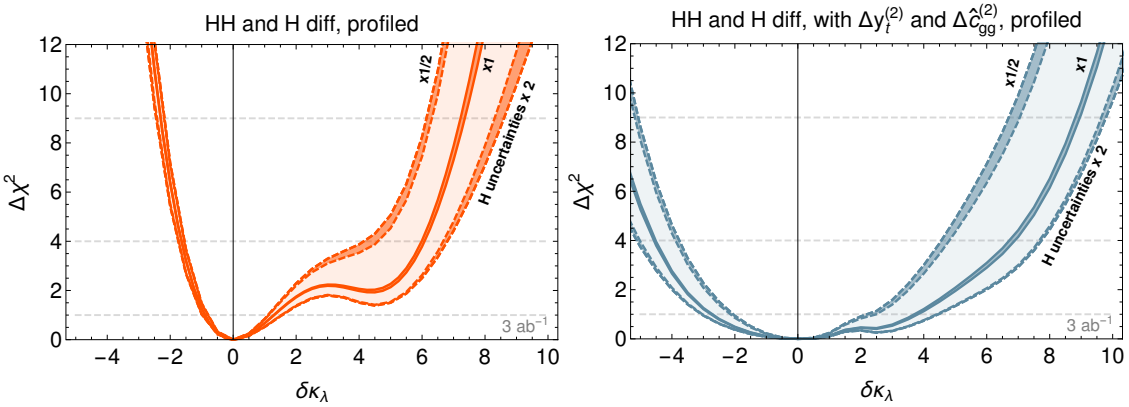

Figure 4.6: Band of variation of the global fit on the Higgs self-coupling obtained by rescaling the single-Higgs measurement uncertainties by a factor in the range $x \in [1/2, 2]$. The lighter shaded bands show the full variation of the fit due to the rescaling. The darker bands show how the fits corresponding to the "optimistic" and "pessimistic" assumptions on the systematic uncertainties (compare Figure 4.5) change for $x = 1/2, 1, 2$. The left panel shows the fit in the linear Lagrangian, while the right panel corresponds to the non-linear case in which $\Delta y_f^{(2)}$ and $\Delta\hat{c}_{gg}^{(2)}$ are treated as independent parameters.

$\pm1\sigma$	$\hat{c}_{gg}$	δc_z	c_{zz}	$c_{z\Box}$	$\hat{c}_{z\gamma}$	$\hat{c}_{\gamma\gamma}$	δy_t	δy_b	δy_τ	$\delta\kappa_\lambda$	$\Delta y_f^{(2)}$	$\Delta\hat{c}_{gg}^{(2)}$
Linear fit	0.06	0.04	0.04	0.02	0.09	0.03	0.06	0.07	0.11	1.0	-	-
Global fit	0.07	0.04	0.04	0.02	0.09	0.03	0.08	0.08	0.11	4.1	0.29	0.45

Table 4.2: 1σ intervals for the linear and non linear scenarios.

fully consistent fit should thus include all possible operators and not just the restricted basis we defined in Equations (3.8) and (3.9). Performing such analysis is beyond the scope of the present work. For illustration we restrict our attention only to two effective operators, $h^2 G_{\mu\nu} G^{\mu\nu}$ and $h^2 \bar{t}t$, whose impact on Higgs pair production via gluon fusion was studied in reference [58].

In the linear EFT Lagrangian the $h^2 G_{\mu\nu} G^{\mu\nu}$ and $h^2 \bar{t}t$ operators are connected to single-Higgs couplings (see Equation 3.9). Treating them as independent operators amounts to including the $\delta y_f^{(2)}$ and $\delta\hat{c}_{gg}^{(2)}$ parameters as free quantities in our fits. For convenience we introduce two new parameters that encode the deviations of $\delta y_f^{(2)}$ and $\hat{c}_{gg}^{(2)}$ from the linear Lagrangian relations:

$$\Delta y_f^{(2)} \equiv \delta y_f^{(2)} - (3\delta y_u - \delta c_z)\,, \qquad \Delta\hat{c}_{gg}^{(2)} \equiv \hat{c}_{gg}^{(2)} - \hat{c}_{gg}\,. \tag{4.6}$$

To understand the impact of $\Delta y_f^{(2)}$ and $\Delta\hat{c}_{gg}^{(2)}$ on the global fit, we give in Table 4.2 the 1σ intervals for the Higgs couplings in the linear and non-linear scenarios. One can see that the non-linear fit mostly affects the determination of κ_λ, whose precision significantly degrades. The impact on the determination of single-Higgs couplings is instead quite limited and is due to the fact that a weaker constraint on the Higgs self-interaction allows to move along the flat direction in the single-Higgs global fit. Indeed we find that the 1σ intervals for $\hat{c}_{gg}$, δy_t and δy_b are slightly larger in the non-linear scenario. The differences are however only marginally relevant.

To better quantify how the determination of κ_λ changes in the non-linear case, we show the χ^2 obtained in the global fit in the right panel of Figure 4.6. The 1σ band in this case becomes $\kappa_\lambda \in [-2, 5]$. We also show how the fit depends on the precision in the measurement of the single-Higgs observables. One can see that a reduction by a factor $1/2$ of the uncertainties on single-Higgs measurements could help significantly in improving the determination of κ_λ, reducing the 1σ band by $\sim 40\%$.

4.4 THE TRILINEAR AT HL-LHC

The possibility of exploiting single-Higgs production channels at hadron colliders to extract information about the Higgs trilinear self-coupling has been recently put forward in the literature [42–44]. The available results are quite encouraging. They show that the new analysis strategy could be competitive with the study of double-Higgs production, which is usually considered the best way to probe the Higgs self-interactions.

The analyses performed so far, however, limited their focus to scenarios in which the only deformation of the SM Lagrangian is a modification of the Higgs potential. This assumption significantly restricts the realm of theories for which the new results are valid. Indeed, in a vast class of new-physics models, corrections to the Higgs trilinear coupling are not generated alone and additional deviations in the other Higgs interactions are simultaneously present. Since the Higgs self-coupling only affects at next-to-leading order the single-Higgs rates, its effects can be easily overwhelmed by even small modifications of the single-Higgs couplings. In this more generic situation a global analysis, taking into account deviations in all the Higgs couplings simultaneously, is essential to fully assess the achievable accuracy. The main aim of the present work has been to perform such analysis. The computations of refs. [42–44] are an essential building block that can be directly implemented in a global fit with all the parameters affecting the Higgs couplings turned on simultaneously.

For definiteness we studied deformations of the SM Lagrangian given by dimension-6 effective operators in the standard model effective field theory (SMEFT) framework. In particular, in addition to deviations in the Higgs self-coupling, we considered distortions of the single-Higgs couplings due to a set of 9 operators that can not be tested with % precision in measurements not involving the Higgs. In the Higgs basis these deformations are encoded in the coefficients δc_z, c_{zz}, $c_{z\Box}$, $\hat{c}_{z\gamma}$, $\hat{c}_{\gamma\gamma}$ and $\hat{c}_{gg}$ which correspond to deformations of the Higgs couplings to gauge bosons, and δy_t, δy_b and δy_τ controlling deformations of the Yukawa's.

To derive our numerical results we considered the HL-LHC upgrade (14 TeV center of mass energy and 3/ab integrated luminosity) and we estimated the precision on single-Higgs measurements through a benchmark derived from the ATLAS and CMS projections [65, 67] (see Table 4.1). Moreover we assumed that the central values of the future experimental measurements will coincide with the SM predictions.

We found that, if only inclusive single-Higgs observables are considered, a global fit involving the 10 free parameters has an (almost) exact flat direction. The flat direction is mostly aligned along the Higgs self-coupling κ_λ, the top Yukawa δy_t and the contact interaction with gluons $\hat{c}_{gg}$, with minor components along δc_z, δy_b and δy_τ (see Figure 4.1). The inclusion of trilinear gauge couplings measurements can only partially lift the flat direction. Very large deviations in κ_λ are however still allowed, so that the Higgs self-interaction remains practically unbounded (see Figure 4.2). This result clearly shows

that the bounds obtained by an exclusive fit including only κ_λ ($\kappa_\lambda \in [-1.1, 4.7]$ at the 1σ level) must be interpreted with great care and are fully valid only in very specific BSM scenarios.

Large deviations in the Higgs self-coupling can also have a back-reaction on the extraction of single-Higgs couplings. As can be seen from Figure 4.3, if large corrections, $|\delta\kappa_\lambda| \sim 10$, are allowed, the precision in the determination of the single-Higgs couplings is significantly degraded. This results shows the necessity of including in the global fit additional observables which could resolve the flat direction.

We explored two possible extensions of the fitting procedure, namely the inclusion of double-Higgs production via gluon fusion and the use of differential measurements in the associated single-Higgs production channels WH, ZH and $t\bar{t}H$.

As expected, an inclusive double-Higgs production measurement can efficiently remove the flat direction, constraining the Higgs trilinear coupling to the range $\kappa_\lambda \in [0.0, 2.5] \cup [4.9, 7.4]$ at the 1σ confidence level (see Figure 4.4). Furthermore, differential double-Higgs distributions can provide additional help to probe large positive deviations in the Higgs trilinear. In particular they can be used to test the additional best fit point at $\kappa_\lambda \sim 6$ and to reduce the 2σ fit range (see right panel of Figure 4.4). When differential double-Higgs measurements are included, the constraint on the Higgs trilinear coupling becomes $\kappa_\lambda \in [0.1, 2.3]$ at the 1σ confidence level, which is strong enough to ensure that the back-reaction on the single-Higgs couplings fit is almost negligible at the HL-LHC. This result proves that neglecting the contributions from κ_λ when performing a fit on single Higgs couplings is a sensible procedure, even in BSM scenarios that can lead to $\mathcal{O}(1)$ deviations in the Higgs self-interactions.

The measurement of the differential distributions in the associated Higgs production channels can also help in determining the Higgs self-coupling. In the present work we performed a preliminary analysis with a simplified treatment of the experimental and theory uncertainties. We found that an exclusive fit on κ_λ can provide order one sensitivity ($\kappa_\lambda \in [-1, 3]$ at 1σ), roughly comparable with the one achievable through double-Higgs measurements (see Figure 4.5). On the other hand, in a global analysis, including deviations in single-Higgs couplings, the sensitivity on κ_λ is strongly reduced and only large deviations $|\delta\kappa_\lambda| \gtrsim 5$ can be probed. Nevertheless, also in this case single-Higgs differential observables can be useful. Combining them with double-Higgs measurements can significantly help to constrain large positive corrections to the Higgs trilinear. To fully evaluate the impact of the differential observables a more careful analysis strategy, together with a detailed assessment of the experimental uncertainties, would be needed. We leave this subject for future work.

Another important aspect we investigated is the dependence of our results on the experimental uncertainties and on the assumptions underlying the EFT parametrization. As shown in the left panel of Figure 4.6, a naive rescaling of all the experimental uncertainties in single-Higgs production affects only mildly the bounds on negative contributions to κ_λ, but has a major impact on the constraints on positive corrections (in particular at the 2σ confidence level).

The assumptions on the EFT description can also strongly modify the determination of κ_λ. As an illustrative example we considered a non-linear EFT Lagrangian in which the double-Higgs couplings to gluons and to tops are treated as independent parameters. This change affects almost exclusively the precision on the Higgs self-coupling, which is reduced by roughly a factor 3 (right panel of Figure 4.6). On the contrary, the global fit

on the single-Higgs couplings is much more stable and only the determination of $\hat{c}_{gg}$ and δy_t becomes marginally worse.

5 TESTING THE HIGGS TRILINEAR AT LEPTON COLLIDERS

5.1 FUTURE MACHINES

In chapter 4, we studied the prospect of measuring the trilinear at the HL-LHC, using higher order corrections from the trilinear in single-Higgs processes, as proposed by references [41–44]. We extended their analysis to try to minimize model dependence on the extraction of the trilinear at the HL-LHC. In this setup, the final gain compared to the determination of the trilinear using double-Higgs production was small, with final constraints on the trilinear of order one. We expect in an hypothetical future 100 TeV machine that the trilinear determination will entirely be dominated by pair-production (thanks to the augmentation of the cross section). Double-Higgs production for an 100 TeV collider has already been studied, for example in [61], and found to bound the trilinear at the 5% level. The next generation of colliders are in preparation and are likely to be colliding electron and positron. Hence it is tempting to fill the gap between these two generations of hadron colliders and ask what leptonic machines and their high precision can contribute to our knowledge of the Higgs potential. Several new colliders projects are currently being studied. They can be classified in two categories: circular and linear machines. While the circular machine struggle to get to high energy due to energy loss from bremsstrahlung,[1] and have a falling luminosity with COM energy, the situation is inverted for linear machines.

The two projects for circular machines are currently under discussion are the future circular collider (e^-e^+) (FCC-ee) and the circular electron positron collider (CEPC), and would be hosted at CERN and in China respectively. These colliders are both expecting a tunnel of order 100 km and a COM mass energy allowing them to probe single-Higgs production. The advantages of these machines are the higher low-energy luminosity and the upgrade path, since the two rings are expected to be reused to host a 100 TeV proton collider; either the future circular collider (proton, proton and ion, ion) (FCC-hh) or super proton-proton Collider (SppC). The energy of this proton-proton collider would allow for direct search of new physics. The linear machines are represented by the international linear collider (ILC) and compact linear collider (CLIC), which are projects led by Japan and CERN respectively. These machines are projecting several runs at different energies and would probably start with low energy runs, before going to higher energy, probing both single- and double-Higgs processes.

As said before, the main advantage of these machines is their precision. The fact "leptonic" cross sections are more sensitive to the COM energy, and the prospect to run at several energies, and the ability to change the beam polarization offers an opportunity to have more observables to constrain the parameter space. Maximizing the number of observable is important, since typical BSM models would, as for proton colliders, modify several couplings simultaneously. A plethora of single-Higgs studies have already tackled this issue, however, they do not take into account the trilinear loop corrections. The work presented here is a natural extension to reference [118], in the sense that it extends the

1 Perliminary report for FCC-ee expect a synchrotron radiation of order 100 MW.

study by adding higher order corrections. For other work studying the power of lepton colliders for single-Higgs couplings see references [119–127]. Analogous to the previous section, we use EFT to encode the different possible deviations while minimizing the underlying assumptions. We then extend the analysis by looking at information brought by high-energy collider, opening the Zhh associated production and WW-fusion channels and show their complementarity in constraining positive and negative deviations of the trilinear respectively. We also take advantage of the fact that the WW-fusion cross section grows with energy, to look at the differential distributions of the di-Higgs invariant mass, and confirm the result of [128] that it helps positive deviation of Higgs self-coupling.

Other future collider projects are worth noting. Two use the possibility of adding a linac to either the LHC or future circular collider (FCC) to collide protons and electrons. The resulting collider would be called respectively large hadron electron collider (LHeC) or future circular collider (hadron, electron) (FCC-he). Finally, the possibility to replace HL-LHC with a project called high energy LHC (HE-LHC), which would use the same tunnel, but replace the magnets to raise the COM to 27 TeV.

This chapter is organized as follows. In section 5.2, we probe the possibility to determine the trilinear using the low energy runs of the four different leptonic machines. We then go on to the realm of the linear colliders to study the effect of adding high-energy run directly probing the trilinear through double-Higgs production, and study the possibility to add differential information to improve the results.

5.2 LOW-ENERGY LEPTON MACHINES

In this section, we study the precision reach on the trilinear Higgs coupling through the exploitation of single-Higgs production measurements. These are the dominant handles available at future circular lepton colliders, like the CEPC and FCC-ee, which cannot easily deliver high luminosities at center-of-mass energies where the Higgs pair production rate becomes sizable. These machines could run above the $e^+e^- \to Zhh$ threshold, at a 350 GeV center-of-mass energy in particular, but the small cross section (in the attobarn range) and the limited integrated luminosity lead to a negligible sensitivity to this channel. The analysis of single-Higgs production can also be relevant for the ILC. While this machine could eventually reach a center-of-mass energy of 500 GeV (or even of 1 TeV) in a staged development, its initial low-energy runs can have an impact on the determination of the trilinear Higgs coupling that is worth investigating.

According to recent reports [129, 130], both CEPC and FCC-ee are planned to collect $5\,\text{ab}^{-1}$ of integrated luminosity at 240 GeV. FCC-ee is also envisioned to collect $1.5\,\text{ab}^{-1}$ at 350 GeV.[2] Although a run at this center-of-mass energy is not officially forecast for the CEPC, it is nevertheless a viable option given its planned tunnel circumference of 100 km. As a general circular collider run scenario, we therefore consider the collection of $5\,\text{ab}^{-1}$ of integrated luminosity at 240 GeV and several benchmark luminosities at 350 GeV, namely 0, $200\,\text{fb}^{-1}$ and $1.5\,\text{ab}^{-1}$.

The full ILC run plan comprises $2\,\text{ab}^{-1}$ of integrated luminosity at 250 GeV, $200\,\text{fb}^{-1}$ at 350 GeV, and $4\,\text{ab}^{-1}$ at 500 GeV, with these luminosities equally shared between runs with two $P(e^-, e^+) = (\pm 0.8, \mp 0.3)$ beam polarization configurations [132, 133]. Additional

2 The current run plan for FCC-ee anticipates to collect $0.2\,\text{ab}^{-1}$ at 350 GeV and $1.5\,\text{ab}^{-1}$ at 365 GeV [131]. Since the vector boson production cross section rises rapidly with the center-of-mass energy, the sensitivity of the FCC-ee will be certainly improved.

results for a 70%/30% repartition of the luminosity between the $P(e^-, e^+) = (\mp 0.8, \pm 0.3)$ polarizations will be provided in section B.2. In this section, we focus only on the runs at 240/250 GeV and 350 GeV, and consider a few benchmarks for the integrated luminosity collected at 350 GeV.

To summarize, we focus on the following benchmark scenarios:

CIRCULAR COLLIDERS (CC) with $5\,ab^{-1}$ at 240 GeV, $\{0, 200\,fb^{-1}, 1.5\,ab^{-1}\}$ at 350 GeV and unpolarized beams. The scenario with only a 240 GeV, $(5\,ab^{-1})$ run corresponds to the CEPC Higgs program, while the 240 GeV, $(5\,ab^{-1})$ + 350 GeV, $(1.5\,ab^{-1})$ scenario corresponds to the FCC-ee Higgs and top-quark programs.

LOW-ENERGY ILC with $2\,ab^{-1}$ at 250 GeV, $\{0, 200\,fb^{-1}, 1.5\,ab^{-1}\}$ at 350 GeV, and integrated luminosities equally shared between $P(e^-, e^+) = (\pm 0.8, \mp 0.3)$ beam polarizations.[3]

Later in this section we also extend these scenarios to cover a continuous range of luminosities at 240 (250) and 350 GeV.

5.2.1 *Higher-order corrections to single-Higgs processes*

As a first step, we analyze how a modification of the trilinear Higgs coupling affects single-Higgs processes. We parametrize possible new physics effects through the quantity κ_λ defined as the ratio between the actual value of the trilinear Higgs coupling λ_3 and its SM expression λ_3^{SM} (the Higgs vacuum expectation value is normalized to $v = 1/(\sqrt{2}G_F)^{1/2} \approx 246\,GeV$),[4]

$$\kappa_\lambda \equiv \frac{\lambda_3}{\lambda_3^{SM}}\,, \qquad \lambda_3^{SM} = \frac{m_h^2}{2v^2}\,. \tag{5.1}$$

While the trilinear coupling does not enter single-Higgs processes at LO, it affects both Higgs production and decay at NLO. The corresponding diagrams for Higgsstrahlung ($e^+e^- \to hZ$) and WW-fusion ($e^+e^- \to \nu\bar{\nu}h$) production processes are shown in Figure 5.1. In addition to the vertex corrections, which are linear in κ_λ, the trilinear coupling also generates corrections quadratic in κ_λ through the wave function renormalization induced by the Higgs self-energy diagram. Such contributions have been computed for electroweak [46, 47, 134] and single-Higgs observables [41–44, 135, 136].

Following reference [43], we can parametrize the NLO corrections to an observable Σ in a process involving a single external Higgs field as

$$\Sigma_{NLO} = Z_H \Sigma_{LO}(1 + \kappa_\lambda C_1)\,, \tag{5.2}$$

where Σ_{LO} denotes the LO value, C_1 is a process-dependent coefficient that encodes the interference between the NLO amplitudes involving κ_λ and the LO ones, while Z_H corresponds to the universal resummed wave-function renormalization and is explicitly given by

$$Z_H = \frac{1}{1 - \kappa_\lambda^2 \delta Z_H}\,, \qquad \text{with} \qquad \delta Z_H = -\frac{9}{16}\frac{G_\mu m_H^2}{\sqrt{2}\pi^2}\left(\frac{2\pi}{3\sqrt{3}} - 1\right) \simeq -0.00154\,. \tag{5.3}$$

3 The current run plan of CLIC anticipates a low-energy operation at 380 GeV as a Higgs factory. We did not consider this run alone as the lack of a separate run at a lower energy will constitute an hindrance to the indirect determination of the trilinear Higgs self-coupling.

4 This parametrization is equivalent to an EFT description in which deviations in the Higgs trilinear self-coupling arise from a dimension-6 operator $|H^\dagger H|^3$.

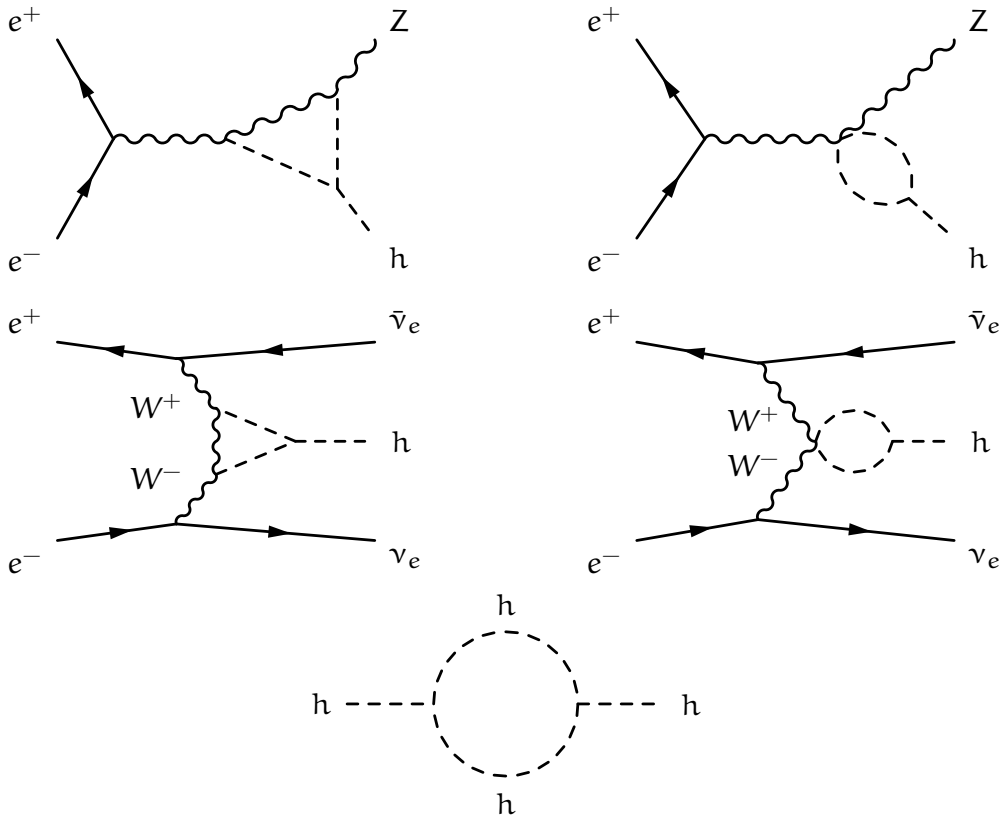

Figure 5.1: One-loop diagrams involving the trilinear Higgs coupling contributing to the main single-Higgs production processes: $e^+e^- \to hZ$ (top row) and $e^+e^- \to \nu\bar{\nu}h$ (middle row). The Higgs self-energy diagram (bottom) gives a universal modification to all Higgs production processes via wave function renormalization.

The impact of a deviation $\delta\kappa_\lambda \equiv \kappa_\lambda - 1$ from the SM value of the trilinear Higgs self-coupling is therefore

$$\delta\Sigma \equiv \frac{\Sigma_{\text{NLO}}}{\Sigma_{\text{NLO}}(\kappa_\lambda = 1)} - 1 \simeq (C_1 + 2\delta Z_H)\delta\kappa_\lambda + \delta Z_H \delta\kappa_\lambda^2 , \tag{5.4}$$

up to subleading corrections of higher orders in δZ_H and C_1.[5] The linear approximation in $\delta\kappa_\lambda$ is usually accurate enough to describe the deviations in single-Higgs processes inside the typical constraint range $|\delta\kappa_\lambda| \lesssim 5$. We will nevertheless use the unexpanded $\delta\Sigma$ expressions throughout this chapter to derive numerical results.

The value of C_1 in Higgsstrahlung ($e^+e^- \to hZ$) and WW-fusion ($e^+e^- \to \nu\bar{\nu}h$) processes are shown in the left panel of Figure 5.2 as functions of the center-of-mass energy $\sqrt{s}$. Very different energy dependences are observed for the two processes. A quick decrease is seen in Higgsstrahlung, from $C_1 \simeq 0.022$ at threshold to about $C_1 \simeq 0.001$ at a center-of-mass energy of 500 GeV. On the other hand, a nearly constant value $C_1 \simeq 0.006$ is observed for the WW-fusion process over the same range of energy. Further numerical values are provided in section B.1 for both production and decay processes. Besides the inclusive production and decay rates, we also checked the impact of a non-zero $\delta\kappa_\lambda$ on the angular asymmetries that can be exploited in $e^+e^- \to hZ \to h\ell^+\ell^-$ measurements

5 We checked explicitly that the one-loop squared term of order $\delta\kappa_\lambda^2$ is subdominant compared to the $\delta Z_H \delta\kappa_\lambda^2$ one.

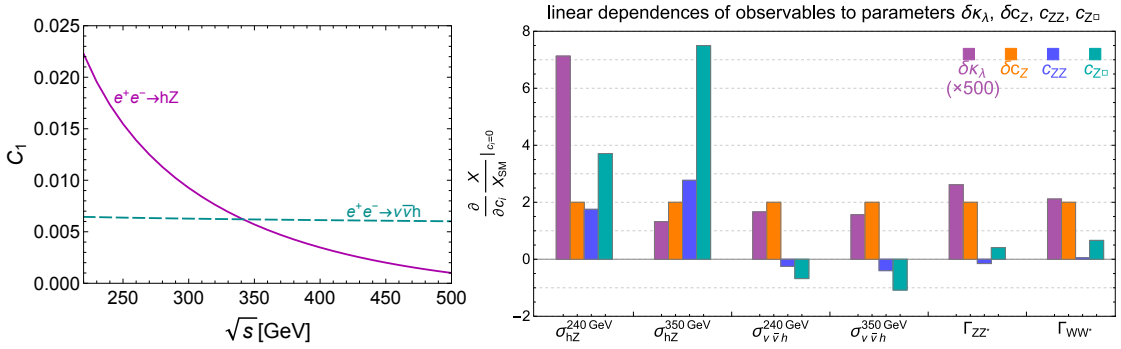

Figure 5.2: LEFT: Value of C_1 (as defined in Equation 5.2) as a function of the center of mass energy $\sqrt{s}$ for the $e^+e^- \to hZ$ and $e^+e^- \to \nu\bar{\nu}h$ single-Higgs production processes. RIGHT: The linear dependence of production and decay rates on the $\delta\kappa_\lambda$, δc_Z, c_{ZZ} and $c_{Z\Box}$ parameters (see subsection 5.2.2 for details on the meaning of these parameters). For $e^+e^- \to \nu\bar{\nu}h$, only the *WW*-fusion contribution is included. The dependence on $\delta\kappa_\lambda$ is amplified by a factor of 500.

(see references [137, 138]). We found that these effects are almost negligible and have no impact on the fits.

To conclude this section, we show in the right panel of Figure 5.2 the linear dependences of a set of production rates and Higgs partial widths on $\delta\kappa_\lambda$ and on three EFT parameters that encode deviations in the Z-boson couplings, δc_Z, c_{ZZ} and $c_{Z\Box}$ (see subsection 5.2.2 for a detailed discussion of the full set of BSM effects we are considering). Only leading-order dependences are accounted for, at one loop for $\delta\kappa_\lambda$ and at tree level for the other parameters. One can see that the various observables have very different dependences on the EFT parameters. For instance, δc_Z affects all the production processes in an energy-independent way.[6] On the contrary, the effects of c_{ZZ} and $c_{Z\Box}$ grow in magnitude for higher center-of-mass energy in both Higgsstrahlung and *WW*-fusion cross sections. It is apparent that the combination of several measurements can allow us to efficiently disentangle the various BSM effects and obtain robust constraints on $\delta\kappa_\lambda$. From the sensitivities shown in Figure 5.2, we can roughly estimate that a set of percent-level measurements in single-Higgs processes has the potential of constraining $\delta\kappa_\lambda$ with a precision better than $\mathcal{O}(1)$ and the other Higgs EFT parameters to the percent level. We will present a detailed quantitative assessment of the achievable precisions in the following.

5.2.2 *Global analysis*

Analysis of Higgs data at lepton colliders alone

Having obtained the one-loop contributions of $\delta\kappa_\lambda$ to single-Higgs observables, we are now ready to determine the precision reach on the Higgs trilinear self-interaction. In order to obtain a robust estimate, we perform here a global fit, taking into account not only deviations in the Higgs self-coupling, but also corrections to the other SM interactions that can affect single-Higgs production processes.

6 In the language of the dimension-six operators, δc_Z is generated by the operator $\mathcal{O}_H = \frac{1}{2}(\partial_\mu|H^2|)^2$, which modifies all Higgs couplings universally via the Higgs wave function renormalization.

For our analysis, we follow reference [118], in which the impact of single-Higgs measurements at lepton colliders on the determination of Higgs and electroweak parameters was investigated. We include in the fit the following processes

- Higgsstrahlung production: $e^+e^- \to hZ$ (rates and distributions),
- Higgs production through WW-fusion: $e^+e^- \to \nu\bar{\nu}h$,
- weak boson pair production: $e^+e^- \to WW$ (rates and distributions),

with Higgs decaying into a gauge boson pair ZZ^*, WW^*, $\gamma\gamma$, $Z\gamma$, gg or pairs of fermions $b\bar{b}$, $c\bar{c}$, $\tau^+\tau^-$, $\mu^+\mu^-$.

New physics effects are parametrized through dimension-six operators within an EFT framework. For definiteness, we express them in the Higgs basis and refer to reference [37] for a detailed discussion of the formalism. Since CP-violating effects are strongly constrained experimentally, we exclusively focus on CP-conserving operators. We also ignore dipole operators and work under the assumption of flavor universality. We relax this assumption only to consider independent deviations in the top, bottom, charm, tau, and muon Yukawa couplings. This add two extra Wilson coefficients to the formalism presented in chapter 3.

To estimate the precision of the measurement of the EFT parameters, we assume that the central values of the experimental measurements coincide with the SM predictions and we neglect theory uncertainties. For simplicity we compute the SM cross sections at LO, neglecting NLO effects coming from SM interactions. These contributions can be important for the experimental analysis, since the modifications they induce in the SM cross sections can be non negligible compared to the experimental accuracy. For the purpose of estimating the bounds on BSM effects, however, they play a negligible role. We adopt a further simplification regarding electroweak precision observables, treating them as perfectly well measured. Such an assumption can significantly reduce the number of parameters to consider and is straightforward to implement in the Higgs basis which transparently separates the Higgs and electroweak parameters. The potential impact of this assumption will be discussed at the end of section 5.4.

Under the above assumptions, we are left with twelve independent dimension-six effective operators that can induce leading-order contributions to single-Higgs and diboson processes. To this set of operators, we add the correction to the Higgs self-coupling parametrized by $\delta\kappa_\lambda$.[7] The full list of parameters included in our fit contains:

- corrections to the Higgs couplings to the gauge bosons: δc_Z, c_{ZZ}, $c_{Z\Box}$, $c_{\gamma\gamma}$, $c_{Z\gamma}$, c_{gg},
- corrections to the Yukawa's: δy_t, δy_c, δy_b, δy_τ, δy_μ,
- corrections to trilinear gauge couplings only: λ_Z,
- correction to the trilinear Higgs self-coupling: $\delta\kappa_\lambda$.

Since our focus is on the future sensitivity to the trilinear Higgs self-coupling, we present results in terms of $\delta\kappa_\lambda$ only, profiling over all other parameters. For a detailed analysis of the sensitivity on the other operators see section B.2 and references [118, 119].

In our fit, we only include terms linear in the coefficients of the EFT operators, neglecting higher-order corrections. This approximation can be shown to provide very accurate results for all the parameters entering in our analysis [118]. The only possible exception is

7 In the notation of reference [37] the $\delta\kappa_\lambda$ parameter corresponds to $\delta\lambda_3/\lambda$.

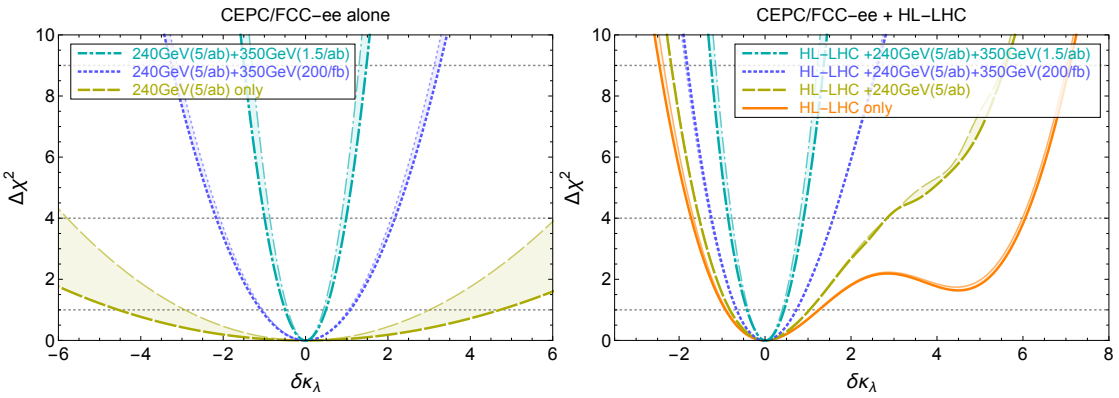

Figure 5.3: Chi-square as a function of $\delta\kappa_\lambda$ after profiling over all other EFT parameters. Three run scenario are considered for circular colliders, with $5\,\text{ab}^{-1}$ at 240 GeV and $\{0,\ 200\,\text{fb}^{-1},\ 1.5\,\text{ab}^{-1}\}$ at 350 GeV, without beam polarization. The shaded areas cover different assumptions about the precision of TGC measurements. LEFT: circular lepton collider measurements only. RIGHT: combination with differential single- and double-Higgs measurements at the HL-LHC.

$\delta\kappa_\lambda$, which can be tested experimentally with much lower precision than the other parameters. Although we checked that a linear approximation is reliable also for $\delta\kappa_\lambda$, we keep Equation 5.4 unexpanded in our numerical analyses. For simplicity, cross terms involving $\delta\kappa_\lambda$ and other EFT coefficients are however neglected, since the strong constraints on the latter coefficients and the loop factor make these contributions irrelevant.

In order to estimate the precision of Higgs measurements at different luminosities, we use a naive scaling with an irreducible 0.1% systematic error. This systematic error has no impact for the benchmark scenarios we consider, but becomes non-negligible for the large-luminosity projections presented at the end of this section (see Figure 5.5). Another important source of uncertainty in our fit comes from the precision on the determination of TGCs. In our analysis, we consider a range of possibilities. In the most conservative case, we assume 1% systematic errors in each bin of the $e^+e^- \to WW$ angular distributions used to constrain anomalous triple gauge couplings (aTGCs) [118]. In the most optimistic case, we assume that aTGCs are constrained much better than all the other parameters, so that they do not affect our fit. This is equivalent to enforcing the following relations among the EFT parameters:

$$\begin{aligned}
\delta g_{1,Z} &= \frac{g^2+g'^2}{2(g^2-g'^2)}\left[-g^2 c_{Z\Box} - g'^2 c_{ZZ} + e^2\frac{g'^2}{g^2+g'^2}c_{\gamma\gamma} + g'^2\frac{g^2-g'^2}{g^2+g'^2}c_{Z\gamma}\right] = 0\,,\\
\delta\kappa_\gamma &= -\frac{g^2}{2}\left(c_{\gamma\gamma}\frac{e^2}{g^2+g'^2} + c_{Z\gamma}\frac{g^2-g'^2}{g^2+g'^2} - c_{ZZ}\right) = 0\,,\\
\lambda_Z &= 0\,.
\end{aligned} \tag{5.5}$$

We start our discussion of the fit results by considering the benchmark scenarios for circular colliders. The profiled $\Delta\chi^2$ fit as a function of $\delta\kappa_\lambda$ is shown in the left panel of Figure 5.3. The $\Delta\chi^2 = 1$ intervals are also reported in Table 5.1.

The numerical results show that a 240 GeV run alone has a very poor discriminating power on the Higgs trilinear coupling, so that only an $\mathcal{O}(few)$ determination is possible (brown dashed lines in the plot). The constraint is also highly sensitive to the precision in the determination of TGCs, as can be inferred from the significantly different bounds

	lepton collider alone		lepton collider + HL-LHC	
	non-zero aTGC	zero aTGC	non-zero aTGC	zero aTGC
HL-LHC alone			$[-0.92, +1.26]$	$[-0.90, +1.24]$
CC 240 GeV (5 ab^{-1})	$[-4.55, +4.72]$	$[-2.93, +3.01]$	$[-0.81, +1.04]$	$[-0.82, +1.03]$
+350 GeV (200 fb^{-1})	$[-1.08, +1.09]$	$[-1.04, +1.04]$	$[-0.66, +0.76]$	$[-0.66, +0.74]$
+350 GeV (1.5 ab^{-1})	$[-0.50, +0.49]$	$[-0.43, +0.43]$	$[-0.43, +0.44]$	$[-0.39, +0.40]$
ILC 250 GeV (2 ab^{-1})	$[-5.72, +5.87]$	$[-5.39, +5.62]$	$[-0.85, +1.13]$	$[-0.85, +1.12]$
+350 GeV (200 fb^{-1})	$[-1.26, +1.26]$	$[-1.18, +1.18]$	$[-0.72, +0.83]$	$[-0.71, +0.80]$
+350 GeV (1.5 ab^{-1})	$[-0.64, +0.64]$	$[-0.56, +0.56]$	$[-0.52, +0.54]$	$[-0.48, +0.50]$

Table 5.1: $\Delta\chi^2 = 1$ bounds on $\delta\kappa_\lambda$ from single-Higgs measurements at circular lepton colliders (denoted as CC) and the ILC. The first column shows the results for lepton colliders alone, while the second shows the combination with differential measurements of both single- and double-Higgs processes at the HL-LHC. For each scenario two benchmarks with conservative and optimistic assumptions on the precision on trilinear gauge couplings are listed. The integrated luminosity is assumed equally shared between $P(e^-, e^+) = (\pm 0.8, \mp 0.3)$ for the ILC.

in the conservative and optimistic aTGCs scenarios. The inclusion of measurements at 350 GeV drastically improves the results. An integrated luminosity of 200 fb^{-1} at 350 GeV, is already sufficient to reduce the uncertainty to the level $|\delta\kappa_\lambda| \lesssim 1$, whereas 1.5 ab^{-1} leads to a precision $|\delta\kappa_\lambda| \lesssim 0.5$.

It is interesting to compare the above results with the constraints coming from an exclusive fit in which only corrections to the trilinear Higgs coupling are considered and all the other parameters are set to zero. With 5 ab^{-1} collected at 240/250 GeV, and irrespectively of the presence of a run at 350 GeV, we find that such a fit gives a precision of approximately 14% in the determination of $\delta\kappa_\lambda$. The strongest constraints come from the measurement of the $e^+e^- \to Zh$ cross section in the 240 GeV run, which is the observable with the largest sensitivity to $\delta\kappa_\lambda$ (see discussion in subsection 5.2.2 and left panel of Figure 5.2). Other processes measured in the 240 GeV and higher-energy runs have only a marginal impact on the exclusive fit.

The exclusive fit provides a bound much stronger than the global analyses, signaling the presence of a nearly flat direction in the global fits. We found that $\delta\kappa_\lambda$ has a strong correlation with δc_Z and c_{gg}, while milder correlations are present with $c_{Z\Box}$ and λ_Z.[8] This result sheds some light on the origin of the improvement in the global fit coming from the combination of the 240 GeV and 350 GeV runs. The latter runs, although probing processes with a smaller direct sensitivity to $\delta\kappa_\lambda$, are useful to reduce the uncertainty on the other EFT parameters. In particular, the 350 GeV run with 1.5 ab^{-1} of integrated luminosity allows for a reduction of the uncertainty on δc_Z, c_{gg}, $c_{Z\Box}$ and λ_Z by a factor of about 4. This in turn helps lifting the flat direction in the global fit. This effect is clearly visible from the left panel of Figure 5.4, which shows the fit on the $\delta\kappa_\lambda$ and δc_Z parameters obtained with a 240 GeV run only and with the inclusion of a 350 GeV run.

8 Notice that a loosely constrained direction involving δc_Z is already present in the global fit not including $\delta\kappa_\lambda$ [118]. The addition of the trilinear Higgs coupling makes this feature even more prominent.

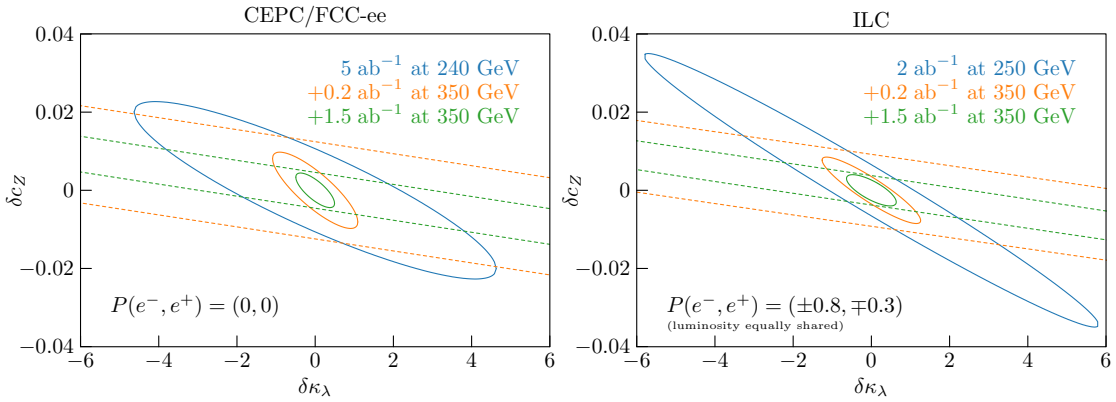

Figure 5.4: Global constraints on δc_Z and $\delta\kappa_\lambda$, obtained from single-Higgs measurements at circular colliders (left panel) and ILC (right panel), illustrating the improvement brought by 350 GeV runs. Dashed lines are for the latter only, while solid lines combined them with the 240/250 GeV one.

Synergy between measurements at the HL-LHC and lepton-colliders

So far, we only considered the precision reach of lepton colliders on the extraction of the trilinear Higgs self-coupling. Significant information on $\delta\kappa_\lambda$ can however also be obtained at the high-luminosity LHC. It is thus interesting to estimate the impact of combining the different sets of measurements.

The Higgs trilinear self-coupling can be accessed at the HL-LHC mainly through the exploitation of the Higgs pair production channel $pp \to hh$. An analysis of this channel within the EFT framework has been presented in reference [58], in which the most promising channel, namely $pp \to hh \to b\bar{b}\gamma\gamma$, has been investigated. A differential analysis (taking into account the Higgs pair invariant mass distribution) allows to constrain $\delta\kappa_\lambda$ to the interval $[-1.0, 1.8]$ at the $\Delta\chi^2 = 1$ level. A second minimum is however present in the fit, which allows for sizable positive deviations in $\delta\kappa_\lambda$, namely an additional interval $\delta\kappa_\lambda \in [3.5, 5.1]$ can not be excluded at the $\Delta\chi^2 = 1$ level. Some improvement can be obtained complementing the pair-production channel with information from single-Higgs channels, which are affected at NLO by the Higgs self-coupling. In this way, the overall precision becomes $\delta\kappa_\lambda \in [-0.9, 1.2]$ at the $\Delta\chi^2 = 1$ level (with the additional minimum at $\delta\kappa_\lambda \sim 5$ excluded) and $\delta\kappa_\lambda \in [-1.7, 6.1]$ at the $\Delta\chi^2 = 4$ level(see chapter 4). To estimate the impact of HL-LHC, we will use here the results of the combined fit with differential single and pair production (corresponding to the orange solid curve in the right panel of Figure 5.3).

The combinations of the HL-LHC fit with our benchmarks for circular lepton colliders are shown in the right panel of Figure 5.3. One can see that a 240 GeV run is already sufficient to completely lift the second minimum at $\delta\kappa_\lambda \sim 5$, thus significantly reducing the $\Delta\chi^2 = 4$ bounds. The precision near the SM point ($\delta\kappa_\lambda = 0$) is however dominated by the HL-LHC measurements, so that the lepton collider data can only marginally improve the $\Delta\chi^2 = 1$ bounds. The situation is reversed for the benchmarks including a 350 GeV run. In this case, the precision achievable at lepton colliders is significantly better than the HL-LHC one. The combination of the LHC and lepton collider data can still allow for a significant improvement in the constraints if limited integrated luminosity can be accumulated in the 350 GeV runs (see Table 5.1). With 1.5 ab^{-1} collected at 350 GeV, on the other hand, the lepton collider measurements completely dominate the bounds.

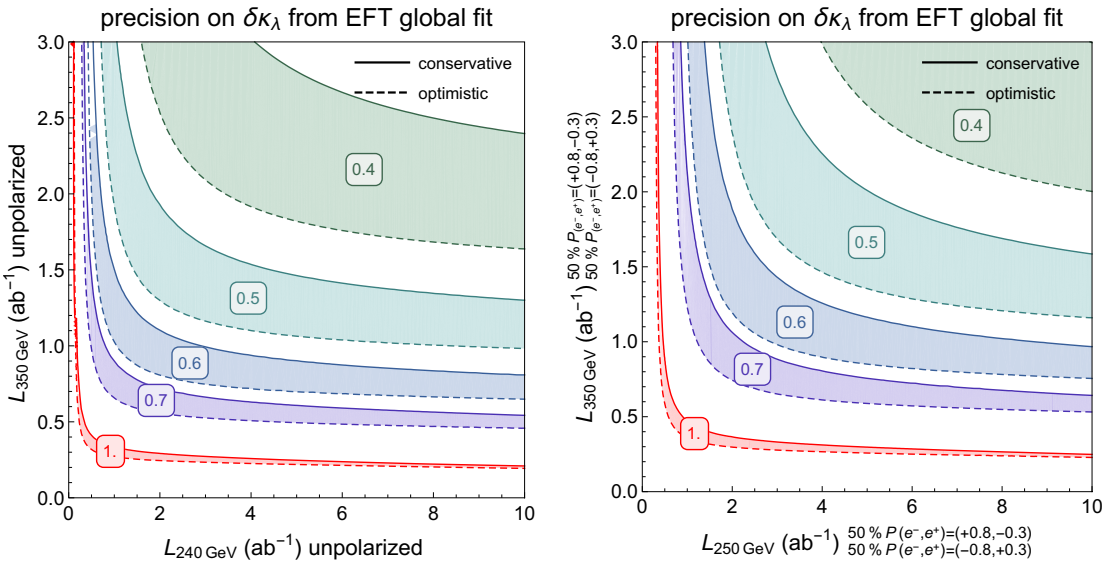

Figure 5.5: $\Delta\chi^2 = 1$ bounds on $\delta\kappa_\lambda$ deriving from single-Higgs and diboson production measurements at lepton colliders as a function of the integrated luminosity collected at both 240/250 and 350 GeV. Conservative (solid) and optimistic (dashed) assumptions are used for the precision of diboson measurements.

Similar results are obtained for the low-energy ILC benchmarks. In this case, the lower integrated luminosity forecast at 250 GeV (2 ab^{-1}) can be compensated through the exploitation of the two different beam polarizations $P(e^-, e^+) = (\pm 0.8, \mp 0.3)$. The only difference with respect to the circular collider case is the fact that the 250 GeV run fit is more stable under changes in the trilinear gauge couplings precision. This is due to the availability of runs with different polarizations, which provide better constraints on the EFT parameters. Analogously to the circular collider scenarios, the combination of the 250 GeV measurements with the HL-LHC data allows to completely lift the minimum at $\delta\kappa_\lambda \sim 5$, while a 350 GeV run would easily surpass the LHC precision. We report the results for the ILC benchmarks in section B.2 (see Figure B.2). For completeness, we mention that an exclusive fit on $\delta\kappa_\lambda$ at the ILC allows for a precision of approximately 32%, significantly better than the one expected through a global fit. Also in this case a nearly flat direction is present when deviations in all the EFT parameters are simultaneously allowed (see right panel of Figure 5.4).

Having observed the significant impact of the combination of measurements at 240/250 GeV and 350 GeV center-of-mass energies, to conclude the discussion, we now explore a continuous range of integrated luminosities accumulated at the various colliders. The $\Delta\chi^2 = 1$ limits as functions of the integrated luminosity are displayed in Figure 5.5 for the circular colliders and the ILC. Conservative and optimistic precisions for TGC measurements are respectively assumed to obtain the solid and dashed curves. The combination of runs at these two different energies always brings drastic improvements. The fastest improvements in precision on the $\delta\kappa_\lambda$ determination is obtained along the $L_{350\,\mathrm{GeV}}/L_{240\,\mathrm{GeV}} \simeq 0.7$ and $L_{350\,\mathrm{GeV}}/L_{250\,\mathrm{GeV}} \simeq 0.5$ lines for circular colliders and the ILC, respectively.

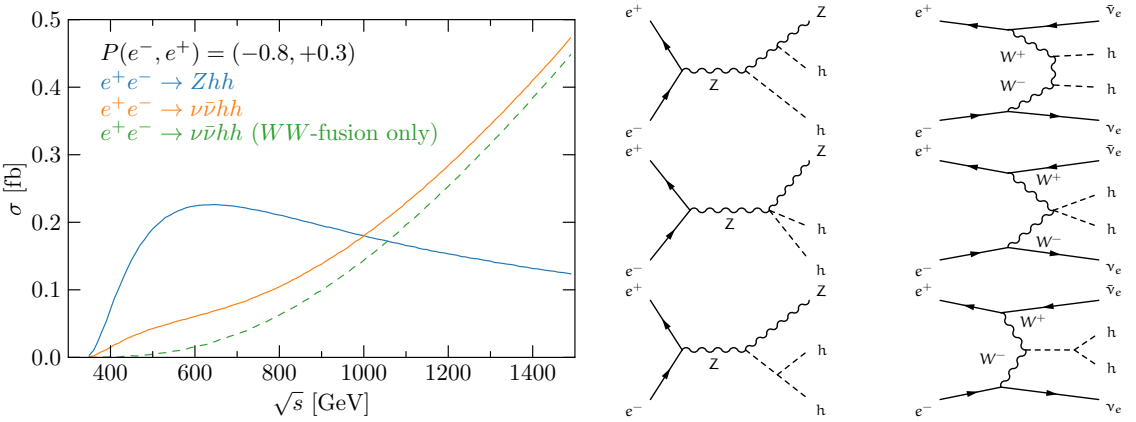

Figure 5.6: Higgs pair production cross sections at lepton colliders as functions of the center-of-mass energy (based on Fig. 7 of reference [141]) and illustrative diagrams. The difference between the two $\nu\bar{\nu}hh$ curves is entirely due to double Higgsstrahlung followed by invisible Z decay.

5.3 HIGH-ENERGY LEPTON MACHINES

Having explored the reach of low-energy lepton colliders in the previous section, we now enlarge our scope to include machines with center-of-mass energies above 350 GeV. They offer the opportunity of probing directly the trilinear Higgs self-coupling through Higgs pair production processes, double Higgsstrahlung $e^+e^- \to Zhh$ and WW-fusion $e^+e^- \to \nu\bar{\nu}hh$ in particular. The precision reach in the determination of $\delta\kappa_\lambda$ at ILC and CLIC has already been studied by the experimental collaborations [139, 140]. These studies performed an exclusive fit, allowing for new-physics effects only in the trilinear Higgs self-coupling.

In this section, we first review the experimental projections on the extraction of the Higgs self-coupling from double-Higgs channels. In this context, we also point out how differential distributions, in particular in the WW-fusion channel, can allow for an enhanced sensitivity to $\delta\kappa_\lambda$. Afterwards, we reconsider Higgs pair production measurements from a global EFT perspective, showing how the determination of $\delta\kappa_\lambda$ is modified by performing a simultaneous fit for all EFT parameters. We also evaluate how these results are modified by combining double-Higgs data with single-Higgs measurements from low-energy runs.

5.3.1 *Higgs pair production*

As already mentioned, Higgs pair production at high-energy lepton machines is accessible mainly through the double Higgsstrahlung $e^+e^- \to Zhh$ and WW-fusion $e^+e^- \to \nu\bar{\nu}hh$ channels. The cross sections for these two production modes as functions of the center-of-mass energy of the collider are shown in Figure 5.6. It is interesting to notice their completely different behavior, so that the relevance of the two channels drastically changes at different machines. At energies below approximately 1 TeV, double Higgsstrahlung is dominant whereas, at higher energy, the channel with the larger cross section is WW-fusion. To be more specific, the cross section of double Higgsstrahlung reaches a maximum at $\sqrt{s} \simeq 600$ GeV before starting to slowly decrease as the s-channel Z boson gets more and more offshell. On the contrary, the $e^+e^- \to \nu\bar{\nu}hh$ cross section initially grows steadily

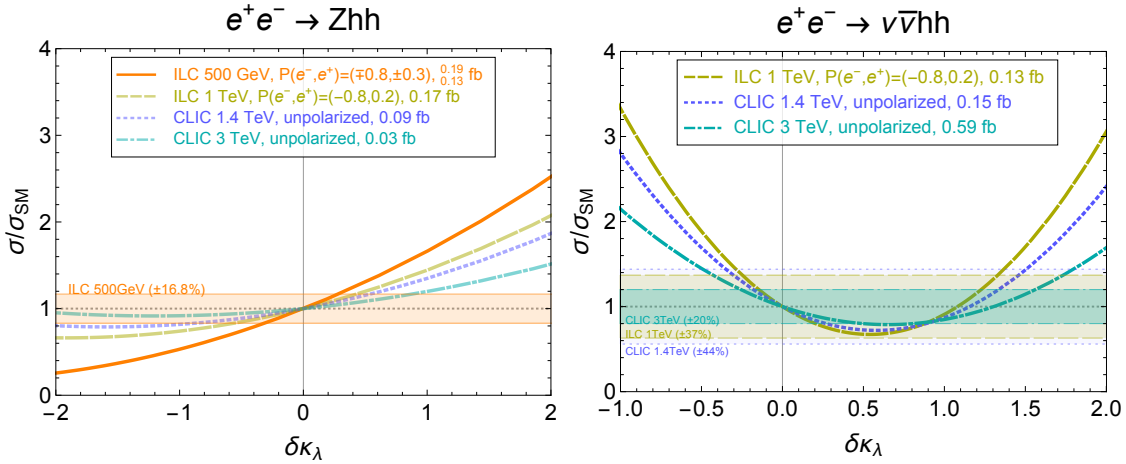

Figure 5.7: Dependence of the Higgs pair production rates on $\delta\kappa_\lambda$ at various center-of-mass energies. Shaded bands display the precision claimed by dedicated experimental studies on the standard-model cross sections. Absolute cross sections are provided in the legend.

with the center-of-mass energy of the collider and adopts a logarithmic behavior above 10 TeV. Notice that the $e^+e^- \to \nu\bar{\nu}hh$ channel receives non-negligible contributions that are not of *WW*-fusion type. The largest of them arises from double Higgsstrahlung followed by a $Z \to \nu\bar{\nu}$ decay. These contributions can however be efficiently identified at sufficiently high center-of-mass energies since the kinematic of the process is significantly different from that of *WW*-fusion. Notice, moreover, that both double-Higgs production cross sections are significantly affected by the beam polarization (see section B.2 and Figure B.3).

The $e^+e^- \to Zhh$ process at the ILC with 500 GeV center-of-mass energy has been thoroughly studied in reference [139]. A total luminosity of 4 ab^{-1}, equally split into two beam polarization runs $P(e^-,e^+) = (\pm0.8, \mp0.3)$, allows for a precision of 21.1% on the cross section determination through the exploitation of the $hh \to b\bar{b}b\bar{b}$ final state. A further improvement can be obtained by also including the $hh \to b\bar{b}WW^*$ channel, in which case the precision reaches 16.8%.

The $e^+e^- \to \nu\bar{\nu}hh$ process has been studied at a 1 TeV center-of-mass energy, in the context of the ILC. A significance of 2.7σ (corresponding to a precision of 37%) could be achieved in the $hh \to b\bar{b}b\bar{b}$ channel, assuming an integrated luminosity $\mathcal{L} = 2$ ab^{-1} and $P(e^-,e^+) = (-0.8,+0.2)$ beam polarization [142].

Studies of the $e^+e^- \to \nu\bar{\nu}hh$ process at CLIC (both at 1.4 TeV and 3 TeV center-of-mass energy) are available in reference [140]. Assuming unpolarized beams and 1.5 ab^{-1}, the precision on the 1.4 TeV cross section could reach 44%. With 1.5 ab^{-1}, the 3 TeV cross section could be measured with a 20% precision. Both $b\bar{b}b\bar{b}$ and $b\bar{b}WW^*$ channels are included in these analyses, though the sensitivity is mainly driven by the former, as shown in Table 28 in reference [140].

The dependence of the Higgs pair production cross sections on $\delta\kappa_\lambda$ is shown in Figure 5.7 for a set of benchmark scenarios. The SM cross section for each benchmark is provided in the legend.[9] Shaded bands show the precisions on the determination of the

9 The ILC 1 TeV SM cross section is obtained from Fig. 7 of reference [141] and scaled from $P(e^-,e^+) = (-0.8,+0.3)$ to $P(e^-,e^+) = (-0.8,+0.2)$. The unpolarized CLIC SM cross sections are taken from reference [140].

	$\Delta\chi^2 = 1$	$\Delta\chi^2 = 4$
ILC 500 GeV	$[-0.31,\ 0.28]$	$[-0.67,\ 0.54]$
ILC 1 TeV	$[-0.25,\ 1.33]$	$[-0.44,\ 1.52]$
ILC combined	$[-0.20,\ 0.23]$	$[-0.37,\ 0.49]$
CLIC 1.4 TeV	$[-0.35,\ 1.51]$	$[-0.60,\ 1.76]$
CLIC 3 TeV	$[-0.26,\ 0.50] \cup [0.81,\ 1.56]$	$[-0.46,\ 1.76]$
CLIC combined	$[-0.22,\ 0.36] \cup [0.90,\ 1.46]$	$[-0.39,\ 1.63]$
+Zhh	$[-0.22,\ 0.34] \cup [1.07,\ 1.28]$	$[-0.39,\ 1.56]$
2 bins in $\nu\bar{\nu}$hh	$[-0.19,\ 0.31]$	$[-0.33,\ 1.23]$
4 bins in $\nu\bar{\nu}$hh	$[-0.18,\ 0.30]$	$[-0.33,\ 1.11]$

Table 5.2: Constraints from an exclusive fit on $\delta\kappa_\lambda$ derived from the measurements of $\nu\bar{\nu}$hh and $e^+e^- \to \nu\bar{\nu}$hh cross sections at ILC and CLIC, with all other parameters fixed to their standard-model values.

SM rates discussed above. Note the experimental collaborations made no forecast for the precision on double Higgsstrahlung at 1 TeV and above.

It is interesting to notice that, around the SM point, the sensitivity of both Higgs pair production channels to $\delta\kappa_\lambda$ gets milder at higher center-of-mass energy. On the contrary, the sensitivity to the other EFT parameters tends to increase with energy. Another important feature is the significant impact of terms quadratic in $\delta\kappa_\lambda$ on the behavior of the cross section around the SM point, especially for the *WW*-fusion channel shown in the right panel of Figure 5.7. For this reason, a linear approximation is in many cases not sufficient to extract reliable bounds. In Table 5.2, we list the $\Delta\chi^2 = 1$ and 4 bounds obtained from the benchmarks ILC and CLIC runs retaining the full dependence of the cross section on $\delta\kappa_\lambda$.

From Figure 5.7, one can see that the interference between diagrams with and without a trilinear Higgs vertex has opposite sign in double Higgsstrahlung and *WW*-fusion. These two processes are thus more sensitive to positive and negative values of $\delta\kappa_\lambda$ respectively. A combination of double Higgsstrahlung and *WW*-fusion measurements could hence be used to maximize the precision for both positive and negative values of $\delta\kappa_\lambda$. Such a scenario could be achieved at the ILC through the combination of a 500 GeV and a 1 TeV run. The impact of such combination can be clearly seen from the plot in the left panel of Figure 5.8.

Being quadratic functions of $\delta\kappa_\lambda$, inclusive cross sections (for each process and collider energy) can match the SM ones not only for $\delta\kappa_\lambda = 0$, but also for an additional value of the trilinear Higgs self-coupling, resulting in a second minimum in the $\Delta\chi^2$. In *WW*-fusion, the SM cross section is also obtained for $\delta\kappa_\lambda \simeq 1.08$, 1.16 and 1.30 at center-of-mass energies of 1, 1.4 and 3 TeV, respectively. Whereas, for double Higgsstrahlung at 500 GeV, the SM cross section is recovered at $\delta\kappa_\lambda \simeq -5.8$. This latter solution poses no practical problem for ILC since it can be excluded by HL-LHC measurements. Alternatively, it can be constrained by Higgs pair production through *WW*-fusion at 1 TeV, as well as through the indirect sensitivity of single-Higgs measurements.

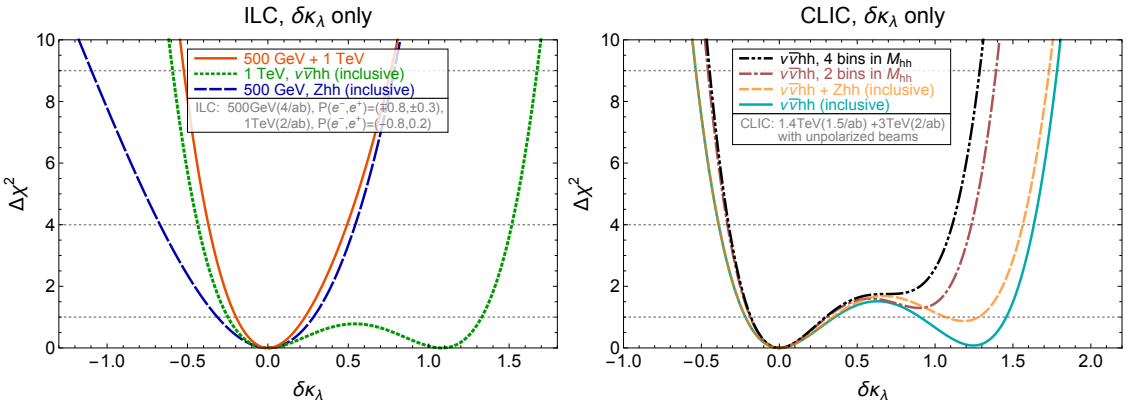

Figure 5.8: Chi-square for the exclusive fit of $\delta\kappa_\lambda$ for various combinations of Higgs pair production measurements at the ILC (left) and CLIC (right).

For CLIC, the secondary solutions at $\delta\kappa_\lambda \simeq 1$ are more problematic. They can be constrained neither by HL-LHC data, nor by single-Higgs measurements which are mostly efficient close to the threshold of the single-Higgsstrahlung production. A more promising possibility is to exploit double Higgsstrahlung rate measurements. At center-of-mass energies above 1 TeV, however, they only provide weak handles on $\delta\kappa_\lambda$. The $e^+e^- \to Zhh$ cross section becomes relatively small, being only 0.08 fb at 1.4 TeV with unpolarized beams. Moreover, the sensitivity to the trilinear Higgs self-coupling decreases with energy, as shown in Figure 5.7. Since the experimental collaborations did not provide an estimate for the CLIC precision achievable on the SM $e^+e^- \to Zhh$ rate, we estimate it by naively rescaling the ILC 500 GeV projections by the total cross section at CLIC. We find that adding this information to inclusive $e^+e^- \to \nu\bar{\nu}hh$ rates measurements only excludes the second minimum to the 1σ level (dashed orange line in the right panel of Figure 5.8).

In addition, we consider the possibility of performing a differential analysis of double-Higgs production through *WW*-fusion, studying whether a fit of the Higgs pair invariant mass distribution M_{hh} can be sufficient to further exclude the $\delta\kappa_\lambda \simeq 1$ points. The M_{hh} distribution shows a good sensitivity to the Higgs trilinear, which mainly affects the shape of the distribution close to the kinematic threshold. This can be observed in Figure 5.9, obtained at the parton level with `MadGraph5` [143] (with `FeynRules` [144] and the `BSMC Characterisation` model [145, 146]) for 1.4 and 3 TeV center-of-mass energies. The solid blue curves correspond to the SM point $\delta\kappa_\lambda = 0$. The dashed red curves are obtained for the other value of $\delta\kappa_\lambda$ at which the $\nu\bar{\nu}hh$ coincides with the SM value ($\delta\kappa_\lambda = 1.16$ for 1.4 TeV and $\delta\kappa_\lambda = 1.30$ for 3 TeV). The dotted cyan distributions are obtained for vanishing trilinear Higgs self-coupling ($\delta\kappa_\lambda = -1$).

We estimate the impact of a differential analysis of the $\nu\bar{\nu}hh$ channel by performing a simple fit of the M_{hh} invariant mass distribution. We consider either two or four bins, whose ranges are listed in Table 5.3. For simplicity, we work at parton level and assume a universal signal over background ratio across all bins. The right panel of Figure 5.8 summarizes the result of the fits. It shows that a differential analysis can be useful in enhancing the precision on $\delta\kappa_\lambda$. In particular, it allows us to exclude the second fit solution $\delta\kappa_\lambda \simeq 1.3$ at the $\Delta\chi^2 = 1$ level, and to reduce significantly the $\Delta\chi^2 = 4$ bounds for positive deviations in the Higgs self-coupling. For instance, the 4-bin fit restricts $\delta\kappa_\lambda$ to the range $[-0.18, 0.30]$ at the $\Delta\chi^2 = 1$ level and $[-0.33, 1.11]$ at $\Delta\chi^2 = 4$ level.

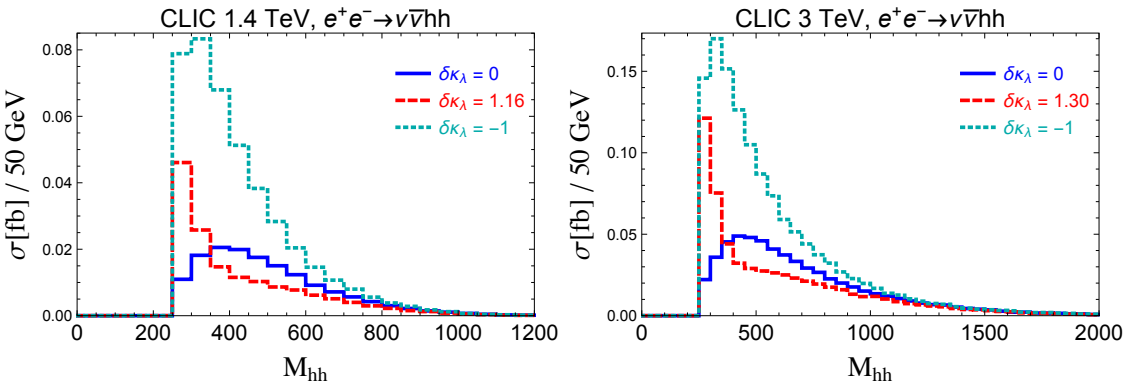

Figure 5.9: Invariant mass distribution of the Higgs pair in $e^+e^- \to \nu\bar{\nu}hh$ at 1.4 TeV (left) and 3 TeV (right). The solid blue curves are obtained in the SM ($\delta\kappa_\lambda = 0$). The red dashed curves are obtained with the other value of $\delta\kappa_\lambda$ which leads to a cross section equal to the SM one. The cyan dotted curves are obtained for vanishing Higgs self-coupling ($\delta\kappa_\lambda = -1$).

	2 bin boundaries [GeV]		4 bin boundaries [GeV]			
1.4 TeV	250-400	400-1400	250-350	350-500	500-600	600-1400
3 TeV	250-500	500-3000	250-450	450-650	650-900	900-3000

Table 5.3: Definitions of the bins used in the Higgs-pair invariant mass distribution of $e^+e^- \to \nu\bar{\nu}hh$ at 1.4 TeV and 3 TeV.

5.3.2 *Global analysis*

It is important to verify whether the results discussed in subsection 5.3.1, obtained assuming new physics affects only the triple-Higgs coupling, are robust in a global framework once all other EFT parameters are taken into consideration. We therefore perform a global analysis at ILC and CLIC including measurements of both double-Higgs (Higgsstrahlung and *WW*-fusion) and single-Higgs processes ($\nu\bar{\nu}h$, Zh, $t\bar{t}h$ and e^+e^-h) in addition to diboson production.

We adopt the following benchmark scenarios chosen by the experimental collaborations for Higgs measurement estimates:

ILC: we follow the scenario in reference [133], assuming ILC can collect 2 ab^{-1} at 250 GeV, 200 fb^{-1} at 350 GeV and 4 ab^{-1} at 500 GeV, equally shared between the $P(e^-, e^+) = (\pm 0.8, \mp 0.3)$ beam polarizations. We also consider the possibility of an additional run at 1 TeV gathering 2 ab^{-1} with one single $P(e^-, e^+) = (-0.8, +0.2)$ beam polarization.

CLIC: we follow reference [140] and assume 500 fb^{-1} at 350 GeV, 1.5 ab^{-1} at 1.4 TeV and 2 ab^{-1} at 3 TeV can be collected with unpolarized beams. It should be noted that a left-handed beam polarization could increase the $\nu\bar{\nu}hh$ cross section and somewhat improve the reach on $\delta\kappa_\lambda$.

For the global fit, we follow the procedure and assumptions adopted for the single-Higgs processes fit at low-energy colliders. We also include the one-loop dependence on $\delta\kappa_\lambda$ in single-Higgs production and decay processes, as done in section 5.2. Such effects are also included in the top-Higgs associated production $e^+e^- \to t\bar{t}h$ and in ZZ-fusion $e^+e^- \to e^+e^-h$, although they have a negligible impact. On the other hand, only the

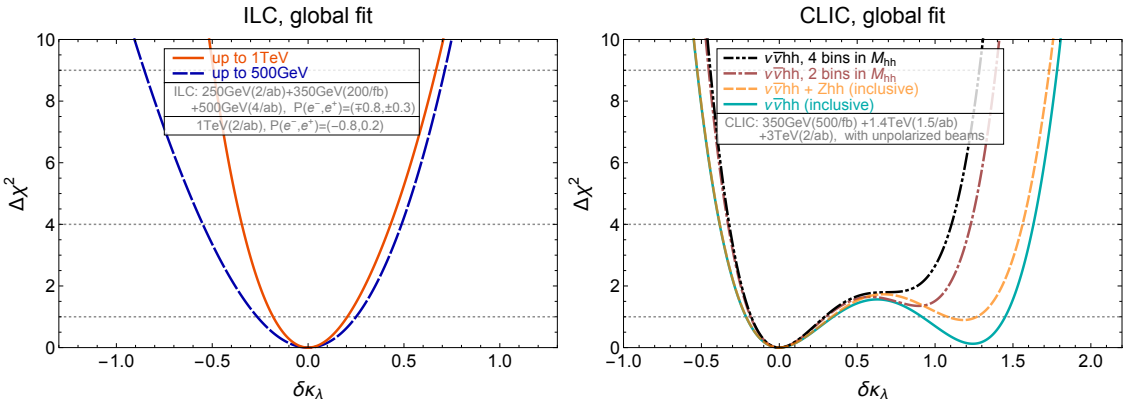

Figure 5.10: Delta chi-square as a function of $\delta\kappa_\lambda$ for the high-energy ILC (left) and CLIC (right) benchmarks. The results are obtained through a global analysis, profiling over all other EFT parameters.

	$\Delta\chi^2 = 1$	$\Delta\chi^2 = 4$
ILC up to 500 GeV	$[-0.27,\ 0.25]$	$[-0.55,\ 0.49]$
ILC up to 1 TeV	$[-0.18,\ 0.20]$	$[-0.35,\ 0.43]$
CLIC	$[-0.22,\ 0.36] \cup [0.91,\ 1.45]$	$[-0.39,\ 1.63]$
+Zhh	$[-0.22,\ 0.35] \cup [1.07,\ 1.27]$	$[-0.39,\ 1.56]$
2 bins in $\nu\bar{\nu}hh$	$[-0.19,\ 0.31]$	$[-0.33,\ 1.23]$
4 bins in $\nu\bar{\nu}hh$	$[-0.18,\ 0.30]$	$[-0.33,\ 1.11]$

Table 5.4: Precision on the determination of $\delta\kappa_\lambda$ obtained through a global fit including pair- and single-Higgs production channels for several benchmark scenarios at ILC and CLIC.

tree-level Higgs self-coupling dependence is considered in Higgs pair production processes, since one-loop corrections are numerically insignificant. As already stressed, the quadratic dependence on $\delta\kappa_\lambda$ in Higgs pair production processes cannot be neglected. In this case, cross terms between $\delta\kappa_\lambda$ and other EFT parameters are also accounted for. The linear approximation is adopted in all other cases. The estimates for the precision of the SM Higgs pair production cross section are taken from references [139, 140, 142] already discussed in the previous section.

The results of the global fit for the ILC and CLIC benchmark scenarios are shown in Figure 5.10. The $\Delta\chi^2 = 1$ and 4 intervals are also listed in Table 5.4. It is interesting to compare these results with the ones obtained through the exclusive fit on $\delta\kappa_\lambda$ discussed in subsection 5.3.1 (see Figure 5.8). The χ^2 curves for ILC (up to 500 GeV or 1 TeV) and CLIC (no binning, 2 bins and 4 bins in M_{hh}) show very mild differences in the global fit with respect to the exclusive one. This demonstrates that the additional EFT parameters are sufficiently well constrained by single-Higgs measurements and therefore have a marginal impact on the global fit. We also analyzed the impact of combining ILC and CLIC measurements with HL-LHC ones. The precision achievable at the LHC is significantly poorer than the one expected at high-energy lepton colliders, so that the latter dominate the overall fit and only a mild improvement is obtained by combination.

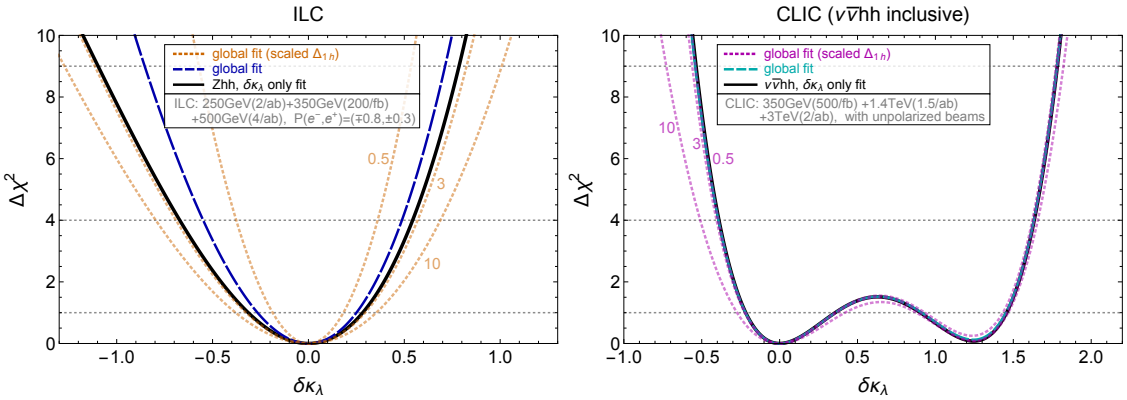

Figure 5.11: LEFT: Chi-square profiled over all EFT parameters but $\delta\kappa_\lambda$ for ILC (up to 500 GeV). RIGHT: The same for CLIC (no binning in M_{hh}). Three scenarios are shown. The solid black curves correspond to the $\delta\kappa_\lambda$ only fit from the double-Higgs measurements. The dashed blue/cyan curves correspond to the global fits in Figure 5.10. The additional dashed curves are obtained by rescaling the uncertainties of single-Higgs measurements (including $e^+e^- \to WW$) by an overall factor. For example, $\Delta_{1h} \times 10$ denotes that the uncertainties of the single-Higgs and diboson measurements are multiplied (worsened) by a factor 10.

We saw that allowing for other EFT deformations beside $\delta\kappa_\lambda$ does not worsen the global fit significantly. This result, however, was by no means guaranteed. To stress this point, we display in Figure 5.11 the profiled χ^2 obtained by artificially rescaling the precision in single-Higgs measurements. The ILC (up to 500 GeV, left panel) and CLIC (no binning in M_{hh}, right panel) benchmarks are used as examples. For each collider, we show the results of the exclusive $\delta\kappa_\lambda$ analysis of the Higgs pair production measurements (solid black curve) and of the global analysis (dashed blue/cyan). The additional dashed curves correspond to global fits in which the precision in single-Higgs and diboson measurements is rescaled by factors ranging from 0.5 to 10. It can be seen that the global fit is sizably affected by such a rescaling, in particular the fit precision is significantly degraded if single-Higgs measurements become worse. This result shows that a comprehensive global analysis of the single-Higgs measurements is crucial for obtaining robust constraints on $\delta\kappa_\lambda$. Notice moreover that an improved precision on single-Higgs measurements could have a positive impact on the determination of the Higgs self-coupling at the ILC.

The impact of the uncertainty on the EFT parameters measurements on the extraction of the Higgs self-coupling from Higgs pair production was also recently investigated in reference [119]. It focused mainly on Higgs pair production through double Higgsstrahlung at ILC 500 GeV and on single-Higgs production in lower-energy runs, taking into account the uncertainties on SM parameters and electroweak precision observables. Loop-level contributions to single-Higgs processes coming from a modified Higgs self-coupling were not included in the fit, and the linear approximation was used to obtain the numerical results. The final fit takes into account runs at 250 and 500 GeV, with 2 and 4 ab^{-1} respectively equally shared between $P(e^-, e^+) = (\mp 0.8, \pm 0.3)$ beam polarizations. The estimated precision on the measurement of $\delta\kappa_\lambda$ is 30%, which is in good agreement with the constraints we obtained in our ILC benchmark scenario.

5.4 THE TRILINEAR AT LEPTON COLLIDERS

In this chapter, we analyzed the precision reach on the determination of the Higgs trilinear self-coupling at future lepton colliders. We covered a comprehensive set of scenarios including low-energy and high-energy machines. The former can only access the Higgs self-interaction indirectly through NLO corrections to single-Higgs processes. High-energy colliders can instead test deviations in the Higgs trilinear coupling directly, through the measurement of Higgs pair production, in particular double Higgsstrahlung and *WW*-fusion.

We performed a global analysis, simultaneously taking into account corrections to the Higgs self-coupling and deviations in EFT parameters affecting Higgs interactions with other SM particles. The results of the analysis are summarized in Figure 5.12 for the various benchmark scenarios considered. For each scenario, three sets of bounds are shown. Thin lines with vertical ends show the precision expected from measurements at lepton colliders only. The superimposed thick bars combine them with HL-LHC measurements. Finally, the thin solid and dotted lines are obtained by combining single-Higgs measurements only at lepton colliders with the single-Higgs HL-LHC bounds (1h). As discussed in the main text, unpolarized beams are assumed for the CEPC, FCC-ee and CLIC. For the ILC runs up to 500 GeV, an equal share of the luminosity at the two $P(e^-, e^+) = (\pm 0.8, \mp 0.3)$ beam polarizations is assumed, whereas a single polarization $P(e^-, e^+) = (-0.8, +0.2)$ is adopted at 1 TeV.

We found that a global analysis is essential to derive robust bounds on $\delta\kappa_\lambda$. This is the case, in particular, if only low-energy lepton machines, such as CEPC or FCC-ee, are available. In this scenario, the Higgs self-coupling can be determined with good accuracy, around 40% at the $\Delta\chi^2 = 1$ level, by exploiting single-Higgs measurements in the $\nu\bar{\nu}h$ and Zh channels as well as diboson production. In order to achieve this accuracy, it is essential to combine runs at different center-of-mass energies, for instance at 240 GeV and at 350 GeV, both with luminosities in the few attobarns range. Measurements at a single energy, in fact, leave a nearly flat direction unresolved in the global fit and lead to a very poor determination of $\delta\kappa_\lambda$. Runs at two different energies can instead significantly reduce the flat direction by better constraining the other EFT parameters.

The high-energy linear colliders making direct measurements of the triple-Higgs self-coupling through pair production still provide the best constraints. Double Higgsstrahlung and *WW*-fusion yield complementary information, being more sensitive to positive and negative deviations in the Higgs self-coupling respectively. It is interesting to notice that the dependence of these two processes on $\delta\kappa_\lambda$ is stronger at lower center-of-mass energy, as shown in Figure 5.7, so that ILC runs at 500 GeV and 1 TeV energy maximize the overall precision allowing for a determination of the trilinear Higgs self-coupling with a 20% uncertainty approximately, at the $\Delta\chi^2 = 1$ level.

High-energy measurements alone, such as the ones available with the 1.4 and 3 TeV CLIC runs, can only rely on $\nu\bar{\nu}hh$ production and have limited sensitivity to positive deviations in $\delta\kappa_\lambda$. In this case, a second minimum in the global fit is present for $\delta\kappa_\lambda \sim 1$. The additional minimum can be excluded by performing a differential analysis exploiting the Higgs pair invariant mass distribution, whose threshold behavior is strongly sensitive to deviations in the Higgs self-coupling. A differential analysis can provide an order-20% determination of $\delta\kappa_\lambda$ at the $\Delta\chi^2 = 1$ level, however values of $\delta\kappa_\lambda \simeq 1$ would still be allowed at the $\Delta\chi^2 = 4$ level.

It is interesting to compare the above results with the ones achievable at the HL-LHC. The HL-LHC is expected to be sensitive only to deviations of $\mathcal{O}(1)$ in the Higgs self-coupling. As one can see from Figure 5.12, this precision is comparable to (or better than) the one achievable at low-energy lepton colliders with low integrated luminosity at 350 GeV runs. This is the case for our circular collider benchmarks with 200 fb^{-1} of integrated luminosity at 350 GeV, as well as for the low-energy runs of the ILC. In these scenarios the HL-LHC data will still play a major role in the determination of $\delta\kappa_\lambda$, while lepton colliders always help constraining large positive $\delta\kappa_\lambda$ that the HL-LHC fails to exclude beyond the $\Delta\chi^2 = 1$ level. On the other hand, with 1 ab^{-1} of luminosity collected at 350 GeV, the lepton collider data starts dominating the combination.

To conclude the discussion, let us come back to our assumption of perfectly well measured electroweak precision observables. It seems fully justified if low-energy runs at the Z-pole are performed. This could for instance be the case at the ILC, CEPC, and FCC-ee which could respectively produce 10^9, 10^{10}, and 10^{12} Z bosons. A Z-pole run for these machines can provide significant improvements with respect to LEP measurements ($2 \cdot 10^7$ Z bosons), making electroweak precision observables basically irrelevant for the extraction of the Higgs trilinear self-coupling.

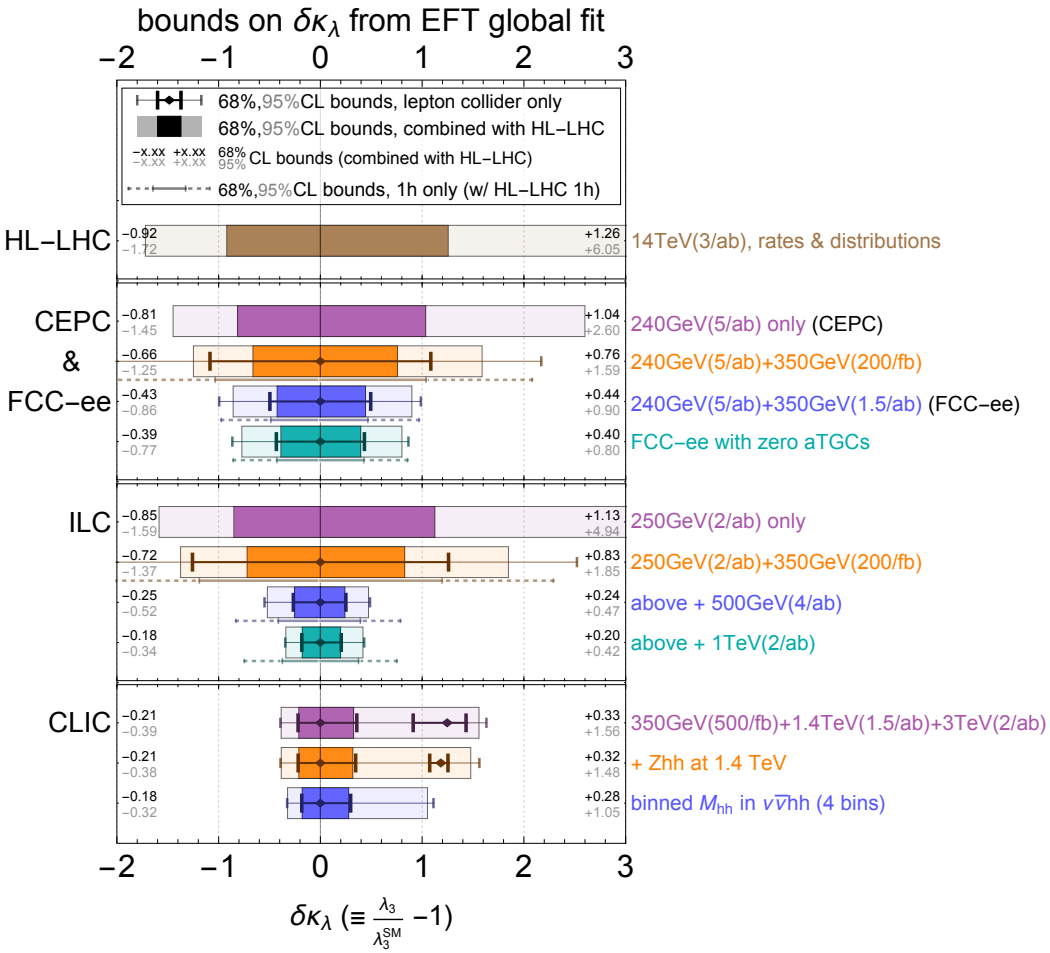

Figure 5.12: Summary of the bounds on $\delta\kappa_\lambda$ from global fits for various future collider scenarios. For the "1h only" scenario, only single-Higgs measurements at lepton colliders are included.

Without a new Z-pole run, evaluating the impact of a limited accuracy on electroweak precision observables might be less straightforward. An analysis of such scenario for the ILC collider has been recently presented in reference [119]. This work explicitly includes present constraints on m_Z, the A_ℓ asymmetry at the Z-pole, $\Gamma_{Z\to ll}$, Γ_Z, Γ_W and forecasts for improved m_W, m_H, and Γ_W measurements, assuming no new run at the Z-pole. In that scenario, it is argued that Higgs measurements can be used to improve the constraints on the electroweak parameters. The achievable precision is sufficient to ensure that electroweak precision observables do not significantly affect the determination of $\delta\kappa_\lambda$.

The precision necessary to decouple electroweak and Higgs parameters determinations in other benchmark scenarios might deserve further exploration. We think that electroweak precision measurements will have a negligible impact on trilinear Higgs self-coupling determination at high-energy machines where Higgs pair production is accessible. This conclusion is supported by the results of section 5.3 showing that the determination of $\delta\kappa_\lambda$ is only mildly affected by the other EFT parameters, once a wide-enough set of single-Higgs measurements is considered. The situation for low-energy colliders, in which the Higgs self-coupling can be accessed only indirectly through single-Higgs processes, is instead less clear. As we saw in section 5.2, the precision on $\delta\kappa_\lambda$ obtained through a global fit is significantly lower than the one estimated through an exclusive analysis. Consequently, the precision of the single-Higgs and triple-gauge coupling extractions has a relevant impact on the fit. In principle, electroweak precision parameters could affect the bounds on single-Higgs couplings and thus indirectly degrade the $\delta\kappa_\lambda$ constraint. This aspect might be worth a more careful investigation, which is however beyond the scope of the present work.

6

PRESENT AND FUTURE OF THE TRILINEAR

The quest for measuring the Higgs boson's properties started just six years ago. Nowadays, we have a good broad picture, of its properties such as the spin, CP nature and its coupling to heavy particles. Nevertheless, the long quest for checking just how close to the SM prediction this new boson is has barely started. Even if the HL-LHC should improve our picture, determining the couplings to lighter particles and studying the Higgs potential is going to require more time and new generations of colliders.

In this section, we decided to focus on the determination of the Higgs trilinear coupling. Despite its simplicity, the Higgs mechanism comes with a lot of puzzles awaiting answer; such has the Hierarchy problem, the stability of the EW vacuum and the possibility to have baryogenesis through a first order phase transition. Deviation from the Ginzburg–Landau ϕ^4 potential could give us information on some of these new physics scenarios. While the two SM parameters governing this potential are easy to measure since they depend on the Fermi constant and the position of the bump in four lepton or two photon mass spectrum, a direct determination of the trilinear and quartic Higgs self-coupling is made extremely challenging by the smallness of the cross section and background of the relevant processes. The current bound on the trilinear of order 20 times the SM value, at the 95% CL level after $35.9\,\text{fb}^{-1}$ of integrated luminosity, are a witness to this fact.

On top of that, the impossibility to directly observe the Higgs boson in the detectors makes the direct determination of its couplings impossible. Only its production followed by subsequent decay or its off-shell effects can be observed. This has strong consequences for the determination of the Higgs couplings since, contrary to the mass, they can not be determined without some assumptions on the underlying theory. Since current LHC results are compatible with the existence of a mass gap between the SM and new physics, EFT is powerful tool to extract these couplings with minimal dependence on the underlying new physics. Nevertheless, since most new physics comes with deviations to several SM couplings, this methode also comes with several new parameters as we saw in section 2.2. Due to the correlation between the different parameters, globals fits with as many observables as possible are needed.

In this work, we reviewed the prospect of measuring the trilinear coupling in this framework at the current and next generation of colliders. We used the new proposal by references [42–44] to first study the prospect of constraining the trilinear at the HL-LHC using higher order corrections to single-Higgs physics. In our framework, the extra parameters resulted in an unconstrained direction in our fit, which called for the addition of extra observables, together with differential information in order to be resolved. Nevertheless, it seems that even with these extra observables, this method should at best complement Higgs-pair production in constraining the trilinear. Even then, the bound at the end of the HL-LHC should reach between $[-0.7, 7]$ times the SM at the 2σ level. Except in the case of dramatic new physics, this will not be enough detect a deviation from the SM. Extrapolating our result to an hypothetical HE-LHC, with an energy of 33 TeV and $10\,\text{ab}^{-1}$ of data, we obtain results which are compatible with reference [147], with a 2σ range of $[0.5, 1.7]$ for the trilinear.

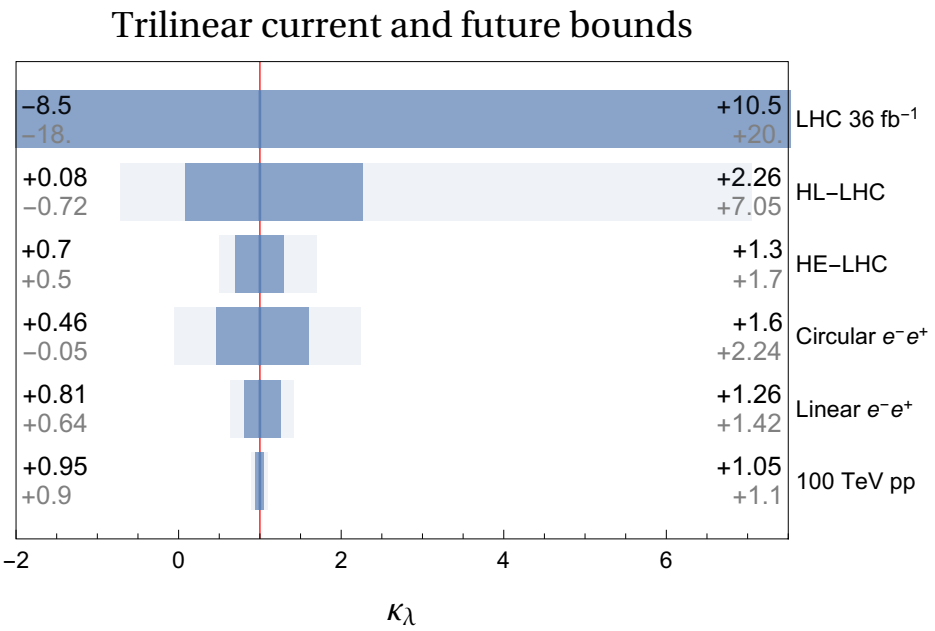

Figure 6.1: Current and future expected bound on the trilinear.

Following our finding regarding the use of higher order corrections in single-Higgs processes, we extended our study to the next generation of leptonic colliders. The high precision of these machines allow, even for circular collider, which do not have access to double-Higs production to improve on the bound the HL-LHC reaching a precision at the 2σ level in the range $[-0.05, 2.24]$ with around $6\,\text{ab}^{-1}$ of luminosity. Linear colliders, thanks to the access to several running energies and to pair production, should manage to obtain even stronger bound, reaching the 50% level.

The final world should not only come from the colliders studied in this work, but also the next generation of high energy hadron colliders, as summarized by Figure 6.1. Thanks to the growth in the double-Higgs cross section, we expect double-Higgs processes to dominate over loop effects in single-Higgs production for extracting the trilinear. A 100 TeV machine combined with a luminosity of $30\,\text{ab}^{-1}$ could determine the trilinear at the 5% level. Nevertheless, the FCC is not going to close the chapter on the Higgs potential; although the trilinear should be constrained at the few percent level, the quartic will only be constrained between $[-4, 16]$ [61] times the SM value. The story continues.

Part III

TESTING NEW PHYSICS USING EFT

7

PARITY OF A SCALAR PARTICLE DECAYING INTO PHOTONS

This chapter of the thesis reproduce the paper [4], with minor modifications and a reworked introduction to link it with the rest of the thesis.

7.1 CONTEXT

In December 2015, the first $3\,\text{fb}^{-1}$ recorded at 13 TeV is released and interesting and unexpected result has been shown by both the ATLAS [148] and CMS [149] collaboration. Both were seeing an excess of event containing two photons with center of mass energy around 750 GeV. The local significance for those two excess were 3.6σ and 2.6σ for ATLAS and CMS respectively. Due to the high resolution of the two experiments, including the look elsewhere effect was diminishing the significance 2σ and 1.2σ. The channel's cleanness, and the fact that two experiments were seeing an excess at the same place rose enthusiasm across the community. This enthusiast was consolidated by further study of the signal [150]. The number of papers on the subject are a witness of this fact. The inspire search [151] currently return a little more than 500 papers. Unfortunately, a few months later, the new results appeared and washed out the bump leaving just the expected smoothly decaying background. Therefore, the previously seen bump was just a statistical fluctuation.

Before learning this fact, we decided to study the prospect to measure the CP properties of this particle using EFT. Even if the results of the paper are not directly useful, since they are based on the assumption the di-photon excess came from a new scalar particle with a cross section of around $8\,\text{fb}^{-1}$, which was later proven not to be the way nature work, we reproduce here the paper [4] since the method used is an interesting showcase of another use of EFT and could easily be adapted for future excesses. Compared to Part ii where we restricted ourself to the SM field content, in this chapter we add a new scalar singlet, allowing the addition of an dimension-5 operator in the EFT which do not break lepton number. Thanks to the lower dimension and the sizable cross section, we can neglect the dimension-6 operator presented in the previous part of the work.

Assuming the excess is real it can be easily interpreted in terms of a spin-0 real singlet (although explanations in terms of spin-1 and spin-2 particles have also received some well-deserved attention). Both production and decay are hence to be mediated by heavier states[1] whose effects can be encoded in a small set of effective operators. Throughout this work we adopt this approach and we explore the potential of the next run of data to unravel the CP nature of this candidate, namely whether it is a scalar or a pseudo-scalar (of course, the 750 GeV singlet could also be an admixture of both scalar and pseudo-scalar, i.e. it could have some interactions that are not invariant under CP transformations, but

1 The model proposed in reference [152] is an exception where the diphoton excess originates from a solitary new degree of freedom without the need for any additional electrically charged particles, nor new strong dynamics. Alternative non-resonant models with long decay chains have also been proposed to *explain* the 750 GeV diphoton excess. In this work, we limit ourselves to the *simplest* interpretation with a single resonance whose couplings to gluons and photons are mediated by additional heavier states charged under QCD and QED.

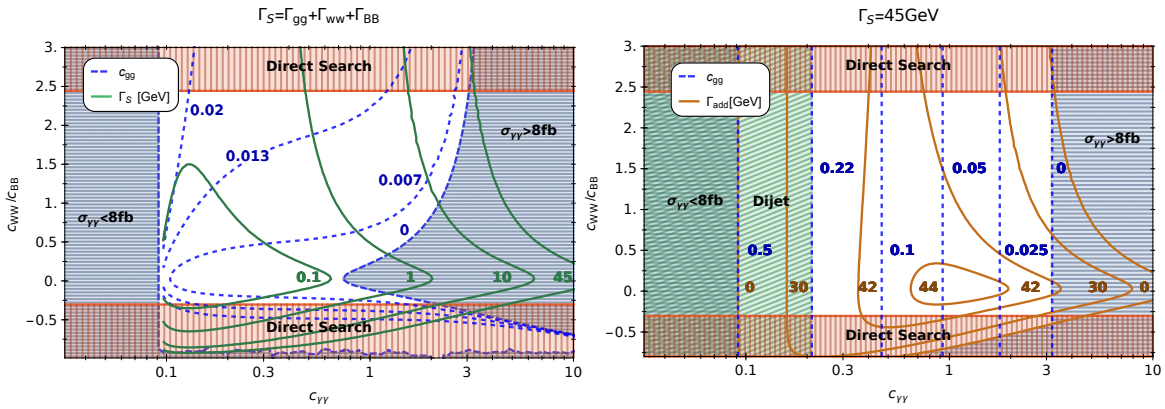

Figure 7.1: Parameter space region in the plane $c_{\gamma\gamma} - c_{WW}/c_{BB}$ compatible with the diphoton excess and current constraints. Regions filled with horizontal lines can not account for the observed signal. Regions filled with vertical lines are in turn bounded by direct searches at 8 TeV. The values of c_{gg} are labeled on dashed contour lines. In the left (right) panel $\Gamma_S = \Gamma_{gg} + \Gamma_{WW} + \Gamma_{BB}$ ($\Gamma_S = 45\,\text{GeV}$) is assumed. The total (additional) width is shown in solid green (brown) lines in the left (right) panel.

we omit this possibility for now.) We start considering a generic parameterization in section 7.2 and discussing the current constraints. Production via gluon fusion (GF) and VBF turn out to be sizable in a large region of the parameter space. However, they are shown to give flat directions that can be only disentangled if new production mechanisms are considered. In this respect, we explore the potential of producing the singlet resonance in association with a SM gauge boson in subsection 7.3.1. The rest of the chapter is structured as follows. In subsection 7.3.2 and 7.3.3, we introduce two asymmetries in the kinematical distributions of GF and VBF events. They are intended to differentiate the two CP hypothesis. The advantage of this approach relies on the fact that most systematic uncertainties cancel out. Statistical uncertainties are on the other hand properly taken into account. We perform simulations to estimate the efficiency for selecting signal and background events in both categories in eight different decay modes: $4\ell, 2j\,2\ell, 2j\ell\,\not{E}_T, 2\gamma\,2j, 4\ell\,2j, 2\ell\gamma\,2j, 4j\,2\ell$ and $4j\,\ell\,\not{E}_T$. We show that after all cuts, sizable efficiencies are obtained for most signals while still keeping backgrounds under control. Despite that we do not attempt to optimize these cuts, all together the eight channels can probe a wide region of the available parameter space within the current run of the LHC, as explained in section 7.4. We conclude in section 8.5.

7.2 PARAMETERIZATION AND CONSTRAINTS

This work aims mainly to provide a guideline for future efforts on the analysis of the parity properties of a resonance S with mass $M \sim 750\,\text{GeV}$. We assume S to be a spin-0 SM gauge singlet. Besides, the production cross section into diphotons mediated by S is assumed to be 8 fb. The question of the spin and parity properties of S is made legitimate by the unexpected character of the excess and thus by the absence of any particular theoretical prejudice towards one hypothesis. Actually we do not focus on any particular model nor

we attempt to address the effective-field theory of S in full generality. In fact, the relevant Lagrangian for our phenomenological study can be parameterized as [153]

$$\mathscr{L} = \frac{1}{2M} S \Big(g_s^2 c_{gg} G^{\mu\nu} G_{\mu\nu} + g^2 c_{WW} W^{\mu\nu} W_{\mu\nu} + g'^2 c_{BB} B^{\mu\nu} B_{\mu\nu} + g_s^2 \tilde{c}_{gg} G^{\mu\nu} \tilde{G}_{\mu\nu} + g^2 \tilde{c}_{WW} W^{\mu\nu} \tilde{W}_{\mu\nu} + g'^2 \tilde{c}_{BB} B^{\mu\nu} \tilde{B}_{\mu\nu} \Big). \tag{7.1}$$

Here, g_s, g and g' stand for the SM $SU(3), SU(2)$ and $U(1)$ gauge couplings, respectively. G, W and B are the corresponding field-strength tensors. For a generic F, $\tilde{F}$ is defined as $\tilde{F}_{\mu\nu} = \frac{1}{2}\epsilon_{\mu\nu\alpha\beta} F^{\alpha\beta}$. The tilded (non-tilded) coefficients are zero if S is a scalar (pseudo-scalar). We disregard further couplings to the SM fermions and to the Higgs doublet since they do not introduce any qualitative change in our analysis. Actually the latter has anyway to be small to pass the constraints from Higgs measurements [154] and ZZ resonant searches [155]. The decay width of S into the different decay modes provided by the interactions above can be easily computed for $M \gg m_{W,Z}$, with $m_{W(Z)}$ the mass of the $W^{\pm}(Z)$ boson. In this limit, the decay widths to the different pairs of gauge bosons are given by

$$\begin{aligned}
\Gamma_{gg} &= 8\pi\alpha_s^2 M \left(c_{gg}^2 + \tilde{c}_{gg}^2\right), \\
\Gamma_{\gamma\gamma} &= \pi\alpha_{em}^2 M \left(c_{\gamma\gamma}^2 + \tilde{c}_{\gamma\gamma}^2\right), \\
\Gamma_{Z\gamma} &= 2\pi\alpha_{em}^2 M \left[\left(c_{BB} t_W - \frac{c_{WW}}{t_W}\right)^2 + \left(\tilde{c}_{BB} t_W - \frac{\tilde{c}_{WW}}{t_W}\right)^2 \right], \\
\Gamma_{ZZ} &= \pi\alpha_{em}^2 M \left[\left(c_{BB} t_W^2 + \frac{c_{WW}}{t_W^2}\right)^2 + \left(\tilde{c}_{BB} t_W^2 + \frac{\tilde{c}_{WW}}{t_W^2}\right)^2 \right], \\
\Gamma_{WW} &= \frac{2\pi\alpha_{em}^2}{s_W^4} M \left(c_{WW}^2 + \tilde{c}_{WW}^2\right),
\end{aligned} \tag{7.2}$$

with $c_{\gamma\gamma} = c_{BB} + c_{WW}$, t_W and s_W the tangent and sine of the Weinberg angle, α_{em} the fine-structure constant and $\alpha_s = g_s^2/(4\pi)$. The photon field-strength coefficient is thus given by $4\pi\alpha_{em} c_{\gamma\gamma}/2M$. The cross section for the single production of S and the subsequent decay into two photons at a center of mass energy $\sqrt{s}$ reads

$$\sigma^{\gamma\gamma}(s) = \frac{1}{s}\frac{1}{M\Gamma_S} \left(\mathcal{C}_{gg}\Gamma_{gg} + \mathcal{C}_{\gamma\gamma}\Gamma_{\gamma\gamma}\right)\Gamma_{\gamma\gamma}, \tag{7.3}$$

where Γ_S stands for the total width. $\mathcal{C}_{gg}$ and $\mathcal{C}_{\gamma\gamma}$ represent instead dimensionless parton luminosities for gluon and photon fusion, respectively. Their values at $8(13)$ TeV have been found to be approximately 174 (2137) and 11 (54), respectively [153]. The single production of S via GF at 13 TeV is thus enhanced with respect to 8 TeV by a factor of ~ 5, which can be in agreement with the absence of departures from the SM predictions in the first LHC run. This in fact translates into a bound on $\sigma^{\gamma\gamma}(8\,\text{TeV}) \lesssim 2\,\text{fb}$ [156, 157]. This observation is no longer true for single production via photon fusion. It is only increased by a factor of ~ 2.9 and therefore in tension with current constraints (see for example [158, 159]). The $c_{\gamma\gamma}$ coupling is bounded from above (below) to avoid too large (small) a diphoton cross section. In the same vein, experimental searches for resonant $Z\gamma$ [160], ZZ [161] and W^+W^- [162] production at 8 TeV set stringent limits on this setup. This information is summarized in Figure 7.1. The allowed parameter space in the $c_{\gamma\gamma} - c_{WW}/c_{BB}$ plane that can explain the excess while evading the current bounds is presented in this plot. For every point in

this plane, c_{gg} has been fixed so that $\sigma^{\gamma\gamma}(13\,\text{TeV}) = 8\,\text{fb}$. The corresponding values are shown in dashed blue lines. The region filled with vertical lines is excluded mainly by W^+W^- and Z searches at 8 TeV. Notice also that the bounds coming from direct searches would be weaker if $\sigma^{\gamma\gamma}(13\,\text{TeV})$ was smaller. The solid green (brown) contour lines stand for the total (additional) width. In the left panel of the figure we assume that Γ_S coincides with these contours. In the right panel we fix it instead to the best-fit value reported by the ATLAS Collaboration [148], $\Gamma_S = 45\,\text{GeV}$, by considering an additional partial width of S into soft (or partially invisible) particles that escape detection.

7.3 DIFFERENT CHANNELS

7.3.1 *Associated production*

It can be seen from Figure 7.1 that resonance searches for massive gauge bosons are only sensitive to the ratio c_{WW}/c_{BB}. It is also apparent that there are other flat directions, i.e. that the different couplings cannot be accessed independently from each others. In fact, even if it was possible to determine Γ_S experimentally, we would have to measure all S decay modes to be able to bound each coupling independently. This seems highly unrealistic, first, because Γ_S might remain out of the experimental resolution, and second because it would require to also tag decays into gluons and (potentially) invisible particles, a notoriously difficult task in the busy hadronic environment of the LHC. Thus, different strategies should be considered in this respect. One possibility relies on S production in association with a gauge boson (a previous study in this direction has been presented in reference [163]). The corresponding Feynman diagram is depicted in the left panel of Figure 7.2, while the cross sections are shown in Figure 7.3. These have been computed by using `MadGraph v5` [143] (`Feynrules v2` [144] has been first used to implement the interactions of Equation 7.1). Other automatic tools have been developed and used [164] to study models aiming at explaining the diphoton excess. In the region of parameter space compatible with the reported excess, the associated production cross sections can be as large as few tens fb. And even for rare decay modes, (e.g. a branching ratio below 0.001 for $S \to ZZ \to 4\ell$), enough events can still be collected with large luminosities. Note also that the corresponding backgrounds are almost negligible (see for example reference [165] for an experimental study of three photon final states). Thus, in Figure 7.4, we elaborate on the idea of resolving flat directions using further production modes. To this end, we consider a hypothetical scenario in which the ratio c_{WW}/c_{BB} has been experimentally established (this measurement can be performed by just observing the ratio of $\gamma\gamma$ events over ZZ or $Z\gamma$ events). Clearly, $c_{\gamma\gamma}$ and c_{gg} cannot just be individually determined by fitting the diphoton excess. This flat direction in the $c_{gg} - c_{\gamma\gamma}$ plane is depicted by the orange band in Figure 7.4 for $\Gamma_S = 45\,\text{GeV}$ and $c_{WW}/c_{BB} = 1$. Now in addition if the associated production $SW^\pm \to 2\gamma\,2j$ is observed to be, for example, $0.01 \pm 0.005\,\text{fb}$, the degeneracy is broken and $c_{\gamma\gamma}$ can be constrained independently, as shown by the vertical band in the figure. The discussion above assumes no substantial direct coupling of S to the SM fermions. If such couplings exist, another contribution to the associated production originates when an EW gauge boson is radiated off from one of the initial quarks (right panel of Figure 7.2). However, the cross section is negligible when linked to light quarks under the assumption that the couplings obey a minimal flavor violation structure and are therefore naturally expected to be of the size of the Yukawa couplings. Flavor constraints

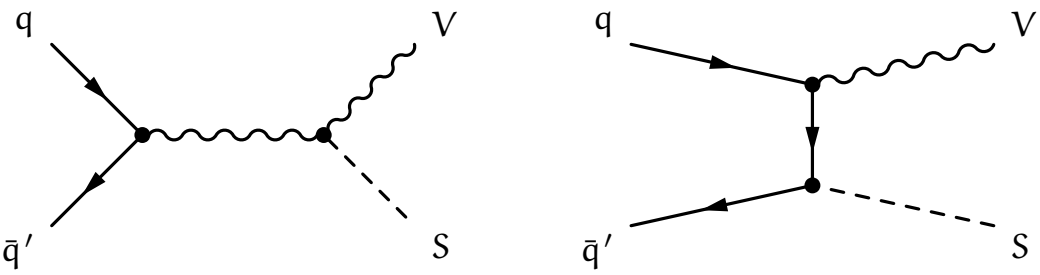

Figure 7.2: Feynman diagrams for S production in association with a gauge boson V. The process on the right panel can only arise for S coupling directly to the light quarks. It has not been considered in our analysis, since it can be neglected under simple flavor assumptions (see the text for details).

would be hard to evade otherwise. If large couplings to the light quarks were nonetheless present, relying on some cancellation to pass flavor constraints, then a detailed study of the kinematic would be worth performing in order to discriminate the various contributions to the associated production. We have checked that the associated production cross section via an initial b quark remains smaller than the contributions computed in Figure 7.3 in most of the parameter space. Finally, we have checked that the gluon-fusion associated production $S + W^{\pm}/Z/\gamma$ together with an extra jet is typically subdominant too, except in the region of small $c_{\gamma\gamma}$ (< 0.1) where it can anyway be reduced by an appropriate cut on the gauge boson p_T and by vetoing the extra jet.

This simple analysis illustrates the importance of considering the associated production mechanisms. Indeed, the argument does not hold equally well for S production in VBF since it turns out to have a remaining large dependence on c_{gg}. The reason is that, contrary to the Higgs case whose couplings to the electroweak gauge bosons appear at the tree level, VBF contamination by gluon initiated processes in the singlet case can be rather large even after tagging on forward jets [166, 167]. Cuts in this respect are provided in subsection 7.3.3. Nonetheless, it is worth to point out that measurements in VBF together with the determination of Γ_S might shed light on possible S hidden decays [168].

On top of it, a last comment concerns the spin-1 alternatives for explaining the diphoton excess. As it has been pointed out in reference [171], these scenarios rely on the production of a 750 GeV vector boson that subsequently decays into a photon and a light scalar. The latter further decays into two collimated photons that, at the detector level, appear to be a single one. This kind of setup can not however give rise to sizable amount of three gauge boson events. Particularly with $W^{\pm}$ in the final state. As a consequence, S production in association with gauge bosons provides a striking signature for disentangling spin-0 and spin-1 models.

The distinctive kinematics of associated production provides different ways to inquire the parity of such a scalar. The polar angle of the radiated vector boson has been highlighted in this respect in the context of Higgs physics (see for example references [172, 173], and reference [174] for related experimental searches at Tevatron). The large Higgs coupling to the longitudinal polarization of the gauge bosons are however instrumental for these studies. The rather small splitting between the Higgs mass and m_Z and m_W is also of major significance for analyses based on the behavior of the cross section near threshold. Accordingly, this observable is no longer suitable for S physics (note that S might not even couple to the longitudinal polarization of the gauge bosons). Related results in this direction have been also pointed out in reference [175]. Further observables

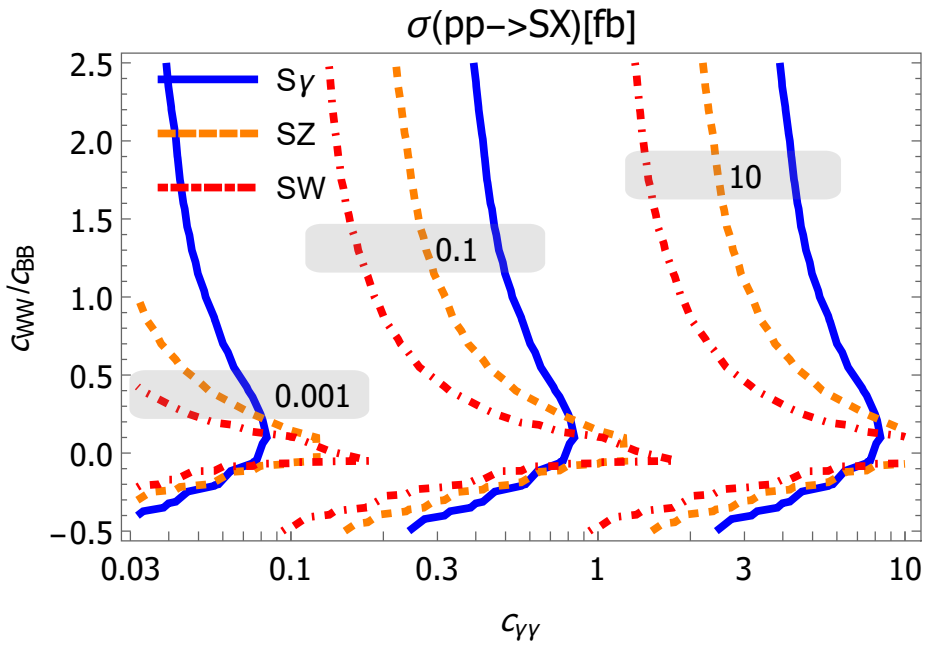

Figure 7.3: Contour lines of the cross sections (in fb) for the associated production channel with an electroweak gauge boson in the plane $c_{\gamma\gamma} - c_{WW}/c_{BB}$. The numbers stand for each group of three contour lines.

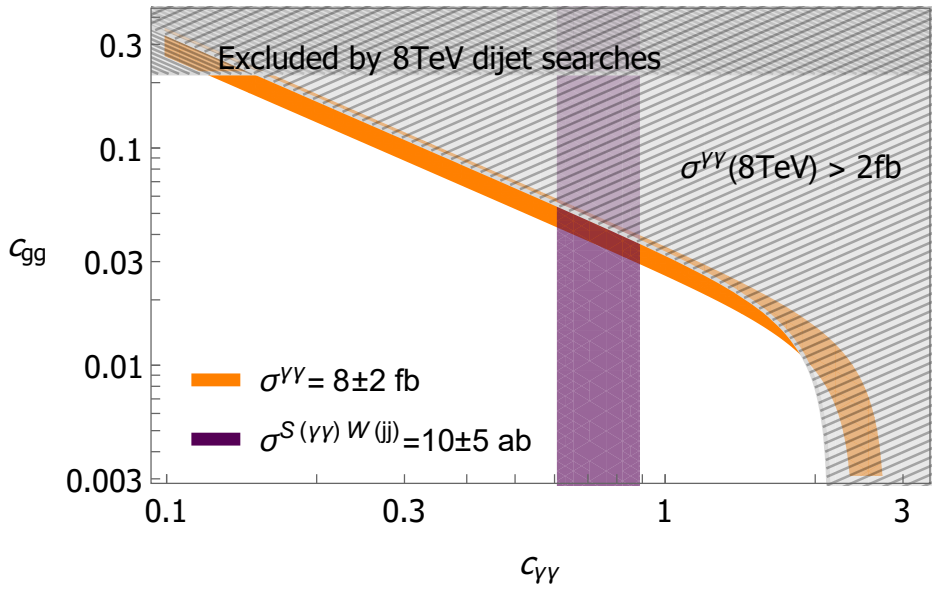

Figure 7.4: Regions in the $c_{\gamma\gamma} - c_{gg}$ plane constrained by the diphoton excess for $c_{WW}/c_{BB} = 1$ for $\Gamma_S = 45\,\text{GeV}$. The vertical band stands for the value of $c_{\gamma\gamma}$ determined by measurements of $pp \to SW^{\pm} \to 2\gamma\,2j$ (see the text for details). Dijet constraints from 8 TeV data [169, 170] are also shown.

for Higgs physics have been presented for example in reference [176]. Several angles between the Higgs momentum and reconstructed momenta of the leptons and jets in the decay of the gauge boson produced in association with the Higgs boson have been identified as discriminating variables to scrutinize the CP properties of S. However, the rather

	4ℓ	$2j\,2\ell$	$2j\,\ell\,\not{E}_T$
ϵ (%)	42	40	30
σ_b (fb)	0.04	34	240

Table 7.1: Estimated signal efficiencies (ϵ) and background cross sections (σ_b) for GF events after the cuts described in the text.

small cross section in this channel compared to GF and VBF makes the latter much more appropriate for an early data analysis. We will thus focus on these channels hereafter.

7.3.2 *Gluon fusion*

The GF production cross section can be conveniently written as

$$\sigma^{GF} = 123 \times \left(\frac{c_{gg}}{0.01}\right)^2 \text{ fb}, \tag{7.4}$$

as computed at LO using `MadGraph`. The `NN23LO1` [177] parton-distribution functions (PDFs) have been used. From the computation of the GF production at higher order in the SM, we expect a large K-factor of order $1.7 - 2$ at NLO. This K-factor will anyway drop in the computation of the asymmetry computed below. We do not include it since a consistent treatment would also require a NLO estimation of the various backgrounds, which is beyond the scope of our analysis. Three different decay modes of S are considered in GF, namely $S \to ZZ$ in both the fully leptonic (4ℓ) and the semileptonic channels ($2j\,2\ell$) as well as $S \to W^+W^-$ with semileptonic decay ($2j\ell\not{E}_T$). In order to tag these events at the experimental level, all events are first required to pass the following set of common cuts. Leptons must have $p_T^\ell > 10\,\text{GeV}$ and $|\eta_\ell| < 2.5$. Jets are instead required to have $p_T^j > 20\,\text{GeV}$ and $\eta_j < 5$. Same-flavor leptons must be separated by $\Delta R > 0.2$ while different-flavor leptons must fulfill $\Delta R > 0.1$. Besides, all leptons must be separated from other jets by $\Delta R > 0.2$, and jets by $\Delta R > 0.4$ among themselves.

Then, exactly two opposite-sign lepton pairs are required in the four-lepton channel. The two with invariant mass closest to m_Z are tagged as coming from one Z, and the other two from the second one. In the semileptonic ZZ decay exactly two opposite-sign leptons and at least two jets must be present. In the semileptonic W^+W^- decay exactly one lepton and at least two jets and $\not{E}_T > 20\,\text{GeV}$ are instead required. The longitudinal momentum of the neutrino can be in this case reconstructed by the $W^\pm$ on-shell condition (see for example reference [178]). Following reference [161], we take the smaller in absolute value among the two possible solutions. There is no further ambiguity in pairing pair of particles with the corresponding massive gauge bosons in any of these channels. We therefore require any reconstructed Z ($W^\pm$) mass to be in a window of $\pm 20\,\text{GeV}$ around m_Z (m_W). Besides, each Z and $W^\pm$ is required to have $p_T > 250\,\text{GeV}$. On top of this, the invariant mass of the four SM tagged particles is required to be in the range $[700, 800]$ GeV. Finally, the event must not pass the VBF criteria, to be defined in the next section.

The window around the mass of the gauge bosons in the previous cuts is required in order to further reduce the background with respect to the signal (which gets only slightly affected). In particular, pair of jets come mainly from QCD radiation and hence their invariant masses do not necessarily peak at the $m_W(m_Z)$ mass. However, if signals with off-shell gauge bosons were to be studied, the corresponding cut should be relaxed. In

this respect, it is worth mentioning reference [179], where the authors claim that the four-lepton channel can get sizable contributions from processes containing a virtual photon.

The efficiencies for selecting events in each of these categories are shown in Table 7.1. The estimated cross sections for the SM backgrounds after passing all cuts are also shown. The irreducible backgrounds dominate in all cases. Therefore, only these have been taking into account. In order to compute all these quantities we have generated parton-level events with `MadGraph v5` which are subsequently passed through `Pythia v6` [180] to account for showering, hadronization and fragmentation effects. The cuts above are finally implemented in `MadAnalysis v5` [181].

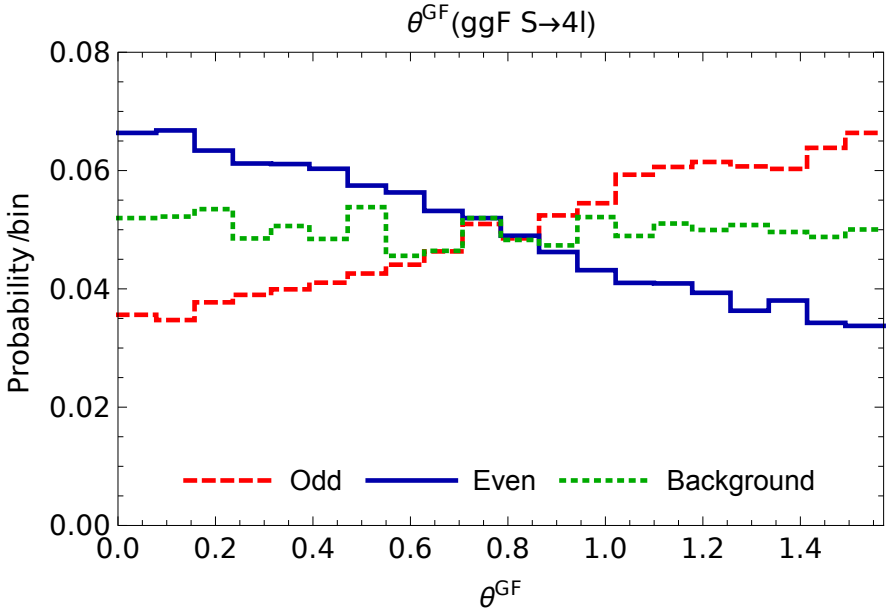

Figure 7.5: θ^{GF} distribution for reconstructed four-lepton signal events for the scalar (solid blue) and the pseudo-scalar (dashed red) cases. The background is shown in dotted green. Signal and background distributions have been independently normalized to unity. Their respective importance will depend on the parameter space point.

Having reconstructed the momenta of the four decay products, we can define the following asymmetry:

$$\mathcal{A}^{GF} = \frac{N(\theta^{GF} > \pi/4) - N(\theta^{GF} < \pi/4)}{N(\theta^{GF} > \pi/4) + N(\theta^{GF} < \pi/4)}, \tag{7.5}$$

where

$$\theta^{GF} = \begin{cases} \theta & \text{if} \quad \theta < \pi/2 \\ \pi - \theta & \text{if} \quad \theta > \pi/2 \end{cases}, \tag{7.6}$$

and

$$\theta = \arccos\left\{ \frac{(p_1 \times p_2)\cdot(p_3 \times p_4)}{|p_1 \times p_2||p_3 \times p_4|} \right\}, \tag{7.7}$$

with $p_{1,2}$ and $p_{3,4}$ the three-momenta of the decay products of each massive gauge boson. This observable has been widely used in Higgs physics (see for example reference [182]). However, the small Higgs mass makes some channels above not suitable for CP studies

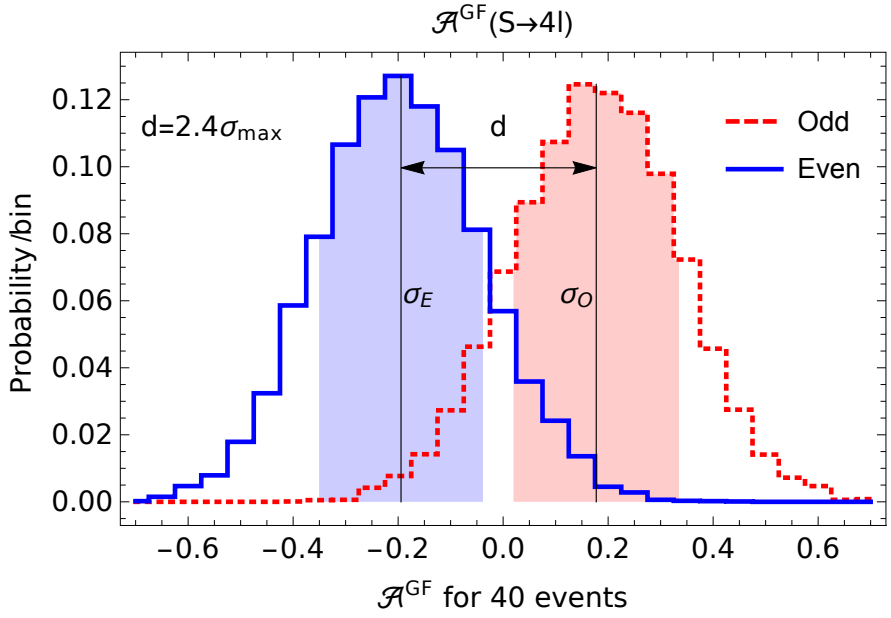

Figure 7.6: $\mathcal{A}^{GF}$ distribution for the scalar (solid blue) and the pseudo-scalar (dashed red) cases with 40 observed events after 10'000 pseudo experiments. The distance (d) between the two central values in terms of the largest σ is also shown.

with this asymmetry, inasmuch as the signal peaks in the region populated by the SM background. For S decays instead, the rather large mass allows us to stay in much more suppressed background regions. Note also that two body S decays could be also considered. As a matter of fact, photon conversion events have been discussed in the Higgs literature [183]. The typical opening angle of the lepton products are however of the order of $m_e/E_\gamma \sim 10^{-6}$, which is well below any present or future experimental sensitivity.

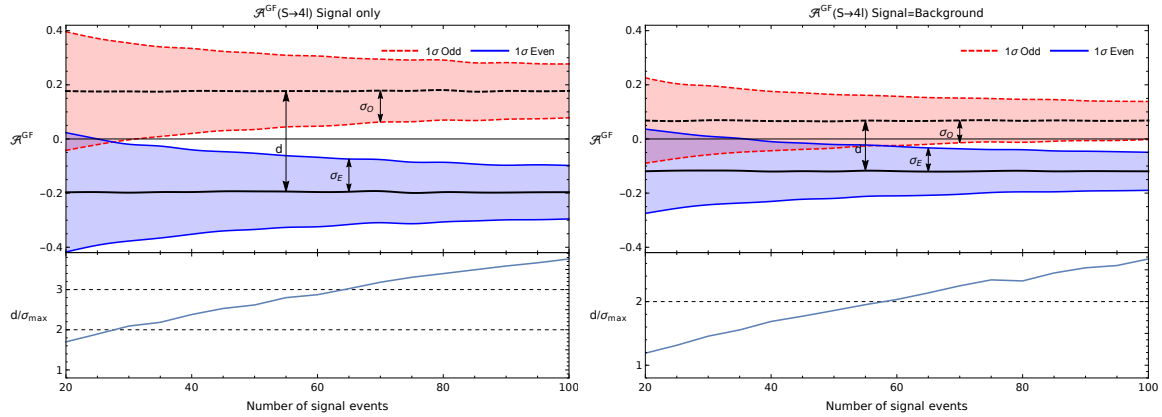

Figure 7.7: One sigma statistical interval for $\mathcal{A}^{GF}$ as a function of the total number of observed events for only signal (left panel) and with as much background as signal (right panel) for the scalar (solid blue) and pseudo-scalar (dashed red) cases. The distance (d) between the two central values in terms of $\sigma_{max} \equiv \max\{\sigma_O, \sigma_E\}$ is also shown.

In four-lepton events, the variable defined in Equation 7.6 takes the form shown in Figure 7.5. No significant departures from this shape are found in other channels. In order to quantify the discrimination power of this asymmetry for a given number N_{obs}

of observed events, we perform 10'000 pseudo experiments with N_{obs} events each.[2] As a matter of example, the distribution followed by $\mathcal{A}^{GF}$ for $N_{obs} = 40$ for signal only is shown in Figure 7.6. The one sigma statistical uncertainty is defined by the symmetric interval around the center of the distribution containing the 68% of the total area. For the matter of example, this is also shown in the figure. These 40 events in the $2j\ell\not{E}_T$ final state can be reached, in the minimal width case, for luminosities as low as $\mathcal{L} \sim 5\,fb^{-1}$ for $(c_{\gamma\gamma}, c_{WW}/c_{BB}) = (2,2)$, while $(c_{\gamma\gamma}, c_{WW}/c_{BB}) = (0.1, 0.1)$ would require $\mathcal{L} > 100\,fb^{-1}$. The large background makes the analysis harder and the luminosity needed to discriminate the two CP hypotheses will be estimated in section 7.4. Figure 7.7 gives the asymmetry $\mathcal{A}^{GF}$ as a function of the total number of observed events under the assumption of negligeable background (left panel) and under the assumption of as many background events as signal events (right panel).

7.3.3 *Vector-boson fusion*

The LO cross section for producing S in association with two jets with p_T larger than 10 GeV, separated by at least $\Delta R > 0.1$ and with dijet invariant mass above 400 GeV, can be approximately written as

$$\sigma^{VBF} = \left[45\,\left(\frac{c_{gg}}{0.01}\right)^2 + 1.2\frac{c_{\gamma\gamma}^2}{(1+r)^2} + 1.7\frac{c_{\gamma\gamma}^2 r}{(1+r)^2} + 43\frac{c_{\gamma\gamma}^2 r^2}{(1+r)^2}\right] fb, \tag{7.8}$$

with $r \equiv c_{WW}/c_{BB}$. The coefficients above have been again computed using `MadGraph` with the `NN23LO1` PDFs. The interference between gluon-initiated diagrams (proportional to c_{gg}) and VBF diagrams is negligible and hence not shown in this equation. Two example diagrams are depicted in Figure 7.8. Hereafter we denote by S^{QCD} and S^{EW} the production computed using each channel alone. S^{QCD} in the plane $c_{\gamma\gamma} - c_{WW}/c_{BB}$ can be easily estimated using this equation in light of the c_{gg} values provided in Figure 7.1. Instead S^{EW} is plotted in Figure 7.9.

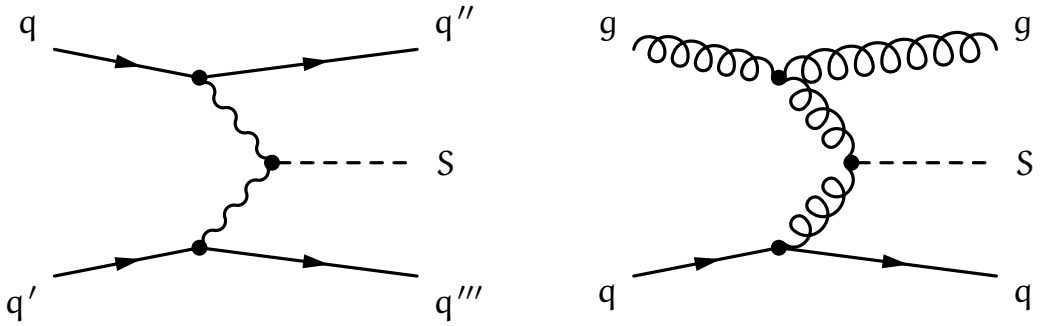

Figure 7.8: Examples of Feynman diagrams for S production via electroweak (left) and QCD (right) with two additional jets.

VBF events can be tagged at the experimental level in five different decay modes of S. These comprise the three possibilities described in the previous section with two additional forward jets, namely $4\ell\,2j$, $4j\,2\ell$ and $4j\,\ell\not{E}_T$, as well as the decay into $\gamma\gamma$ and $\ell^+\ell^-\gamma$. Events are first selected by imposing the same common cuts as in GF, while photons should be separated from any other tagged particle by $\Delta R > 0.2$. When more than two

2 These results could have been obtained analytically as shown in Appendix C.

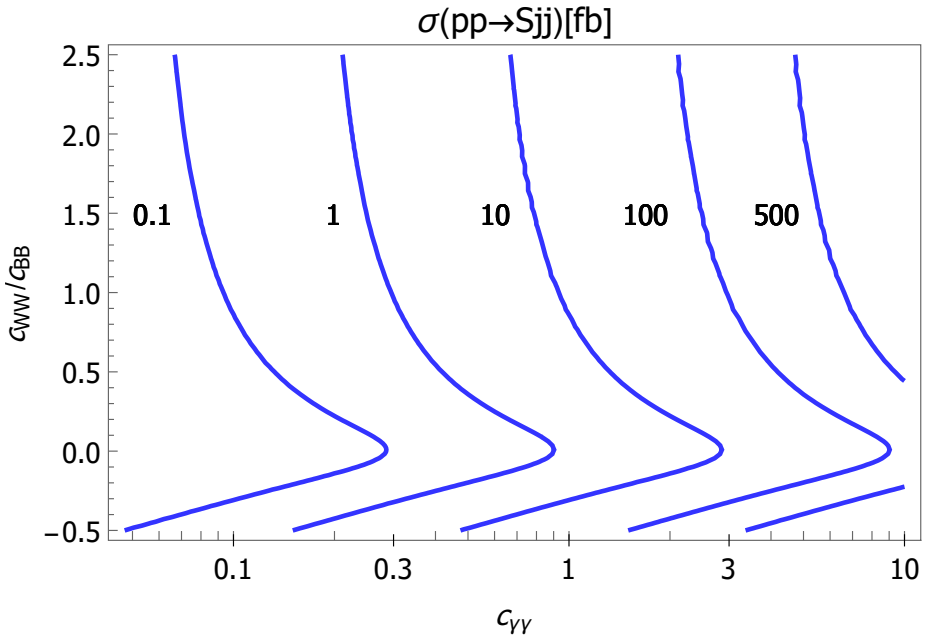

Figure 7.9: Contour lines in the plane $c_{WW}/c_{BB} - c_{\gamma\gamma}$ of S production cross sections (in fb) with two forward jets initiated by electroweak gauge bosons and after the parton-level VBF cuts described in the text.

jets are present, forward-jet candidates are selected to be those two jets with invariant mass $m_{j_1 j_2}$ less similar to m_Z (or m_W) among the four leading jets. They are subsequently required to fulfill the VBF criteria. This is defined by $m_{j_1 j_2} > 500\,\text{GeV}$, $\eta_{j_1}\eta_{j_2} < 0$, $|\Delta\eta_{j_1 j_2}| > 3$ and $\Delta R_{j_1 j_2} > 0.4$. These cuts are motivated by previous searches for heavy Higgs bosons [155]. Any reconstructed Z ($W^\pm$) is again required to have a mass within a window of $\pm 20\,\text{GeV}$ around m_Z (m_W). Besides, the p_T of the two leading photons as well as the p_T of each reconstructed Z and $W^\pm$ must be still larger than 250 GeV. Finally, we require the invariant mass of the two reconstructed SM gauge bosons to be in the range [700, 800] GeV. The efficiencies for selecting events in each of these categories, referred to events generated using the parton-level cuts in Equation 7.8, are shown in Table 7.2 for S^{QCD} and S^{EW}. Notice that gluon-initiated VBF can be dominant due to the rather large coefficient in front of c_{gg} in Equation 7.8. This result contrasts with the Higgs case, the reason being that, unlike the singlet S, the Higgs boson couples to the electroweak gauge bosons at the tree level.

	$2\gamma\,2j$	$4\ell\,2j$	$2\ell\,\gamma\,2j$	$4j\,2\ell$	$4j\,\ell\,\not{E}_T$
ϵ_{QCD}	6	12	14	11	9
ϵ_{EW}	18	15	18	15	12
σ_b (fb)	0.42	0.001	0.03	1.8	15

Table 7.2: Estimated signal efficiencies (ϵ, in percent) and background cross sections (σ_b) for VBF events after the cuts described in the text. Gluon-initiated processes (QCD) can very much contaminate pure EW VBF.

The estimated background cross sections are also shown in Table 7.2. The irreducible backgrounds dominate each category. The channels $4j\,2\ell$ and $4j\,\ell\,\not{E}_T$ are mostly populated

by Drell–Yan and $W^{\pm}$ production with radiated jets, rather than by diboson events. These cross sections are of similar magnitude to those reported in the figures of reference [155], which uses slightly different cuts. We construct the following asymmetry for VBF events:

$$\mathcal{A}^{\mathrm{VBF}} = \frac{N(\theta^{\mathrm{VBF}} > \pi/4) - N(\theta^{\mathrm{VBF}} < \pi/4)}{N(\theta^{\mathrm{VBF}} > \pi/4) + N(\theta^{\mathrm{VBF}} < \pi/4)}, \tag{7.9}$$

where, analogously to the GF case,

$$\theta^{\mathrm{VBF}} = \begin{cases} \theta & \text{if} \quad \theta < \pi/2 \\ \pi - \theta & \text{if} \quad \theta > \pi/2 \end{cases}, \tag{7.10}$$

with θ the angle between the p_T of the two tagged forward jets. This observable has been

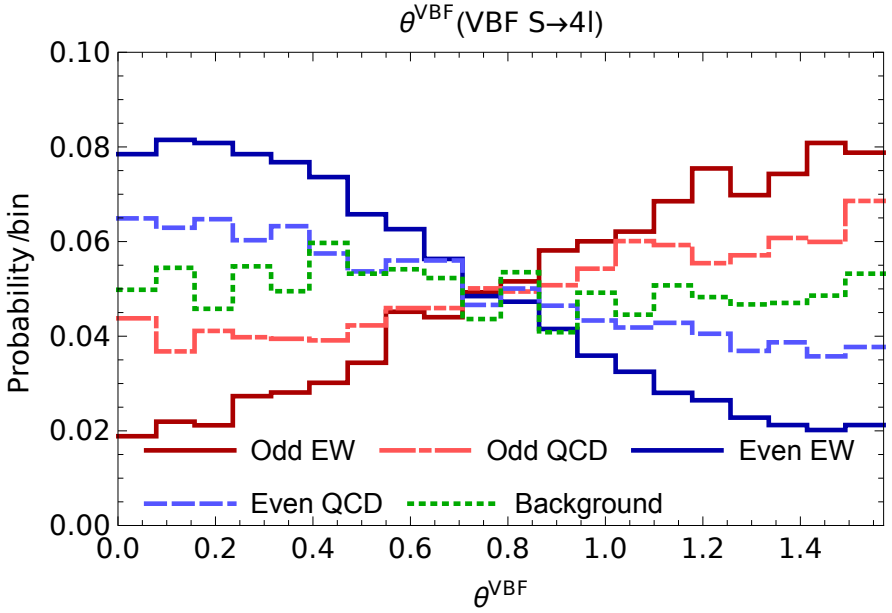

Figure 7.10: θ^{VBF} distribution for reconstructed four-lepton signal events for the scalar (blue) and the pseudo-scalar (red) cases. Solid and dashed lines stand for S^{EW} and S^{QCD} respectively. The background is shown in dotted green. Signal and background distributions have been independently normalized to unity. Their respective importance will depend on the parameter space point.

previously considered in the literature in the context of Higgs studies (see for example reference [184, 185]). As a matter of example, we show the distribution for θ^{VBF} as reconstructed in four-lepton signal events in Figure 7.10. As in the GF case, the distribution in other channels does not present significant differences. The discrimination power of this angle is apparent from the plot. In order to quantify it for a given number N_{obs} of observed events we proceed as in the previous section. Figure 7.11 shows the distribution followed by $\mathcal{A}^{\mathrm{VBF}}$ for $N_{\mathrm{obs}} = 40$ and $S^{\mathrm{QCD}} = S^{\mathrm{EW}}$, under the assumption that the background is negligible. In the 2j2γ channel, this number of events can be reached with luminosities of order $\mathcal{L} \sim 60\,\mathrm{fb}^{-1}$ for $(c_{\gamma\gamma}, c_{WW}/c_{BB}) = (2,2)$, while $(c_{\gamma\gamma}, c_{WW}/c_{BB}) = (0.1, 0.1)$ requiress $\mathcal{L} \sim 200\,\mathrm{fb}^{-1}$. We plot the one sigma statistical interval as a function of the total number of observed events in Figure 7.12 under the assumption of no background (left panel) and as much background as signal (right panel). It turns out that less than 40 (60) events are necessary to start disentangling the CP properties of S if there is no background

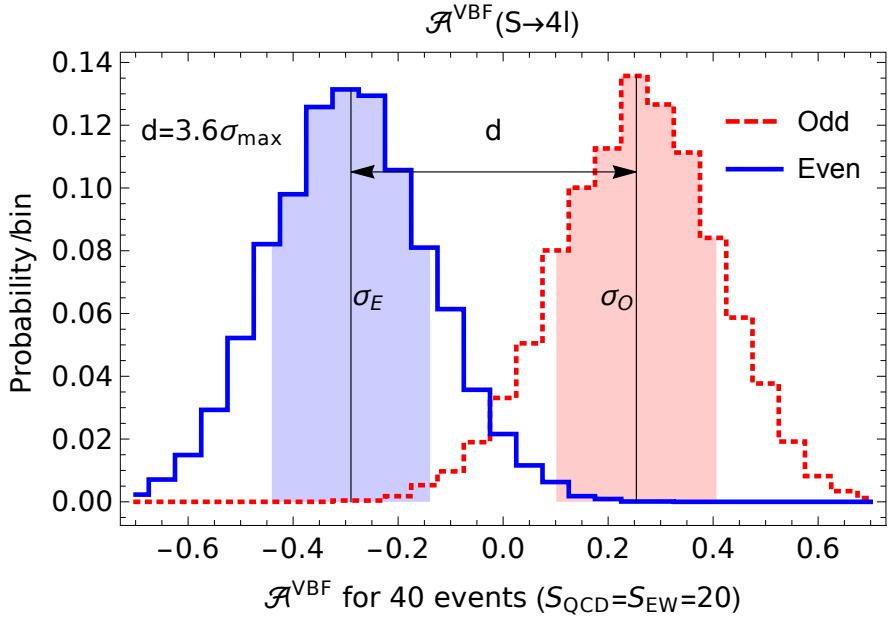

Figure 7.11: $\mathcal{A}^{VBF}$ distribution for the scalar (solid blue) and the pseudo-scalar (dashed red) cases with 40 observed events and $S^{QCD} = S^{EW}$ after 10'000 pseudo experiments. The distance (d) between the two central values in terms of the largest σ is shown in the lower panels.

(if there is as much background as signal). Despite this result being apparently much better than the one obtained in GF (see Figure 7.7), in practice VBF is much suppressed (see Equation 7.4 and Figure 7.9) and they are hence complementary.

7.4 RESULTS

For each point in the parameter space region and for each of the eight event categories i defined for GF and VBF, we compute $\mathcal{A}^{GF}$ and $\mathcal{A}^{VBF}$ by estimating the number of signal and background events. For a fixed luminosity, the latter can be derived from Table 7.1 and 7.2. The number of signal events in each case can be in turn computed as

$$N_{signal} = \sum_i \sigma \times BR(S \to i) \times \epsilon_i, \tag{7.11}$$

where ϵ_i stands for the corresponding experimental efficiency as provided in Table 7.1 and 7.2, too. We assume these efficiencies to be independent of the coefficients of the operators in Equation 7.1. We have checked that this is the case in almost the whole parameter space, small variations arising only in the VBF $2\gamma\,2j$ channel for $c_{WW} \ll c_{\gamma\gamma}$. At any rate, this region is dominated by S^{QCD} and therefore not sensitive to these variations. Figure 7.13 shows the regions where, with a total luminosity of $300\,fb^{-1}$, the CP-odd hypothesis can be excluded at the 2σ level in favor of the CP-even using the two asymmetries separately (in the left panel no extra sources for Γ_S are considered while in the right panel $\Gamma_S = 45\,GeV$ instead). These regions are defined by requiring the mean value of $\mathcal{A}$ in the odd case to be separated by at least 2σ from the mean value of $\mathcal{A}$ in the even case. For the matter of an example, this separation (d) is also shown in Figure 7.6 and 7.11.

The separation between the two hypothesis exceeds 1.5σ throughout the parameter space. It is important to mention that small variations on the efficiency and cross section of the $2\gamma\,2j$ channel can make the corresponding region to look notably different *for a*

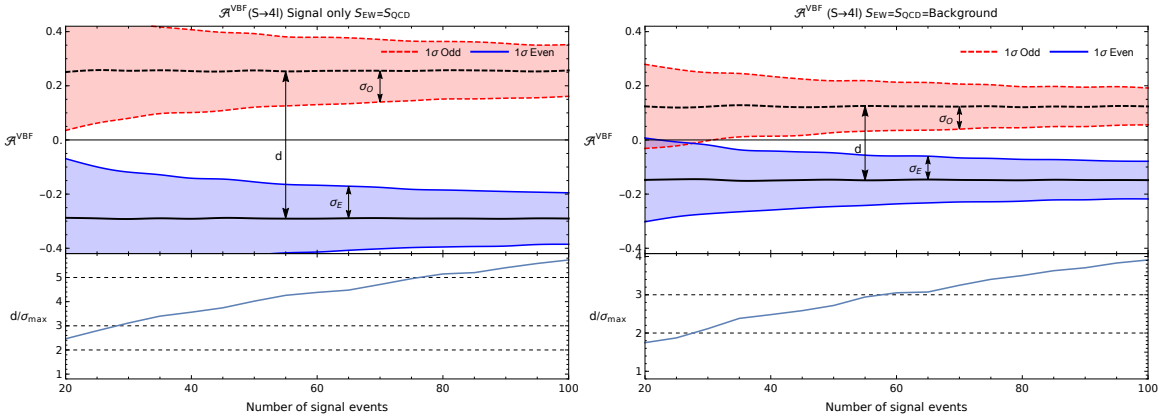

Figure 7.12: One sigma statistical interval for $\mathcal{A}^{VBF}$ as a function of the total number of observed events for only signal (left panel) and as much background as signal (right panel) for the scalar (solid blue) and pseudo-scalar (dashed red) cases. $S^{QCD} = S^{EW}$ has been assumed in both panels. The distance (d) between the two central values in terms of $\sigma_{max} \equiv \max\{\sigma_O, \sigma_E\}$ is shown in the lower panels.

fixed luminosity. In that respect, an optimisation of the different cuts, as well as other more sophisticated analyses like the matrix-element method used [186] in the four-lepton Higgs decay channel, can help covering larger regions of the parameter space. At any rate, even with the basic cuts used in our analysis, luminosities slightly larger than 300 fb^{-1} will be sufficient to test at the 2σ confidence level the whole parameter space compatible with 8 TeV constraints and 13 TeV data.

The area excluded by searches at 8 TeV (see Figure 7.1) has been superimposed. Note that this area would be smaller if the required diphoton cross section at 13 TeV was smaller than the 8 fb that we are using throughout this chapter. With 30 fb^{-1} only a small portion of the available parameter space can be tested.

It can be shown that GF and VBF channels are complementary, the former being mostly sensitive to the upper region with even small $c_{\gamma\gamma}$. It is also worth emphasizing the role played by semileptonic W^+W^- decays. This is in contrast with Higgs physics, for which considering these final states is not even possible, inasmuch as the signal peaks in the region populated by the huge $W^{\pm}+$ jets background. At any rate, the dominant channel is given by $S \to \gamma\gamma$ in VBF. Indeed, the fact that gluon-initiated processes can also contaminate the EW VBF selection makes this channel sensitive even to regions of small EW couplings, which require large c_{gg}.

7.5 CONCLUSIONS

In this chapter, we have studied methods to measure the CP properties of scalar resonance, which was initially discovered through its decay to photons. This was motived by the interesting excess seen by both ATLAS and CMS. As history proved, we lost the bet that this excess had a physical origin. Nevertheless, our method could be modified and applied to any future scalar resonance coupling to gauge bosons. We started by discussing how associated production with a gauge boson could resolve the flat direction and allow us to extract the individual coupling to photon and gluon. We then used the constraints available to define the parameter space of interest. We studied the potential of LHC to

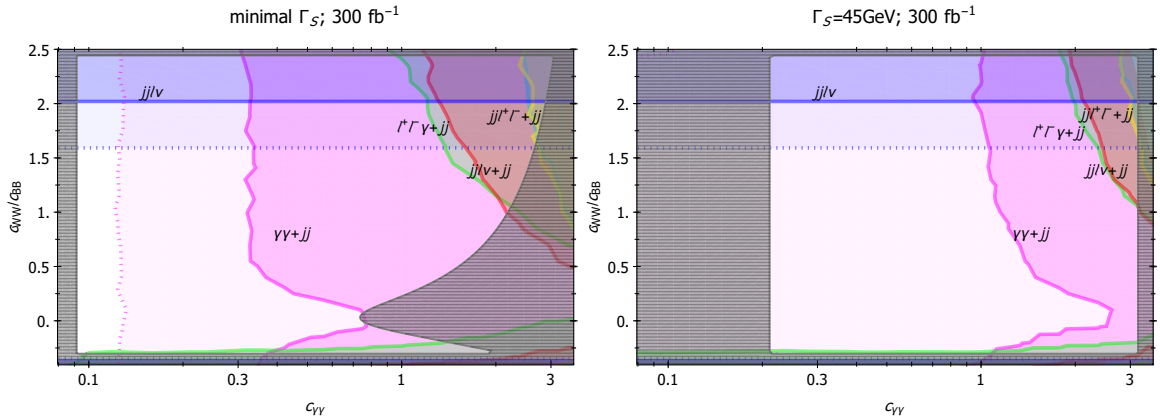

Figure 7.13: Parameter space regions for which the CP odd and even hypothesis can be disentangled at the 2σ level with $300\,\text{fb}^{-1}$. The region where the CP nature can be determined by the different channels is given by the area above the corresponding line. The grey striped regions are excluded (see Figure 7.1). In the left panel we assume no extra contributions to Γ_S, while in the right panel we fix $\Gamma_S = 45\,\text{GeV}$. The light area enclosed by the dashed lines stands for the 1.7σ region.

unravel the CP nature of such a scalar. Two different asymmetries were covered in this regard. These are to be constructed out of events produced in gluon and vector-boson fusion respectively. We have shown that events in these categories can be efficiently tagged at the experimental level while keeping backgrounds under control. We have emphasized that as few as ~ 50 events are needed to separate the CP even and odd hypotheses. This event count can be reached in different regions of the parameter space during the next LHC run. In particular, for the full run all the parameter space region is expected to be probed, relying mainly on the VBF $2\gamma\,2j$ channel.

8

PROBING LIGHT TOP PARTNERS WITH CP VIOLATION

This chapter of the thesis reproduces the paper [1] with minor modifications and a reworked introduction to link it with the rest of the thesis.

8.1 INTRODUCTION

In this chapter, we want to compare the constraints on composite Higgs (CH) models coming from direct searches from the LHC and from indirect searches coming from low energy precision measurements. From an EFT point of view, the approach is very different for the two cases. Direct searches rely on the production and decay of the new heavy particle, which bring us to the same situation as chapter 7. Therefore, we are clearly outside of the range of validity of the Standard Model EFT and need at least one additional field. In this case, however, we use a simplified model. This model is based on the minimal structure capturing the relevant information of a class of UV physics and allows for extraction of stronger bounds thanks to the extra assumptions.

On the other hand, for the low energy constraint, we are in the complete opposite situation since the energy scale is well below the mass of the new states (which are already constrained to appear close or above the TeV scale). We want to reverse the situation of Part ii; instead of trying to extract bounds with little model dependence, we want to use the generic bounds set by experimentalists and translate them for our simplified model. The experimental bounds are given in terms of dipole operators and the Weinberg operator, we can find in Equations (2.13) and (2.11) with a different normalization:

$$\mathscr{L}_{eff} = -d_q \frac{i}{2}\bar{q}\sigma^{\mu\nu}\gamma^5 q A_{\mu\nu} - \tilde{d}_q \frac{ig_s}{2}\bar{q}\sigma^{\mu\nu}T^a\gamma^5 q G^a_{\mu\nu} - w\frac{1}{3}f^{abc}G^a_{\mu\sigma}G^{b,\sigma}_{\nu}\widetilde{G}^{c,\mu\nu}\,. \quad (8.1)$$

Although these operators also appear in section 2.2, we are technically in a different situation. Due to the very low scale of the experiment, heavy SM particles such as the top quark are also integrated out. Starting from the simplified model, we can naturally integrate out the heavy physics and obtain the value of d and w in term of our UV physics. This is where the advantage of EFT is made clear, since the computation of the low energy coefficient can be achieved an unambiguous way using standard pertubative techniques.

8.2 EFFECTS OF COMPOSITE HIGGS MODELS

An appealing solution to the naturalness problem is based on the idea that the Higgs boson is not an elementary state, but rather a composite object coming from some new strongly-coupled dynamics at the TeV scale. This idea reached nowadays a quite compelling embodiment, which is denoted as "composite Higgs" scenario.[1] Its main assumption is the identification of the Higgs with a pseudo-Nambu-Goldstone boson [188–194], which, in minimal realizations, is associated to an $SO(5) \to SO(4)$ symmetry-breaking pattern [195]. An additional, fundamental ingredient is the generation of fermion masses

1 See references [18, 60, 187] for extensive reviews.

through the partial-compositeness mechanism [196]. The latter hypothesis is necessary to keep under control dangerously large flavor-breaking effects and is strictly needed at least for the top quark sector.

An important consequence of partial compositeness is the presence of composite partners of the SM fermions. Among them, the partners of the top play the most important role: besides controlling the generation of the top mass, they also govern the leading contributions to the radiatively-induced Higgs potential [197–200]. For this reason the top partners are directly connected with the amount of fine tuning and must be relatively light (around the TeV scale) to ensure that naturalness is preserved [201].

The presence of light top partners has deep consequences for the phenomenology of CH models. First of all, being charged under QCD, they have sizable production cross sections at hadron colliders, hence constituting one of the privileged ways to directly test the CH paradigm at the LHC. The bounds are nowadays surpassing 1 TeV (see for instance the constraints from pair production of charge-5/3 partners [202, 203]), thus starting to put some pressure on the natural parameter space of the models.

Light top partners give also rise to sizable corrections to precision observables, which can be used as powerful indirect probes of the composite dynamics. For instance, large effects are expected in electroweak precision measurements, such as the S and T parameters and the Z coupling to the bottom quark. In this case the tight experimental constraints translate into exclusions on the top partner masses around the TeV scale [204–206], which are competitive with the ones from direct searches.

In this chapter we will focus on another interesting effect due to light top partners, namely the generation of sizable contributions to flavor physics, in particular to CP-violating observables. These effects are due to the presence of additional complex phases in the top partners interactions. Such phases are expected in generic composite Higgs scenarios. Complex parameters can in fact be present in the composite sector interactions if CP-violation is allowed. Furthermore, even if the strongly-coupled dynamics is assumed to be CP preserving, complex mixings of the elementary SM fermions with the composite sector are still needed in many models to generate the non-trivial phase of the CKM matrix. For instance this is the case in scenarios in which the left-handed top field is mixed with multiple composite operators. Examples of such models are the minimal MCHM_5 constructions [195].

Among the possible CP-violating effects, some of the most relevant ones are the generation of dipole moments for the light leptons and quarks. Light top partners generically induce contributions to dipole operators at two-loop level through Barr–Zee-type diagrams [207].[2] Additional two-loop contributions are also generated for the gluonic Weinberg operator [209]. All these effects arise from the presence of CP-violating Higgs interactions involving the top and its partners. As we will see, in a large class of models, the main contributions come from derivative Higgs interactions induced by the non-linear Goldstone structure.[3]

The Barr–Zee effects and the Weinberg operator, in turn, give rise to sizable corrections to the electron [215–217], neutron [218] and diamagnetic atoms [219] EDMs. All these effects are tightly constrained by the present data, moreover the experimental sensitivity

2 Additional contributions can arise at the one-loop level in specific flavor set-ups, such as the "anarchic" scenario [208]. They are however absent in other flavor constructions. We will discuss these aspects later on.

3 Analogous effects due to effective CP-violating Higgs interactions, including anomalous top and bottom Yukawa couplings, have been studied in the context of the SM effective field theory [210–214].

is expected to increase by more than one order of magnitude in the near future [217, 220, 221]. As we will see, the present bounds allow to probe top partners masses of order *few* TeV and can be competitive with the direct LHC searches. The future improvements in the EDM experiments will push the exclusions beyond the 10 TeV scale, arguably making these indirect searches the most sensitive probes of top partners.

For our analysis we adopt the effective parametrizations developed in reference [222] and already used in the investigation of the bounds coming from electroweak precision measurements [205]. This framework allows for a model-independent description of the Higgs dynamics (including the whole non-linear Goldstone structure) and of the relevant composite resonances. As we will see, top partners contributions to the dipole operators are saturated by infrared (IR) effects. The leading corrections come from the lightest composite states and can be fully captured by the effective framework. IR saturation is instead not present for the contributions to the Weinberg operator, therefore, we expect non-negligible UV corrections to be present. The UV contributions, however, are expected to be independent of the IR effects and therefore should not lead to cancellations. The light top partners contributions can thus be interpreted as a lower estimate of the full CP-violating contributions and can be safely used to derive robust constraints.

It must be stressed that, depending on the specific flavor structure, additional contributions to flavor-violating and CP-violating observables can be present. Typical effects can arise from partners of the light-generation SM fermions as well as from heavy vector resonances with electroweak or QCD quantum numbers. All these effects are generically expected in "anarchic partial compositeness" scenarios [223–226] and lead to additional constraints on the composite dynamics [60, 227–237]. Focussing first of all on the quark sector, strong bounds on the resonance masses, of order $5-10$ TeV, come from $\Delta F = 2$ observables, in particular $s \to d$ transitions that can be tested in Kaon physics. One-loop contributions to $\Delta F = 1$ and CP-violating observables, for instance the neutron EDM, are also induced by partners of the light SM quarks. Contributions of comparable size can also be induced by the top partners due to the presence of relatively large mixing angles with the light SM fermions. The current constraints on $\Delta F = 1$ transitions and on the neutron EDM translate into bounds on the resonance masses of order *few* TeV. If the "anarchic" construction is naively extended to the lepton sector, more dangerous flavor effects arise [237]. In this case large one-loop contributions to the electron EDM and to $\mu \to e\gamma$ transitions are generated, which can be compatible with the present experimental bounds only if the scale of new physics is of order $50-100$ TeV. In this scenario the two-loop contributions from top partners are clearly subdominant. Due to the extremely strong bounds, however, we find the naive "anarchic partial compositeness" scenario too fine-tuned to be considered as a fully satisfactory set-up.

Models featuring flavor symmetries can significantly help in reducing the experimental constraints. Several scenarios based on $U(3)$ [238] or $U(2)$ [239] symmetries in the quark sector have been proposed. In these cases leading contributions to flavor-violating and CP-violating observables are reduced and a compositeness scale around *few* TeV is still allowed. The flavor symmetry structure can also be extended to the lepton sector [240], thus keeping under control the one-loop contributions to the electron EDM and $\mu \to e\gamma$ transitions. In these scenarios the two-loop CP-violating effects we consider in this chapter can still be present and can give significant bounds on the mass of the top partners. Notice that additional phenomenological handles are typically present in these models due to the sizable amount of compositeness of the light generation fermions [241–246].

Another appealing flavor scenario, which has been recently proposed in the literature, is based on a departure from the classical partial compositeness paradigm for the light SM fermions [247–250]. In these models only the top quark (or at most the third generation fermions) are assumed to be partially composite objects at the TeV scale, while the Yukawa couplings of the light SM fermions are generated by a dynamical mechanism at much higher energy scales. This construction leads to an effective minimal flavor violation structure and efficiently reduces all flavor-violating and CP-violating effects, most noticeably in the lepton sector [250]. The bounds on the masses of the composite states are lowered to the *few* TeV range, thus allowing for natural models with a small amount of fine-tuning. In these scenarios CP-violating effects from top partners are expected to play a major role and can lead to the strongest bounds on the compositeness scale.

The chapter is organized as follows. In section 8.3 we analyze the generation of CP-violating dipole moments induced by light top partners in a simplified set-up with only one composite fermion multiplet. We show that dipole operators are mainly due to running effects coming from effective contact Higgs interactions, and we derive full analytical expressions for the CP-violating effects. Afterwards we discuss the bounds on the top partner masses coming from electron, neutron and mercury EDM measurements and we compare them with the exclusions from direct searches at the LHC and future colliders. In section 8.4 we extend the analysis to non-minimal scenarios, investigating the effects due to the presence of additional light top partner multiplets. Finally we conclude in section 8.5.

8.3 CP VIOLATION FROM TOP PARTNERS

To discuss the general features of CP violation in composite models, and in particular the generation of electron and neutron EDMs, in this section we focus on a simplified model containing only one multiplet of top partners. As we will see, this set-up retains all the main features of more complex models, but allows us to obtain a simpler qualitative and quantitative understanding of CP-violating effects. Non-minimal scenarios with multiple top partners will be discussed in section 8.4.

For definiteness, we restrict our attention to the class of minimal composite Higgs models based on the global symmetry breaking pattern $SO(5) \to SO(4)$ [195].[4] This pattern gives rise to only one Goldstone Higgs doublet and preserves an $SO(3)_c$ custodial symmetry, which helps in keeping under control corrections to the electroweak precision parameters. Motivated by fine-tuning considerations (see references [201, 251]), we assume that the $SU(2)_L$ doublet $q_L = (t_L, b_L)$ is linearly mixed with composite operators in the **14** representation of $SO(5)$. The right-handed top component is instead identified with a fully composite chiral singlet coming from the strongly-coupled dynamics. This scenario is usually dubbed **14+1** model [201, 222].

The possible quantum numbers of the top partners are determined by the unbroken $SO(4)$ symmetry. From the decomposition $\mathbf{14} = \mathbf{9} \oplus \mathbf{4} \oplus \mathbf{1}$, one infers that the partners can fill the nineplet, fourplet or singlet representations of $SO(4)$. As we will see, the main CP-violating effects typically arise form the lightest top partner multiplet. Restricting the analysis to a limited set of partners is thus usually a good approximation. For simplicity

4 In order to accommodate the correct fermion hypercharges an additional $U(1)_X$ global Abelian subgroup is needed (see for instance reference [60]).

in this section we will consider a scenario in which the lightest partners transform in the fourplet representation.

The most general leading-order effective action for the SM quarks and a light composite fourplet ψ_4 can be written in the Callan–Coleman–Wess–Zumino (CCWZ) framework [252, 253] (see reference [60] for an in-depth review of the formalism) as

$$\begin{aligned}\mathscr{L} = {} & i\bar{q}_L \not{D} q_L + i\bar{t}_R \not{D} t_R + i\overline{\psi}_4(\not{D} - i\not{e})\psi_4 - \left(m_4 \overline{\psi}_{4L}\psi_{4R} + \text{h.c.}\right) \\ & + \left(-i\, c_t \overline{\psi}^i_{4R}\gamma^\mu d^i_\mu t_R + \frac{y_{Lt}}{2} f(U^t \overline{q}^{\mathbf{14}}_L U)_{55} t_R + y_{L4} f(U^t \overline{q}^{\mathbf{14}}_L U)_{i5}\psi^i_{4R} + \text{h.c.}\right) . \quad (8.2)\end{aligned}$$

In the above formula $q^{\mathbf{14}}_L$ denotes the embedding of the q_L doublet into the representation **14**, explicitly given by

$$q^{\mathbf{14}}_L = \begin{pmatrix} 0 & 0 & 0 & 0 & -ib_L \\ 0 & 0 & 0 & 0 & -b_L \\ 0 & 0 & 0 & 0 & -it_L \\ 0 & 0 & 0 & 0 & t_L \\ -ib_L & -b_L & -it_L & t_L & 0 \end{pmatrix} . \quad (8.3)$$

The Goldstone Higgs components Π_i, in the real fourplet notation, are encoded in the matrix

$$U = \exp\left[i\frac{\sqrt{2}}{f}\Pi_i \widehat{T}^i\right] , \quad (8.4)$$

where f is the Goldstone decay constant and $\widehat{T}^i$ $(i = 1, \dots, 4)$ are the generators of the $SO(5)/SO(4)$ coset. In the first line of Equation 8.2, D_μ denotes the usual covariant derivative containing the SM gauge fields. The d_μ and e_μ symbols denote the CCWZ operators, defined as

$$U^t[A_\mu + i\partial_\mu]U = e^a_\mu T^a + d^i_\mu \widehat{T}^i , \quad (8.5)$$

with T^a $(a = 1, \dots, 6)$ the $SO(4)$ generators and A_μ the SM gauge fields rewritten in an $SO(5)$ notation.

We can now easily identify possible sources of CP violation. The effective Lagrangian in Equation 8.2 contains four free parameters, namely m_4, y_{Lt}, y_{L4} and c_t. In general all of them are complex. By using chiral rotations, however, three parameters can be made real, so that only one physical complex phase is present in the model. It can be easily seen that m_4 can be always made real by a phase redefinition of ψ_{4L}. This redefinition does not affect the other parameters. The complex phases of the remaining three parameters are instead connected. The elementary-composite mixing parameters y_{Lt} and y_{L4} can be made real through phase rotations of t_R and ψ_{4R}, shifting all the complex phases into c_t. CP-violating effects are thus controlled by the complex phase of the combination $c_t y^*_{Lt} y_{L4}$.

Complex values of the elementary-composite mixing parameters can in general be present even if CP invariance is imposed in the composite sector (so that m_4 and c_t are real). This is the case, for instance if the q_L doublet is coupled with two composite operators in the UV, *e.g.* with an operator $\mathcal{O}_L$ corresponding to the fourplet partners and with another $\mathcal{O}_R$ corresponding to the composite t_R. It is however also possible that a

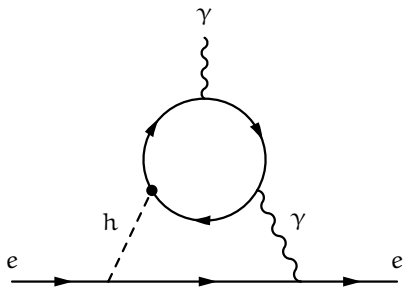

Figure 8.1: Barr–Zee type diagram giving rise to the contribution to the electron EDM.

single dominant mixing with $\mathcal{O}_L$ is present. In this case one expects y_{Lt} and y_{L4} to have the same complex phase, thus avoiding CP-violation from top partners if the composite sector preserves CP.

It is also interesting to notice that, in the set-up we are considering, CP-violation is unavoidably linked to the presence of d_μ-interaction operators. If the term $-i\,c_t\overline{\psi}^i_{4R}\gamma^\mu d^i_\mu t_R$ is not present in the effective Lagrangian, CP is preserved. We will see in subsection 8.4.2, that a similar result is also valid in more generic models with additional top partners and multiple physical complex phases.

8.3.1 *Electron EDM*

The presence of CP-violating interactions of the top and its partners can give rise to sizable contributions to EDMs. In particular an EDM for the electron,

$$\mathscr{L}_{eff} = -d_e\frac{i}{2}\bar{e}\sigma^{\mu\nu}\gamma^5 eA_{\mu\nu}\,, \tag{8.6}$$

arises at two-loop level through Barr–Zee diagrams involving CP-violating Higgs interactions [207] (see Figure 8.1). In this subsection we will investigate in detail how this effect arises and derive explicit expressions to compute it.

To discuss the CP-violating effects it is convenient to choose a field basis in which the physical complex phase is put into c_t, while the remaining parameters are real. In this basis, CP-violating Higgs couplings to the top quark and its partners arise only from the $-i\,c_t\overline{\psi}^i_{4R}\gamma^\mu d^i_\mu t_R$ operator. At leading order in the v/f expansion, where $v \simeq 246\,\text{GeV}$ denotes the Higgs vacuum expectation value, we obtain

$$-i\,c_t\overline{\psi}^i_{4R}\gamma^\mu d^i_\mu t_R + \text{h.c.} \supset i\frac{c_t}{f}\partial_\mu h\left(\overline{\widehat{X}}_{2/3R}\gamma^\mu t_R - \overline{\widehat{T}}_R\gamma^\mu t_R\right) + \text{h.c.}\,, \tag{8.7}$$

where we used the decomposition of the ψ_4 fourplet into components with definite quantum numbers under the SM group

$$\psi_4 = \frac{1}{\sqrt{2}}\begin{pmatrix} -iB + iX_{5/3} \\ -B - X_{5/3} \\ -i\widehat{T} - i\widehat{X}_{2/3} \\ \widehat{T} - \widehat{X}_{2/3} \end{pmatrix}. \tag{8.8}$$

The components of ψ_4 correspond to two $SU(2)_L$ doublets, namely $(\widehat{T}, B)$ and $(X_{5/3}, \widehat{X}_{2/3})$, with hypercharges $1/6$ and $7/6$ respectively.

The main contributions to the electron EDM arise from Barr–Zee diagrams involving a virtual photon. Additional corrections come from diagrams involving a virtual Z boson. These contributions, however, are proportional to the vector coupling of the Z to the charged leptons, which is accidentally small in the SM [207, 210]. They are thus strongly suppressed and can be safely neglected.

Since the photon couplings are flavor-blind and diagonal, the most convenient way to evaluate the Barr–Zee diagrams is to perform the computation in the mass eigenstate basis. In this way each fermionic state gives an independent contribution to the electron EDM. From the explicit form of the couplings in Equation 8.7 it can be seen that only the charge-2/3 fields have CP-violating interactions involving the Higgs, thus these states are the only ones relevant for our computation.

The spectrum of the charge-2/3 states is quite simple. One combination of the $\widetilde{T}$ and $\widetilde{X}_{2/3}$ fields (which we denote by $X_{2/3}$) does not mix with the elementary fields and has a mass $m_{X_{2/3}} = |m_4|$. The orthogonal combination

$$T = \frac{1}{\sqrt{2+\cos(2v/f)+\cos(4v/f)}}\Big[(\cos(v/f)+\cos(2v/f))\,\widehat{T} \tag{8.9}$$

$$+\,((\cos(v/f)-\cos(2v/f))\,\widehat{X}_{2/3}\Big]\,, \tag{8.10}$$

is mixed with the elementary top field and its mass acquires a shift controlled by the y_{L4} parameter, plus an additional subleading correction due to electroweak symmetry breaking,

$$m_T \simeq \sqrt{m_4^2+y_{L4}^2 f^2}\left[1-\frac{5}{4}\frac{y_{L4}^2 f^2}{m_4^2}\frac{v^2}{f^2}+\cdots\right]. \tag{8.11}$$

The top mass is mostly determined by the y_{Lt} parameter and, at leading order in the v/f expansion, reads

$$m_{top}^2 \simeq \frac{1}{2}\frac{m_4^2}{m_4^2+y_{L4}^2 f^2} y_{Lt}^2 v^2\,. \tag{8.12}$$

The full spectrum of the model also includes the $X_{5/3}$ field with electric charge 5/3 and mass $m_{X_{5/3}} = |m_4|$ and the B field with electric charge $-1/3$ and mass $m_B = \sqrt{m_4^2+y_{L4}^2 f^2}$. Notice that the $X_{5/3}$ and $X_{2/3}$ states are always the lightest top partners in the present set-up.

In order to compute the electron EDM, we need to determine the flavor-diagonal CP-violating couplings of the Higgs to the fermion mass eigenstates, in particular the top, the T and the $X_{2/3}$. It turns out that the $X_{2/3}$ field does not have such coupling, as a consequence of the fact that it has no mass mixing with the elementary states. The relevant couplings are thus given by

$$\frac{1}{f}\partial_\mu h\left[c_{top}\bar{t}_R\gamma^\mu t_R + c_T\bar{T}_R\gamma^\mu T_R\right], \tag{8.13}$$

where, at leading order in v/f,

$$c_T = -c_{top} \tag{8.14}$$

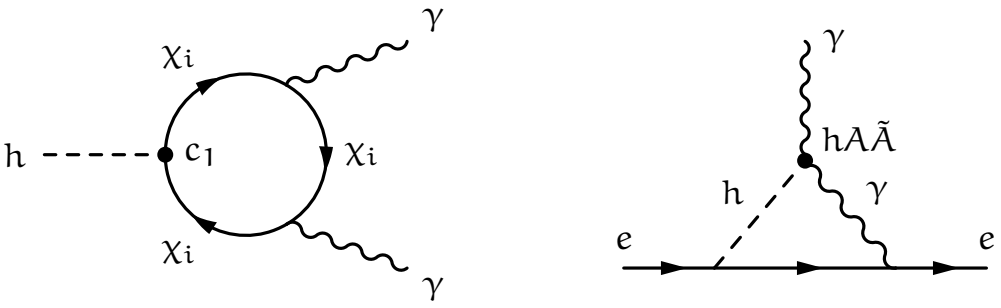

Figure 8.2: Contribution to the electron EDM from running.

$$= \mathrm{Im}\, c_t \, \sin 2\varphi_R$$
$$= \sqrt{2}v \frac{y_{L4} y_{Lt} f}{m_4^2 + y_{L4}^2 f^2} \mathrm{Im}\, c_t = 2\, \mathrm{Im}\, c_t \, \frac{y_{L4} f}{\sqrt{m_4^2 + y_{L4}^2 f^2}} \frac{m_{top}}{m_4} \,.$$

In the above expression φ_R denotes the rotation angle that diagonalizes the mass matrix of the t_R and T_R fields. Notice that the operators in Equation 8.13 are necessarily CP-odd and their coefficients are real.

The result in Equation 8.14 shows that the CP-violating couplings for the top quark and the T field have opposite coefficients. This relation is exact at all orders and is a consequence of the fact that the interactions coming from the d_μ-operator in the Lagrangian (8.2) are strictly off-diagonal. The trace of the coupling matrix must therefore vanish, so that the sum of the coefficients of the diagonal interactions in the mass eigenstate basis is aways zero. This result can be easily generalized to scenarios with multiple top partners and with d_μ interactions that involve both fermion chiralities. In this case the sum of the coefficients of the CP-violating Higgs interactions over all fermions vanishes independently for each coupling chirality, namely $\sum_i c_{iL} = \sum_i c_{iR} = 0$.

Electron EDM as a running effect

Instead of presenting straight away the full result of the computation of the Barr–Zee diagrams, we find more instructive to follow a simplified approach that allows us to highlight a deeper physical origin of the EDMs. The full result will be presented in Figure 8.3.1.

As a first step we focus on a single fermion mass eigenstate with CP-violating interactions analogous to the ones in Equation 8.13. It is straightforward to see that such couplings give rise at one loop to CP-violating effective interactions among the Higgs and two photons, originating from diagrams analogous to the one shown in the left panel of Figure 8.2. Parametrizing the CP-violating Higgs interactions as

$$\mathscr{L} \supset \frac{c_{iL,R}}{f} \partial_\mu h \bar{\chi}_i \gamma^\mu P_{L,R} \chi_i \,, \tag{8.15}$$

where $P_{L,R} = (1 \mp \gamma^5)/2$ are the left and right chirality projectors, we find that the one-loop matrix element squared is given by

$$|\mathcal{M}|^2 = \pm i \frac{N_c}{2\pi^2 s} e^2 Q_{f_i}^2 \, \varepsilon_{\mu\nu\rho\sigma} \, \varepsilon^\nu(\lambda_1, k_1) \, \varepsilon^\mu(\lambda_2, k_2) \, k_1^\rho k_2^\sigma \, \frac{c_{iL,R}}{f} m_i^2 F(4m_i^2/s) \,. \tag{8.16}$$

where the F function is defined as

$$F(\tau) = \begin{cases} \frac{1}{2}\left[\log\frac{1+\sqrt{1-\tau}}{1-\sqrt{1-\tau}} - i\pi\right]^2 & \text{for } \tau < 1 \\ -2\arcsin^2(1/\sqrt{\tau}) & \text{for } \tau \geqslant 1 \end{cases} . \tag{8.17}$$

In Equation 8.16, Q_{f_i} denotes the fermion electric charge (in the present set-up $Q_{f_i} = 2/3$), $k_{1,2}$ and $\varepsilon^{\mu,\nu}(\lambda_{1,2}, k_{1,2})$ are the momenta and the polarization vectors of the photons, while $s = (k_1 + k_2)^2$ coincides with m_h^2 for an on-shell Higgs.

The above result can be matched onto a series of CP-violating effective operators analogous to $(\Box^n H^2) A_{\mu\nu}\widetilde{A}^{\mu\nu}$, where A is the photon field strength and $\widetilde{A}_{\mu\nu} = 1/2\varepsilon_{\mu\nu\rho\sigma}A^{\rho\sigma}$ is the dual field-strength tensor. For this purpose it is convenient to expand $|\mathcal{M}|^2$ as a series in s/m_i^2. In particular, for $4m_i^2 > s$ we find that the first terms in the expansion are

$$f(4m_i^2/s) \simeq -\frac{s}{2m_i^2} - \frac{s^2}{24m_i^4} + \cdots . \tag{8.18}$$

The leading term matches onto the effective operator

$$\mp\frac{e^2 N_c Q_{f_i}^2}{16v\pi^2}\frac{c_{iL,R}}{f} H^2 A_{\mu\nu}\widetilde{A}^{\mu\nu} , \tag{8.19}$$

while the second term in the series corresponds to an effective operator involving two additional derivatives.

At the one-loop level, the $H^2 F_{\mu\nu}\widetilde{F}^{\mu\nu}$ effective operator gives rise to a logarithmically divergent diagram (see right panel of Figure 8.2) that induces a running for the electron EDM operator. The divergence, and thus the running, is eventually regulated by the Higgs mass m_h. The effective operator in Equation 8.19 leads to the contribution

$$\frac{d_e}{e} = \mp\frac{N_c}{64\pi^4} e^2 Q_{f_i}^2 \frac{y_e}{\sqrt{2}}\frac{c_{iL,R}}{f}\log\frac{m_i^2}{m_h^2} , \tag{8.20}$$

where y_e denotes the electron Yukawa coupling.

To find the full contribution to d_e in our simplified **14 + 1** model, we need to sum over the contributions of the T resonance and of the top. In this way we find the leading logarithmically-enhanced contribution to the electron EDM

$$\frac{d_e}{e} = -\frac{e^2}{48\pi^4}\frac{y_e}{\sqrt{2}}\frac{c_T}{f}\log\frac{m_T^2}{m_{top}^2} . \tag{8.21}$$

We will see in Figure 8.3.1 that this is the dominant contribution to the electron EDM, and additional threshold effects are subleading.

A few comments are in order. Although the result in Equation 8.21 is logarithmically enhanced for large m_T, its overall coefficient c_T is inversely proportional to the top partner mass (see Equation 8.14). The overall effect is thus dominated by the contributions coming from the lightest top partners and is largely insensitive to the UV details of the theory.

It is also interesting to notice that the argument of the logarithm is given by the ratio of the T resonance mass and the top mass, whereas the Higgs mass that appeared in Equation 8.20 is not present in the final result. This can be understood by comparing the contributions of the T and top loops to the electron EDM running. As schematically

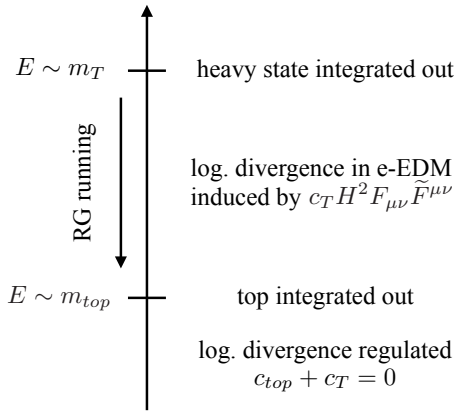

Figure 8.3: Schematic cartoon explaining the generation of an electron EDM as a two-loop running effect due to the top partners.

shown in Figure 8.3, at the m_T scale a contribution to the $H^2 A_{\mu\nu}\widetilde{A}^{\mu\nu}$ effective operator is generated, giving rise to a running for the electron EDM. A second contribution, exactly opposite to the first one, is then generated at the top mass scale, stopping the running. The exact compensation of the T and top contributions is a consequence of the relation $c_T = -c_{top}$.

This feature is not a peculiarity of our simple set-up, but is quite generic. Since the sum of all the CP violating coefficients $c_{iL,R}$ vanishes, the total contributions to the effective operator $H^2 A_{\mu\nu}\widetilde{A}^{\mu\nu}$ sum up to zero and the running effects in the electron EDM are always regulated at the top mass scale. This result has an interesting consequence for Higgs physics, since it forbids sizable CP-violating contributions to the Higgs decay into a photon pair. Effects of this type can only come from higher-dimension operators like $(\Box^n H^2) A_{\mu\nu}\widetilde{A}^{\mu\nu}$, and are necessarily suppressed by additional factors $(m_h^2/m_i^2)^n$. The contributions from heavy top partners are thus typically negligible, while relevant corrections can only come from the top quark.

The full result

We can now present the full computation of the top partners contribution to the electron EDM. For this purpose it is convenient to rewrite the CP-violating Higgs interactions in an equivalent form. Integrating by parts and using the equations of motion for the fermions (or equivalently by a suitable field redefinition), we can rewrite the interactions arising from the d_μ operators as CP-odd Yukawa couplings

$$\frac{c_{iL,R}}{f}\partial_\mu h \overline{\chi}_i \gamma^\mu P_{L,R}\chi_i \to \pm i\frac{c_{iL,R}}{f} m_i\, h\, \overline{\chi}_i \gamma^5 \chi_i\,. \tag{8.22}$$

The full two-loop Barr–Zee diagram involving CP-odd top Yukawa's has been computed in references [207, 210, 254]. Using these results we find that the full two-loop contribution to the electron EDM for a generic set of fermionic resonances is given by

$$\frac{d_e}{e} = 4\frac{N_c}{f}\frac{\alpha}{(4\pi)^3}\frac{y_e}{\sqrt{2}}\sum_i Q_{f_i}^2 (c_{iR} - c_{iL}) f_1(x_i)\,, \tag{8.23}$$

where $x_i = m_i^2/m_h^2$ and the f_1 function is given by

$$f_1(x) = \frac{2x}{\sqrt{1-4x}}\left[\mathrm{Li}_2\left(1 - \frac{1-\sqrt{1-4x}}{2x}\right) - \mathrm{Li}_2\left(1 - \frac{1+\sqrt{1-4x}}{2x}\right)\right], \tag{8.24}$$

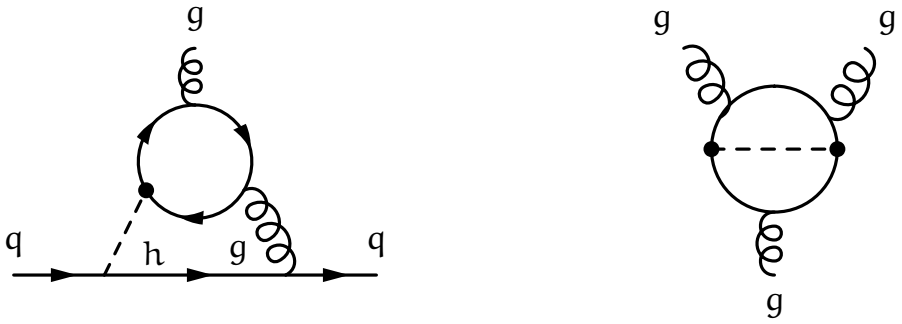

Figure 8.4: Two-loop diagrams giving rise to a cromoelectic dipole moment for the light quarks (left) and to the Weinberg operator (right).

with Li_2 denoting the usual dilogarithm $\mathrm{Li}_2(x) = -\int_0^x du \frac{1}{u}\log(1-u)$.

To make contact with the result obtained in the previous section, we can expand the $f_1(x)$ function for large x (i.e. large fermion masses $m_i \gg m_h$), obtaining

$$\sum_i (c_{iR} - c_{iL}) f_1(x_i) = \sum_i (c_{iR} - c_{iL}) \left[\log x_i + \frac{1}{x_i}\left(\frac{5}{18} + \frac{1}{6}\log x_i\right) + \cdots\right], \tag{8.25}$$

where we used $\sum_i c_{iR} = \sum_i c_{iL} = 0$. We can see that the leading logarithmic term exactly matches the result in Equation 8.20. As expected, the subleading terms are suppressed by powers of m_h^2/m_i^2 and would match the contributions from higher-derivatives effective operators. It is interesting to notice that the subleading terms are also further suppressed by accidentally small numerical coefficients, and are almost negligible already for the top contributions.

8.3.2 *CP-violating effects for the light quarks*

The anomalous top and top partner couplings with the Higgs give also rise to additional CP-violating effects. The main ones are electric and chromoelectric dipole moments for the light quarks and a contribution to the gluonic Weinberg operator [209]. The light quark EDMs arise through two-loop diagrams similar to the one giving rise to the electron EDM (see Figure 8.1), but with the electron line replaced by a quark line. The chromoelectric dipole moments (CEDMs) arise instead from Barr–Zee-type diagrams involving gluons, as shown in the left panel of Figure 8.4. Finally the Weinberg operator is generated by two-loop diagrams of the type shown in the right panel of Figure 8.4. Notice that the Weinberg operator arises from diagrams that involve only the couplings of the Higgs to the top and top partners, hence it is independent of the light quark Yukawa's.

The dipole moments of the light quarks and the Weinberg operator can be parametrized through the following effective Lagrangian

$$\mathscr{L}_{\mathrm{eff}} = -d_q \frac{i}{2}\bar{q}\sigma^{\mu\nu}\gamma^5 q A_{\mu\nu} - \tilde{d}_q \frac{ig_s}{2}\bar{q}\sigma^{\mu\nu}T^a\gamma^5 q G^a_{\mu\nu} - w\frac{1}{3}f^{abc}G^a_{\mu\sigma}G^{b,\sigma}_{\nu}\widetilde{G}^{c,\mu\nu}, \tag{8.26}$$

where $q = u, d$ denote the first generation quarks, $\widetilde{G}^{a,\mu\nu} = \frac{1}{2}\varepsilon^{\mu\nu\rho\sigma}G^a_{\rho\sigma}$ is the dual QCD field-strength tensor and T^a are the color generators, normalized as $\mathrm{Tr}[T^a, T^b] = \delta_{ab}/2$.

The quark EDMs and CEDMs can be straightforwardly computed as we did in the previous subsection for the electron EDM. The full results are given by

$$d_q = -4Q_q \frac{N_c}{f} e \frac{\alpha}{(4\pi)^3}\frac{y_q}{\sqrt{2}}\sum_i Q^2_{f_i}(c_{iR} - c_{iL}) f_1(x_i), \tag{8.27}$$

$$\widetilde{d}_q = -\frac{2}{f}\frac{\alpha_s}{(4\pi)^3}\frac{y_q}{\sqrt{2}}\sum_i (c_{iR} - c_{iL}) f_1(x_i)\,, \tag{8.28}$$

where y_q denote the light quark Yukawa couplings.

Let us now consider the Weinberg operator. The structure of the two-loop diagram contributing to this operator makes it sensitive to a larger set of CP-violating sources. Differently from the Barr–Zee-type contributions, the diagrams giving rise to the Weinberg operator involve a fermion loop with two insertions of Higgs couplings. As a consequence they receive contributions not only from the diagonal Higgs interactions, but also from the off-diagonal couplings involving two different fermion mass eigenstates [255].

Three sets of diagrams give rise to contributions to the Weinberg operator. The first set includes diagrams involving a CP-even Yukawa coupling and a CP-odd derivative Higgs interaction coming from the d_μ operator. As we already mentioned, these contributions can also come from fermion loops involving two different fermionic mass eigenstates. In fact, in generic composite Higgs theories, including the simplified set-up considered in this section, the Higgs couplings to the top and top partners also have off-diagonal terms. This is true both for the Yukawa couplings and for the interactions coming from the d_μ operator.

The second class of contributions comes from diagrams involving two Yukawa couplings. In a large class of models the diagonal Yukawa couplings are always CP-even, in such case the contributions to the Weinberg operator can only come from diagrams involving two off-diagonal Higgs interactions.

Diagrams in the third class involve two d_μ derivative Higgs interactions. Since diagonal couplings of this type are necessarily CP-odd, the only contributions of this kind to the Weinberg operator come from the off-diagonal Higgs interactions. Such interactions can have both a CP-even and a CP-odd component.

Notice that, in the model we are considering in this section, only the first class of contributions is present, while diagrams involving two Yukawa couplings or two d_μ interactions do not give rise to CP-violating effects. The absence of contributions induced only by the Yukawa couplings is a consequence of the fact that, through a field redefinition, all complex phases can be removed from the mass parameters and from the mixings between the composite resonances and the elementary states. In this basis the only CP-violating vertices come from the d_μ interactions. Diagrams involving only d_μ couplings are instead absent since in our simplified set-up with only one light multiplet all these interactions have the same complex phase, which cancels out in the final result. We will discuss this in detail in the following.

The contribution to the Weinberg operator coming from a set of fermions with Yukawa couplings of the form

$$\mathcal{L} = -\frac{1}{\sqrt{2}}\sum_{i,j}\overline{\psi}_i\left[y_{ij} + i\widetilde{y}_{ij}\gamma^5\right]\psi_j h\,, \tag{8.29}$$

is given by [255]

$$w = \frac{g_s^3}{4(4\pi)^4}\sum_{i,j}\frac{\mathrm{Re}[y_{ij}\widetilde{y}^*_{ij}]}{m_i m_j} f_3(x_i, x_j)\,, \tag{8.30}$$

where the function f_3 is defined as

$$f_3(x_i, x_j) = 2x_i x_j \int_0^1 dv \int_0^1 du \frac{u^3 v^3 (1-v)}{[x_i u v(1-v) + x_j v(1-u) + (1-v)(1-u)]^2} + (x_i \leftrightarrow x_j)\,.$$

(8.31)

This result can be straightforwardly adapted to our set-up by rewriting the d_μ interactions as Yukawa couplings (see Equation 8.22)

$$\frac{1}{f}\partial_\mu h \sum_{i,j} c_{ijL,R}\bar{\chi}_i\gamma^\mu P_{L,R}\chi_j \to \frac{1}{f}h\sum_{i,j} i c_{ijL,R} m_j \bar{\chi}_{iL,R}\chi_{jR,L} + \text{h. c.}\,, \tag{8.32}$$

corresponding to the following contributions to y_{ij} and $\widetilde{y}_{ij}$

$$\Delta y_{ij} = i\frac{m_i - m_j}{\sqrt{2}f}c_{ijL,R}\,, \qquad \Delta\widetilde{y}_{ij} = \mp\frac{m_i + m_j}{\sqrt{2}f}c_{ijL,R}\,. \tag{8.33}$$

This formula shows that, if d_μ operators involving only left- or right-handed fermions are present, Δy_{ij} and $\Delta\widetilde{y}_{ij}$ always have the same complex phase. In this case, the product of two d_μ-symbol vertices $\Delta y_{ij}\Delta\widetilde{y}^*_{ij}$ appearing in Equation 8.30 is real and does not lead to CP-violating effects. This explicitly proves that diagrams with two d_μ interactions do not contribute to the Weinberg operator in the **14 +1** set-up we are considering in this section.

The contribution to the Weinberg operator in Equation 8.30 can be conveniently rewritten by using a simple approximation for the f_3 function. If $x_{i,j} \gg 1$ the $f_3(x_i, x_j)$ function is well approximated by $f_3 \simeq 1 - 1/3\bar{x}$, where $\bar{x}$ is the largest between x_i and x_j. For practical purposes, if one of the resonances in the loop has a mass $m \gtrsim 500\,\text{GeV}$, one can safely use the approximation $f_3 = 1$. The only case in which this estimate is not fully accurate is for loops involving only the top quark, in which case $f_3(x_t, x_t) \simeq 0.88$. Also in this case, however, the approximation $f_3 = 1$ is valid up to $\sim 10\%$ deviations.

By using straightforward algebraic manipulations, it can be shown that

$$\begin{aligned} w &\simeq \frac{g_s^3}{4(4\pi)^4}\sum_{i,j}\frac{\text{Re}[y_{ij}\widetilde{y}^*_{ij}]}{m_i m_j} \\ &= -\frac{g_s^3}{4(4\pi)^4}\text{Re}\,\text{Tr}\left[\frac{2}{f}\Upsilon\left(c_R M^{-1} - M^{-1}c_L\right) - \frac{2}{f^2}i\,c_R M^{-1}c_L M + i\,\Upsilon M^{-1}\Upsilon M^{-1}\right], \end{aligned} \tag{8.34}$$

where Υ_{ij} denotes the matrix of Yukawa couplings, defined as

$$\sum_{i,j} h\Upsilon_{ij}\bar{\chi}_{iL}\chi_{jR} + \text{h. c.}\,, \tag{8.35}$$

and M is the fermion mass matrix, defined as $\sum_{ij} M_{ij}\bar{\chi}_{iL}\chi_{jR} + \text{h. c.}$.

Neutron and Mercury EDM

The quark electric and chromoelectric dipole operators and the Weinberg operator generate contributions to the neutron EDM d_n.[5] The explicit expression is given by [210]

$$\frac{d_n}{e} \simeq (1.0 \pm 0.5)\left[0.63\left(\frac{d_d}{e} - 0.25\,\frac{d_u}{e}\right) + 1.1\left(\widetilde{d}_d + 0.5\,\widetilde{d}_u\right) + 10^{-2}\,\text{GeV}\,w\right], \tag{8.36}$$

5 Additional contributions to the neutron EDM can be generated by a top dipole moment through running effects. If the top dipole is generated at loop level, as expected in many CH scenarios, these corrections are however quite small and well below the current experimental bounds [60].

where we took into account running effects from the top mass scale to the typical hadronic scale $\mu_H \simeq 1\,GeV$.[6]

The CEDMs of the light quarks give also rise to EDMs for the diamagnetic atoms. At present the most stringent experimental constraints come from the limits on the EDM of mercury (Hg). The latter can be estimated as [210]

$$\frac{d_{Hg}}{e} \simeq -0.9 \cdot 10^{-4} \left(4^{+8}_{-2}\right) \left(\tilde{d}_u - \tilde{d}_d - 0.76 \cdot 10^{-3}\,GeV\, w\right) . \tag{8.37}$$

It is interesting to compare the size of the various contributions to the neutron and mercury EDMs. From Equation 8.27 and (8.28) we can see that

$$d_q = \frac{8}{3} e Q_q \frac{\alpha}{\alpha_s} \tilde{d}_q \simeq 0.06\, Q_q\, \tilde{d}_q\,, \tag{8.38}$$

where we set $Q_{f_i} = 2/3$, as in the model we consider in this section. The contributions to d_n coming from light quark EDMs is therefore suppressed by almost one order of magnitude with respect to the one from the quark CEDMs.

Let us now consider the contributions from the Weinberg operator. Due to the different structure of the top partner contributions, the effects due to the Weinberg operator and the ones from the Barr–Zee diagrams can not be exactly compared as we did for the electric and chromoelectric moments. To get an idea of the relative importance we can however use a rough approximation, namely

$$w \sim \frac{g_s^3}{(4\pi^4)} \frac{1}{f^2} \mathrm{Im}\, c_t \sim \frac{g_s}{4 m_q} \left(\frac{m_T}{f}\right)^2 \frac{1}{\log m_T/m_t} \tilde{d}_q \sim 40\,GeV^{-1} \left(\frac{m_T}{f}\right)^2 \frac{1}{\log m_T/m_t} \tilde{d}_q\,. \tag{8.39}$$

This estimate is quite close to the exact result (Equation 8.49), as we will see in subsection 8.3.3. An interesting feature of the contributions to the Weinberg operator is the fact that they are controlled by the compositeness scale f, and are nearly independent of the top partner masses. As a consequence their relative importance with respect to the quark dipole contributions grows for large m_T/f.

Using the estimate in Equation 8.39 we find that, for $m_T \sim f$, the w contributions to the mercury EDM are suppressed by almost two orders of magnitude with respect to the quark CEDMs ones. We thus expect the Weinberg operator to play a role for d_{Hg} only for sizable values of the ratio m_T/f, namely $m_T/f \gtrsim 10$. On general ground one expects $m_T \sim g_* f$, with g_* the typical composite sector coupling. The contributions from the Weinberg operator to d_{Hg} are thus relevant only for new dynamics that are close to be fully strongly-coupled.

The situation is significantly different for the neutron EDM. In this case the contributions from the Weinberg operator are suppressed by a factor $\sim 1/4$ if the top partners are light ($m_T/f = 1$). For heavier partner masses, $m_T/f \gtrsim 3$, the bounds coming from the Weinberg operator can thus become competitive with the ones from the quark CEDMs. We will discuss this point more quantitatively in the following.

6 For simplicity we neglected additional running between the resonances masses and the top mass.

8.3.3 *Experimental bounds*

We can now discuss the constraints coming from the experimental data. The present searches for electron [215, 216], neutron [24, 218] and mercury [219] EDMs give null results and can thus be used to extract the following constraints

$$|d_e| < 9.4 \cdot 10^{-29}\, e\,\mathrm{cm} \qquad \text{at } 90\%\ \mathrm{CL}\,, \tag{8.40}$$

$$|d_n| < 2.9 \cdot 10^{-26}\, e\,\mathrm{cm} \qquad \text{at } 95\%\ \mathrm{CL}\,, \tag{8.41}$$

$$\left|d_{Hg}\right| < 7.4 \cdot 10^{-30}\, e\,\mathrm{cm} \qquad \text{at } 95\%\ \mathrm{CL}\,. \tag{8.42}$$

Near-future experiments are expected to significantly improve the bounds on the neutron and electron EDMs. The neutron EDM bounds could be improved up to $|d_n| < 10^{-27}\, e\,\mathrm{cm}$ [220]. On the other hand, the ACME collaboration estimates the future sensitivity on the electron EDM to be [221]

$$|d_e| \lesssim 0.5 \cdot 10^{-29}\, e\,\mathrm{cm} \qquad (\text{ACME II}) \tag{8.43}$$

and

$$|d_e| \lesssim 0.3 \cdot 10^{-30}\, e\,\mathrm{cm} \qquad (\text{ACME III}) \tag{8.44}$$

that correspond to an improvement of the current constraints by more than two orders of magnitude.[7]

It is interesting to compare the impact of the different bounds on the parameter space of composite Higgs models. An easy way to perform the comparison is to focus on the constraints on the EDM of the electron and on the EDMs and CEDMs of the light quarks. As can be seen from Equations (8.23), (8.27) and (8.28) in the **14 +1** model with a light fourplet all these effects depend on the quantity[8]

$$\widetilde{\gamma} \equiv \frac{v}{f} \sum_i (c_{iR} - c_{iL}) f_1(x_i)\,. \tag{8.45}$$

The bounds on $\widetilde{\gamma}$ can thus be used to compare the strength of the various experimental searches. For simplicity we will neglect corrections coming from the Weinberg operator, and we will assume that the electron and light quark Yukawa's coincide with the SM ones.

The constraints from the electron EDM measurements read

$$\begin{aligned} &|\widetilde{\gamma}| < 0.029 && \text{current bound}\,,\\ &|\widetilde{\gamma}| \lesssim 1.5 \times 10^{-3} && \text{ACME II}\,,\\ &|\widetilde{\gamma}| \lesssim 1.0 \times 10^{-4} && \text{ACME III}\,. \end{aligned} \tag{8.46}$$

The bounds from the neutron EDM measurement are

$$\begin{aligned} &|\widetilde{\gamma}| < [0.08, 0.23] && \text{current bound}\,,\\ &|\widetilde{\gamma}| \lesssim [0.003, 0.01] && \text{improved bound}\,. \end{aligned} \tag{8.47}$$

7 An additional bound on the electron EDM has been reported in reference [217], $|d_e| < 1.3 \cdot 10^{-28}\, e\,\mathrm{cm}$ at 90% CL, which is slightly weaker than the current ACME constraint. This experiment is currently limited by statistics and in the future is expected to allow for a precision $\sim 10^{-30}\, e\,\mathrm{cm}$.

8 As we discussed before, in the **14 + 1** with a light fourplet only charge-2/3 partners contribute to Barr–Zee diagrams, thus $Q_{f_i} = 2/3$ in Equations (8.23) and (8.27).

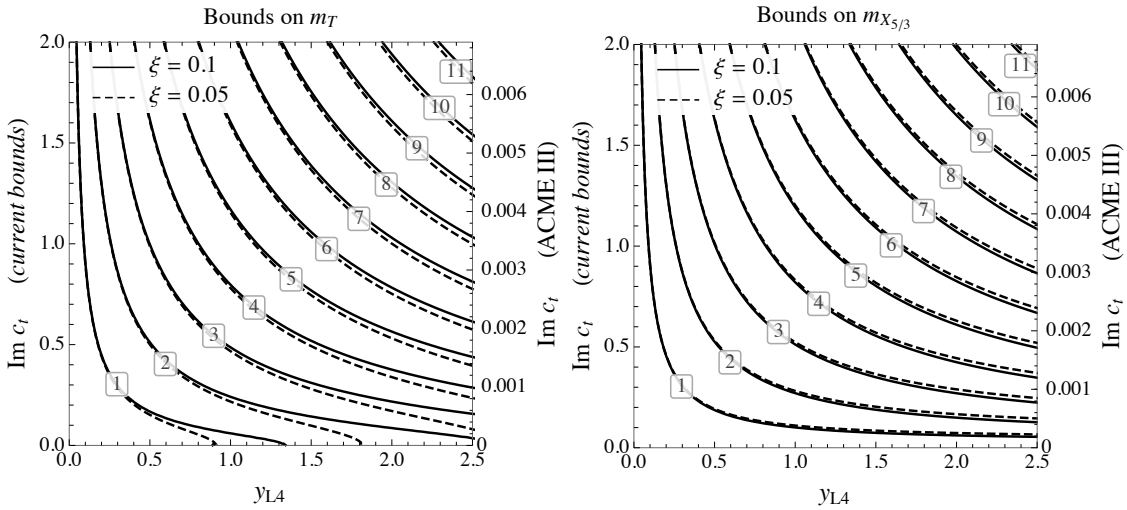

Figure 8.5: Bounds on the mass of the T (left panel) and $X_{5/3}$ (right panel) states derived from the constraints on the electron EDM. The bounds are expressed in TeV and are presented as a function of the elementary–composite mixing y_{L4} and of the imaginary part of c_t. The labels on the left vertical axis corresponds to the present bounds, while the ones on the right axis correspond to the ACME III projections. The solid and dashed lines correspond to the choice $\xi = 0.1$ and $\xi = 0.05$ respectively.

Finally the bounds from the mercury EDM are

$$|\widetilde{\gamma}| < [0.06, 0.4]\,. \tag{8.48}$$

Notice that for the neutron and mercury EDM bounds we took into account the error range in the estimates in Equations (8.36) and (8.37).

From the above results we find that, at present, the electron EDM measurements give the strongest constraints. The future improvements on the neutron EDM constraints could strengthen the present electron EDM bounds by a factor of order 3. These constraints, however, will be easily surpassed by the new electron EDM experiments, which can improve the current bounds by a factor of ~ 20 in the near future (ACME II) and by more than two orders of magnitude afterwards (ACME III).

The constraints on the top partner masses in the **14 + 1** scenario are shown in Figure 8.5 as a function of the y_{L4} mixing parameter and of the imaginary part of the c_t coupling. The value of the y_{Lt} mixing has been fixed by requiring that the correct top mass is reproduced. In the left panel we show the bounds on the mass of the T partner, while in the right panel we show the bounds on the mass of the lightest top partner in the multiplet, namely the $X_{5/3}$ state. The solid and dashed lines show the bounds for $\xi \equiv v^2/f^2 = 0.1$ and $\xi = 0.05$ respectively, which roughly correspond to the present constraints on ξ coming from Higgs couplings measurements [256] and to the projected bounds for high-luminosity LHC [70, 257, 258]. The impact of ξ on the bounds is however quite mild. Notice that the T mass, even without any constraint from the electron EDM (i.e. for $\mathrm{Im}c_t = 0$) is still bounded from below. This is due to the fact that, even setting $m_4 = m_{X_{5/3}} = 0$, m_T still gets a contribution from the mixing with the elementary states, which translates into $m_T = |y_{L4} f|$.

Using simple power counting considerations [59, 222] we can estimate the typical size of the y_{L4} and c_t parameters to be $y_{L4} \sim y_{Lt} \sim y_{top}$ and $c_t \sim 1$. Barring accidental suppressions in the complex CP-violating phase of c_t, we get that the present constraints

from the electron EDM correspond to bounds on the top partner masses in the range $2-4\,\text{TeV}$. The ACME II experiment will extend the exclusion range to masses of order $10-20\,\text{TeV}$, whereas masses in the range $50-100\,\text{TeV}$ will be tested by ACME III.

Another useful way to quantify the strength of the electron EDM bounds is to fix the mass of the top partners and derive the amount of suppression needed in the complex phase of c_t to pass the experimental bounds. Choosing masses of order $3\,\text{TeV}$, roughly of the order of the possible direct bounds from high-luminosity LHC, we can see that the present constraints still allow for order one complex phases. ACME II will lower the bound to $\sim 5\%$, while ACME III will be able to constrain CP-violating phases significantly below the 1% level.

It is important to stress that the bounds coming from the electron and light quark EDMs crucially depend on the assumption that the light fermion Yukawa couplings are not (strongly) modified with respect to the SM predictions. If the light fermion masses are generated through partial compositeness, this assumption is typically satisfied. One indeed expects all Yukawa couplings to deviate from their SM values only by corrections of order ξ. The current bounds $\xi \lesssim 0.1$ guarantee that the Yukawa couplings agree within $\sim 10\%$ with their SM values.

It is however conceivable that substantial modifications of the partial compositeness structure could exist for the light fermions. In such a case large deviations of the Yukawa couplings could be present. Strong suppression in some or all the light fermion Yukawa's would modify the relative importance of the constraints coming from the experimental measurements. As we discussed before, the contributions to the electron EDM are controlled by the electron Yukawa, whereas the light quark EDM and CEDM are proportional to the u and d Yukawa's. The experimental constraints on the electron and neutron EDM thus carry complementary information and can become more or less relevant in different contexts.

It is interesting to notice that the contributions to the Weinberg operator are independent of the light fermion Yukawa's and only depend on the top and top partners couplings to the Higgs. They can thus be used to extract bounds that are in principle more model independent than the ones coming from the electron and light quark EDMs. Using the approximation in Equation 8.34, we find that the contribution to the Weinberg operator in the **14 + 1** model with a light fourplet is

$$w \simeq -\frac{g_s^3}{2(4\pi)^4 f}\text{Re}\,\text{Tr}[\Upsilon c_R M^{-1}] \tag{8.49}$$

$$= \frac{2g_s^3}{(4\pi)^4}\frac{\sqrt{2}\,y_{L4}}{f^2 y_{Lt}}\text{Im}\,c_t \tag{8.50}$$

$$\simeq \frac{2g_s^3}{(4\pi)^4}\frac{y_{L4}m_4}{\sqrt{m_4^2+y_{L4}^2 f^2}}\frac{v}{f^2\,m_{top}}\text{Im}\,c_t\,. \tag{8.51}$$

An interesting aspect of this formula is the fact that it depends on the top partners masses only indirectly. The dependence on m_4 only appears when we rewrite the y_{Lt} parameter as a function of the top mass. This feature indicates that the contributions to the Weinberg operator are not controlled by the lightest resonances, as was the case for the dipole operators, but instead can receive sizable contributions from the UV dynamics. Of course, since the IR and UV contributions are in general independent, we do not expect them to cancel each other. The result in Equation 8.49 can thus be used as a lower estimate to obtain constraints on the parameter space of the model.

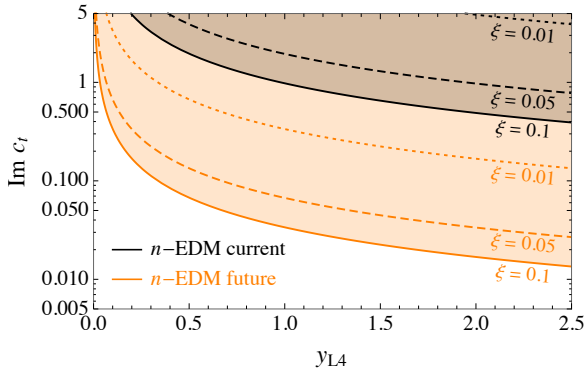

Figure 8.6: Bounds on the CP-violating part of the c_t coupling as a function of the y_{L4} mixing derived from the current and projected constraints on the neutron EDM. The results are derived by using the constraints on the Weinberg operator

In Figure 8.6 we show the bounds in the $(\mathrm{Im}\, c_t, y_{L4})$ plane coming from the current (black lines) and projected (orange lines) neutron EDM measurements for various values of ξ ($\xi = 0.1, 0.05, 0.01$). These results are obtained by taking into account only the contributions from the Weinberg operator in (Equation 8.36) (we use the lower estimate of the effect to derive the numerical results), and neglecting the ones from the quark dipole operators. We can see that, for $\xi = 0.1$, the current neutron EDM constraints typically forbid values of Im c_t larger than ~ 1. These bounds are competitive with the current ones from the electron EDM (see Figure 8.5) if the top partner masses are $m_{X_{5/3}} \gtrsim 5 - 6\,\mathrm{TeV}$, whereas they are weaker for lighter resonances. Notice that the bound from the Weinberg operator roughly scales like f^{-2}, so it quickly degrades for smaller values of ξ. The bound from the electron EDM has instead a much milder dependence on ξ.

Future improvements on the neutron EDM measurements (orange lines in Figure 8.6) could strengthen the bounds by more than one order of magnitude. The improved bounds, for $\xi = 0.1$, would be comparable to the present ones from the electron EDM for $m_{X_{5/3}} \simeq 1\,\mathrm{TeV}$. Notice however that the projected improvement in the electron EDM constraints (ACME III) would make the Weinberg operator bounds relevant only for very heavy top partners ($M_{X_{5/3}} \gtrsim 20\,\mathrm{TeV}$).

8.3.4 *Comparison with direct top partner searches*

It is also interesting to compare the bounds from CP-violating effects with the direct searches for top partners. We start the discussion by considering the constraints coming from the LHC. The strongest bounds on the mass of a light fourplet come from searches for the exotic charge-5/3 top partner, the $X_{5/3}$, which decays exclusively into Wt. So far the experimental searches focussed mainly on top partners pair production. The strongest bounds come from searches in the lepton plus jets final state, whose present constraints are $m_{X_{5/3}} > 1250\,\mathrm{GeV}$ (ATLAS collaboration [202]) and $m_{X_{5/3}} > 1320\,\mathrm{GeV}$ (CMS collaboration [203]).

Additional bounds come from searches in the same-sign dilepton final state, whose sensitivity is only slightly lower than the one in the lepton plus jets channel. The present bounds for pair-produced top partners are $m_{X_{5/3}} > 1160\,\mathrm{GeV}$ from the CMS analysis

in reference [259] and $m_{X_{5/3}} > 990\,GeV$ from the ATLAS analysis in reference [260].[9] Interestingly, searches for charge-5/3 resonances in same-sign dileptons are sensitive not only to pair production but also to single production. This aspect was investigated in reference [261] for the 8 TeV LHC searches. The same-sign dilepton search was found to be sensitive to single production with relatively high efficiencies, namely ~ 50% of the pair-production signal efficiency for the ATLAS search and ~ 10% for the CMS one. The 13 TeV searches are analogous to the 8 TeV ones, so one expects similar efficiencies to apply. The sensitivity to single production can significantly enhance the bounds for large values of c_t. Indeed this coupling controls the $WX_{5/3}t$ vertex [251],

$$g_{WX_{5/3}t_R} = \frac{g}{\sqrt{2}} c_t \frac{v}{f}\,, \tag{8.52}$$

that mediates single production in association with a top quark.[10]

Interestingly, the searches in lepton plus jets and same-sign dilepton final states are sensitive not only to charge-5/3 resonances but also to states with charge $-1/3$ decaying into Wt. The bounds reported in the experimental analyses for resonances with charge $5/3$ and $-1/3$ are quite close, thus signaling similar search efficiencies. A reasonable estimate of the bounds can thus be obtained by just adding the production cross sections for both types of partners. As we discussed before, the fourplet multiplet contains a state with charge $-1/3$, the B, which decays into Wt with a branching ratio close to 100%. If the mass split between the $X_{5/3}$ and B states is below ~ 200 GeV, which requires relatively small value of y_{L4} ($y_{L4} \lesssim 1$ in the case $m_{X_{5/3}} \sim 1-2\,TeV$ and $\xi \simeq 0.1$), the same-sign dilepton signal is enhanced by almost a factor 2, with a significant impact on the exclusion bounds [251, 261].

The direct bounds on the mass of the $X_{5/3}$ resonance from the LHC searches are shown by the shaded green regions in Figure 8.7. The current bounds are shown in the left panel, while the projections for the future LHC runs are in the right panel. For definiteness we set $\xi = 0.1$ (which roughly corresponds on the bound coming from precision electroweak tests [205] and from present Higgs couplings measurements [256]) and $y_{L4} = 1$. We also fix y_{R4} by requiring the top mass to have the correct value.

As we discussed before, the strongest indirect constraints from CP-violating effects come from the electron EDM measurements. The current bounds are shown in the figure by the black lines, while the ACME II projections are given by the orange lines. The bounds are presented for different values of the complex phase of c_t, namely $\sin(\mathrm{Arg}\, c_t) = 1, 0.3, 0.1, 0.03$. One can see that indirect bounds tend to be stronger than the ones from direct searches for larger values of the top partners masses. If the complex phase of c_t is not too small, $\sin(\mathrm{Arg}\, c_t) \gtrsim 0.1$, the current ACME constraints can easily probe resonance masses ~ 2 TeV, which are not tested by the run-2 LHC data. Moreover it can be seen that the additional parameter space region probed by taking into account single production (corresponding to the improved LHC bounds at large c_t) can be also covered by the electron EDM constraints if $\sin(\mathrm{Arg}\, c_t) \gtrsim 0.1$ for current searches and $\sin(\mathrm{Arg}\, c_t) \gtrsim 0.05$ for the high-luminosity LHC and ACME II.

9 The ATLAS analysis is only available for 3.2/fb integrated luminosity at 13 TeV. This explains the significantly lower bound with respect to the CMS analysis, which instead exploits 35.9 fb^{-1} integrated luminosity.

10 Experimental searches for singly-produced heavy quarks decaying into Zt/b [262, 263], ht/b [264, 265] and Wb [266, 267] are also available in the literature. The bounds from these searches on fourplet top partners are however weaker than the ones we derived with the recast of the same-sign dilepton searches.

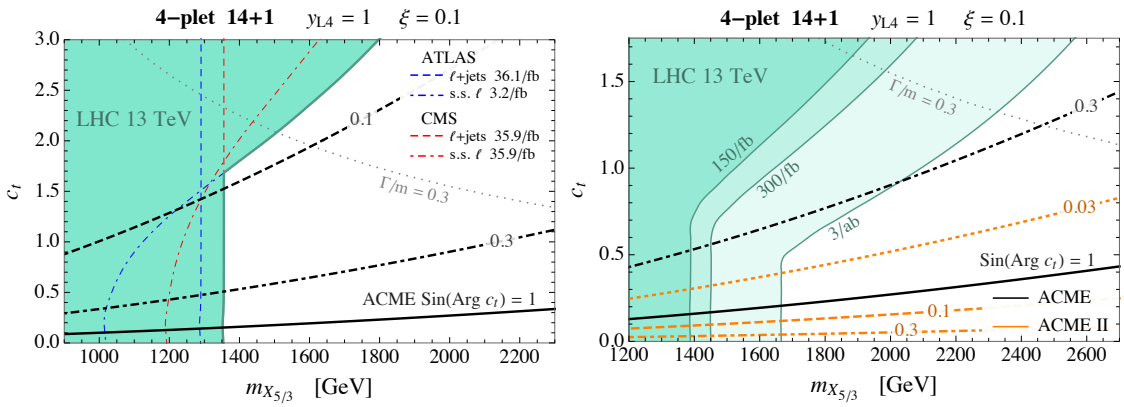

Figure 8.7: Bounds on the c_t coupling as a function of the mass of the $X_{5/3}$ resonance for the scenario with a light fourplet in the **14 +1** model (for the choice $\xi = 0.1$ and $y_{L4} = 1$). The current bounds from the LHC data and from the constraints on the electron EDM are shown in the left panel, whereas the projections for the future LHC runs and the estimate of the future ACME II constraints are shown in the right panel. In the left panel we also show separately the direct bounds from the lepton plus jets (dashed lines) and for the same-sign dilepton analyses (dot-dashed lines) for ATLAS (blue) and CMS (red). The bound from the electron EDM current (black lines) and improved ACME II searches (orange lines) are shown for different choices of the complex phase of c_t ($\sin(\mathrm{Arg}\, c_t) = 1, 0.3, 0.1, 0.03$ for the solid, dashed, dot-dashed and dotted lines respectively). In the region above the dotted gray line the width of the $X_{5/3}$ resonance is above 30% of its mass.

For different values of ξ the results in Figure 8.7 change only mildly. The indirect bounds are nearly unaffected, while the direct searches are modified due to the rescaling of the single production coupling (see Equation 8.52). The dependence of the direct bounds on y_{L4} is also mild, since this parameter only controls the split between the $X_{5/3}$ and B masses. The bound on c_t coming from the electron EDM instead scales roughly linearly with y_{L4} as can be seen from Equations (8.14) and (8.21).

Finally, in Figure 8.8, we compare the estimate for the direct exclusion reach at a future 100 TeV hadron machine (FCC-hh) with the indirect bounds from the estimates of the ACME III sensitivity. In the left panel we set $\xi = 0.05$ which roughly corresponds to the high-luminosity LHC reach, while in the right panel we set $\xi = 0.01$ which is the projected sensitivity at a high-energy linear lepton collider (eg. ILC at 500 GeV center of mass energy with $\sim 500\,\mathrm{fb}^{-1}$ integrated luminosity [258]). As one can see, in the absence of strong suppressions in the complex phase of c_t, the ACME III reach can easily surpass the FCC-hh ones in a large part of the parameter space of the **14 + 1** model.

8.4 NON-MINIMAL MODELS

In order to highlight the main features of CP-violation due to the top partners, in the previous section we focused on a simplified scenario with only one light multiplet. In generic realizations of the composite Higgs idea, however, it is not uncommon to find non-minimal set-ups with multiple light top partners. In the following we will discuss how the results we got in the simplified **14 +1** model are modified in the presence of additional light resonances. In addition we will consider an alternative scenario in which both the left-handed and right-handed top quark components are realized as elementary states.

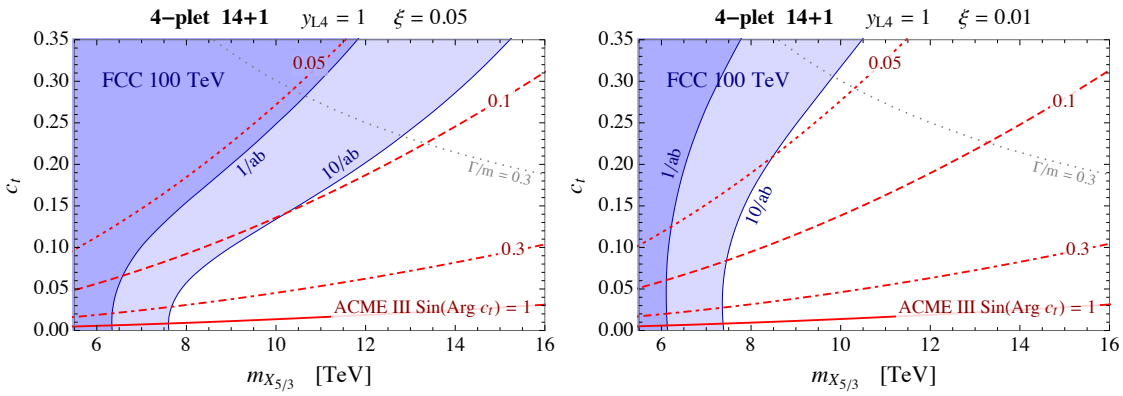

Figure 8.8: Future direct and indirect exclusion bounds on the c_t coupling as a function of the mass of the $X_{5/3}$ resonance for the scenario with a light fourplet in the **14 +1** model (for the choice $y_{L4} = 1$). The left and right panels correspond to $\xi = 0.05$ and $\xi = 0.01$ respectively. The direct bounds from top partners searches at FCC-hh are given by the blue shaded regions (for integrated luminosities $1\,ab^{-1}$ and $10\,ab^{-1}$). The red lines correspond to the indirect exclusions for the estimated ACME III sensitivity.

This set-up can be interpreted as an effective description of the MCHM$_5$ holographic scenario [195].

8.4.1 *The* **14** + **1** *model with a light singlet*

As a first example we consider a more complete version of the **14 + 1** model, including not only a light fourplet, but also a light singlet. The Lagrangian of the model is given by the terms in (8.2) plus the following additional operators involving the singlet ψ_1

$$\begin{aligned}\mathcal{L} =& i\overline{\psi}_1 \not{D}\psi_1 - \left(m_1 \overline{\psi}_{1L}\psi_{1R} + h.c.\right) \\ &+ \left(y_{L1} f (U^t \overline{q}^{14}_L U)_{55}\psi_{1R} - i c_L \overline{\psi}^i_{4L}\gamma^\mu d^i_\mu \psi_{1L} - i c_R \overline{\psi}^i_{4R}\gamma^\mu d^i_\mu \psi_{1R} + h.c.\right) . \end{aligned} \tag{8.53}$$

The above Lagrangian contains four free parameters, that are in general complex. By field redefinitions two parameters can be made real, thus leaving two additional CP-violating sources corresponding to the complex phases of the combinations $c_L m_1 m_4^* y_{L1}^* y_{L4}$ and $c_R y_{L1}^* y_{L4}$. A convenient choice of phases is obtained by making the mass parameter m_1 and the elementary-composite mixing y_{L1} real. This choice makes manifest that CP-violating effects are necessarily related to the d_μ-symbol operators, and are controlled by the c_L and c_R parameters (on top of the c_t parameter we discussed in the previous section).

The mass of the singlet eigenstate $\widetilde{T}$ is

$$m_{\widetilde{T}} \simeq |m_1| \left[1 + \frac{1}{4}\frac{y_{L1}^2 f^2}{m_1^2}\frac{v^2}{f^2} + \cdots\right] . \tag{8.54}$$

while the spectrum of the remaining states coincides with the one described in subsection 8.3.1, apart from modifications arising at higher order in v/f.

The CP-violating Higgs couplings to the top partners are given by

$$-i\, c_{L,R}\overline{\psi}^i_{4L,R}\gamma^\mu d^i_\mu \psi_{1L,R} + h.c. \supset i\frac{c_{L,R}}{f}\partial_\mu h \left(\overline{\widetilde{X}}_{2/3L,R}\gamma^\mu \widetilde{T}_{L,R} - \overline{\widetilde{T}}_{L,R}\gamma^\mu \widetilde{T}_{L,R}\right) + h.c.\,, \tag{8.55}$$

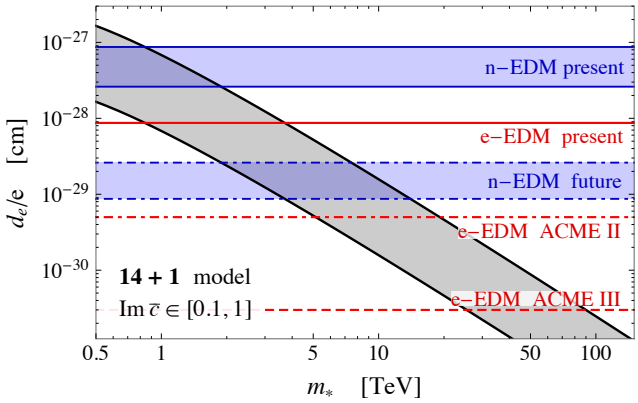

Figure 8.9: Estimate of the bound on the lightest top partner mass in the **14 +1** model with a fourplet and a singlet. The gray band shows the estimate of the corrections to the electron EDM given in (8.58) for $\mathrm{Im}\,\bar{c} \in [0.1, 1]$. The solid red line shows the bound from the present electron EDM measurements, while the dot-dashed and dotted ones show the expected future limits. The blue bands show the constraints from the present and near-future neutron EDM measurements.

where we only included the leading order terms in the v/f expansion. As in the simplified set-up we discussed in the previous section, also in the extended **14+1** model the CP-violating effects arise only from charge 2/3 fields.

In the mass-eigenstate basis the coefficients of the CP-violating interactions that give rise to Barr–Zee-type contributions (see Equation 8.16) read

$$\begin{cases} c_{\mathrm{top,L}} = \sqrt{2}v \dfrac{y_{L1} y_{L4} m_4 f}{m_1 (m_4^2 + y_{L4}^2 f^2)} \mathrm{Im}\, c_L \\ c_{T,L} = \sqrt{2}v \dfrac{y_{L1} y_{L4} m_1 m_4 f}{(m_4^2 + y_{L4}^2 f^2)(m_4^2 + y_{L4}^2 f^2 - m_1^2)} \mathrm{Im}\, c_L \\ c_{\widetilde{T},L} = -\sqrt{2}v \dfrac{y_{L1} y_{L4} m_4 f}{m_1 (m_4^2 + y_{L4}^2 f^2 - m_1^2)} \mathrm{Im}\, c_L \end{cases} \tag{8.56}$$

for the left-handed field interactions and

$$\begin{cases} c_{\mathrm{top,R}} = -\sqrt{2}v \dfrac{y_{L4} y_{Lt} f}{m_4^2 + y_{L4}^2 f^2} \mathrm{Im}\, c_t \\ c_{T,R} = \sqrt{2}v \left[\dfrac{y_{L4} y_{Lt} f}{m_4^2 + y_{L4}^2 f^2} \mathrm{Im}\, c_t - \dfrac{y_{L4} y_{L1} f}{m_4^2 + y_{L4}^2 f^2 - m_1^2} \mathrm{Im}\, c_R \right] \\ c_{\widetilde{T},R} = \sqrt{2}v \dfrac{y_{L4} y_{L1} f}{m_4^2 + y_{L4}^2 f^2 - m_1^2} \mathrm{Im}\, c_R \end{cases} \tag{8.57}$$

for the right-handed ones.

Interestingly, all CP-violating couplings show a similar power-counting scaling, independently of the fact that they originate from a d-symbol operator involving the t_R or involving only top partners. We generically expect $y_{L4} \sim y_{L1} \sim y_{Lt} \sim y_{\mathrm{top}}$, $m_4 \sim m_1 \sim m_*$ and $c_L \sim c_R \sim c_t \sim 1$, so that all the couplings scale like $c \sim v f y_{\mathrm{top}}^2 / m_*^2$. As a consequence the contributions to the Barr–Zee effects coming from the various d-symbol operators will be roughly of the same size. Using these estimates we can easily derive the typical size of the contributions to the electron EDM as a function of the top partners mass scale m_*,

$$\frac{d_e}{e} \sim \frac{e^2}{48\pi^4} \frac{y_e}{\sqrt{2}} \mathrm{Im}\,\bar{c}\, \frac{y_{\mathrm{top}}^2 v}{m_*^2} \log \frac{m_*^2}{m_{\mathrm{top}}^2}\,. \tag{8.58}$$

In the above formula we included a factor $\mathrm{Im}\,\bar{c}$, which encodes the typical size of the CP-violating part of the d-symbol operator couplings. An analogous formula can be straightforwardly derived for the contributions to the quark dipole moments.

In Figure 8.9 we compare the estimate in Equation 8.58 with the present and projected future bounds from measurements of the electron and neutron EDM. To take into account possible accidental suppressions we vary the factor $\mathrm{Im}\,\bar{c}$ in the range $[0.1, 1]$. One can see that the present bounds can roughly test top partner masses of order *few* TeV. The near-future improvements in the electron and neutron EDMs can push the bounds in the range $5 - 10\,\mathrm{TeV}$, while ACME III could test partners with masses of order $40 - 100\,\mathrm{TeV}$. We checked that the estimate in Equation 8.58 is in good agreement with the results obtained through a numerical scan on the parameter space of the model.

8.4.2 *The* **5** + **5** *2-site model*

As a second scenario we consider the 2-site construction presented in references [198, 268] (see also reference [269] for a similar set-up). This model is based on an extended set of global symmetries that ensure the calculability of the Higgs potential. For definiteness we will focus on the scenario in which the q_L and t_R fields are both elementary and are mixed with composite operators transforming in the fundamental representation of $SO(5)$ (we thus dub this set-up the "**5+5**" model). This model can also be interpreted as a "deconstructed" version of the MCHM_5 holographic scenario [195].

The field content of the **5+5** 2-site model contains one set of composite top partners that transform as a fourplet and as a singlet under the unbroken $SO(4)$ symmetry. The effective Lagrangian of the model can be written as

$$\begin{aligned}\mathcal{L} = {} & i\bar{q}_L \not{D} q_L + i\bar{t}_R \not{D} t_R + i\overline{\psi}_4 (\not{D} - i\not{e})\psi_4 + i\overline{\psi}_1 \not{D}\psi_1 - \left(m_4 \overline{\psi}_{4L}\psi_{4R} + m_1 \overline{\psi}_{1L}\psi_{1R} + \mathrm{h.c.}\right) \\ & + \left(y_L f \bar{q}^5_L U \Psi + y_R f \bar{t}^5_R U \Psi - i c_L \overline{\psi}^i_{4L} \gamma^\mu d^i_\mu \psi_{1L} - i c_R \overline{\psi}^i_{4R} \gamma^\mu d^i_\mu \psi_{1R} + \mathrm{h.c.}\right) , \end{aligned} \tag{8.59}$$

where $\Psi = (\psi_4, \psi_1)$ denotes the $SO(5)$ multiplet in the fundamental $SO(5)$ representation built from the ψ_4 and ψ_1 fields. Notice that the $SO(4)$ symmetry would allow for four independent mixing terms of the elementary q_L and t_R fields with the ψ_4 and ψ_1 multiplets. The structure in Equation 8.59 is dictated by the requirement of calculability of the Higgs potential.

All the parameters in the effective Lagrangian can in general be complex. By field redefinitions, three parameters can be made real, leaving 4 physical complex phases. A convenient choice, which we will use in the following, is to remove the phases from the elementary-composite mixings y_L and y_R and from one of the top partners mass parameters, either m_1 or m_4. With this convention, the coefficients of the d_μ-symbol operators remain in general complex.

Two free parameters can be chosen by fixing the top and Higgs masses. The top mass, at leading order in the v/f expansion is given by

$$m^2_{\mathrm{top}} \simeq \frac{1}{2} \frac{y_L^2 y_R^2 f^2 |m_4 - m_1|^2}{(|m_4|^2 + y_L^2 f^2)(|m_1|^2 + y_R^2 f^2)} v^2 . \tag{8.60}$$

The Higgs mass can be conveniently related to the masses of the top partners, namely [198] (see also reference [199, 200])

$$m_h \simeq m_{top} \frac{\sqrt{2N_c}}{\pi} \frac{m_T m_{\widetilde{T}}}{f} \sqrt{\frac{\log(m_T/m_{\widetilde{T}})}{m_T^2 - m_{\widetilde{T}}^2}}\,, \tag{8.61}$$

where $N_c = 3$ is the number of QCD colors, while m_T and $m_{\widetilde{T}}$ denote the masses of the top partners with the quantum numbers of the top left and top right components respectively. The T and $\widetilde{T}$ masses are approximately given by

$$m_T \simeq \sqrt{|m_4|^2 + y_L^2 f^2}\,, \qquad m_{\widetilde{T}} \simeq \sqrt{|m_1|^2 + y_R^2 f^2}\,. \tag{8.62}$$

This relation (8.61) is valid with fair accuracy, $\sim 20\%$, and is only mildly modified by the presence of additional heavier top partners.

Remarkably, (8.61) implies a tight relation between the mass of the lightest top partners and the Goldstone decay constant f, namely

$$m_{lightest} \lesssim \frac{\pi}{\sqrt{3}} \frac{m_h}{m_{top}} f \simeq 1.4\, f\,. \tag{8.63}$$

Exclusion bounds on the top partner masses can thus be translated into lower bounds on the compositeness scale f. The relation in (8.63) is saturated only if $m_T \simeq m_{\widetilde{T}} \simeq m_{lightest}$. If the T and $\widetilde{T}$ masses are significantly far apart, the lightest partner can be even a factor of ~ 2 lighter than the estimate in Equation 8.63.

Let us now discuss the CP-violating effects. We start by considering the properties of the Yukawa couplings. We saw that in the **14 + 1** model, all the mass parameters and elementary-composite mixings can be made real by field redefinitions, therefore the Yukawa couplings alone can not generate CP-violating effects. The situation is different in the **5+5** set-up, in which one physical complex phase can not be removed from the $y_{L,R}$ and $m_{4,1}$ parameters. In principle this could allow for CP-violating Yukawa couplings. Noticeably, in the fermion mass eigenstate basis, only the off-diagonal Yukawa interactions can be complex, while the diagonal ones are necessarily real. We will now present a general proof of this result that will allow us to identify the structural properties from which it stems and the class of models for which it is valid.

The dynamics of the various resonances and their couplings with the Higgs can be encoded into a formal effective Lagrangian obtained by integrating out all the top partner fields in the gauge interaction basis. The only fields remaining in this effective description are the elementary components q_L and t_R.[11] Notice that these fields have an overlap with the whole set of mass eigenstates, thus they can describe any of them by just imposing the appropriate mass-shell condition. The effective Lagrangian contains operators with the generic form

$$i\bar{q}_L^5 p^{2n} \not{p} q_L^5\,, \qquad i\bar{t}_R^5 p^{2n} \not{p} t_R^5\,, \tag{8.64}$$

which correct the kinetic terms of the q_L and t_R fields. These operators, however, are necessarily real, so they do not give rise to CP-violating effects. The effective Lagrangian also contains a unique "mass" term, namely

$$\overline{m}\, \bar{q}_L^5 U t_R^5 + h.c.\,, \tag{8.65}$$

11 This effective description is analogous to the "holographic" effective Lagrangian in extra-dimensional models, which is a function of the UV boundary values of the extra-dimensional fields [270, 271].

which is the only invariant allowed by the symmetry structure of the model that does not contain derivatives. This operator gives rise not only to the mass terms but also to the Yukawa couplings.

The $\overline{m}$ coefficient is in general complex. Nevertheless, when we redefine the fields to make the masses real, we automatically remove all complex phases from $\overline{m}$. In such a way also the diagonal Yukawa couplings are automatically made real. Notice that this result is true only in models in which a single "mass" invariant is present. If multiple invariants are allowed, the Yukawa couplings are not "aligned" with the masses, thus making the masses real in general does not remove the complex phases from the diagonal Yukawa couplings. A scenario with multiple invariants can be obtained by embedding both the q_L and the t_R fields in the **14** representation of SO(5).

Since the diagonal Yukawa couplings are real, the only interactions that can generate CP-violating contributions through Barr–Zee-type effects are the ones coming from the d-symbol operators. Their explicit form at leading order in the v/f expansion (using the convention in Equation 8.16) reads

$$\begin{cases} c_{top,L} = -\sqrt{2}vfy_L^2 \dfrac{\mathrm{Im}[c_L(m_1 m_4^* + y_R^2 f^2)]}{(|m_4|^2 + y_L^2 f^2)(|m_1|^2 + y_R^2 f^2)} \\ c_{X_{2/3},L} = -\sqrt{2}vfy_R^2 \dfrac{\mathrm{Im}\, c_L}{|m_1|^2 + y_R^2 f^2 - |m_4|^2} \\ c_{T,L} = \dfrac{\sqrt{2}vf}{|m_4|^2 + y_L^2 f^2 - |m_1|^2 - y_R^2 f^2}\left[y_R^2 \mathrm{Im}\, c_L - y_L^2 \dfrac{\mathrm{Im}[c_L(m_1 m_4^* + y_R^2 f^2)]}{|m_4|^2 + y_L^2 f^2}\right] \\ c_{\widetilde{T},L} = -(c_{top,L} + c_{X_{2/3},L} + c_{T,L}) \end{cases} \tag{8.66}$$

for the left-handed field interactions and

$$\begin{cases} c_{top,R} = \dfrac{\sqrt{2}vfy_R^2}{|m_1|^2 + y_R^2 f^2}\left[\dfrac{\mathrm{Im}[c_R(m_1^* m_4 + y_L^2 f^2)]}{|m_4|^2 + y_L^2 f^2} + \mathrm{Im}[c_R m_1^*/m_4^*]\right] \\ c_{X_{2/3},R} = -\sqrt{2}vfy_R^2 \dfrac{\mathrm{Im}[c_R m_1^*/m_4^*]}{|m_1|^2 + y_R^2 f^2 - |m_4|^2} \\ c_{T,R} = -\dfrac{\sqrt{2}vf}{|m_4|^2 + y_L^2 f^2 - |m_1|^2 - y_R^2 f^2}\left[y_L^2 \mathrm{Im}\, c_R - y_R^2 \dfrac{\mathrm{Im}[c_R(m_1^* m_4 + y_L^2 f^2)]}{|m_4|^2 + y_L^2 f^2}\right] \\ c_{\widetilde{T},R} = -(c_{top,R} + c_{X_{2/3},R} + c_{T,R}) \end{cases} \tag{8.67}$$

for the right-handed ones.

Interestingly, the dependence of the CP-violating coefficients on the elementary-composite mixings and on the masses of the top partners is analogous to the one we found in the **14 + 1** set-up. This result confirms that the CP-violating effects in composite Higgs scenarios share some "universal" structure and are generically expected to be sizable independently of the details of the model.

Using the explicit expressions for the top mass in Equation 8.60, one finds that the elementary-composite mixing parameters can be estimated as $y_L \sim y_R \sim y_{top} m_{lightest}/f$. Putting this result together with the estimate in Equation 8.63, we can express the corrections to the electron EDM as a function of the compositeness scale f, namely

$$\frac{d_e}{e} \sim \frac{e^2}{48\pi^4}\frac{y_e}{\sqrt{2}}\mathrm{Im}\,\tilde{c}\,\frac{m_{top}}{1.4f^2}\log\frac{(1.4f)^2}{m_{top}^2}\,. \tag{8.68}$$

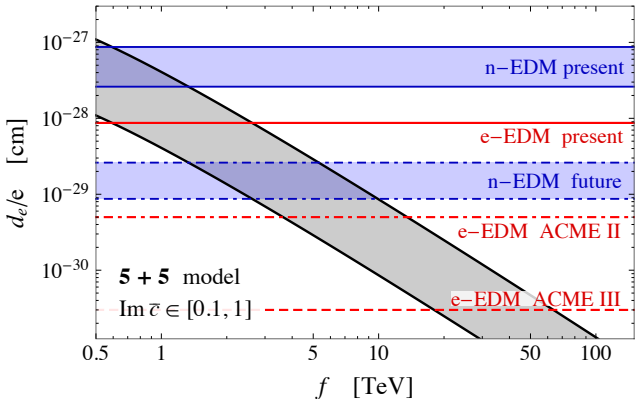

Figure 8.10: Estimate of the bound on the compositeness scale f in the **5 + 5** model. The gray band shows the estimate of the corrections to the electron EDM given in Equation 8.68 for $\mathrm{Im}\,\bar{c} \in [0.1, 1]$. The solid red line shows the bound from the present electron EDM measurements, while the dot-dashed and dotted ones show the expected future limits. The blue bands show the constraints from the present and near-future neutron EDM measurements.

This is a quite remarkable result, since it allows us to convert directly the bounds on dipole operators into constraints on f. The numerical value of the estimate in Equation 8.68 is shown in Figure 8.10, together with the experimental bounds. To allow for a certain amount of cancellation we varied the parameter $\mathrm{Im}\,\bar{c}$ in the range $[0.1, 1]$. The present data give bounds $f \gtrsim 1\,\mathrm{TeV}$. Near-future improvements in the electron and neutron EDMs will test $f \sim 5\,\mathrm{TeV}$, while the ACME III expected reach could probe $f \sim 50\,\mathrm{TeV}$. Notice that these bounds are much stronger than the ones coming from direct searches. As shown in reference [251], the LHC searches for top partners can now exclude the **5 + 5** model for $f \simeq 780\,\mathrm{GeV}$, while the high-luminosity LHC program could only slightly increase the bound up to $f \simeq 1.1\,\mathrm{TeV}$.

It must be noticed that the estimate in Equation 8.68 should be interpreted as a lower bound on the corrections to the electron EDM. To derive it we assumed that the relation in Equation 8.63 is saturated. As we discussed before, this is true only if the T and $\widetilde{T}$ masses are comparable. In generic parameter space points the lightest partners can be even a factor ~ 2 lighter than the estimate, thus leading to EDM contributions larger by a factor ~ 4. The presence of multiple CP-violating couplings can also give rise to, small, additional enhancements. We verified by a numerical scan that the bounds in Figure 8.10 reproduce quite well the minimal constraints on f as a function of the typical size of the complex phases. They can thus be considered as robust constraints on the compositeness scale.

It is important to mention that the value of ξ can be directly connected to the amount of fine-tuning [201]. In CH scenarios the v/f ratio is not a free parameter, but rather a dynamical quantity fixed by the minimization of the radiatively-induced Higgs potential. In generic parameter space points ξ is expected to be of order one. Therefore, requiring a large separation between the Higgs vacuum expectation value and f implies a minimal amount of tuning of order $1/\xi$.[12] The constraints coming from the electron and neutron EDMs can thus be reinterpreted as bounds on the minimal amount of fine-tuning in the **5+5** 2-site model. While $f \sim 1\,\mathrm{TeV}$ allows for a relatively low tuning ($\xi \sim 0.1$), the future

12 Note that additional sources of tuning can be present due to peculiarities of the Higgs potential [201].

bounds are expected to test regions of the parameter space with a tuning significantly below 1%.

To conclude the discussion about the **5+5** model, we consider the contributions to the Weinberg operator. Within the approximation in Equation 8.34 we find

$$w \simeq \frac{g_s^3}{\sqrt{2}(4\pi)^4} \frac{\mathrm{Im}(c_R - c_L) + \sqrt{2}\,\mathrm{Im}(c_R c_L^*)}{f^2} \frac{|m_4|^2 - |m_1|^2}{|m_4 - m_1|^2} \,. \tag{8.69}$$

Analogously to what we found for the **14 +1** model (see subsection 8.3.3), the top partners contributions to the Weinberg operator do not decouple in the limit of heavy resonances. The explicit result in Equation 8.69 shows that, in addition to contributions linear in the $c_{L,R}$ parameters, quadratic pieces are present. The latter come from diagrams involving two Higgs interactions coming from the d-symbol operators. Notice that the above result is reliable only if $m_4 - m_1$ is not too small. In the limit $m_4 = m_1$, the top mass vanishes (compare Equation 8.60) and the approximation in Equation 8.34 is not valid.

To give an idea of the strength of the experimental bounds we fix the parameters by the relations $m_4 \sim m_1$ and $c_L \sim c_R$, moreover we set $\xi = 0.1$. The current bounds on the neutron EDM translate into a bound $c_{L,R} \lesssim 1$, whereas the expected improved measurements will allow to probe $c_{L,R} \sim 0.1$.

8.5 CONCLUSIONS

In this work we analyzed CP-violating effects induced by light top partners in composite Higgs scenarios. We found that the main effects arise at two-loop level through Barr–Zee-type diagrams and generate sizable contributions to the dipole moments of the electron and of the light SM quarks. Additional, although typically subleading, contributions are induced for the purely-gluonic Weinberg operator.

Noticeably, in a large class of models, Barr–Zee effects arise exclusively from top partner interactions involving the derivative of the Higgs field, namely $\partial_\mu h \bar{\chi}_i \gamma^\mu \chi_j$. The diagonal Yukawa couplings, instead, are necessarily CP-conserving, thus not contributing to the light SM fermions dipole operators. This result is valid in all models in which the effective Lagrangian contains only one invariant mass term for the top quark (see subsection 8.4.2). Notice that this class of models is the most motivated one from a flavor perspective, since a suppression of flavor-violating effects mediated by the Higgs [231] is also present. Without such feature very strong bounds from Higgs-mediated flavor-changing neutral currents would be present.

We found that the overall structure of the CP-violating effects, and in particular the dependence on the masses of the top partners, is a rather universal feature and depends only mildly on the details of the model. The main contributions to the electron and light quark dipole moments can be interpreted as a running effect. At the one-loop level the top quark and its partners give rise to CP-odd contact interactions of the Higgs with the gauge fields (namely $H^2 A_{\mu\nu} \widetilde{A}^{\mu\nu}$ with the photons and $H^2 G^a_{\mu\nu} \widetilde{G}^{a\,\mu\nu}$ with the gluons). These operators, in turn, induce a running for the EDMs and CEDMs of the light SM fermions. We explicitly computed how the contributions due to the top and its partners can be matched onto the CP-violating Higgs contact interactions. In particular we found that running effects are always regulated at the top mass scale, since the top contribution to the Higgs contact operators exactly balances the ones coming from the top partners. Additional threshold contributions are found to be accidentally suppressed and numerically negligible.

In our analysis we focussed exclusively on the role of the top and its partners and we did not take into account possible effects related to additional resonances. We also neglected the details of the flavor structure both in the quark and in the lepton sectors. These aspects are expected not to spoil the overall picture we described in this work. They could however have some impact on the bounds, which is worth exploring. We leave this aspect for future investigation.

Although the CP-violating effects arise only at two-loop level, the present experimental bounds are tight enough to give non-trivial constraints on the top partners masses. The strongest bounds come from the measurement of the electron EDM, and can be used to probe top partners masses in the *few* TeV range (see Figure 8.5 and Figure 8.9). Upgraded experiments are expected to improve the bounds by one order of magnitude in the near future (ACME II) and by more than two orders of magnitude at a later stage (ACME III), hence pushing the indirect exclusions for top partners well above $10-20\,\text{TeV}$ (Figure 8.9). Bounds from neutron EDM measurements are slightly weaker than the ones from electron EDM, but could nevertheless test resonance masses in the $5-10\,\text{TeV}$ range in the near future.

In a large part of the parameter space of explicit models, the indirect bounds coming from the electron EDM are competitive with the LHC direct searches for heavy vector-like quarks (see Figure 8.7). In particular CP-violating effects are induced by the same operators that control the single-production vertices. In the absence of accidental cancellations or of accidentally small CP-violating phases, the indirect bounds from CP violation tend to surpass the ones from single production searches. The expected ACME II constraints will cover most of the LHC direct search reach even for complex phases as small as *few* %. ACME III could instead give constraints comparable with the direct ones achievable at future high-energy hadron colliders such as FCC-hh with 100 TeV center of mass energy (see Figure 8.8).

Interestingly, in specific scenarios such as the **5+5** 2-site model, the constraints fom CP-violating effects can be translated into bounds on the Higgs compositeness scale f. While the present constraints are of order $f \gtrsim 1\,\text{TeV}$, future improvements can push the bounds well above the $5-10\,\text{TeV}$ range (see Figure 8.10). In these scenarios the constraints on f can also be translated into lower bounds on the amount of fine tuning. For $f \sim 1\,\text{TeV}$ the minimal fine-tuning is of order $5-10\%$, whereas it becomes 0.1% for $f \sim 10\,\text{TeV}$.

9 CLOSING WORDS

In this thesis we saw the power EFTs. After a brief introduction to the SM in chapter 1, we presented the Higgs basis, a natural extension to the SM assuming the Higgs is part of a doublet and the existence of an energy gap between the SM and BSM physics. We extended the SM by adding dimension-6 operators and used the freedom available in the choice of independent operators to define the so called Higgs basis. This basis is suitable, as its name indicates, to study and constrain Higgs physics.

In Part ii, we used this framework to study the ability of current and future generations of colliders to extract information on the hard to grasp trilinear Higgs self-coupling. The goal was to use a large fraction of the information available, using higher order effects in single-Higgs production and pair production, to probe the self-coupling. Since indirect effects of new physics are expected to modify the Higgs production and decay through several simultaneous effects, the use of EFT is a consistent way to minimize theory dependence on the extraction of the parameter. Unlike the κ modifier, EFT retains the symmetry structure, allowing for a consistent expansion in the scale of new physics, and allows the introduction of new vertex structures.

We started by selecting the operators relevant for Higgs physics, adding some extra assumption such as the absence of CP violation and flavor universality. This allowed us to parametrize deviations from the SM in a quite generic way. Our different assumptions add a non-negligible model dependence but are a necessity, since making fewer assumptions on new physics, means more parameters need to be constrained. Unfortunately, the number of observables are limited, causing the appearance of unconstrained directions, as we discovered in our initial fit using only the single-Higgs inclusive information. This raises the interesting question of hidden assumptions; single-Higgs fits without loop corrections from the trilinear assume that deviation in the self-coupling are such that the loop contribution is negligible. Fortunately, as we argued, this condition is not too restrictive since in most models deviations in the self-coupling have the same order as other deviations, making the higher order corrections from the trilinear negligible.

We then discussed the possibility of adding differential information to fix these issues and found that these new observables could help to constrain the second mimimum appearing in the fit using pair-production only. Unfortunately, we found that the HL-LHC will only give mild constraints of order one on the trilinear. Nevertheless, the method of using loop effects in single production is a huge potential gain for the next generation of colliders, since they are very likely to be e^-e^+ machine, which will measure single-Higgs coupling with great precision. We tested both the prospect of the circular machines, which have higher low energy luminosity, but can not probe double-Higgs production and the linear machine which can study pair-production. We found that the ability of those machines to run at different energies should give us enough observables to improve the bound from the HL-LHC. Nevertheless, in order to reach the sub 10% precision, we are going to have to wait for a 100 TeV proton proton collider.

After that, we continued our tour of EFTs and extended the usual standard model EFT by adding a field. This was motived by the interesting excess seen by ATLAS and CMS in the di-photon invariant mass. A similar use of EFT is also made in DM searches, where dark matter is expected to be produced in decay of a heavy mediator. While in the DM case, An EFT is used to search for new particle and set lower bounds on its mass, in our case EFT is used to probe the CP properties of the particle which could have been responsible for the bumps seen in the di-photon spectrum. We started by using the differents experimental constraints to define the region of parameter space of interest, followed by a discussion on how using extra channel could resolve unconstrained direction in the parameter space. We then focused on the CP property of the hypothetical new field. We saw the HL-LHC could, thanks to the use of several CP sensitive asymmetries, constrain the properties of a possible new scalar for a broad range of the parameter space. Unfortunately, as known, the bump was only a statistical fluke, however, the method used could easily be re-used for the next excess in which a scalar couples to gauge bosons.

In the second chapter of Part iii, we moved some distance away from EFT to look at a simplified model. The idea of simplified models is to keep only the relevant structure of a type of theory, in order to study their effects in a generic way. In this case, we studied composite Higgs models. The goal was to compare the low-energy constraints arising from dipole moments with the constraints coming from direct searches at the LHC. Interestingly, the constraints on different dipoles are formulated by the experimentalists as bounds on Wilson coefficients of higher dimensional effective operators. Integrating out the heavy state of our model, we could match our simplified model to the effective Lagrangian and hence bound its parameter space. The situation is different in the collider case, since the bounds are obtained by considering direct production of the new particle, therefore, directly using the simplified model allows to obtain stronger bounds. Interestingly, the low energy experiment can, thanks to its high precision, give competitive bounds with the one coming from LHC. This situation should not change in the future, since the second planned upgrade, should reach sensitivity comparable from the one from FCC.

The content of this thesis is a reflection to the actual status of the LHC. While the machine is performing extremely well and has already recorded $100\,\text{fb}^{-1}$ at $13\,\text{TeV}$, no unambiguous trace of BSM physics was found.[1] A plethora of analyses have confirmed the ability of the SM to precisely describe the world surrounding us. It gives the opportunity to phenomenologists, to devise innovative ways to maximize the information extracted from the data, in order to constrain SM couplings, study anomalies, or bound the parameter space of new theories.

1 With the exception of indirect hints for new physics in the flavor sector.

Part IV

APPENDIX

A

THE TRILINEAR AT HADRON COLLIDERS

A.1 PARAMETRIZING EFT CROSS SECTIONS USING MADGRAPH

In this appendix, we present a sketch of how cross sections can be parametrized in terms of the dimension-6 Wilson coefficients using `Feynrules` [144] and `MadGraph` [143]. In order to keep the discussion short, we present the case where only two Wilson coefficients are present and the diagrams contain only one dimension-6 vertex, since the generalization is trivial. For definiteness, we compute the $e^-e^+ \to \nu_e\bar{\nu}_e hh$ cross section with only two dimension-6 terms present

$$\mathscr{L} = \mathscr{L}_{SM} c_1 \frac{e\sqrt{g^2+g'^2}}{2} Z_{\mu\nu}A^{\mu\nu} - c_2 v h^3. \tag{A.1}$$

We renamed the Wilson coefficient to simplify the notation.

The cross section can be parametrized as:

$$\sigma = \sigma_{SM} + c_1\sigma_{SM,1} + c_2\sigma_{SM,2} + c_1c_2\sigma_{1,2} + c_1^2\sigma_{1,1} + c_2^2\sigma_{2,2}\,. \tag{A.2}$$

Where σ_{SM} is the SM cross section, $\sigma_{SM,i}$ is the contribution of the interference diagrams between the SM and the dimension-6 operator with coefficient c_i when $c_i = 1$ and finally $\sigma_{i,j}$ is the contribution from diagram with the Wilson coefficient c_ic_j when their values are 1.

Several possibilities are available to obtain the σ using `MadGraph`. The simplest is just to compute a grid of 6 points and fit either using constant relative error or the error reported by the Monte Carlo. Nevertheless, some care is needed since the different methods are not necessarily numerically stable. It can happen, due to the normalization of the c_i and the energy dependence of the dimension-6 vertex, that some $\sigma_{i,i}$ are orders of magnitude bigger than the other coefficients, jeopardizing the numerical stability of the method. In order to avoid this issue, we take advantage of the freedom `Feynrules` and `MadGraph` offer us to compute the coefficients one by one, with the only error coming from the Monte Carlo integration and the different physic assumptions.

The trick is to take advantage of the `MadGraph` mechanism to select diagrams. Indeed, each coupling can be linked to an "interaction order"[1] that `MadGraph` use to compute only the relevant contribution. For example, giving the dimension-6 Wilson coefficients an interaction order called "NP" and a value 1, we can select diagram using the two different kinds of notation

```
e- e+ > ve ve~ h h NP==1
e- e+ > ve ve~ h h NP^2==1
```

Some caution is needed since "=" mean "$\leqslant$" and "==" mean strictly equal. The first line without the `^2` means that we are only allowing diagram with 1 insertion of a dimension-6 vertex. Since we are at the diagram level, the command would compute the sum of the

1 We redirect the reader to both the `Feynrules` [144] and `MadGraph` [143] manuals for more detail on the implementation.

interference and the squared diagram with one dimension-6 vertex. While the second line is at the amplitude level. It means it only computes the amplitude elements with 1 dimension-6 coefficient. This would give the sum of the interference between the SM and all the dimension-6 diagrams. Since we want to select the amplitude with a given Wilson coefficient, we will use the second notation. We do not exactly achieve the wanted goal since with this notation, we would obtain

$$c_1 \sigma_{SM,1} + c_2 \sigma_{SM,2} \tag{A.3}$$

In order to fix this problem, we could either set c_1 or c_2 to 0. Nevertheless, this would not work in order to separate $\sigma_{1,1}$ from $\sigma_{1,2}$ and $\sigma_{2,2}$. For this, we need to modify the `Feynrules` model and define 2 new kinds of interaction order; C1 and C2 and give them to c_1 and c_2 respectively. Once that is done, we can set the coefficient to one, and compute the different σ using the notation:

```
e- e+ > ve ve~ h h C1==0 C2==0
e- e+ > ve ve~ h h C1==1 C2==0
e- e+ > ve ve~ h h C1==0 C2==1
e- e+ > ve ve~ h h C1==1 C2==1
e- e+ > ve ve~ h h C1==2 C2==0
e- e+ > ve ve~ h h C1==0 C2==2
```

The first line computes the SM cross section, then we have the two interferences between dimension-6 and theSM, the $c_1 c_2$ terms and finally the two quadratic term. Of course this involves running `MadGraph` several time. The situation quickly becomes tedious when the number of Wilson coefficient grows but this can be easily automatized by generating the "runcard" using a scripting language like `python` or `mathematica`. It should also be noted that some care is needed when setting the interaction order when in the presence of dependent coefficients so all the good diagrams are indeed included.

A.2 HIGGS PRODUCTION AND DECAY RATES IN THE EFT FRAMEWORK

In this appendix we report the expressions for the production and decay rates of the Higgs boson as a function of the EFT parameters. The numerical results have been obtained at LO through `Feynrules` [144] and `MadGraph` [143] by using the model "Higgs effective Lagrangian" [272].

We start by listing the dependence on the single-Higgs couplings deformations (δc_z, c_{zz}, $c_{z\Box}$, $\hat{c}_{z\gamma}$, $\hat{c}_{\gamma\gamma}$, $\hat{c}_{gg}$, δy_t, δy_b, δy_τ). The modification of the total cross sections for associated production (ZH and WH) and VBF depend on the collider energy. The results at 7, 8, 13, 14, 33 and 100 TeV are given by

$$\frac{\sigma_{ZH}}{\sigma_{ZH}^{SM}} = 1 + \delta c_z \begin{pmatrix} 2.0 \\ 2.0 \\ 2.0 \\ 2.0 \\ 2.0 \\ 2.0 \end{pmatrix} + c_{z\Box} \begin{pmatrix} 7.6 \\ 7.8 \\ 8.3 \\ 8.4 \\ 9.1 \\ 10.0 \end{pmatrix} + c_{zz} \begin{pmatrix} 3.4 \\ 3.4 \\ 3.5 \\ 3.6 \\ 3.7 \\ 4.0 \end{pmatrix} - \hat{c}_{z\gamma} \begin{pmatrix} 0.060 \\ 0.061 \\ 0.067 \\ 0.068 \\ 0.077 \\ 0.086 \end{pmatrix} - \hat{c}_{\gamma\gamma} \begin{pmatrix} 0.028 \\ 0.028 \\ 0.030 \\ 0.032 \\ 0.034 \\ 0.037 \end{pmatrix}, \tag{A.4}$$

$$\frac{\sigma_{WH}}{\sigma_{WH}^{SM}} = 1 + \delta c_z \begin{pmatrix} 2.0 \\ 2.0 \\ 2.0 \\ 2.0 \\ 2.0 \\ 2.0 \end{pmatrix} + c_{z\Box} \begin{pmatrix} 9.3 \\ 9.4 \\ 10.0 \\ 10.1 \\ 11.1 \\ 12.1 \end{pmatrix} + c_{zz} \begin{pmatrix} 4.4 \\ 4.4 \\ 4.6 \\ 4.6 \\ 5.0 \\ 5.3 \end{pmatrix} - \hat{c}_{z\gamma} \begin{pmatrix} 0.082 \\ 0.084 \\ 0.094 \\ 0.095 \\ 0.110 \\ 0.126 \end{pmatrix} - \hat{c}_{\gamma\gamma} \begin{pmatrix} 0.044 \\ 0.045 \\ 0.048 \\ 0.049 \\ 0.054 \\ 0.060 \end{pmatrix}, \quad \text{(A.5)}$$

$$\frac{\sigma_{VBF}}{\sigma_{VBF}^{SM}} = 1 + \delta c_z \begin{pmatrix} 2.0 \\ 2.0 \\ 2.0 \\ 2.0 \\ 2.0 \\ 2.0 \end{pmatrix} - c_{z\Box} \begin{pmatrix} 2.2 \\ 2.2 \\ 2.5 \\ 2.5 \\ 3.0 \\ 3.7 \end{pmatrix} - c_{zz} \begin{pmatrix} 0.81 \\ 0.83 \\ 0.89 \\ 0.90 \\ 1.04 \\ 1.27 \end{pmatrix} + \hat{c}_{z\gamma} \begin{pmatrix} 0.029 \\ 0.030 \\ 0.033 \\ 0.034 \\ 0.041 \\ 0.051 \end{pmatrix} + \hat{c}_{\gamma\gamma} \begin{pmatrix} 0.0113 \\ 0.0117 \\ 0.0129 \\ 0.0131 \\ 0.0156 \\ 0.0193 \end{pmatrix}, \quad \text{(A.6)}$$

where we employ the VBF cross section definition of reference [49], namely we apply the following cuts on the two forward jets: $p_{T,j} > 20\,\text{GeV}$, $|\eta_j| < 5$, and $m_{jj} > 250\,\text{GeV}$.

The cross sections of the gluon fusion and $t\bar{t}H$ production modes are instead modified in an energy-independent way [49]. This is a consequence of the fact that at LO the gluon fusion energy scale is fixed by the Higgs bosons on-shell condition and is therefore $\sqrt{s}$ independent, while the modification of $t\bar{t}H$ is simply due to a rescaling of the top Yukawa.

$$\frac{\sigma_{ggF}}{\sigma_{ggF}^{SM}} = 1 + 2\hat{c}_{gg} + 2.06\delta y_t - 0.06\delta y_b\,, \quad \text{(A.7)}$$

$$\frac{\sigma_{ttH}}{\sigma_{ttH}^{SM}} = 1 + 2\delta y_t\,. \quad \text{(A.8)}$$

The modifications of the decay widths are given by [49]

$$\frac{\Gamma_{\gamma\gamma}}{\Gamma_{\gamma\gamma}^{SM}} = 1 + 2.56\,\delta c_z + 2.13\,c_{z\Box} + 0.98\,c_{zz} - 0.066\hat{c}_{z\gamma} - 2.46\,\hat{c}_{\gamma\gamma} - 0.56\,\delta y_t\,, \quad \text{(A.9)}$$

$$\frac{\Gamma_{Z\gamma}}{\Gamma_{Z\gamma}^{SM}} = 1 + 2.11\,\delta c_z - 3.4\,\hat{c}_{z\gamma} - 0.113\,\delta y_t\,, \quad \text{(A.10)}$$

$$\frac{\Gamma_{WW}}{\Gamma_{WW}^{SM}} = 1 + 2.0\,\delta c_z + 0.67\,c_{z\Box} + 0.05\,c_{zz} - 0.0182\,\hat{c}_{z\gamma} - 0.0051\,\hat{c}_{\gamma\gamma}\,, \quad \text{(A.11)}$$

$$\frac{\Gamma_{ZZ}}{\Gamma_{ZZ}^{SM}} = 1 + 2.0\,\delta c_z + 0.33\,c_{z\Box} + 0.19\,c_{zz} - 0.0081\,\hat{c}_{z\gamma} - 0.00111\,\hat{c}_{\gamma\gamma}\,, \quad \text{(A.12)}$$

$$\frac{\Gamma_{\tau\tau}}{\Gamma_{\tau\tau}^{SM}} = 1 + 2.0\,\delta y_\tau\,, \quad \text{(A.13)}$$

$$\frac{\Gamma_{bb}}{\Gamma_{bb}^{SM}} = 1 + 2.0\,\delta y_b\,, \quad \text{(A.14)}$$

$$\frac{\Gamma_H}{\Gamma_H^{SM}} = 1 + 0.171\,\hat{c}_{gg} + 0.006\,c_{zz} - 0.0091\,\hat{c}_{z\gamma} + 0.15\,c_{z\Box} - 0.0061\,\hat{c}_{\gamma\gamma} + 0.48\,\delta c_z + 1.15\,\delta y_b + 0.23\,\delta y_t + 0.13\,\delta y_\tau\,, \quad \text{(A.15)}$$

C^Γ [%]	$\gamma\gamma$	ZZ	WW	$f\bar{f}$	gg
H	0.49	0.83	0.73	0	0.66

Table A.1: Coefficients parametrizing the corrections to the Higgs partial widths due to loops involving the Higgs self-coupling (see Equation A.17) [43].

where in the modification of the decay to two photons we made use of the one-loop result[2] of reference [273], suitably translated to the Higgs basis and evaluated at the renormalization scale $\mu = m_h$. The analog result for the decay to $Z\gamma$ is not yet available in the literature, and we only include the known terms. In any case, the corresponding branching ratio will be measured with a limited precision and the impact of the missing one-loop corrections is going to be negligible.

For completeness we also report the expressions for the dependence of the Higgs rates on the modification of the Higgs self-coupling κ_λ. These results were derived in reference [43]. The modification to the Higgs production and decay rates can be parametrized as

$$\frac{\sigma}{\sigma_{SM}} = 1 + (\kappa_\lambda - 1)C^\sigma + \frac{(\kappa_\lambda^2 - 1)\delta Z_H}{1 - \kappa_\lambda^2 \delta Z_H}, \tag{A.16}$$

and

$$\frac{\Gamma}{\Gamma_{SM}} = 1 + (\kappa_\lambda - 1)C^\Gamma + \frac{(\kappa_\lambda^2 - 1)\delta Z_H}{1 - \kappa_\lambda^2 \delta Z_H}. \tag{A.17}$$

In the above expressions the term linear in κ_λ comes from diagrams that contribute directly to the production and decay processes. The corresponding coefficients C^σ and C^Γ for the inclusive cross sections are given in Tables A.1 and A.2. The last terms in Equations (A.16) and (A.17) comes from a rescaling of the Higgs kinetic term due to the self-energy diagram involving two insertions of the Higgs self-coupling. The corresponding quantity δZ_H is given by

$$\delta Z_H = -\frac{9}{16}\frac{G_\mu m_H^2}{\sqrt{2}\pi^2}\left(\frac{2\pi}{3\sqrt{3}} - 1\right) \simeq -0.0015\,. \tag{A.18}$$

We now report the expressions for the Higgs pair production differential cross section. This cross-section has been calculated in the EFT framework in reference [58], as a function of the parameters δy_t, $\delta y_t^{(2)}$, $\hat{c}_{gg}$, $\hat{c}_{gg}^{(2)}$, and κ_λ. The ratio of the inclusive cross-section for Higgs-pair production to the corresponding SM prediction can be written as

$$\begin{aligned}\frac{\sigma(pp \to hh)}{\sigma_{SM}(pp \to hh)} = {} & A_1\,(1+\delta y_t)^4 + A_2\,(\delta y_t^{(2)})^2 + A_3\,\kappa_\lambda^2\,(1+\delta y_t)^2 + A_4\,\kappa_\lambda^2\,\hat{c}_{gg}^2 \\ & + A_5\,(\hat{c}_{gg}^{(2)})^2 + A_6\,(1+\delta y_t)^2\,\delta y_t^{(2)} + A_7\,\kappa_\lambda\,(1+\delta y_t)^3 \\ & + A_8\,\kappa_\lambda\,(1+\delta y_t)\,\delta y_t^{(2)} + A_9\,\kappa_\lambda\,\hat{c}_{gg}\,\delta y_t^{(2)} + A_{10}\,\hat{c}_{gg}^{(2)}\,\delta y_t^{(2)}\end{aligned}$$

2 We observed that the NLO corrections in the $\gamma\gamma$ decay have no impact on the global fit once enough observables are included to remove the flat directions.

C^{σ} [%]	ggF	VBF	WH	ZH	$t\bar{t}H$
7 TeV	0.66	0.65	1.06	1.23	3.87
8 TeV	0.66	0.65	1.05	1.22	3.78
13 TeV	0.66	0.64	1.03	1.19	3.51
14 TeV	0.66	0.64	1.03	1.18	3.47

Table A.2: Coefficients parametrizing the corrections to the Higgs production cross sections due to loops involving the Higgs self-coupling (see Equation A.16) [43].

$$+ A_{11}\,\kappa_\lambda\,\hat{c}_{gg}\,(1+\delta y_t)^2 + A_{12}\,\hat{c}_{gg}^{(2)}\,(1+\delta y_t)^2$$
$$+ A_{13}\,\kappa_\lambda^2\,\hat{c}_{gg}\,(1+\delta y_t) + A_{14}\,\kappa_\lambda\,\hat{c}_{gg}^{(2)}\,(1+\delta y_t) + A_{15}\,\kappa_\lambda\,\hat{c}_{gg}\,\hat{c}_{gg}^{(2)}\,, \tag{A.19}$$

Notice that this parametrization can be used for the full uncut cross section and also for the cross section obtained after imposing cuts and acceptance factors. Moreover we can use the same expression to parametrize the differential cross section in each bin of the Higgs-pair invariant mass distribution. We report in Table A.3 the inclusive and differential SM cross section at 14 TeV after imposing the cuts devised in reference [58], as well as the values of the A_i.

Finally we consider the differential distributions for the Higgs associated production channels. In Table A.4 we list the dependence of the differential cross section in ZH and WH on the single-Higgs EFT parameters. The results are presented for the binned invariant mass $\hat{s}$ distribution. The cross sections have been computed by analyzing the events generated at LO by `MadGraph` through a custom made C++ code based on the `MadAnalysis5` library [181, 274]. The coefficients that parametrize the dependence of the WH, ZH and $t\bar{t}H$ production channels on the Higgs self-coupling are listed in Table A.5.

In Tables A.6 and A.7 we list the estimates of the systematic uncertainties on the binned differential distributions. To estimate the expected errors on the inclusive cross sections, we compared the ATLAS projections for the 300/fb and 3/ab experimental uncertainties and assumed that they come from a sum in quadrature of systematic and statistical ones. In the "optimistic" scenario in Table A.6, we rescaled the statistical uncertainty by the square root of the ratio of SM number of events in each bin, whereas we kept the systematic errors constant. In the "pessimistic" scenario we rescaled the total (statistical plus systematic) uncertainty according to the number of events in each bin.

m_{hh}^{reco} [GeV]	inclusive	250–400	400–550	550–700	700–850	850–1000	1000–
σ_{SM} [fb]	1.6	0.27	0.8	0.36	0.13	0.042	0.021
A_1	1.7	2.3	1.7	1.5	1.3	1.2	1.2
A_2	2.7	1.8	2.1	3.2	4.7	6.4	9.1
A_3	0.12	0.27	0.11	0.057	0.034	0.022	0.011
A_4	0.042	0.094	0.037	0.026	0.024	0.023	0.022
A_5	1.5	0.62	0.69	1.5	3.5	7.1	20.
A_6	-3.8	-4.0	-3.6	-3.8	-4.2	-4.5	-4.6
A_7	-0.82	-1.5	-0.84	-0.51	-0.36	-0.26	-0.17
A_8	0.98	1.4	0.96	0.83	0.78	0.73	0.67
A_9	0.45	0.81	0.46	0.33	0.23	0.14	0.003
A_{10}	2.2	2.1	2.0	2.4	2.8	2.5	-0.56
A_{11}	-0.32	-0.88	-0.33	-0.081	0.03	0.087	0.13
A_{12}	-1.0	-2.3	-1.3	-0.6	0.33	1.6	4.1
A_{13}	0.12	0.33	0.11	0.044	0.02	0.0092	0.0014
A_{14}	0.46	0.82	0.44	0.36	0.29	0.13	-0.27
A_{15}	0.41	0.48	0.31	0.39	0.57	0.81	1.3

Table A.3: Coefficients parametrizing the inclusive and differential cross section for double Higgs production via gluon fusion at $\sqrt{s} = 14\,TeV$. By σ_{SM} we denote the SM cross section, while A_1–A_{15} are the coefficients parametrizing the dependence of the cross on the EFT parameters as defined in Equation A.19. The numerical results correspond to the ones derived in the analyses of reference [58].

$\sqrt{s}$	$\sqrt{\hat{s}}/m_{\text{threshold}}$	WH						ZH					
		ϵ_{SM}	δc_z	$c_{z\Box}$	c_{zz}	$\hat{c}_{z\gamma}$	$\hat{c}_{\gamma\gamma}$	ϵ_{SM}	δc_z	$c_{z\Box}$	c_{zz}	$\hat{c}_{z\gamma}$	$\hat{c}_{\gamma\gamma}$
7 TeV	$[1.0-1.1]$	19 %	1.99	4.95	2.68	-0.0270	-0.0215	20 %	2.00	4.14	2.14	-0.0220	-0.0123
	$[1.1-1.2]$	20 %	2.00	5.84	3.10	-0.0349	-0.0258	21 %	2.00	4.81	2.42	-0.0290	-0.0154
	$[1.2-1.5]$	35 %	2.00	7.40	3.80	-0.0504	-0.0334	34 %	2.01	6.44	3.07	-0.0447	-0.0226
	$[1.5-2.0]$	18 %	2.01	12.4	5.71	-0.116	-0.0598	17 %	2.01	10.5	4.44	-0.0853	-0.0393
	$[2.0-3.0]$	7 %	2.01	23.	9.38	-0.271	-0.117	6 %	1.98	19.7	6.90	-0.192	-0.0780
8 TeV	$[1.0-1.1]$	19 %	2.01	4.93	2.66	-0.0275	-0.0215	20 %	2.00	4.10	2.12	-0.0231	-0.0126
	$[1.1-1.2]$	20 %	1.97	5.73	3.05	-0.0337	-0.0252	20 %	2.01	4.90	2.49	-0.0299	-0.0158
	$[1.2-1.5]$	34 %	2.01	7.51	3.81	-0.0533	-0.0342	35 %	2.01	6.40	3.05	-0.0453	-0.0226
	$[1.5-2.0]$	19 %	1.99	12.1	5.56	-0.113	-0.0582	18 %	2.00	10.6	4.51	-0.0872	-0.0400
	$[2.0-3.0]$	7 %	2.02	22.3	9.12	-0.264	-0.114	6 %	1.95	20.0	6.99	-0.202	-0.0804
13 TeV	$[1.0-1.1]$	18 %	2.02	4.96	2.70	-0.0265	-0.0216	19 %	2.02	4.06	2.09	-0.0226	-0.0121
	$[1.1-1.2]$	19 %	1.97	5.81	3.08	-0.0344	-0.0256	20 %	2.00	4.86	2.45	-0.0300	-0.0157
	$[1.2-1.5]$	34 %	2.00	7.44	3.76	-0.0532	-0.0339	34 %	1.98	6.37	3.04	-0.0445	-0.0222
	$[1.5-2.0]$	19 %	2.02	11.9	5.46	-0.111	-0.0572	18 %	2.01	10.6	4.53	-0.0887	-0.0406
	$[2.0-3.0]$	8 %	1.99	22.6	9.20	-0.269	-0.116	7 %	2.00	20.4	7.29	-0.196	-0.0808
14 TeV	$[1.0-1.1]$	18 %	2.00	5.01	2.72	-0.0267	-0.0217	19 %	2.01	4.14	2.12	-0.0237	-0.0126
	$[1.1-1.2]$	19 %	2.00	5.81	3.10	-0.0337	-0.0255	20 %	2.01	4.86	2.49	-0.0284	-0.0156
	$[1.2-1.5]$	34 %	2.01	7.44	3.76	-0.0535	-0.0340	34 %	2.00	6.35	3.02	-0.0448	-0.0221
	$[1.5-2.0]$	19 %	1.98	11.8	5.40	-0.112	-0.0572	18 %	1.98	10.5	4.44	-0.0873	-0.0396
	$[2.0-3.0]$	8 %	2.03	22.6	9.05	-0.276	-0.117	7 %	1.96	20.3	7.27	-0.193	-0.0800
33 TeV	$[1.0-1.1]$	17 %	1.98	4.96	2.68	-0.0274	-0.0216	18 %	2.02	4.16	2.16	-0.0228	-0.0124
	$[1.1-1.2]$	18 %	2.01	5.77	3.07	-0.0338	-0.0254	19 %	1.99	4.77	2.41	-0.0282	-0.0150
	$[1.2-1.5]$	33 %	1.99	7.43	3.73	-0.0544	-0.0340	34 %	1.99	6.45	3.08	-0.0453	-0.0225
	$[1.5-2.0]$	20 %	2.00	12.00	5.54	-0.110	-0.0574	19 %	2.02	10.4	4.37	-0.0862	-0.0390
	$[2.0-3.0]$	9 %	2.02	23.3	9.56	-0.274	-0.119	8 %	2.00	19.8	6.97	-0.190	-0.0777
100 TeV	$[1.0-1.1]$	16 %	2.01	4.92	2.66	-0.0271	-0.0215	17 %	2.02	3.98	2.05	-0.0238	-0.0118
	$[1.1-1.2]$	18 %	2.04	5.82	3.09	-0.0344	-0.0257	18 %	2.00	5.02	2.60	-0.0282	-0.0157
	$[1.2-1.5]$	33 %	1.97	7.48	3.77	-0.054	-0.0341	33 %	2.00	6.45	3.09	-0.0445	-0.0224
	$[1.5-2.0]$	20 %	2.02	11.9	5.47	-0.111	-0.0573	20 %	1.99	10.5	4.38	-0.0860	-0.0389
	$[2.0-3.0]$	10 %	1.99	23.1	9.40	-0.275	-0.118	9 %	2.00	20.0	6.90	-0.195	-0.0782

Table A.4: Effective field theory coefficient for each bin in the $\hat{s}$ differential distribution. The bins extrema are expressed in units of $m_{\text{threshold}} \equiv m_V + m_h$. The ϵ_{SM} columns list the percentage of events that belong to each bin in the SM distribution.

C^{σ} [%]	$[1.0-1.1]$	$[1.1-1.2]$	$[1.2-1.5]$	$[1.5-2.0]$	$[2.0-3.0]$
WH	1.78 (0.18)	1.44 (0.19)	1.02 (0.34)	0.52 (0.19)	0.06 (0.08)
ZH	2.08 (0.19)	1.64 (0.20)	1.12 (0.34)	0.51 (0.18)	0.21 (0.07)
$t\bar{t}H$	8.57 (0.02)	6.63 (0.08)	4.53 (0.33)	2.83 (0.33)	1.61 (0.18)

Table A.5: Coefficients parametrizing the corrections to the differential Higgs production cross sections at 13 TeV in the WH, ZH and $t\bar{t}H$ channels due to loops involving the Higgs self-coupling (see Equation A.16). The bins extrema are expressed in units of $m_{\text{threshold}}$, defined as $m_{\text{threshold}} \equiv m_V + m_h$ for WH and ZH, and $m_{\text{threshold}} \equiv 2m_t + m_h$ for $t\bar{t}H$. In parentheses we give the fraction of events belonging to each bin in the SM distribution. The results are taken from reference [43].

Process		Systematic	$[1.0-1.1]$	$[1.1-1.2]$	$[1.2-1.5]$	$[1.5-2.0]$	$[2.0-3.0]$
$H \to \gamma\gamma$	$t\bar{t}H$	0.04	0.74	0.41	0.23	0.23	0.3
	WH	0.08	0.37	0.37	0.28	0.36	0.54
	ZH	0.03	0.62	0.61	0.47	0.63	0.99
$H \to ZZ$	$t\bar{t}H$	0.05	0.98	0.53	0.29	0.29	0.39
	WH	0.07	0.33	0.32	0.25	0.32	0.48
	ZH	0.09	0.42	0.41	0.32	0.42	0.65
$H \to b\bar{b}$	WH	0.33	0.48	0.48	0.42	0.47	0.61
	ZH	0.10	0.23	0.22	0.18	0.23	0.34

Table A.6: Estimated relative uncertainties on the determination of the differential distributions in the associated Higgs production channels. These estimates correspond to the "optimistic" scenario in which the systematic uncertainties are assumed to be the same for each bin and only the statistical uncertainty is rescaled according to the number of events in each bin.

Process		$[1.0-1.1]$	$[1.1-1.2]$	$[1.5-1.2]$	$[2.0-1.5]$	$[2.0-3.0]$
$H \to \gamma\gamma$	$t\bar{t}H$	0.78	0.43	0.24	0.24	0.31
	WH	0.41	0.4	0.3	0.4	0.6
	ZH	0.63	0.62	0.47	0.63	0.99
$H \to ZZ$	$t\bar{t}H$	1.04	0.56	0.3	0.3	0.4
	WH	0.37	0.36	0.27	0.35	0.53
	ZH	0.46	0.45	0.35	0.47	0.72
$H \to b\bar{b}$	WH	0.86	0.84	0.62	0.82	1.26
	ZH	0.3	0.3	0.23	0.31	0.48

Table A.7: Estimated relative uncertainties on the determination of the differential distributions in the associated Higgs production channels. These estimates correspond to the "pessimistic" scenario in which the total (statistical plus systematic) uncertainty is rescaled according to the number of events in each bin.

B

THE TRILINEAR AT LEPTON COLLIDERS

B.1 ONE-LOOP CORRECTIONS FROM $\delta\kappa_\lambda$

C_1 (inclusive rates)	$\sqrt{s}$ [GeV]						
	240	250	350	500	1000	1400	3000
$e^+e^- \to hZ$	0.017	0.015	0.0057	0.00099	-0.0012	-0.0011	-0.00054
$e^+e^- \to \nu\bar{\nu}h$ ★	0.0064	0.0064	0.0062	0.0061	0.0059	0.0058	0.0057
$e^+e^- \to e^+e^-h$ ★	0.0070	0.0070	0.0069	0.0067	0.0065	0.0065	0.0063
$e^+e^- \to t\bar{t}h$				0.086	0.017	0.0094	0.0037

Table B.1: Values of C_1 for the total cross-sections of Higgs production processes. ★ The numbers are for WW or ZZ fusion only.

In this appendix we collect the numerical values of the coefficients C_1, defined in Equation 5.2, which encode the corrections to single-Higgs processes due to a deformation of the Higgs trilinear coupling. In Table B.1 we report the C_1 coefficients for the total cross-section of the main single-Higgs production modes, namely Higgsstrahlung, vector-boson fusion and associated production with top quarks. Several values of the center-of-mass energy $\sqrt{s}$ are reported in the table, corresponding to the benchmark runs of future lepton colliders considered in main text. The calculation has been performed with the help of the public tools `FeynArts`, `FormCalc`, `LoopTools`, and `CUBA` [275–277].

Notice that the values of C_1 for Higgsstrahlung, WW-boson fusion and ZZ-boson fusion are independent of the beam polarization if we restrict ourselves to diagrams up to one loop, as we did in our analysis. As for $e^+e^- \to t\bar{t}h$, the Higgs self-coupling gives rise to tiny beam polarization effects. Given the small impact of the latter production mode in our analysis, we can safely neglect such effects. The dependence of the C_1 coefficients on the collider energy is also shown in Figure B.1.

Besides the inclusive rates, we also checked the impact of a modified Higgs trilinear coupling on the angular asymmetries that can be built for the $e^+e^- \to hZ \to h\ell^+\ell^-$ case (see references [137, 138]). We found that these effects are almost negligible and have no impact on our analysis.

For completeness, we also report in Table B.2 the C_1 coefficients for the Higgs partial widths [43].

B.2 ADDITIONAL RESULTS

In this appendix, we collect some additional numerical results and plots that were not included in the main text.

In Figure B.2, we show the profiled $\Delta\chi^2$ as a function of $\delta\kappa_\lambda$ for the low-energy ILC benchmark considered in section 5.2, including 2 ab^{-1} of integrated luminosity at 250 GeV and either 200 fb^{-1} or 1.5 ab^{-1} at 350 GeV with luminosities equally split into $P(e^-, e^+) =$

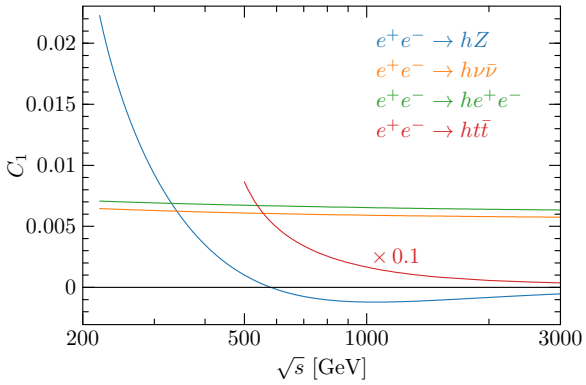

Figure B.1: Value of C_1 as a function of the center-of-mass energy $\sqrt{s}$ for the $e^+e^- \to hZ$, $e^+e^- \to \nu\bar{\nu}h$, $e^+e^- \to he^+e^-$ and $e^+e^- \to ht\bar{t}$ single Higgs production processes. Notice that the result for Higgs production in association with a top-quark pair has been rescaled by a factor of 0.1.

C_1	ZZ	WW	$\gamma\gamma$	gg	$f\bar{f}$
on-shell h decay	0.0083	0.0073	0.0049	0.0066	0

Table B.2: Values of C_1 for the Higgs partial widths from reference [43].

$(\mp 0.8, \pm 0.3)$ beam polarizations. In the left panel, we show the global fit for the ILC alone, while in the right panel we combine these results with the differential single- and double-Higgs measurements at the high-luminosity LHC. The corresponding 68% CL intervals are listed in Table 5.1.

In Table B.3, Table B.4 and Table B.5, we consider three alternative benchmark scenarios for the low-energy ILC runs. The three scenarios differ from the one considered in the main text by different choices of beam polarizations and luminosity splitting among them. The total integrated luminosities are the same as in the main benchmark, namely $2\,ab^{-1}$ at 250 GeV, $200\,fb^{-1}$ or $1.5\,ab^{-1}$ at 350 GeV. In Table B.3, we consider $P(e^-, e^+) = (\mp 0.8, \pm 0.3)$ beam polarizations with luminosity split between them according to a 70%/30% ratio. In Table B.4 and Table B.5, we consider $P(e^-, e^+) = (\mp 0.8, 0)$ beam polarizations with luminosity split between them with a 50%/50% ratio and a 70%/30% ratio respectively.

If only ILC data is included in the fit, the precision achievable in the case of a $P(e^-, e^+) = (\mp 0.8, \pm 0.3)$ polarization with a 70%/30% luminosity split is slightly better than the one of the other scenarios. The impact is however marginal and basically disappears once the ILC data is combined with the high-luminosity LHC one. We find that the differences in the fits are mainly due to the dependence of the pair production cross sections on the beam polarizations. In Figure B.3, we show this dependence for the double Higgs-strahlung and WW-fusion pair production cross sections. These results are obtained with `MadGraph5` [143] and do not take into account beam-structure effects. One can see that the largest cross sections are obtained for a $P(e^-, e^+) = (-0.8, +0.3)$ beam polarization. The cross sections for $P(e^-, e^+) = (0, 0)$ are smaller by a factor ~ 2, while a much larger suppression is present for $P(e^-, e^+) = (+0.8, -0.3)$.[1]

1 Amusingly, one can note that, at leading order and independently of the center-of-mass energy, the inclusive double Higgsstrahlung production cross section with a $P(e^-, e^+) = (+0.8, -0.3)$ beam polarization configuration deviates from the unpolarized cross section by less than 1%.

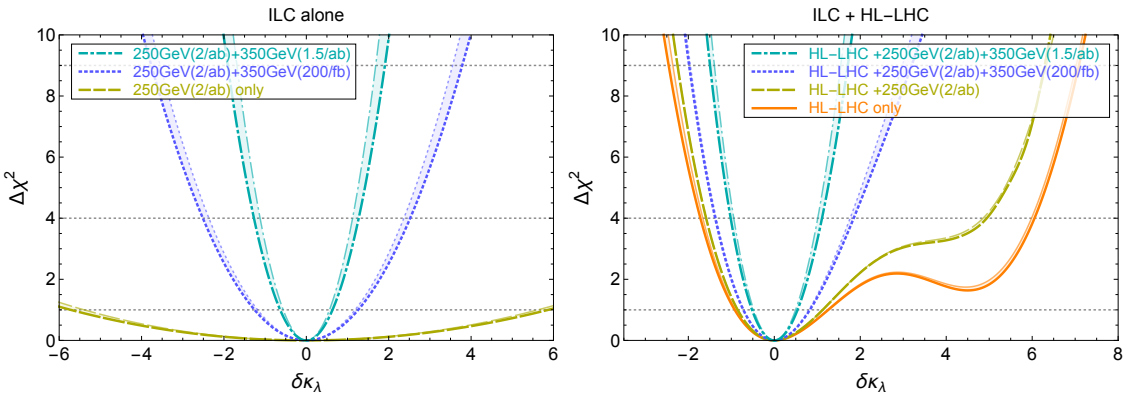

Figure B.2: Delta Chi-square profiled over all EFT parameters but $\delta\kappa_\lambda$. Three run scenarios are considered for ILC, with 2 ab^{-1} at 250 GeV and $\{0, 200\,fb^{-1}, 1.5\,ab^{-1}\}$ at 350 GeV, with luminosities equally split into $P(e^-, e^+) = (\mp 0.8, \pm 0.3)$ beam polarizations. The shaded areas cover different assumptions about the precision of TGC measurements. LEFT: ILC measurements only. RIGHT: combination with differential single and double Higgs measurements at the HL-LHC.

$P(e^-, e^+) = (\mp 0.8, \pm 0.3)$	ILC alone		ILC + HL-LHC	
70% 30%	non-zero aTGCs	zero aTGCs	non-zero aTGCs	zero aTGCs
250 GeV(2/ab)	$[-4.98, +5.14]$	$[-4.68, +4.86]$	$[-0.84, +1.12]$	$[-0.85, +1.11]$
250 GeV(2/ab)+350 GeV(200/fb)	$[-1.18, +1.18]$	$[-1.12, +1.12]$	$[-0.71, +0.80]$	$[-0.69, +0.78]$
250 GeV(2/ab)+350 GeV(1.5/ab)	$[-0.62, +0.62]$	$[-0.54, +0.54]$	$[-0.50, +0.52]$	$[-0.47, +0.48]$

Table B.3: 1σ bounds on $\delta\kappa_\lambda$ from single-Higgs measurements at low-energy ILC. In this table we consider a benchmark scenario with integrated luminosity split into $P(e^-, e^+) = (\mp 0.8, \pm 0.3)$ beam polarization with a 70%/30% ratio.

As a last result, we show the impact of the inclusion of the $\delta\kappa_\lambda$ parameter in the global fit of the EFT operators. For definiteness, we focus on the circular lepton colliders benchmarks. For the fit, we use the 12 EFT parameters considered in the main text, namely

$$\delta c_Z\,,\quad c_{ZZ}\,,\quad c_{Z\Box}\,,\quad c_{\gamma\gamma}\,,\quad c_{Z\gamma}\,,\quad c_{gg}\,,\quad \delta y_t\,,\quad \delta y_c\,,\quad \delta y_b\,,\quad \delta y_\tau\,,\quad \delta y_\mu\,,\quad \lambda_Z\,. \tag{B.1}$$

As done in reference [118], it is convenient to slightly redefine the EFT parameters connected to the Higgs decays into $\gamma\gamma$, $Z\gamma$ and gg. In particular we define

$$\frac{\Gamma_{\gamma\gamma}}{\Gamma^{SM}_{\gamma\gamma}} \simeq 1 - 2\bar{c}_{\gamma\gamma}\,, \qquad \frac{\Gamma_{Z\gamma}}{\Gamma^{SM}_{Z\gamma}} \simeq 1 - 2\bar{c}_{Z\gamma}\,, \tag{B.2}$$

and

$$\frac{\Gamma_{gg}}{\Gamma^{SM}_{gg}} \simeq 1 + 2\bar{c}^{\,eff}_{gg} \simeq 1 + 2\,\bar{c}_{gg} + 2.10\,\delta y_t - 0.10\,\delta y_b\,, \tag{B.3}$$

with

$$\bar{c}_{\gamma\gamma} \simeq \frac{c_{\gamma\gamma}}{8.3\times 10^{-2}}\,, \qquad \bar{c}_{Z\gamma} \simeq \frac{c_{Z\gamma}}{5.9\times 10^{-2}}\,, \qquad \bar{c}_{gg} \simeq \frac{c_{gg}}{8.3\times 10^{-3}}\,. \tag{B.4}$$

$P(e^-, e^+) = (\mp 0.8, 0)$	ILC alone		ILC + HL-LHC	
50% 50%	non-zero aTGCs	zero aTGCs	non-zero aTGCs	zero aTGCs
250 GeV(2/ab)	$[-6.37, +6.58]$	$[-5.98, +6.27]$	$[-0.86, +1.13]$	$[-0.85, +1.13]$
250 GeV(2/ab)+350 GeV(200/fb)	$[-1.40, +1.40]$	$[-1.32, +1.32]$	$[-0.74, +0.87]$	$[-0.73, +0.85]$
250 GeV(2/ab)+350 GeV(1.5/ab)	$[-0.71, +0.71]$	$[-0.62, +0.62]$	$[-0.55, +0.59]$	$[-0.52, +0.54]$

Table B.4: $\Delta\chi^2 = 1$ bounds on $\delta\kappa_\lambda$ from single-Higgs measurements at low-energy ILC. In this table we consider a benchmark scenario with integrated luminosity equally split into $P(e^-, e^+) = (\mp 0.8, 0)$ beam polarization.

$P(e^-, e^+) = (\mp 0.8, 0)$	ILC alone		ILC + HL-LHC	
70% 30%	non-zero aTGCs	zero aTGCs	non-zero aTGCs	zero aTGCs
250 GeV(2/ab)	$[-5.61, +5.83]$	$[-5.27, +5.49]$	$[-0.85, +1.13]$	$[-0.85, +1.13]$
250 GeV(2/ab)+350 GeV(200/fb)	$[-1.32, +1.33]$	$[-1.25, +1.25]$	$[-0.73, +0.85]$	$[-0.72, +0.83]$
250 GeV(2/ab)+350 GeV(1.5/ab)	$[-0.69, +0.69]$	$[-0.60, +0.60]$	$[-0.54, +0.57]$	$[-0.50, +0.52]$

Table B.5: $\Delta\chi^2 = 1$ bounds on $\delta\kappa_\lambda$ from single-Higgs measurements at the low-energy ILC. In this table, we consider a benchmark scenario with integrated luminosity split into $P(e^-, e^+) = (\mp 0.8, 0)$ beam polarization with a 70%/30% ratio.

First of all, we focus on the fit obtained from low-energy lepton colliders only. In this case, the top Yukawa coupling and the Higgs contact interaction with gluons can not be accessed independently as they can only be tested through the Higgs decay into gg. The δy_t and c_{gg} parameters always appear in the combination as shown in Equation B.3. In the global fit we include only the $\bar{c}_{gg}^{\text{eff}}$ parameter and not c_{gg} and δy_t separately. The precision on the various EFT parameters with and without the inclusion of $\delta\kappa_\lambda$ is shown in the upper panel of Figure B.4. One can see that, if only a 240 GeV run is available, the inclusion of the Higgs self-coupling in the fit significantly degrades the precision on δc_Z and $\bar{c}_{gg}^{\text{eff}}$. In this case, as we already discussed in the text, the precision on $\delta\kappa_\lambda$ is very low. The situation changes drastically in the presence of runs at 350 GeV. In this case, the precision on $\bar{c}_{gg}^{\text{eff}}$ is effectively decoupled from the determination of the Higgs trilinear coupling. Some correlation of $\delta\kappa_\lambda$ with δc_Z is still present with 200 fb^{-1} of integrated luminosity at 350 GeV, while a much milder effect remains with 1.5 ab^{-1} of integrated luminosity.

In the lower panel of Figure B.4, we show the global fit obtained after combination with high-luminosity LHC measurements. In this case, the top Yukawa and the Higgs contact interaction with gluons can be independently tested. The results of the global fit show that the inclusion of the Higgs trilinear coupling affects only the determination of δc_Z. The impact is however much smaller than in the fit with lepton collider data only. The other EFT parameters are affected in a negligible way.

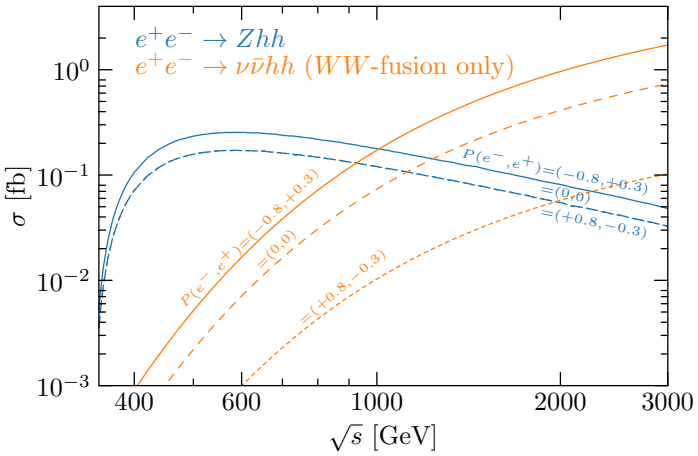

Figure B.3: Higgs pair production cross sections at as functions of the center-of-mass energy for different choices of the beam polarizations. The solid curves correspond to $P(e^-, e^+) = (-0.8, +0.3)$, the dotted ones to $P(e^-, e^+) = (+0.8, -0.3)$, and the dashed one to $P(e^-, e^+) = (0, 0)$. Notice that the dashed and dotted lines for $e^+e^- \to Zhh$ overlap with each other.

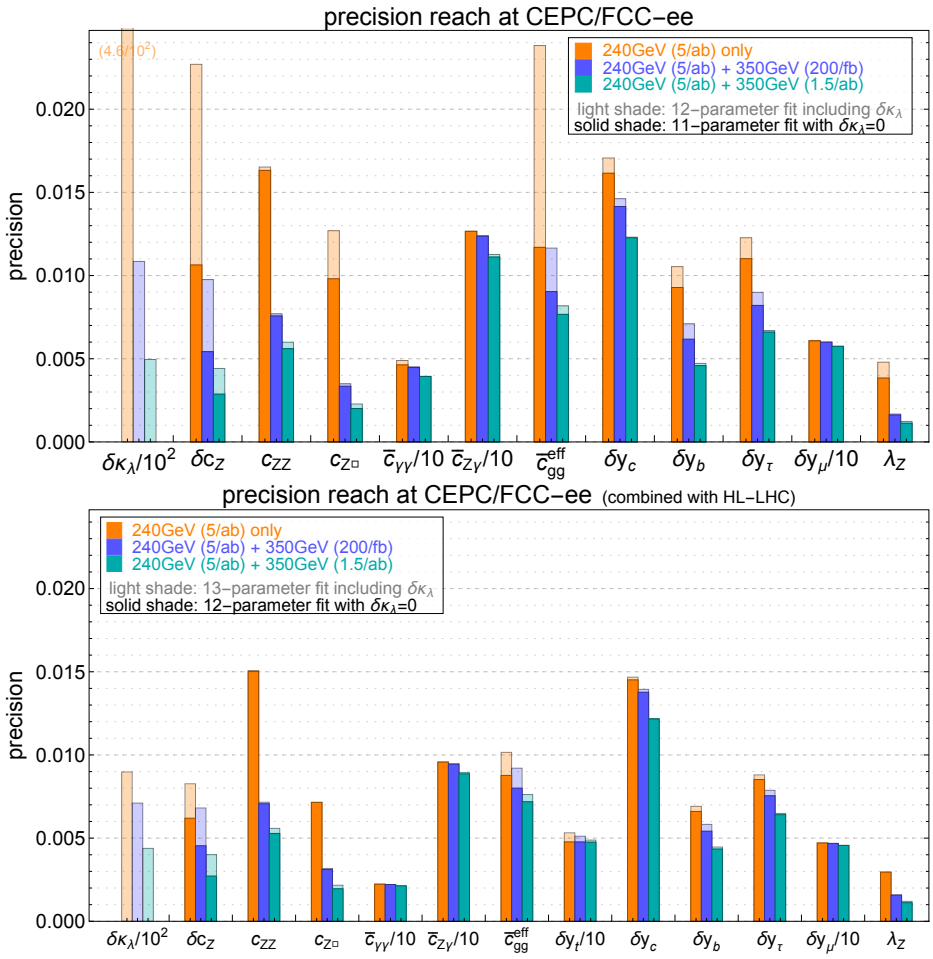

Figure B.4: Precision reach (one sigma constraints) at the CEPC with 5 ab^{-1} at 240 GeV and 200 fb^{-1} or 1.5 ab^{-1} integrated luminosity at 350 GeV. The upper panel shows the results of a global fit obtained from linear collider data only. The lower panel shows how the fit is modified by the inclusion of high-luminosity LHC measurements. The light-shade regions correspond to the full fit including $\delta\kappa_\lambda$, while the solid-shade regions correspond to the fit with $\delta\kappa_\lambda = 0$.

C

STATISTICAL REFINEMENT ON ASYMMETRY

In chapter 7, we studied several asymmetries sensitive to the CP properties of a scalar particle. While we used Monte Carlo simulations to generate our results, analytic methods could have been used instead. The expression of our asymmetry can be summarized as

$$A = \frac{R - L}{R + L}, \tag{C.1}$$

with R, L the number of event respectively on the right or left of the threshold value. In our case the threshold was $\frac{\Pi}{4}$. Defining $N = R + L$ as the total number of events, we can compute the probability to obtain an asymmetry value a:

$$\begin{aligned} P(\mathcal{A} = a) &= P\left(\frac{R - L}{R + L} = a\right) && \text{(C.2)} \\ &= P\left(L = \frac{N(1-a)}{2}\right) && \text{(C.3)} \\ &= \mathcal{B}\left(\frac{N(1-a)}{2}, N, p\right). && \text{(C.4)} \end{aligned}$$

Here $\mathcal{B}(k, n, p)$ is the binomial distribution with k the number of events with value on the left of the threshold, n the total number of events and p the probability to be on the left of the threshold. (Each event has a probability p to be on the left of the threshold and $1 - p$ to be on the right side. Repeating the experiment n time, we obtain the definition of the binomial and therefore $P(L = k) = \mathcal{B}(k, N, p)$.) The allowed values for the asymmetry are given by $\mathcal{A} \in \{\frac{N-2L}{N} \,|\, 0 \leqslant L \leqslant N \subset \mathbb{N}\}$. Using this fact, we can compute expected value and variance

$$\begin{aligned} E[\mathcal{A}] &= \sum_{L=0}^{N} \frac{N - 2L}{N} \mathcal{B}(l, N, p) = 1 - 2p\,, && \text{(C.5)} \\ \mathrm{Var}[\mathcal{A}] &= E\left[(\mathcal{A} - E[\mathcal{A}])^2\right] = -4\frac{p(p-1)}{N}\,. && \text{(C.6)} \end{aligned}$$

Integrating the distribution 7.5 and 7.10 taking into account the different contribution $\mathcal{A}_i$, we can obtain the probability

$$p = \sum_i \frac{\sigma_i \epsilon_i}{\sum_j \sigma_j \epsilon_j} \int_0^{\frac{\pi}{2}} \mathcal{A}_i \, d\theta\,. \tag{C.7}$$

The metric we used can be expressed by

$$\frac{d}{\sigma_{max}} = \frac{|m_O - m_E|}{\mathrm{Max}[\sigma_E, \sigma_O]} = \frac{|p_O - p_E|}{\sqrt{p(p-1)}}\sqrt{N}\,, \tag{C.8}$$

where the p in the denominator is the probability leading to the maximal variance and m denote the respective mean value. We checked that the plots 7.12 and 7.7 indeed reproduce the $\sqrt{N}$ behavior.

D

TOP PARTNERS PRODUCTION CROSS SECTION

In this appendix, We extend Table 1 and 2 of reference [251]. We give the numeric values for the production cross section of top partners at 13 TeV. The pair production is computed at next to next to leading order (NNLO) using `top++` [278], while single production in association with a W is approximated for an unit coupling at NLO following the method of reference [251] using `MCFM` [279–282].

M[GeV]	σ_{pair} [fb]	σ_{single} [fb]	M[GeV]	σ_{pair} [fb]	σ_{single} [fb]
500	3.36	1.56×10^{3}	2000	1.38×10^{-4}	2.23×10^{1}
600	1.16	1.08×10^{3}	2100	8.23×10^{-5}	1.76×10^{1}
700	4.55×10^{-1}	7.70×10^{2}	2200	4.93×10^{-5}	1.38×10^{1}
800	1.96×10^{-1}	5.57×10^{2}	2300	2.96×10^{-5}	1.09×10^{1}
900	9.03×10^{-2}	4.08×10^{2}	2400	1.77×10^{-5}	8.62
1000	4.4×10^{-2}	3.03×10^{2}	2500	1.06×10^{-5}	6.84
1100	2.24×10^{-2}	2.27×10^{2}	2600	6.34×10^{-6}	5.5
1200	1.18×10^{-2}	1.72×10^{2}	2700	3.77×10^{-6}	4.32
1300	6.39×10^{-3}	1.31×10^{2}	2800	2.23×10^{-6}	3.48
1400	3.54×10^{-3}	1.00×10^{2}	2900	1.31×10^{-6}	2.77
1500	2.00×10^{-3}	7.74×10^{1}	3000	7.6×10^{-7}	2.21
1600	1.15×10^{-3}	6.03×10^{1}	3100	4.38×10^{-7}	1.74
1700	6.66×10^{-4}	4.66×10^{1}	3200	2.5×10^{-7}	1.38
1800	3.91×10^{-4}	3.62×10^{1}	3300	1.41×10^{-7}	1.11
1900	2.31×10^{-4}	2.87×10^{1}	3400	7.87×10^{-8}	8.81×10^{-1}

Table D.1: Single and pair-production of top partners cross section.

GLOSSARY

ACME	advanced cold molecule electron EDM. 115–121, 123, 126, 128
aTGC	anomalous triple gauge coupling. 67, 68
ATLAS	a toroidal LHC apparatus. 1, 3, 31, 42, 46, 51, 53, 54, 57, 85, 88, 98, 118–120, 130, 137
BSM	beyond the standard model. 1, 13, 32, 34, 36, 37, 58, 61, 65, 66, 129, 130
C	charge conjugation. 17
CCWZ	Callan–Coleman–Wess–Zumino. 105
CEDM	chromoelectric dipole moment. 111, 114, 115, 117, 127
CEPC	circular electron positron collider. 61–63, 78, 79, 145
CERN	conseil européen pour la recherche nucléaire. 1, 61
CH	composite Higgs. 1, 2, 101, 102, 113, 126, 130
CKM	Cabibbo–Kobayashi–Maskawa. 13, 15, 17, 102
CLIC	compact linear collider. 61, 63, 71–78
CMB	cosmic microwave background. 17
CMS	compact muon solenoid. 1, 3, 31, 41, 42, 49, 53, 57, 85, 98, 118–120, 130
COM	center of mass. 32, 61, 62
CP	charge conjugation and parity. 2, 13–15, 17, 21, 23, 29, 33, 81, 85, 86, 90, 92, 94, 96–99, 102–113, 116–130, 147
DM	dark matter. 1, 130
EDM	electric dipole moment. 17, 102–104, 106–111, 113–120, 122, 123, 125–128
EFT	effective field theory. 1, 2, 18, 19, 24, 26, 31–34, 37–39, 45–49, 51–53, 55, 56, 58, 62, 63, 65–71, 73, 75–78, 80, 81, 85, 101, 129, 130, 134, 136–138, 143, 144
EW	electroweak. 10, 14, 21, 22, 31, 45, 81, 95, 98
EWSB	electroweak symmetry breaking. 9, 19, 29, 30

FCC future circular collider. 62, 82, 130
FCC-ee future circular collider (e^-e^+). 61–63, 78, 79
FCC-he future circular collider (hadron, electron). 62
FCC-hh future circular collider (proton, proton and ion, ion). 61, 120, 121, 128

GF gluon fusion. 86, 87, 91, 94, 96–98
ggF gluon gluon fusion. 42
GUT grand unification theory. 16, 17

HE-LHC high energy LHC. 62, 81
HL-LHC high luminosity LHC. 2, 29, 32, 35, 37, 39, 41–43, 45–47, 51, 54, 57, 58, 61, 62, 67–70, 73, 74, 76, 78, 79, 81, 82, 129, 130, 143

ILC international linear collider. 61, 62, 68–80, 120, 141–144
IR infrared. 103, 117

LEP large electron-positron collider. 21, 79
LHC large hadron collider. 1, 2, 16, 18, 19, 21, 25, 29, 31, 33, 36, 37, 39, 41, 42, 44, 47–50, 52, 62, 69, 70, 76, 81, 86–88, 98, 99, 101–104, 116–120, 126, 128, 130, 142, 144, 145
LHeC large hadron electron collider. 62
LO leading order. 21, 30, 31, 34, 35, 53, 63, 66, 134, 135, 137

MCHM$_5$ minimal composite Higgs model with the fermions in the **5** of SO(5). 102, 121, 123

NLO next to leading order. 31, 34, 35, 63, 66, 69, 78, 91, 136, 149
NNLO next to next to leading order. 149

PMNS Pontecorvo–Maki–Nakagawa–Sakata. 13

QCD quantum chromo-dynamics. 10, 16, 85, 91, 94, 95
QED quantum electrodynamics. 85
QFT quantum field theory. 7, 19

SILH	strongly interacting light Higgs. 37
SM	standard model. 1, 2, 7, 10, 12–14, 16–22, 24, 26, 29–39, 41–44, 46, 48, 50–53, 55, 57, 63–66, 69, 72–78, 81, 82, 85–88, 91–93, 95, 101–107, 115, 117, 127, 129, 130, 133, 134
SMEFT	standard model effective field theory. 57
SppC	super proton-proton Collider. 61
SUSY	super symmetry. 1
TGC	triple gauge coupling. 45, 46, 48, 49, 67, 70
UV	ultraviolet. 16, 17, 31, 34, 37, 101, 103, 105, 109, 117, 124
VBF	vector boson fusion. 42, 48, 51, 53, 86, 89, 91, 94–99
vev	vacuum expectation value. 10, 12, 17, 21, 25, 29, 40

BIBLIOGRAPHY

[1] G. Panico, M. Riembau, and T. Vantalon. "Probing light top partners with CP violation." In: (2017). arXiv: 1712.06337 [hep-ph].

[2] S. Di Vita, G. Durieux, C. Grojean, J. Gu, Z. Liu, G. Panico, M. Riembau, and T. Vantalon. "A global view on the Higgs self-coupling at lepton colliders." In: (2017). arXiv: 1711.03978 [hep-ph].

[3] S. Di Vita, C. Grojean, G. Panico, M. Riembau, and T. Vantalon. "A global view on the Higgs self-coupling." In: *JHEP* 09 (2017), p. 069. DOI: 10.1007/JHEP09(2017)069. arXiv: 1704.01953 [hep-ph].

[4] M. Chala, C. Grojean, M. Riembau, and T. Vantalon. "Deciphering the CP nature of the 750 GeV resonance." In: *Phys. Lett.* B760 (2016), pp. 220–227. DOI: 10.1016/j.physletb.2016.06.050. arXiv: 1604.02029 [hep-ph].

[5] L. Evans and P. Bryant. "LHC Machine." In: *JINST* 3 (2008), S08001. DOI: 10.1088/1748-0221/3/08/S08001.

[6] G. Aad et al. "Observation of a new particle in the search for the Standard Model Higgs boson with the ATLAS detector at the LHC." In: *Phys. Lett.* B716 (2012), pp. 1–29. DOI: 10.1016/j.physletb.2012.08.020. arXiv: 1207.7214 [hep-ex].

[7] S. Chatrchyan et al. "Observation of a new boson at a mass of 125 GeV with the CMS experiment at the LHC." In: *Phys. Lett.* B716 (2012), pp. 30–61. DOI: 10.1016/j.physletb.2012.08.021. arXiv: 1207.7235 [hep-ex].

[8] S. L. Glashow. "The renormalizability of vector meson interactions." In: *Nucl. Phys.* 10 (1959), pp. 107–117. DOI: 10.1016/0029-5582(59)90196-8.

[9] A. Salam and J. C. Ward. "Weak and electromagnetic interactions." In: *Nuovo Cim.* 11 (1959), pp. 568–577. DOI: 10.1007/BF02726525.

[10] S. Weinberg. "A Model of Leptons." In: *Phys. Rev. Lett.* 19 (1967), pp. 1264–1266. DOI: 10.1103/PhysRevLett.19.1264.

[11] P. W. Higgs. "Broken Symmetries and the Masses of Gauge Bosons." In: *Phys. Rev. Lett.* 13 (1964), pp. 508–509. DOI: 10.1103/PhysRevLett.13.508.

[12] F. Englert and R. Brout. "Broken Symmetry and the Mass of Gauge Vector Mesons." In: *Phys. Rev. Lett.* 13 (1964), pp. 321–323. DOI: 10.1103/PhysRevLett.13.321.

[13] G. S. Guralnik, C. R. Hagen, and T. W. B. Kibble. "Global Conservation Laws and Massless Particles." In: *Phys. Rev. Lett.* 13 (1964), pp. 585–587. DOI: 10.1103/PhysRevLett.13.585.

[14] R. Barbieri. *Ten Lectures on the ElectroWeak Interactions*. Scuola Normale Superiore, 2007. ISBN: 9788876423116. arXiv: 0706.0684 [hep-ph].

[15] M. Peskin and D. Schroeder. *An Introduction To Quantum Field Theory*. Frontiers in Physics. Avalon Publishing, 1995. ISBN: 9780813345437.

[16] M. Schwartz. *Quantum Field Theory and the Standard Model*. Quantum Field Theory and the Standard Model. Cambridge University Press, 2014. ISBN: 9781107034730.

[17] J. F. Donoghue, E. Golowich, and B. R. Holstein. *Dynamics of the Standard Model*. Cambridge Monographs on Particle Physics, Nuclear Physics and Cosmology. Cambridge University Press, 1992. DOI: 10.1017/CBO9780511524370.

[18] R. Contino. "The Higgs as a Composite Nambu-Goldstone Boson." In: *Physics of the large and the small, TASI 09, proceedings of the Theoretical Advanced Study Institute in Elementary Particle Physics, Boulder, Colorado, USA, 1-26 June 2009*. 2011, pp. 235–306. DOI: 10.1142/9789814327183_0005. arXiv: 1005.4269 [hep-ph]. URL: http://inspirehep.net/record/856065/files/arXiv:1005.4269.pdf.

[19] N. Cabibbo. "Unitary Symmetry and Leptonic Decays." In: *Phys. Rev. Lett.* 10 (1963). [,648(1963)], pp. 531–533. DOI: 10.1103/PhysRevLett.10.531.

[20] M. Kobayashi and T. Maskawa. "CP Violation in the Renormalizable Theory of Weak Interaction." In: *Prog. Theor. Phys.* 49 (1973), pp. 652–657. DOI: 10.1143/PTP.49.652.

[21] J. H. Christenson, J. W. Cronin, V. L. Fitch, and R. Turlay. "Evidence for the 2π Decay of the K_2^0 Meson." In: *Phys. Rev. Lett.* 13 (4 July 1964), pp. 138–140. DOI: 10.1103/PhysRevLett.13.138. URL: https://link.aps.org/doi/10.1103/PhysRevLett.13.138.

[22] B. Pontecorvo. "Inverse beta processes and nonconservation of lepton charge." In: *Sov. Phys. JETP* 7 (1958). [Zh. Eksp. Teor. Fiz.34,247(1957)], pp. 172–173.

[23] Z. Maki, M. Nakagawa, and S. Sakata. "Remarks on the unified model of elementary particles." In: *Prog. Theor. Phys.* 28 (1962), pp. 870–880. DOI: 10.1143/PTP.28.870.

[24] J. M. Pendlebury et al. "Revised experimental upper limit on the electric dipole moment of the neutron." In: *Phys. Rev.* D92.9 (2015), p. 092003. DOI: 10.1103/PhysRevD.92.092003. arXiv: 1509.04411 [hep-ex].

[25] C. Patrignani et al. "Review of Particle Physics." In: *Chin. Phys.* C40.10 (2016), p. 100001. DOI: 10.1088/1674-1137/40/10/100001.

[26] J. C. Pati and A. Salam. "Lepton Number as the Fourth Color." In: *Phys. Rev.* D10 (1974). [Erratum: Phys. Rev.D11,703(1975)], pp. 275–289. DOI: 10.1103/PhysRevD.10.275,10.1103/PhysRevD.11.703.2.

[27] H. Georgi and S. L. Glashow. "Unity of All Elementary Particle Forces." In: *Phys. Rev. Lett.* 32 (1974), pp. 438–441. DOI: 10.1103/PhysRevLett.32.438.

[28] R. D. Peccei and H. R. Quinn. "Constraints Imposed by CP Conservation in the Presence of Instantons." In: *Phys. Rev.* D16 (1977), pp. 1791–1797. DOI: 10.1103/PhysRevD.16.1791.

[29] R. D. Peccei and H. R. Quinn. "CP Conservation in the Presence of Instantons." In: *Phys. Rev. Lett.* 38 (1977), pp. 1440–1443. DOI: 10.1103/PhysRevLett.38.1440.

[30] A. D. Sakharov. "Violation of CP Invariance, c Asymmetry, and Baryon Asymmetry of the Universe." In: *Pisma Zh. Eksp. Teor. Fiz.* 5 (1967). [Usp. Fiz. Nauk161,61(1991)], pp. 32–35. DOI: 10.1070/PU1991v034n05ABEH002497.

[31] G. D'Amico, M. Nardecchia, P. Panci, F. Sannino, A. Strumia, R. Torre, and A. Urbano. "Flavour anomalies after the R_{K^*} measurement." In: *JHEP* 09 (2017), p. 010. DOI: 10.1007/JHEP09(2017)010. arXiv: 1704.05438 [hep-ph].

[32] G. W. Bennett et al. "Final Report of the Muon E821 Anomalous Magnetic Moment Measurement at BNL." In: *Phys. Rev.* D73 (2006), p. 072003. DOI: 10.1103/PhysRevD.73.072003. arXiv: hep-ex/0602035 [hep-ex].

[33] R. Alonso, E. E. Jenkins, A. V. Manohar, and M. Trott. "Renormalization Group Evolution of the Standard Model Dimension Six Operators III: Gauge Coupling Dependence and Phenomenology." In: *JHEP* 04 (2014), p. 159. DOI: 10.1007/JHEP04(2014)159. arXiv: 1312.2014 [hep-ph].

[34] B. Grzadkowski, M. Iskrzynski, M. Misiak, and J. Rosiek. "Dimension-Six Terms in the Standard Model Lagrangian." In: *JHEP* 10 (2010), p. 085. DOI: 10.1007/JHEP10(2010)085. arXiv: 1008.4884 [hep-ph].

[35] R. Contino, M. Ghezzi, C. Grojean, M. Muhlleitner, and M. Spira. "Effective Lagrangian for a light Higgs-like scalar." In: *JHEP* 07 (2013), p. 035. DOI: 10.1007/JHEP07(2013)035. arXiv: 1303.3876 [hep-ph].

[36] D. de Florian et al. "Handbook of LHC Higgs Cross Sections: 4. Deciphering the Nature of the Higgs Sector." In: (2016). DOI: 10.23731/CYRM-2017-002. arXiv: 1610.07922 [hep-ph].

[37] A. Falkowski. "Higgs Basis: Proposal for an EFT basis choice for LHC HXSWG." In: (Mar. 2015). URL: https://cds.cern.ch/record/2001958.

[38] G. Aad et al. "Study of the spin and parity of the Higgs boson in diboson decays with the ATLAS detector." In: *Eur. Phys. J.* C75.10 (2015). [Erratum: Eur. Phys. J.C76,no.3,152(2016)], p. 476. DOI: 10.1140/epjc/s10052-015-3685-1, 10.1140/epjc/s10052-016-3934-y. arXiv: 1506.05669 [hep-ex].

[39] V. Khachatryan et al. "Constraints on the spin-parity and anomalous HVV couplings of the Higgs boson in proton collisions at 7 and 8 TeV." In: *Phys. Rev.* D92.1 (2015), p. 012004. DOI: 10.1103/PhysRevD.92.012004. arXiv: 1411.3441 [hep-ex].

[40] G. Aad et al. "Measurements of the Higgs boson production and decay rates and constraints on its couplings from a combined ATLAS and CMS analysis of the LHC pp collision data at $\sqrt{s} = 7$ and 8 TeV." In: *JHEP* 08 (2016), p. 045. DOI: 10.1007/JHEP08(2016)045. arXiv: 1606.02266 [hep-ex].

[41] M. McCullough. "An Indirect Model-Dependent Probe of the Higgs Self-Coupling." In: *Phys. Rev.* D90.1 (2014). [Erratum: Phys. Rev.D92,no.3,039903(2015)], p. 015001. DOI: 10.1103/PhysRevD.90.015001, 10.1103/PhysRevD.92.039903. arXiv: 1312.3322 [hep-ph].

[42] M. Gorbahn and U. Haisch. "Indirect probes of the trilinear Higgs coupling: $gg \to h$ and $h \to \gamma\gamma$." In: *JHEP* 10 (2016), p. 094. DOI: 10.1007/JHEP10(2016)094. arXiv: 1607.03773 [hep-ph].

[43] G. Degrassi, P. P. Giardino, F. Maltoni, and D. Pagani. "Probing the Higgs self coupling via single Higgs production at the LHC." In: *JHEP* 12 (2016), p. 080. DOI: 10.1007/JHEP12(2016)080. arXiv: 1607.04251 [hep-ph].

[44] W. Bizon, M. Gorbahn, U. Haisch, and G. Zanderighi. "Constraints on the trilinear Higgs coupling from vector boson fusion and associated Higgs production at the LHC." In: *JHEP* 07 (2017), p. 083. DOI: 10.1007/JHEP07(2017)083. arXiv: 1610.05771 [hep-ph].

[45] M. Farina, G. Panico, D. Pappadopulo, J. T. Ruderman, R. Torre, and A. Wulzer. "Energy helps accuracy: electroweak precision tests at hadron colliders." In: *Phys. Lett.* B772 (2017), pp. 210–215. DOI: 10.1016/j.physletb.2017.06.043. arXiv: 1609.08157 [hep-ph].

[46] G. Degrassi, M. Fedele, and P. P. Giardino. "Constraints on the trilinear Higgs self coupling from precision observables." In: *JHEP* 04 (2017), p. 155. DOI: 10.1007/JHEP04(2017)155. arXiv: 1702.01737 [hep-ph].

[47] G. D. Kribs, A. Maier, H. Rzehak, M. Spannowsky, and P. Waite. "Electroweak oblique parameters as a probe of the trilinear Higgs boson self-interaction." In: *Phys. Rev.* D95.9 (2017), p. 093004. DOI: 10.1103/PhysRevD.95.093004. arXiv: 1702.07678 [hep-ph].

[48] S. Wertz. *Search for double Higgs production with the ATLAS and CMS experiments*. talk given at 'Higgs Couplings', Heidelberg. 2017.

[49] A. Falkowski. "Effective field theory approach to LHC Higgs data." In: *Pramana* 87.3 (2016), p. 39. DOI: 10.1007/s12043-016-1251-5. arXiv: 1505.00046 [hep-ph].

[50] A. Pomarol and F. Riva. "Towards the Ultimate SM Fit to Close in on Higgs Physics." In: *JHEP* 01 (2014), p. 151. DOI: 10.1007/JHEP01(2014)151. arXiv: 1308.2803 [hep-ph].

[51] A. Efrati, A. Falkowski, and Y. Soreq. "Electroweak constraints on flavorful effective theories." In: *JHEP* 07 (2015), p. 018. DOI: 10.1007/JHEP07(2015)018. arXiv: 1503.07872 [hep-ph].

[52] O. Bessidskaia Bylund, F. Maltoni, I. Tsinikos, E. Vryonidou, and C. Zhang. "Probing top quark neutral couplings in the Standard Model Effective Field Theory at NLO in QCD." In: *JHEP* 05 (2016), p. 052. DOI: 10.1007/JHEP05(2016)052. arXiv: 1601.08193 [hep-ph].

[53] D. Buarque Franzosi and C. Zhang. "Probing the top-quark chromomagnetic dipole moment at next-to-leading order in QCD." In: *Phys. Rev.* D91.11 (2015), p. 114010. DOI: 10.1103/PhysRevD.91.114010. arXiv: 1503.08841 [hep-ph].

[54] F. Maltoni, E. Vryonidou, and C. Zhang. "Higgs production in association with a top-antitop pair in the Standard Model Effective Field Theory at NLO in QCD." In: *JHEP* 10 (2016), p. 123. DOI: 10.1007/JHEP10(2016)123. arXiv: 1607.05330 [hep-ph].

[55] J. Elias-Miro, J. R. Espinosa, E. Masso, and A. Pomarol. "Higgs windows to new physics through d=6 operators: constraints and one-loop anomalous dimensions." In: *JHEP* 11 (2013), p. 066. DOI: 10.1007/JHEP11(2013)066. arXiv: 1308.1879 [hep-ph].

[56] The ATLAS collaboration. "Search for new phenomena in $t\bar{t}$ final states with additional heavy-flavour jets in pp collisions at $\sqrt{s} = 13$ TeV with the ATLAS detector." In: (2016).

[57] R. Contino, A. Falkowski, F. Goertz, C. Grojean, and F. Riva. "On the Validity of the Effective Field Theory Approach to SM Precision Tests." In: *JHEP* 07 (2016), p. 144. DOI: 10.1007/JHEP07(2016)144. arXiv: 1604.06444 [hep-ph].

[58] A. Azatov, R. Contino, G. Panico, and M. Son. "Effective field theory analysis of double Higgs boson production via gluon fusion." In: *Phys. Rev.* D92.3 (2015), p. 035001. DOI: 10.1103/PhysRevD.92.035001. arXiv: 1502.00539 [hep-ph].

[59] G. F. Giudice, C. Grojean, A. Pomarol, and R. Rattazzi. "The Strongly-Interacting Light Higgs." In: *JHEP* 06 (2007), p. 045. DOI: 10.1088/1126-6708/2007/06/045. arXiv: hep-ph/0703164 [hep-ph].

[60] G. Panico and A. Wulzer. "The Composite Nambu-Goldstone Higgs." In: *Lect. Notes Phys.* 913 (2016), pp.1–316. DOI: 10.1007/978-3-319-22617-0. arXiv: 1506.01961 [hep-ph].

[61] R. Contino et al. "Physics at a 100 TeV pp collider: Higgs and EW symmetry breaking studies." In: *CERN Yellow Report* 3 (2017), pp. 255–440. DOI: 10.23731/CYRM-2017-003.255. arXiv: 1606.09408 [hep-ph].

[62] J. de Blas, M. Chala, M. Perez-Victoria, and J. Santiago. "Observable Effects of General New Scalar Particles." In: *JHEP* 04 (2015), p. 078. DOI: 10.1007/JHEP04(2015)078. arXiv: 1412.8480 [hep-ph].

[63] A. Falkowski. *The validity of theories with a modified triple higgs coupling*. talk given at 'HH Subgroup Meeting', CERN. 2016.

[64] A. Falkowski and R. Rattazzi. "Which EFT?" to appear.

[65] "Projected Performance of an Upgraded CMS Detector at the LHC and HL-LHC: Contribution to the Snowmass Process." In: *Proceedings, 2013 Community Summer Study on the Future of U.S. Particle Physics: Snowmass on the Mississippi (CSS2013): Minneapolis, MN, USA, July 29-August 6, 2013*. 2013. arXiv: 1307.7135 [hep-ex]. URL: http://inspirehep.net/record/1244669/files/arXiv:1307.7135.pdf.

[66] M. E. Peskin. "Estimation of LHC and ILC Capabilities for Precision Higgs Boson Coupling Measurements." In: *Proceedings, 2013 Community Summer Study on the Future of U.S. Particle Physics: Snowmass on the Mississippi (CSS2013): Minneapolis, MN, USA, July 29-August 6, 2013*. 2013. arXiv: 1312.4974 [hep-ph]. URL: http://www.slac.stanford.edu/econf/C1307292/docs/submittedArxivFiles/1312.4974.pdf.

[67] *Projections for measurements of Higgs boson signal strengths and coupling parameters with the ATLAS detector at a HL-LHC*. Tech. rep. ATL-PHYS-PUB-2014-016. Geneva: CERN, Oct. 2014. URL: http://cds.cern.ch/record/1956710.

[68] C. Anastasiou, C. Duhr, F. Dulat, E. Furlan, T. Gehrmann, F. Herzog, A. Lazopoulos, and B. Mistlberger. "High precision determination of the gluon fusion Higgs boson cross-section at the LHC." In: *JHEP* 05 (2016), p. 058. DOI: 10.1007/JHEP05(2016)058. arXiv: 1602.00695 [hep-ph].

[69] *Prospective results for vector-boson fusion-mediated Higgs-boson searches in the four lepton final state at the High Luminosity Large Hadron Collider*. Tech. rep. ATL-PHYS-PUB-2016-008. Geneva: CERN, Apr. 2016. URL: http://cds.cern.ch/record/2145377.

[70] *Projections for measurements of Higgs boson cross sections, branching ratios and coupling parameters with the ATLAS detector at a HL-LHC*. Tech. rep. ATL-PHYS-PUB-2013-014. Geneva: CERN, Oct. 2013. URL: http://cds.cern.ch/record/1611186.

[71] C. Grojean, E. Salvioni, M. Schlaffer, and A. Weiler. "Very boosted Higgs in gluon fusion." In: *JHEP* 05 (2014), p. 022. DOI: 10.1007/JHEP05(2014)022. arXiv: 1312.3317 [hep-ph].

[72] A. Azatov, C. Grojean, A. Paul, and E. Salvioni. "Taming the off-shell Higgs boson." In: *Zh. Eksp. Teor. Fiz.* 147 (2015). [J. Exp. Theor. Phys.120,354(2015)], pp. 410–425. DOI: 10.1134/S1063776115030140,10.7868/S0044451015030039. arXiv: 1406.6338 [hep-ph].

[73] A. Azatov, C. Grojean, A. Paul, and E. Salvioni. "Resolving gluon fusion loops at current and future hadron colliders." In: *JHEP* 09 (2016), p. 123. DOI: 10.1007/JHEP09(2016)123. arXiv: 1608.00977 [hep-ph].

[74] A. Butter, O. J. P. Éboli, J. Gonzalez-Fraile, M. C. Gonzalez-Garcia, T. Plehn, and M. Rauch. "The Gauge-Higgs Legacy of the LHC Run I." In: *JHEP* 07 (2016), p. 152. DOI: 10.1007/JHEP07(2016)152. arXiv: 1604.03105 [hep-ph].

[75] A. Falkowski, M. Gonzalez-Alonso, A. Greljo, D. Marzocca, and M. Son. "Anomalous Triple Gauge Couplings in the Effective Field Theory Approach at the LHC." In: *JHEP* 02 (2017), p. 115. DOI: 10.1007/JHEP02(2017)115. arXiv: 1609.06312 [hep-ph].

[76] *Update of the prospects for the $H \to Z\gamma$ search at the High-Luminosity LHC*. Tech. rep. ATL-PHYS-PUB-2014-006. Geneva: CERN, May 2014. URL: http://cds.cern.ch/record/1703276.

[77] N. Kauer and G. Passarino. "Inadequacy of zero-width approximation for a light Higgs boson signal." In: *JHEP* 08 (2012), p. 116. DOI: 10.1007/JHEP08(2012)116. arXiv: 1206.4803 [hep-ph].

[78] F. Caola and K. Melnikov. "Constraining the Higgs boson width with ZZ production at the LHC." In: *Phys. Rev.* D88 (2013), p. 054024. DOI: 10.1103/PhysRevD.88.054024. arXiv: 1307.4935 [hep-ph].

[79] J. M. Campbell, R. K. Ellis, and C. Williams. "Bounding the Higgs width at the LHC using full analytic results for $gg- > e^-e^+\mu^-\mu^+$." In: *JHEP* 04 (2014), p. 060. DOI: 10.1007/JHEP04(2014)060. arXiv: 1311.3589 [hep-ph].

[80] V. Khachatryan et al. "Constraints on the Higgs boson width from off-shell production and decay to Z-boson pairs." In: *Phys. Lett.* B736 (2014), pp. 64–85. DOI: 10.1016/j.physletb.2014.06.077. arXiv: 1405.3455 [hep-ex].

[81] G. Aad et al. "Constraints on the off-shell Higgs boson signal strength in the high-mass ZZ and *WW* final states with the ATLAS detector." In: *Eur. Phys. J.* C75.7 (2015), p. 335. DOI: 10.1140/epjc/s10052-015-3542-2. arXiv: 1503.01060 [hep-ex].

[82] C. Englert and M. Spannowsky. "Limitations and Opportunities of Off-Shell Coupling Measurements." In: *Phys. Rev.* D90 (2014), p. 053003. DOI: 10.1103/PhysRevD.90.053003. arXiv: 1405.0285 [hep-ph].

[83] G. Cacciapaglia, A. Deandrea, G. Drieu La Rochelle, and J.-B. Flament. "Higgs couplings: disentangling New Physics with off-shell measurements." In: *Phys. Rev. Lett.* 113.20 (2014), p. 201802. DOI: 10.1103/PhysRevLett.113.201802. arXiv: 1406.1757 [hep-ph].

[84] *Off-shell Higgs signal strength measurement using high-mass H→ZZ→ 4l events at High Luminosity LHC*. Tech. rep. ATL-PHYS-PUB-2015-024. Geneva: CERN, July 2015. URL: https://cds.cern.ch/record/2037715.

[85] S. Biswas, E. Gabrielli, and B. Mele. "Single top and Higgs associated production as a probe of the Htt coupling sign at the LHC." In: *JHEP* 01 (2013), p. 088. DOI: 10.1007/JHEP01(2013)088. arXiv: 1211.0499 [hep-ph].

[86] M. Farina, C. Grojean, F. Maltoni, E. Salvioni, and A. Thamm. "Lifting degeneracies in Higgs couplings using single top production in association with a Higgs boson." In: *JHEP* 05 (2013), p. 022. DOI: 10.1007/JHEP05(2013)022. arXiv: 1211.3736 [hep-ph].

[87] F. Demartin, F. Maltoni, K. Mawatari, and M. Zaro. "Higgs production in association with a single top quark at the LHC." In: *Eur. Phys. J.* C75.6 (2015), p. 267. DOI: 10.1140/epjc/s10052-015-3475-9. arXiv: 1504.00611 [hep-ph].

[88] F. Bishara, U. Haisch, P. F. Monni, and E. Re. "Constraining Light-Quark Yukawa Couplings from Higgs Distributions." In: *Phys. Rev. Lett.* 118.12 (2017), p. 121801. DOI: 10.1103/PhysRevLett.118.121801. arXiv: 1606.09253 [hep-ph].

[89] G. Bonner and H. E. Logan. "Constraining the Higgs couplings to up and down quarks using production kinematics at the CERN Large Hadron Collider." In: (2016). arXiv: 1608.04376 [hep-ph].

[90] H. Khanpour, S. Khatibi, and M. Mohammadi Najafabadi. "Probing Higgs boson couplings in H+γ production at the LHC." In: *Phys. Lett.* B773 (2017), pp. 462–469. DOI: 10.1016/j.physletb.2017.09.005. arXiv: 1702.05753 [hep-ph].

[91] M. Farina, C. Grojean, and E. Salvioni. "(Dys)Zphilia or a custodial breaking Higgs at the LHC." In: *JHEP* 07 (2012), p. 012. DOI: 10.1007/JHEP07(2012)012. arXiv: 1205.0011 [hep-ph].

[92] *Higgs cross section working group*. https://cern.ch/twiki/bin/view/LHCPhysics/LHCHXSWG.

[93] Q.-H. Cao, Y. Liu, and B. Yan. "Measuring trilinear Higgs coupling in WHH and ZHH productions at the high-luminosity LHC." In: *Phys. Rev.* D95.7 (2017), p. 073006. DOI: 10.1103/PhysRevD.95.073006. arXiv: 1511.03311 [hep-ph].

[94] V. D. Barger, T. Han, and R. J. N. Phillips. "Double Higgs Boson Bremsstrahlung From *W* and Z Bosons at Supercolliders." In: *Phys. Rev.* D38 (1988), p. 2766. DOI: 10.1103/PhysRevD.38.2766.

[95] M. Moretti, S. Moretti, F. Piccinini, R. Pittau, and A. D. Polosa. "Higgs boson self-couplings at the LHC as a probe of extended Higgs sectors." In: *JHEP* 02 (2005), p. 024. DOI: 10.1088/1126-6708/2005/02/024. arXiv: hep-ph/0410334 [hep-ph].

[96] J. Baglio, A. Djouadi, R. Gröber, M. M. Mühlleitner, J. Quevillon, and M. Spira. "The measurement of the Higgs self-coupling at the LHC: theoretical status." In: *JHEP* 04 (2013), p. 151. DOI: 10.1007/JHEP04(2013)151. arXiv: 1212.5581 [hep-ph].

[97] R. Contino, C. Grojean, M. Moretti, F. Piccinini, and R. Rattazzi. "Strong Double Higgs Production at the LHC." In: *JHEP* 05 (2010), p. 089. DOI: 10.1007/JHEP05(2010)089. arXiv: 1002.1011 [hep-ph].

[98] M. J. Dolan, C. Englert, N. Greiner, and M. Spannowsky. "Further on up the road: hhjj production at the LHC." In: *Phys. Rev. Lett.* 112 (2014), p. 101802. DOI: 10.1103/PhysRevLett.112.101802. arXiv: 1310.1084 [hep-ph].

[99] M. J. Dolan, C. Englert, N. Greiner, K. Nordstrom, and M. Spannowsky. "hhjj production at the LHC." In: *Eur. Phys. J.* C75.8 (2015), p. 387. DOI: 10.1140/epjc/s10052-015-3622-3. arXiv: 1506.08008 [hep-ph].

[100] F. Bishara, R. Contino, and J. Rojo. "Higgs pair production in vector-boson fusion at the LHC and beyond." In: *Eur. Phys. J.* C77.7 (2017), p. 481. DOI: 10.1140/epjc/s10052-017-5037-9. arXiv: 1611.03860 [hep-ph].

[101] U. Baur, T. Plehn, and D. L. Rainwater. "Probing the Higgs selfcoupling at hadron colliders using rare decays." In: *Phys. Rev.* D69 (2004), p. 053004. DOI: 10.1103/PhysRevD.69.053004. arXiv: hep-ph/0310056 [hep-ph].

[102] R. Grober and M. Muhlleitner. "Composite Higgs Boson Pair Production at the LHC." In: *JHEP* 06 (2011), p. 020. DOI: 10.1007/JHEP06(2011)020. arXiv: 1012.1562 [hep-ph].

[103] R. Contino, M. Ghezzi, M. Moretti, G. Panico, F. Piccinini, and A. Wulzer. "Anomalous Couplings in Double Higgs Production." In: *JHEP* 08 (2012), p. 154. DOI: 10.1007/JHEP08(2012)154. arXiv: 1205.5444 [hep-ph].

[104] V. Barger, L. L. Everett, C. B. Jackson, and G. Shaughnessy. "Higgs-Pair Production and Measurement of the Triscalar Coupling at LHC(8,14)." In: *Phys. Lett.* B728 (2014), pp. 433–436. DOI: 10.1016/j.physletb.2013.12.013. arXiv: 1311.2931 [hep-ph].

[105] H.-J. He, J. Ren, and W. Yao. "Probing new physics of cubic Higgs boson interaction via Higgs pair production at hadron colliders." In: *Phys. Rev.* D93.1 (2016), p. 015003. DOI: 10.1103/PhysRevD.93.015003. arXiv: 1506.03302 [hep-ph].

[106] *Prospects for measuring Higgs pair production in the channel* $H(\to \gamma\gamma)H(\to b\bar{b})$ *using the ATLAS detector at the HL-LHC*. Tech. rep. ATL-PHYS-PUB-2014-019. Geneva: CERN, Oct. 2014. URL: http://cds.cern.ch/record/1956733.

[107] *Study of the double Higgs production channel* $H(\to b\bar{b})H(\to \gamma\gamma)$ *with the ATLAS experiment at the HL-LHC*. Tech. rep. ATL-PHYS-PUB-2017-001. Geneva: CERN, Jan. 2017. URL: http://cds.cern.ch/record/2243387.

[108] U. Baur, T. Plehn, and D. L. Rainwater. "Examining the Higgs boson potential at lepton and hadron colliders: A Comparative analysis." In: *Phys. Rev.* D68 (2003), p. 033001. DOI: 10.1103/PhysRevD.68.033001. arXiv: hep-ph/0304015 [hep-ph].

[109] M. J. Dolan, C. Englert, and M. Spannowsky. "Higgs self-coupling measurements at the LHC." In: *JHEP* 10 (2012), p. 112. DOI: 10.1007/JHEP10(2012)112. arXiv: 1206.5001 [hep-ph].

[110] D. E. Ferreira de Lima, A. Papaefstathiou, and M. Spannowsky. "Standard model Higgs boson pair production in the ($b\bar{b}$)($b\bar{b}$) final state." In: *JHEP* 08 (2014), p. 030. DOI: 10.1007/JHEP08(2014)030. arXiv: 1404.7139 [hep-ph].

[111] *Projected sensitivity to non-resonant Higgs boson pair production in the* $b\bar{b}b\bar{b}$ *final state using proton–proton collisions at HL-LHC with the ATLAS detector*. Tech. rep. ATL-PHYS-PUB-2016-024. Geneva: CERN, Oct. 2016. URL: https://cds.cern.ch/record/2221658.

[112] A. Papaefstathiou, L. L. Yang, and J. Zurita. "Higgs boson pair production at the LHC in the $b\bar{b}W^+W^-$ channel." In: *Phys. Rev.* D87.1 (2013), p. 011301. DOI: 10.1103/PhysRevD.87.011301. arXiv: 1209.1489 [hep-ph].

[113] A. J. Barr, M. J. Dolan, C. Englert, and M. Spannowsky. "Di-Higgs final states augMT2ed – selecting hh events at the high luminosity LHC." In: *Phys. Lett.* B728 (2014), pp. 308–313. DOI: 10.1016/j.physletb.2013.12.011. arXiv: 1309.6318 [hep-ph].

[114] F. Goertz, A. Papaefstathiou, L. L. Yang, and J. Zurita. "Higgs boson pair production in the D=6 extension of the SM." In: *JHEP* 04 (2015), p. 167. DOI: 10.1007/JHEP04(2015)167. arXiv: 1410.3471 [hep-ph].

[115] Q.-H. Cao, B. Yan, D.-M. Zhang, and H. Zhang. "Resolving the Degeneracy in Single Higgs Production with Higgs Pair Production." In: *Phys. Lett.* B752 (2016), pp. 285–290. DOI: 10.1016/j.physletb.2015.11.045. arXiv: 1508.06512 [hep-ph].

[116] Q.-H. Cao, G. Li, B. Yan, D.-M. Zhang, and H. Zhang. "Double Higgs production at the 14 TeV LHC and the 100 TeV pp-collider." In: (2016). arXiv: 1611.09336 [hep-ph].

[117] S. Boselli, C. M. Carloni Calame, G. Montagna, O. Nicrosini, F. Piccinini, and A. Shivaji. "Higgs decay into four charged leptons in the presence of dimension-six operators." In: (2017). arXiv: 1703.06667 [hep-ph].

[118] G. Durieux, C. Grojean, J. Gu, and K. Wang. "The leptonic future of the Higgs." In: *JHEP* 09 (2017), p. 014. DOI: 10.1007/JHEP09(2017)014. arXiv: 1704.02333 [hep-ph].

[119] T. Barklow, K. Fujii, S. Jung, M. E. Peskin, and J. Tian. "Model-Independent Determination of the Triple Higgs Coupling at e^+e^- Colliders." In: (2017). arXiv: 1708.09079 [hep-ph].

[120] T. Barklow, K. Fujii, S. Jung, R. Karl, J. List, T. Ogawa, M. E. Peskin, and J. Tian. "Improved Formalism for Precision Higgs Coupling Fits." In: (2017). arXiv: 1708.08912 [hep-ph].

[121] J. de Blas, M. Ciuchini, E. Franco, S. Mishima, M. Pierini, L. Reina, and L. Silvestrini. "Electroweak precision observables and Higgs-boson signal strengths in the Standard Model and beyond: present and future." In: *JHEP* 12 (2016), p. 135. DOI: 10.1007/JHEP12(2016)135. arXiv: 1608.01509 [hep-ph].

[122] B. Henning, X. Lu, and H. Murayama. "What do precision Higgs measurements buy us?" In: (2014). arXiv: 1404.1058 [hep-ph].

[123] J. Ellis, P. Roloff, V. Sanz, and T. You. "Dimension-6 Operator Analysis of the CLIC Sensitivity to New Physics." In: (2017). arXiv: 1701.04804 [hep-ph].

[124] S.-F. Ge, H.-J. He, and R.-Q. Xiao. "Probing new physics scales from Higgs and electroweak observables at e^+e^- Higgs factory." In: *JHEP* 10 (2016), p. 007. DOI: 10.1007/JHEP10(2016)007. arXiv: 1603.03385 [hep-ph].

[125] N. Craig, M. Farina, M. McCullough, and M. Perelstein. "Precision Higgsstrahlung as a Probe of New Physics." In: *JHEP* 03 (2015), p. 146. DOI: 10.1007/JHEP03(2015)146. arXiv: 1411.0676 [hep-ph].

[126] J. Ellis and T. You. "Sensitivities of Prospective Future e^+e^- Colliders to Decoupled New Physics." In: *JHEP* 03 (2016), p. 089. DOI: 10.1007/JHEP03(2016)089. arXiv: 1510.04561 [hep-ph].

[127] H. Khanpour and M. Mohammadi Najafabadi. "Constraining Higgs boson effective couplings at electron-positron colliders." In: *Phys. Rev.* D95.5 (2017), p. 055026. DOI: 10.1103/PhysRevD.95.055026. arXiv: 1702.00951 [hep-ph].

[128] R. Contino, C. Grojean, D. Pappadopulo, R. Rattazzi, and A. Thamm. "Strong Higgs Interactions at a Linear Collider." In: *JHEP* 02 (2014), p. 006. DOI: 10.1007/JHEP02(2014)006. arXiv: 1309.7038 [hep-ph].

[129] A. Blondel. *Summary FCC-ee experiments*. Presentation at the FCC Week, Berlin. June 2017. URL: https://indico.cern.ch/event/556692/contributions/2487579/attachments/1469993/2274251/99-Blondel-FCC-ee-summary-Berlin.pdf.

[130] M. Ruan. *Status & Updates from CEPC Simulation -Detector optimization, IAS HKUST*. Jan. 2017. URL: http://ias.ust.hk/program/shared_doc/2017/201701hep/HEP_20170124_Manqi_Ruan.pdf.

[131] P. Janot. "Physics Perspectives for a Future Circular Collider: FCC-ee." In: (Nov. 2017). URL: https://indico.cern.ch/event/666889/.

[132] K. Fujii et al. "Physics Case for the International Linear Collider." In: (2015). arXiv: 1506.05992 [hep-ex].

[133] T. Barklow, J. Brau, K. Fujii, J. Gao, J. List, N. Walker, and K. Yokoya. "ILC Operating Scenarios." In: (2015). arXiv: 1506.07830 [hep-ex].

[134] J. J. van der Bij. "Does Low-energy Physics Depend on the Potential of a Heavy Higgs Particle?" In: *Nucl. Phys.* B267 (1986), pp. 557–565. DOI: 10.1016/0550-3213(86)90131-8.

[135] C. Shen and S.-h. Zhu. "Anomalous Higgs-top coupling pollution of the triple Higgs coupling extraction at a future high-luminosity electron-positron collider." In: *Phys. Rev.* D92.9 (2015), p. 094001. DOI: 10.1103/PhysRevD.92.094001. arXiv: 1504.05626 [hep-ph].

[136] F. Maltoni, D. Pagani, A. Shivaji, and X. Zhao. "Trilinear Higgs coupling determination via single-Higgs differential measurements at the LHC." In: (2017). arXiv: 1709.08649 [hep-ph].

[137] M. Beneke, D. Boito, and Y.-M. Wang. "Anomalous Higgs couplings in angular asymmetries of $H \to Z\ell^+\ell^-$ and $e^+ e^- \to HZ$." In: *JHEP* 11 (2014), p. 028. DOI: 10.1007/JHEP11(2014)028. arXiv: 1406.1361 [hep-ph].

[138] N. Craig, J. Gu, Z. Liu, and K. Wang. "Beyond Higgs Couplings: Probing the Higgs with Angular Observables at Future $e^+ e^-$ Colliders." In: *JHEP* 03 (2016), p. 050. DOI: 10.1007/JHEP03(2016)050. arXiv: 1512.06877 [hep-ph].

[139] C. F. Dürig. "Measuring the Higgs Self-coupling at the International Linear Collider." In: *DESY-THESIS-2016-027* (). DOI: 10.3204/PUBDB-2016-04283.

[140] H. Abramowicz et al. "Higgs physics at the CLIC electron–positron linear collider." In: *Eur. Phys. J.* C77.7 (2017), p. 475. DOI: 10.1140/epjc/s10052-017-4968-5. arXiv: 1608.07538 [hep-ex].

[141] J. Tian and K. Fujii. "Measurement of Higgs couplings and self-coupling at the ILC." In: *PoS* EPS-HEP2013 (2013), p. 316. arXiv: 1311.6528 [hep-ph].

[142] C. F. Dürig, J. Tian, J. List, K. Fujii, and M. Kurata. *Update on Higgs self-coupling analyses for ILD*. Apr. 2015. URL: https://agenda.linearcollider.org/event/6557/contributions/31788/attachments/26208/40162/duerig_alcw2015.pdf.

[143] J. Alwall, R. Frederix, S. Frixione, V. Hirschi, F. Maltoni, O. Mattelaer, H. .-.-S. Shao, T. Stelzer, P. Torrielli, and M. Zaro. "The automated computation of tree-level and next-to-leading order differential cross sections, and their matching to parton shower simulations." In: *JHEP* 07 (2014), p. 079. DOI: 10.1007/JHEP07(2014)079. arXiv: 1405.0301 [hep-ph].

[144] A. Alloul, N. D. Christensen, C. Degrande, C. Duhr, and B. Fuks. "FeynRules 2.0 - A complete toolbox for tree-level phenomenology." In: *Comput. Phys. Commun.* 185 (2014), pp. 2250–2300. DOI: 10.1016/j.cpc.2014.04.012. arXiv: 1310.1921 [hep-ph].

[145] A. Falkowski, B. Fuks, K. Mawatari, K. Mimasu, F. Riva, and V. Sanz. "Rosetta: an operator basis translator for Standard Model effective field theory." In: *Eur. Phys. J.* C75.12 (2015), p. 583. DOI: 10.1140/epjc/s10052-015-3806-x. arXiv: 1508.05895 [hep-ph].

[146] B. Fuks and K. Mawatari. "BSMC Characterisation." In: *FeynRules Model* (). URL: http://feynrules.irmp.ucl.ac.be/wiki/BSMCharacterisation.

[147] D. Goncalves, T. Han, F. Kling, T. Plehn, and M. Takeuchi. "Higgs Pair Production at Future Hadron Colliders: From Kinematics to Dynamics." In: (2018). arXiv: 1802.04319 [hep-ph].

[148] The ATLAS collaboration. "Search for resonances decaying to photon pairs in 3.2 fb^{-1} of pp collisions at $\sqrt{s}$ = 13 TeV with the ATLAS detector." In: (2015).

[149] CMS Collaboration. "Search for new physics in high mass diphoton events in proton-proton collisions at 13TeV." In: (2015).

[150] The corresponding talks are available in https://indico.in2p3.fr/event/12279/session/12/contribution/163/material/slides/1.pdf and https://indico.in2p3.fr/event/12279/session/12/contribution/218/material/slides/0.pdf.

[151] A complete list of references can be found in, http://inspirehep.net/search?p=refersto%3Arecid%3A1410174.

[152] Y. Kats and M. J. Strassler. "Resonances from QCD bound states and the 750 GeV diphoton excess." In: *JHEP* 05 (2016). [Erratum: JHEP07,044(2016)], p. 092. DOI: 10.1007/JHEP05(2016)092,10.1007/JHEP07(2016)044. arXiv: 1602.08819 [hep-ph].

[153] R. Franceschini, G. F. Giudice, J. F. Kamenik, M. McCullough, A. Pomarol, R. Rattazzi, M. Redi, F. Riva, A. Strumia, and R. Torre. "What is the $\gamma\gamma$ resonance at 750 GeV?" In: *JHEP* 03 (2016), p. 144. DOI: 10.1007/JHEP03(2016)144. arXiv: 1512.04933 [hep-ph].

[154] The ATLAS and CMS Collaborations. "Measurements of the Higgs boson production and decay rates and constraints on its couplings from a combined ATLAS and CMS analysis of the LHC pp collision data at $\sqrt{s}$ = 7 and 8 TeV." In: (2015).

[155] G. Aad et al. "Search for an additional, heavy Higgs boson in the $H \to ZZ$ decay channel at $\sqrt{s} = 8$ TeV in pp collision data with the ATLAS detector." In: *Eur. Phys. J.* C76.1 (2016), p. 45. DOI: 10.1140/epjc/s10052-015-3820-z. arXiv: 1507.05930 [hep-ex].

[156] CMS Collaboration. "Search for an Higgs Like resonance in the diphoton mass spectra above 150 GeV with 8 TeV data." In: (2014).

[157] G. Aad et al. "Search for high-mass diphoton resonances in pp collisions at $\sqrt{s} = 8$ TeV with the ATLAS detector." In: *Phys. Rev.* D92.3 (2015), p. 032004. DOI: 10.1103/PhysRevD.92.032004. arXiv: 1504.05511 [hep-ex].

[158] L. A. Harland-Lang, V. A. Khoze, and M. G. Ryskin. "The production of a diphoton resonance via photon-photon fusion." In: *JHEP* 03 (2016), p. 182. DOI: 10.1007/JHEP03(2016)182. arXiv: 1601.07187 [hep-ph].

[159] G. Panico, L. Vecchi, and A. Wulzer. "Resonant Diphoton Phenomenology Simplified." In: *JHEP* 06 (2016), p. 184. DOI: 10.1007/JHEP06(2016)184. arXiv: 1603.04248 [hep-ph].

[160] G. Aad et al. "Search for new resonances in $W\gamma$ and $Z\gamma$ final states in pp collisions at $\sqrt{s} = 8$ TeV with the ATLAS detector." In: *Phys. Lett.* B738 (2014), pp. 428–447. DOI: 10.1016/j.physletb.2014.10.002. arXiv: 1407.8150 [hep-ex].

[161] V. Khachatryan et al. "Search for a Higgs boson in the mass range from 145 to 1000 GeV decaying to a pair of W or Z bosons." In: *JHEP* 10 (2015), p. 144. DOI: 10.1007/JHEP10(2015)144. arXiv: 1504.00936 [hep-ex].

[162] G. Aad et al. "Search for a high-mass Higgs boson decaying to a W boson pair in pp collisions at $\sqrt{s} = 8$ TeV with the ATLAS detector." In: *JHEP* 01 (2016), p. 032. DOI: 10.1007/JHEP01(2016)032. arXiv: 1509.00389 [hep-ex].

[163] A. Alves, A. G. Dias, and K. Sinha. "The 750 GeV S-cion: Where else should we look for it?" In: *Phys. Lett.* B757 (2016), pp. 39–46. DOI: 10.1016/j.physletb.2016.03.052. arXiv: 1512.06091 [hep-ph].

[164] F. Staub et al. "Precision tools and models to narrow in on the 750 GeV diphoton resonance." In: *Eur. Phys. J.* C76.9 (2016), p. 516. DOI: 10.1140/epjc/s10052-016-4349-5. arXiv: 1602.05581 [hep-ph].

[165] G. Aad et al. "Search for new phenomena in events with at least three photons collected in pp collisions at $\sqrt{s}$ = 8 TeV with the ATLAS detector." In: *Eur. Phys. J.* C76.4 (2016), p. 210. DOI: 10.1140/epjc/s10052-016-4034-8. arXiv: 1509.05051 [hep-ex].

[166] J. D. Bjorken. "Rapidity gaps and jets as a new physics signature in very high-energy hadron hadron collisions." In: *Phys. Rev.* D47 (1993), pp. 101–113. DOI: 10.1103/PhysRevD.47.101.

[167] V. Del Duca, G. Klamke, D. Zeppenfeld, M. L. Mangano, M. Moretti, F. Piccinini, R. Pittau, and A. D. Polosa. "Monte Carlo studies of the jet activity in Higgs + 2 jet events." In: *JHEP* 10 (2006), p. 016. DOI: 10.1088/1126-6708/2006/10/016. arXiv: hep-ph/0608158 [hep-ph].

[168] J. F. Kamenik, B. R. Safdi, Y. Soreq, and J. Zupan. "Comments on the diphoton excess: critical reappraisal of effective field theory interpretations." In: *JHEP* 07 (2016), p. 042. DOI: 10.1007/JHEP07(2016)042. arXiv: 1603.06566 [hep-ph].

[169] G. Aad et al. "Search for new phenomena in the dijet mass distribution using $p-p$ collision data at $\sqrt{s} = 8$ TeV with the ATLAS detector." In: *Phys. Rev.* D91.5 (2015), p. 052007. DOI: 10.1103/PhysRevD.91.052007. arXiv: 1407.1376 [hep-ex].

[170] CMS Collaboration. "Search for Resonances Decaying to Dijet Final States at $\sqrt{s} = 8$ TeV with Scouting Data." In: (2015).

[171] M. Chala, M. Duerr, F. Kahlhoefer, and K. Schmidt-Hoberg. "Tricking Landau–Yang: How to obtain the diphoton excess from a vector resonance." In: *Phys. Lett.* B755 (2016), pp. 145–149. DOI: 10.1016/j.physletb.2016.02.006. arXiv: 1512.06833 [hep-ph].

[172] D. J. Miller, S. Y. Choi, B. Eberle, M. M. Muhlleitner, and P. M. Zerwas. "Measuring the spin of the Higgs boson." In: *Phys. Lett.* B505 (2001). [,1825(2001)], pp. 149–154. DOI: 10.1016/S0370-2693(01)00317-3. arXiv: hep-ph/0102023 [hep-ph].

[173] S. Y. Choi, D. J. Miller, M. M. Muhlleitner, and P. M. Zerwas. "Identifying the Higgs spin and parity in decays to Z pairs." In: *Phys. Lett.* B553 (2003), pp. 61–71. DOI: 10.1016/S0370-2693(02)03191-X. arXiv: hep-ph/0210077 [hep-ph].

[174] T. Aaltonen et al. "Tevatron Constraints on Models of the Higgs Boson with Exotic Spin and Parity Using Decays to Bottom-Antibottom Quark Pairs." In: *Phys. Rev. Lett.* 114.15 (2015), p. 151802. DOI: 10.1103/PhysRevLett.114.151802. arXiv: 1502.00967 [hep-ex].

[175] A. Djouadi, J. Ellis, R. Godbole, and J. Quevillon. "Future Collider Signatures of the Possible 750 GeV State." In: *JHEP* 03 (2016), p. 205. DOI: 10.1007/JHEP03(2016)205. arXiv: 1601.03696 [hep-ph].

[176] R. Godbole, D. J. Miller, K. Mohan, and C. D. White. "Boosting Higgs CP properties via VH Production at the Large Hadron Collider." In: *Phys. Lett.* B730 (2014), pp. 275–279. DOI: 10.1016/j.physletb.2014.01.069. arXiv: 1306.2573 [hep-ph].

[177] R. D. Ball et al. "Parton distributions with LHC data." In: *Nucl. Phys.* B867 (2013), pp. 244–289. DOI: 10.1016/j.nuclphysb.2012.10.003. arXiv: 1207.1303 [hep-ph].

[178] N. F. da Silva Fernandes de Castro. "Study of the Wtb vertex structure at the ATLAS experiment." PhD thesis. Coimbra U., 2008. URL: http://weblib.cern.ch/abstract?CERN-THESIS-2008-083.

[179] D. Stolarski and R. Vega-Morales. "Probing a Virtual Diphoton Excess." In: *Phys. Rev.* D93.5 (2016), p. 055008. DOI: 10.1103/PhysRevD.93.055008. arXiv: 1601.02004 [hep-ph].

[180] T. Sjostrand, S. Mrenna, and P. Z. Skands. "PYTHIA 6.4 Physics and Manual." In: *JHEP* 05 (2006), p. 026. DOI: 10.1088/1126-6708/2006/05/026. arXiv: hep-ph/0603175 [hep-ph].

[181] E. Conte, B. Dumont, B. Fuks, and C. Wymant. "Designing and recasting LHC analyses with MadAnalysis 5." In: *Eur. Phys. J.* C74.10 (2014), p. 3103. DOI: 10.1140/epjc/s10052-014-3103-0. arXiv: 1405.3982 [hep-ph].

[182] The ATLAS collaboration. "Study of the spin and parity of the Higgs boson in HVV decays with the ATLAS detector." In: (2015).

[183] F. Bishara, Y. Grossman, R. Harnik, D. J. Robinson, J. Shu, and J. Zupan. "Probing CP Violation in $h \to \gamma\gamma$ with Converted Photons." In: *JHEP* 04 (2014), p. 084. DOI: 10.1007/JHEP04(2014)084. arXiv: 1312.2955 [hep-ph].

[184] C. Englert, D. Goncalves-Netto, K. Mawatari, and T. Plehn. "Higgs Quantum Numbers in Weak Boson Fusion." In: *JHEP* 01 (2013), p. 148. DOI: 10.1007/JHEP01(2013)148. arXiv: 1212.0843 [hep-ph].

[185] A. Djouadi, R. M. Godbole, B. Mellado, and K. Mohan. "Probing the spin-parity of the Higgs boson via jet kinematics in vector boson fusion." In: *Phys. Lett.* B723 (2013), pp. 307–313. DOI: 10.1016/j.physletb.2013.04.060. arXiv: 1301.4965 [hep-ph].

[186] Y. Chen, E. Di Marco, J. Lykken, M. Spiropulu, R. Vega-Morales, and S. Xie. "8D likelihood effective Higgs couplings extraction framework in $h \to 4\ell$." In: *JHEP* 01 (2015), p. 125. DOI: 10.1007/JHEP01(2015)125. arXiv: 1401.2077 [hep-ex].

[187] B. Bellazzini, C. Csáki, and J. Serra. "Composite Higgses." In: *Eur. Phys. J.* C74.5 (2014), p. 2766. DOI: 10.1140/epjc/s10052-014-2766-x. arXiv: 1401.2457 [hep-ph].

[188] D. B. Kaplan and H. Georgi. "SU(2) x U(1) Breaking by Vacuum Misalignment." In: *Phys. Lett.* 136B (1984), pp. 183–186. DOI: 10.1016/0370-2693(84)91177-8.

[189] D. B. Kaplan, H. Georgi, and S. Dimopoulos. "Composite Higgs Scalars." In: *Phys. Lett.* 136B (1984), pp. 187–190. DOI: 10.1016/0370-2693(84)91178-X.

[190] H. Georgi, D. B. Kaplan, and P. Galison. "Calculation of the Composite Higgs Mass." In: *Phys. Lett.* 143B (1984), pp. 152–154. DOI: 10.1016/0370-2693(84)90823-2.

[191] T. Banks. "CONSTRAINTS ON SU(2) x U(1) BREAKING BY VACUUM MISALIGNMENT." In: *Nucl. Phys.* B243 (1984), pp. 125–130. DOI: 10.1016/0550-3213(84)90389-4.

[192] H. Georgi and D. B. Kaplan. "Composite Higgs and Custodial SU(2)." In: *Phys. Lett.* 145B (1984), pp. 216–220. DOI: 10.1016/0370-2693(84)90341-1.

[193] M. J. Dugan, H. Georgi, and D. B. Kaplan. "Anatomy of a Composite Higgs Model." In: *Nucl. Phys.* B254 (1985), pp. 299–326. DOI: 10.1016/0550-3213(85)90221-4.

[194] S. Dimopoulos and J. Preskill. "Massless Composites With Massive Constituents." In: *Nucl. Phys.* B199 (1982), pp. 206–222. DOI: 10.1016/0550-3213(82)90345-5.

[195] K. Agashe, R. Contino, and A. Pomarol. "The Minimal composite Higgs model." In: *Nucl. Phys.* B719 (2005), pp. 165–187. DOI: 10.1016/j.nuclphysb.2005.04.035. arXiv: hep-ph/0412089 [hep-ph].

[196] D. B. Kaplan. "Flavor at SSC energies: A New mechanism for dynamically generated fermion masses." In: *Nucl. Phys.* B365 (1991), pp. 259–278. DOI: 10.1016/S0550-3213(05)80021-5.

[197] R. Contino, L. Da Rold, and A. Pomarol. "Light custodians in natural composite Higgs models." In: *Phys. Rev.* D75 (2007), p. 055014. DOI: 10.1103/PhysRevD.75.055014. arXiv: hep-ph/0612048 [hep-ph].

[198] O. Matsedonskyi, G. Panico, and A. Wulzer. "Light Top Partners for a Light Composite Higgs." In: *JHEP* 01 (2013), p. 164. DOI: 10.1007/JHEP01(2013)164. arXiv: 1204.6333 [hep-ph].

[199] D. Marzocca, M. Serone, and J. Shu. "General Composite Higgs Models." In: *JHEP* 08 (2012), p. 013. DOI: 10.1007/JHEP08(2012)013. arXiv: 1205.0770 [hep-ph].

[200] A. Pomarol and F. Riva. "The Composite Higgs and Light Resonance Connection." In: *JHEP* 08 (2012), p. 135. DOI: 10.1007/JHEP08(2012)135. arXiv: 1205.6434 [hep-ph].

[201] G. Panico, M. Redi, A. Tesi, and A. Wulzer. "On the Tuning and the Mass of the Composite Higgs." In: *JHEP* 03 (2013), p. 051. DOI: 10.1007/JHEP03(2013)051. arXiv: 1210.7114 [hep-ph].

[202] M. Aaboud et al. "Search for pair production of heavy vector-like quarks decaying to high-p_T W bosons and b quarks in the lepton-plus-jets final state in pp collisions at $\sqrt{s} = 13$ TeV with the ATLAS detector." In: *JHEP* 10 (2017), p. 141. DOI: 10.1007/JHEP10(2017)141. arXiv: 1707.03347 [hep-ex].

[203] CMS Collaboration. "Search for top quark partners with charge 5/3 in the single-lepton final state at $\sqrt{s} = 13$ TeV." In: (2017).

[204] C. Anastasiou, E. Furlan, and J. Santiago. "Realistic Composite Higgs Models." In: *Phys. Rev.* D79 (2009), p. 075003. DOI: 10.1103/PhysRevD.79.075003. arXiv: 0901.2117 [hep-ph].

[205] C. Grojean, O. Matsedonskyi, and G. Panico. "Light top partners and precision physics." In: *JHEP* 10 (2013), p. 160. DOI: 10.1007/JHEP10(2013)160. arXiv: 1306.4655 [hep-ph].

[206] M. Carena, L. Da Rold, and E. Pontón. "Minimal Composite Higgs Models at the LHC." In: *JHEP* 06 (2014), p. 159. DOI: 10.1007/JHEP06(2014)159. arXiv: 1402.2987 [hep-ph].

[207] S. M. Barr and A. Zee. "Electric Dipole Moment of the Electron and of the Neutron." In: *Phys. Rev. Lett.* 65 (1990). [Erratum: Phys. Rev. Lett.65,2920(1990)], pp. 21–24. DOI: 10.1103/PhysRevLett.65.21.

[208] M. König, M. Neubert, and D. M. Straub. "Dipole operator constraints on composite Higgs models." In: *Eur. Phys. J.* C74.7 (2014), p. 2945. DOI: 10.1140/epjc/s10052-014-2945-9. arXiv: 1403.2756 [hep-ph].

[209] S. Weinberg. "Larger Higgs Exchange Terms in the Neutron Electric Dipole Moment." In: *Phys. Rev. Lett.* 63 (1989), p. 2333. DOI: 10.1103/PhysRevLett.63.2333.

[210] J. Brod, U. Haisch, and J. Zupan. "Constraints on CP-violating Higgs couplings to the third generation." In: *JHEP* 11 (2013), p. 180. DOI: 10.1007/JHEP11(2013)180. arXiv: 1310.1385 [hep-ph].

[211] J. Kopp and M. Nardecchia. "Flavor and CP violation in Higgs decays." In: *JHEP* 10 (2014), p. 156. DOI: 10.1007/JHEP10(2014)156. arXiv: 1406.5303 [hep-ph].

[212] Y. T. Chien, V. Cirigliano, W. Dekens, J. de Vries, and E. Mereghetti. "Direct and indirect constraints on CP-violating Higgs-quark and Higgs-gluon interactions." In: *JHEP* 02 (2016). [JHEP02,011(2016)], p. 011. DOI: 10.1007/JHEP02(2016)011. arXiv: 1510.00725 [hep-ph].

[213] V. Cirigliano, W. Dekens, J. de Vries, and E. Mereghetti. "Constraining the top-Higgs sector of the Standard Model Effective Field Theory." In: *Phys. Rev.* D94.3 (2016), p. 034031. DOI: 10.1103/PhysRevD.94.034031. arXiv: 1605.04311 [hep-ph].

[214] K. Fuyuto and M. Ramsey-Musolf. "Top Down Electroweak Dipole Operators." In: (2017). arXiv: 1706.08548 [hep-ph].

[215] J. Baron et al. "Order of Magnitude Smaller Limit on the Electric Dipole Moment of the Electron." In: *Science* 343 (2014), pp. 269–272. DOI: 10.1126/science.1248213. arXiv: 1310.7534 [physics.atom-ph].

[216] J. Baron et al. "Methods, Analysis, and the Treatment of Systematic Errors for the Electron Electric Dipole Moment Search in Thorium Monoxide." In: *New J. Phys.* 19.7 (2017), p. 073029. DOI: 10.1088/1367-2630/aa708e. arXiv: 1612.09318 [physics.atom-ph].

[217] W. B. Cairncross, D. N. Gresh, M. Grau, K. C. Cossel, T. S. Roussy, Y. Ni, Y. Zhou, J. Ye, and E. A. Cornell. "Precision Measurement of the Electron's Electric Dipole Moment Using Trapped Molecular Ions." In: *Phys. Rev. Lett.* 119.15 (2017), p. 153001. DOI: 10.1103/PhysRevLett.119.153001. arXiv: 1704.07928 [physics.atom-ph].

[218] C. A. Baker et al. "An Improved experimental limit on the electric dipole moment of the neutron." In: *Phys. Rev. Lett.* 97 (2006), p. 131801. DOI: 10.1103/PhysRevLett.97.131801. arXiv: hep-ex/0602020 [hep-ex].

[219] B. Graner, Y. Chen, E. G. Lindahl, and B. R. Heckel. "Reduced Limit on the Permanent Electric Dipole Moment of Hg199." In: *Phys. Rev. Lett.* 116.16 (2016). [Erratum: Phys. Rev. Lett.119,no.11,119901(2017)], p. 161601. DOI: 10.1103/PhysRevLett.119.119901,10.1103/PhysRevLett.116.161601. arXiv: 1601.04339 [physics.atom-ph].

[220] R. Picker. "How the minuscule can contribute to the big picture: the neutron electric dipole moment project at TRIUMF." In: *JPS Conf. Proc.* 13 (2017), p. 010005. DOI: 10.7566/JPSCP.13.010005. arXiv: 1612.00875 [physics.ins-det].

[221] Doyle. J. Doyle, "Search for the Electric Dipole Moment of the Electron with Thorium Monoxide – The ACME Experiment," 2016. http://online.kitp.ucsb.edu/online/nuclear_c16/doyle/. Talk at the KITP Conference: Symmetry Tests in Nuclei and Atoms.

[222] A. De Simone, O. Matsedonskyi, R. Rattazzi, and A. Wulzer. "A First Top Partner Hunter's Guide." In: *JHEP* 04 (2013), p. 004. DOI: 10.1007/JHEP04(2013)004. arXiv: 1211.5663 [hep-ph].

[223] Y. Grossman and M. Neubert. "Neutrino masses and mixings in nonfactorizable geometry." In: *Phys. Lett.* B474 (2000), pp. 361–371. DOI: 10.1016/S0370-2693(00)00054-X. arXiv: hep-ph/9912408 [hep-ph].

[224] T. Gherghetta and A. Pomarol. "Bulk fields and supersymmetry in a slice of AdS." In: *Nucl. Phys.* B586 (2000), pp. 141–162. DOI: 10.1016/S0550-3213(00)00392-8. arXiv: hep-ph/0003129 [hep-ph].

[225] S. J. Huber and Q. Shafi. "Fermion masses, mixings and proton decay in a Randall-Sundrum model." In: *Phys. Lett.* B498 (2001), pp. 256–262. DOI: 10.1016/S0370-2693(00)01399-X. arXiv: hep-ph/0010195 [hep-ph].

[226] S. J. Huber. "Flavor violation and warped geometry." In: *Nucl. Phys.* B666 (2003), pp. 269–288. DOI: 10.1016/S0550-3213(03)00502-9. arXiv: hep-ph/0303183 [hep-ph].

[227] K. Agashe, G. Perez, and A. Soni. "Flavor structure of warped extra dimension models." In: *Phys. Rev.* D71 (2005), p. 016002. DOI: 10.1103/PhysRevD.71.016002. arXiv: hep-ph/0408134 [hep-ph].

[228] C. Csaki, A. Falkowski, and A. Weiler. "The Flavor of the Composite Pseudo-Goldstone Higgs." In: *JHEP* 09 (2008), p. 008. DOI: 10.1088/1126-6708/2008/09/008. arXiv: 0804.1954 [hep-ph].

[229] C. Csaki, A. Falkowski, and A. Weiler. "A Simple Flavor Protection for RS." In: *Phys. Rev.* D80 (2009), p. 016001. DOI: 10.1103/PhysRevD.80.016001. arXiv: 0806.3757 [hep-ph].

[230] O. Gedalia, G. Isidori, and G. Perez. "Combining Direct & Indirect Kaon CP Violation to Constrain the Warped KK Scale." In: *Phys. Lett.* B682 (2009), pp. 200–206. DOI: 10.1016/j.physletb.2009.10.097. arXiv: 0905.3264 [hep-ph].

[231] K. Agashe and R. Contino. "Composite Higgs-Mediated FCNC." In: *Phys. Rev.* D80 (2009), p. 075016. DOI: 10.1103/PhysRevD.80.075016. arXiv: 0906.1542 [hep-ph].

[232] M. Bauer, S. Casagrande, U. Haisch, and M. Neubert. "Flavor Physics in the Randall-Sundrum Model: II. Tree-Level Weak-Interaction Processes." In: *JHEP* 09 (2010), p. 017. DOI: 10.1007/JHEP09(2010)017. arXiv: 0912.1625 [hep-ph].

[233] N. Vignaroli. "Δ F=1 constraints on composite Higgs models with LR parity." In: *Phys. Rev.* D86 (2012), p. 115011. DOI: 10.1103/PhysRevD.86.115011. arXiv: 1204.0478 [hep-ph].

[234] R. Barbieri, D. Buttazzo, F. Sala, D. M. Straub, and A. Tesi. "A 125 GeV composite Higgs boson versus flavour and electroweak precision tests." In: *JHEP* 05 (2013), p. 069. DOI: 10.1007/JHEP05(2013)069. arXiv: 1211.5085 [hep-ph].

[235] A. Azatov, G. Panico, G. Perez, and Y. Soreq. "On the Flavor Structure of Natural Composite Higgs Models & Top Flavor Violation." In: *JHEP* 12 (2014), p. 082. DOI: 10.1007/JHEP12(2014)082. arXiv: 1408.4525 [hep-ph].

[236] J. Yepes and A. Zerwekh. "Top partner-resonance interplay in a composite Higgs framework." In: (2017). arXiv: 1711.10523 [hep-ph].

[237] B. Keren-Zur, P. Lodone, M. Nardecchia, D. Pappadopulo, R. Rattazzi, and L. Vecchi. "On Partial Compositeness and the CP asymmetry in charm decays." In: *Nucl. Phys.* B867 (2013), pp. 394–428. DOI: 10.1016/j.nuclphysb.2012.10.012. arXiv: 1205.5803 [hep-ph].

[238] M. Redi and A. Weiler. "Flavor and CP Invariant Composite Higgs Models." In: *JHEP* 11 (2011), p. 108. DOI: 10.1007/JHEP11(2011)108. arXiv: 1106.6357 [hep-ph].

[239] R. Barbieri, D. Buttazzo, F. Sala, and D. M. Straub. "Flavour physics from an approximate $U(2)^3$ symmetry." In: *JHEP* 07 (2012), p. 181. DOI: 10.1007/JHEP07(2012)181. arXiv: 1203.4218 [hep-ph].

[240] M. Redi. "Leptons in Composite MFV." In: *JHEP* 09 (2013), p. 060. DOI: 10.1007/JHEP09(2013)060. arXiv: 1306.1525 [hep-ph].

[241] C. Delaunay, O. Gedalia, S. J. Lee, G. Perez, and E. Ponton. "Ultra Visible Warped Model from Flavor Triviality and Improved Naturalness." In: *Phys. Rev.* D83 (2011), p. 115003. DOI: 10.1103/PhysRevD.83.115003. arXiv: 1007.0243 [hep-ph].

[242] C. Delaunay, O. Gedalia, S. J. Lee, G. Perez, and E. Ponton. "Extraordinary Phenomenology from Warped Flavor Triviality." In: *Phys. Lett.* B703 (2011), pp. 486–490. DOI: 10.1016/j.physletb.2011.08.031. arXiv: 1101.2902 [hep-ph].

[243] L. Da Rold, C. Delaunay, C. Grojean, and G. Perez. "Up Asymmetries From Exhilarated Composite Flavor Structures." In: *JHEP* 02 (2013), p. 149. DOI: 10.1007/JHEP02(2013)149. arXiv: 1208.1499 [hep-ph].

[244] C. Delaunay, C. Grojean, and G. Perez. "Modified Higgs Physics from Composite Light Flavors." In: *JHEP* 09 (2013), p. 090. DOI: 10.1007/JHEP09(2013)090. arXiv: 1303.5701 [hep-ph].

[245] M. Redi, V. Sanz, M. de Vries, and A. Weiler. "Strong Signatures of Right-Handed Compositeness." In: *JHEP* 08 (2013), p. 008. DOI: 10.1007/JHEP08(2013)008. arXiv: 1305.3818.

[246] C. Delaunay, T. Flacke, J. Gonzalez-Fraile, S. J. Lee, G. Panico, and G. Perez. "Light Non-degenerate Composite Partners at the LHC." In: *JHEP* 02 (2014), p. 055. DOI: 10.1007/JHEP02(2014)055. arXiv: 1311.2072 [hep-ph].

[247] L. Vecchi. "A Flavor Sector for the Composite Higgs." In: *Phys. Lett.* B727 (2013), pp. 130–135. DOI: 10.1016/j.physletb.2013.08.006. arXiv: 1206.4701 [hep-ph].

[248] O. Matsedonskyi. "On Flavour and Naturalness of Composite Higgs Models." In: *JHEP* 02 (2015), p. 154. DOI: 10.1007/JHEP02(2015)154. arXiv: 1411.4638 [hep-ph].

[249] G. Cacciapaglia, H. Cai, T. Flacke, S. J. Lee, A. Parolini, and H. Serôdio. "Anarchic Yukawas and top partial compositeness: the flavour of a successful marriage." In: *JHEP* 06 (2015), p. 085. DOI: 10.1007/JHEP06(2015)085. arXiv: 1501.03818 [hep-ph].

[250] G. Panico and A. Pomarol. "Flavor hierarchies from dynamical scales." In: *JHEP* 07 (2016), p. 097. DOI: 10.1007/JHEP07(2016)097. arXiv: 1603.06609 [hep-ph].

[251] O. Matsedonskyi, G. Panico, and A. Wulzer. "Top Partners Searches and Composite Higgs Models." In: *JHEP* 04 (2016), p. 003. DOI: 10.1007/JHEP04(2016)003. arXiv: 1512.04356 [hep-ph].

[252] S. R. Coleman, J. Wess, and B. Zumino. "Structure of phenomenological Lagrangians. 1." In: *Phys. Rev.* 177 (1969), pp. 2239–2247. DOI: 10.1103/PhysRev.177.2239.

[253] C. G. Callan Jr., S. R. Coleman, J. Wess, and B. Zumino. "Structure of phenomenological Lagrangians. 2." In: *Phys. Rev.* 177 (1969), pp. 2247–2250. DOI: 10.1103/PhysRev.177.2247.

[254] D. Stockinger. "The Muon Magnetic Moment and Supersymmetry." In: *J. Phys.* G34 (2007), R45–R92. DOI: 10.1088/0954-3899/34/2/R01. arXiv: hep-ph/0609168 [hep-ph].

[255] D. A. Dicus. "Neutron Electric Dipole Moment From Charged Higgs Exchange." In: *Phys. Rev.* D41 (1990), p. 999. DOI: 10.1103/PhysRevD.41.999.

[256] G. Aad et al. "Constraints on new phenomena via Higgs boson couplings and invisible decays with the ATLAS detector." In: *JHEP* 11 (2015), p. 206. DOI: 10.1007/JHEP11(2015)206. arXiv: 1509.00672 [hep-ex].

[257] *CMS at the High-Energy Frontier. Contribution to the Update of the European Strategy for Particle Physics*. Tech. rep. CMS-NOTE-2012-006. CERN-CMS-NOTE-2012-006. Geneva: CERN, Oct. 2012. URL: https://cds.cern.ch/record/1494600.

[258] S. Dawson et al. "Working Group Report: Higgs Boson." In: *Proceedings, 2013 Community Summer Study on the Future of U.S. Particle Physics: Snowmass on the Mississippi (CSS2013): Minneapolis, MN, USA, July 29-August 6, 2013*. 2013. arXiv: 1310.8361 [hep-ex]. URL: http://inspirehep.net/record/1262795/files/arXiv:1310.8361.pdf.

[259] CMS Collaboration. "Search for heavy vector-like quarks decaying to same-sign dileptons." In: (2017).

[260] The ATLAS collaboration. "Search for new physics using events with b-jets and a pair of same charge leptons in 3.2 fb^{-1} of pp collisions at $\sqrt{s} = 13$ TeV with the ATLAS detector." In: (2016).

[261] O. Matsedonskyi, G. Panico, and A. Wulzer. "On the Interpretation of Top Partners Searches." In: *JHEP* 12 (2014), p. 097. DOI: 10.1007/JHEP12(2014)097. arXiv: 1409.0100 [hep-ph].

[262] A. M. Sirunyan et al. "Search for single production of a vector-like T quark decaying to a Z boson and a top quark in proton-proton collisions at sqrt(s) = 13 TeV." In: (2017). arXiv: 1708.01062 [hep-ex].

[263] A. M. Sirunyan et al. "Search for single production of vector-like quarks decaying to a Z boson and a top or a bottom quark in proton-proton collisions at $\sqrt{s} = 13$ TeV." In: *JHEP* 05 (2017), p. 029. DOI: 10.1007/JHEP05(2017)029. arXiv: 1701.07409 [hep-ex].

[264] V. Khachatryan et al. "Search for single production of a heavy vector-like T quark decaying to a Higgs boson and a top quark with a lepton and jets in the final state." In: *Phys. Lett.* B771 (2017), pp. 80–105. DOI: 10.1016/j.physletb.2017.05.019. arXiv: 1612.00999 [hep-ex].

[265] CMS Collaboration. "Search for a singly produced vector-like quark B decaying to a b quark and a Higgs boson in a fully hadronic final state using boosted topologies." In: (2017).

[266] The ATLAS collaboration. "Search for single production of vector-like quarks decaying into Wb in pp collisions at $\sqrt{s} = 13$ TeV with the ATLAS detector." In: (2016).

[267] A. M. Sirunyan et al. "Search for single production of vector-like quarks decaying into a b quark and a W boson in proton-proton collisions at $\sqrt{s} = 13$ TeV." In: *Phys. Lett.* B772 (2017), pp. 634–656. DOI: 10.1016/j.physletb.2017.07.022. arXiv: 1701.08328 [hep-ex].

[268] G. Panico and A. Wulzer. "The Discrete Composite Higgs Model." In: *JHEP* 09 (2011), p. 135. DOI: 10.1007/JHEP09(2011)135. arXiv: 1106.2719 [hep-ph].

[269] S. De Curtis, M. Redi, and A. Tesi. "The 4D Composite Higgs." In: *JHEP* 04 (2012), p. 042. DOI: 10.1007/JHEP04(2012)042. arXiv: 1110.1613 [hep-ph].

[270] R. Contino and A. Pomarol. "Holography for fermions." In: *JHEP* 11 (2004), p. 058. DOI: 10.1088/1126-6708/2004/11/058. arXiv: hep-th/0406257 [hep-th].

[271] G. Panico and A. Wulzer. "Effective action and holography in 5D gauge theories." In: *JHEP* 05 (2007), p. 060. DOI: 10.1088/1126-6708/2007/05/060. arXiv: hep-th/0703287 [hep-th].

[272] A. Alloul, B. Fuks, and V. Sanz. "Phenomenology of the Higgs Effective Lagrangian via FEYNRULES." In: *JHEP* 04 (2014), p. 110. DOI: 10.1007/JHEP04(2014)110. arXiv: 1310.5150 [hep-ph].

[273] C. Hartmann and M. Trott. "Higgs Decay to Two Photons at One Loop in the Standard Model Effective Field Theory." In: *Phys. Rev. Lett.* 115.19 (2015), p. 191801. DOI: 10.1103/PhysRevLett.115.191801. arXiv: 1507.03568 [hep-ph].

[274] E. Conte, B. Fuks, and G. Serret. "MadAnalysis 5, A User-Friendly Framework for Collider Phenomenology." In: *Comput. Phys. Commun.* 184 (2013), pp. 222–256. DOI: 10.1016/j.cpc.2012.09.009. arXiv: 1206.1599 [hep-ph].

[275] T. Hahn and M. Perez-Victoria. "Automatized one loop calculations in four-dimensions and D-dimensions." In: *Comput. Phys. Commun.* 118 (1999), pp. 153–165. DOI: 10.1016/S0010-4655(98)00173-8. arXiv: hep-ph/9807565 [hep-ph].

[276] T. Hahn. "Generating Feynman diagrams and amplitudes with FeynArts 3." In: *Comput. Phys. Commun.* 140 (2001), pp. 418–431. DOI: 10.1016/S0010-4655(01)00290-9. arXiv: hep-ph/0012260 [hep-ph].

[277] T. Hahn. "CUBA: A Library for multidimensional numerical integration." In: *Comput. Phys. Commun.* 168 (2005), pp. 78–95. DOI: 10.1016/j.cpc.2005.01.010. arXiv: hep-ph/0404043 [hep-ph].

[278] M. Czakon and A. Mitov. "Top++: A Program for the Calculation of the Top-Pair Cross-Section at Hadron Colliders." In: *Comput. Phys. Commun.* 185 (2014), p. 2930. DOI: 10.1016/j.cpc.2014.06.021. arXiv: 1112.5675 [hep-ph].

[279] J. M. Campbell and R. K. Ellis. "Radiative corrections to Z b anti-b production." In: *Phys. Rev.* D62 (2000), p. 114012. DOI: 10.1103/PhysRevD.62.114012. arXiv: hep-ph/0006304 [hep-ph].

[280] J. M. Campbell, R. K. Ellis, and F. Tramontano. "Single top production and decay at next-to-leading order." In: *Phys. Rev.* D70 (2004), p. 094012. DOI: 10.1103/PhysRevD.70.094012. arXiv: hep-ph/0408158 [hep-ph].

[281] J. M. Campbell, R. Frederix, F. Maltoni, and F. Tramontano. "Next-to-Leading-Order Predictions for t-Channel Single-Top Production at Hadron Colliders." In: *Phys. Rev. Lett.* 102 (2009), p. 182003. DOI: 10.1103/PhysRevLett.102.182003. arXiv: 0903.0005 [hep-ph].

[282] J. M. Campbell, R. Frederix, F. Maltoni, and F. Tramontano. "NLO predictions for t-channel production of single top and fourth generation quarks at hadron colliders." In: *JHEP* 10 (2009), p. 042. DOI: 10.1088/1126-6708/2009/10/042. arXiv: 0907.3933 [hep-ph].